OAK RIDGE NATIONAL LABORATORY LIBRARIES
3 4456 0550421 9

CENTRAL RESEARCH LIBRARY

ORNL-TM-4597

Cy 34

DYNAMIC EXPERIMENTS FOR HEAT TRANSFER AND MIXING STUDIES IN LMFBR FUEL ASSEMBLIES

D. W. Wilson
T. W. Kerlin

OAK RIDGE NATIONAL LABORATORY
CENTRAL RESEARCH LIBRARY
DOCUMENT COLLECTION
LIBRARY LOAN COPY
DO NOT TRANSFER TO ANOTHER PERSON
If you wish someone else to see this document, send in name with document and the library will arrange a loan.
UCN-7969
(3 3-67)

OAK RIDGE NATIONAL LABORATORY
OPERATED BY UNION CARBIDE CORPORATION • FOR THE U.S. ATOMIC ENERGY COMMISSION

Printed in the United States of America. Available from
National Technical Information Service
U.S. Department of Commerce
5285 Port Royal Road, Springfield, Virginia 22151
Price: Printed Copy $7.60; Microfiche $1.45

This report was prepared as an account of work sponsored by the United States Government. Neither the United States nor the United States Atomic Energy Commission, nor any of their employees, nor any of their contractors, subcontractors, or their employees, makes any warranty, express or implied, or assumes any legal liability or responsibility for the accuracy, completeness or usefulness of any information, apparatus, product or process disclosed, or represents that its use would not infringe privately owned rights.

ORNL-TM-4597
UC-79, -79e and to Recipients
of -79m and -79p Who Do Not
Receive Copies Under -79e

Contract No. W-7405-eng-26

INSTRUMENTATION AND CONTROLS DIVISION

DYNAMIC EXPERIMENTS FOR HEAT TRANSFER AND MIXING STUDIES IN LMFBR FUEL ASSEMBLIES

D. W. Wilson[1] and T. W. Kerlin[1]

A thesis presented to the Graduate Council of the University of Tennessee, Knoxville, in partial fulfillment of the requirements for the degree Master of Science.

June 1974

---

[1]Nuclear Engineering Department, the University of Tennessee, Knoxville.

NOTICE This document contains information of a preliminary nature and was prepared primarily for internal use at the Oak Ridge National Laboratory. It is subject to revision or correction and therefore does not represent a final report.

OAK RIDGE NATIONAL LABORATORY
Oak Ridge, Tennessee 37830
operated by
UNION CARBIDE CORPORATION
for the
U. S. ATOMIC ENERGY COMMISSION

OAK RIDGE NATIONAL LABORATORY LIBRARIES

3 4456 0550421 9

ACKNOWLEDGMENTS

This work was performed in cooperation with the Instrumentation and Controls Division of the Oak Ridge National Laboratory which is operated by Union Carbide Corporation for the U.S. Atomic Energy Commission.

Financial support for this work was also provided by an AEC Traineeship in Nuclear Engineering.

The author wishes to express his deep appreciation to the individuals who contributed to various phases of this work.

Dr. T. W. Kerlin, who served as advisor, suggested this project and provided invaluable guidance and instruction throughout the study.

Mr. D. N. Fry and Mr. C. B. Stokes of the Oak Ridge National Laboratory were responsible for performing the experiments and were helpful consultants.

I would also like to thank my wife, Susan, for her help in the preparation of this manuscript.

ABSTRACT

Dynamic experiments were performed on an electrically heated mockup of a Liquid Metal Fast Breeder Reactor (LMFBR) fuel assembly (the Fuel Failure Mockup at Oak Ridge National Laboratory) to determine the temperature-to-power frequency response. The experimental frequency response results were analyzed and interpreted to give information on flow and heat transfer patterns in the fuel assembly.

The experimental frequency response was obtained by perturbing the power supplied to a single heated rod in the 19 rod assembly with a pseudorandom binary sequence signal and then analyzing simultaneously the input signal and the resultant output temperature signals measured at several points in the assembly.

Simplified theoretical models were used to aid in interpreting the results. One model was based on an assumption of well mixed flow and the other on slug flow.

A method was developed to provide information on energy flow patterns. Preliminary use of this method clearly showed the presence of edge swirl effects and the dependency of edge swirl on the smoothness of the can that contained the test section.

Additional analysis showed that slug flow could be distinguished from well mixed flow and that slug flow was predominant at the beginning of the heated section and well mixed flow was predominant at the exit of the heated section.

This study gives the first experience with a new experimental technique that appears to have the capability of providing useful information on energy flow patterns and flow mechanisms in a mockup of LMFBR fuel assemblies.

TABLE OF CONTENTS

LIST OF FIGURES

FIGURE PAGE

FIGURE PAGE

FIGURE PAGE

FIGURE PAGE

FIGURE PAGE

FIGURE PAGE

CHAPTER I

INTRODUCTION

I. STATEMENT OF PROBLEM

The purpose of this study was to make a preliminary assessment of the usefulness of dynamic experiments for providing information on flow and heat transfer patterns in an electrically heated mockup of a Liquid Metal Fast Breeder Reactor (LMFBR) fuel assembly.

II. IMPORTANCE OF PROBLEM

The question of whether small fuel cladding failures in a fuel pin would cause cladding failures of adjacent fuel pins and resultant propagation of failures is very important to the LMFBR program. To answer this question, Argonne National Laboratory has been assigned the overall responsibility for the fuel-failure propagation investigation, and a broad program has been outlined in which in-pile experiments supported by out-of-pile tests play a major role.

Out-of-pile fuel-failure-propagation experiments are performed at the Oak Ridge National Laboratory (ORNL) Fuel Failure Mockup (FFM) facility. The FFM is an electrically-heated sodium-cooled mockup of an LMFBR fuel assembly. This facility is used to subject simulated LMFBR core assemblies to thermal and hydraulic testing at typical operating conditions. The main purpose of the FFM is to investigate the effect

of various types of flow blockages on the temperature profiles in the core, downstream of the blockage.

This study will be concerned only with the tests on bundles with no blockages which were performed to give a reference point for the tests on bundles with installed blockages.

The FFM fuel assembly has 19 rods while the Fast Test Reactor fuel assembly will have 217 rods. The use of techniques developed in this study may help determine the validity of using the results from a 19 rod bundle to predict the behavior of a 217 rod bundle.

III. RATIONALE FOR THE USE OF DYNAMIC TESTING IN HEAT TRANSFER STUDIES

Dynamics tests have the potential for providing information about the system that is not available from results of steady state tests. For example, a temperature rise at some point in the system that resulted from heat input in some other part of the system could be measured, but steady state measurements could not give any detailed information on the mechanism for heat transfer. All that could be concluded is that the heat arrived at the measurement point. A dynamics test would involve time varying heater inputs with resulting time varying temperatures. The delay and shape of the temperature response to a heat input perturbation could be interpreted to yield information on the influence of flow conditions on heat transfer. A major objective of this work is to bring this general observation on the potential benefits of dynamic testing into specific use for the analysis of the FFM.

CHAPTER II

FFM SYSTEM DESCRIPTION

The configuration of the FFM test section is shown in Figure II-1. Sodium enters at the lower "T", flows vertically through the test section and exits at the upper "T". Both ends of the test section are closed with seal welds and bolted flanges. Figure II-1 shows that the bundle has an unheated entrance length followed by a heated section and an unheated exit length.

The 19 rod bundle was supplied with appropriate control equipment to regulate power from 0 to 22 kw per pin. Thus, the electrical power supplied to the bundle could be varied from 0 to 418 kw.

The rods have a diameter of 0.23 inch and are separated by the 0.056 inch diameter helical wrap as shown in Section A-A of Figure II-1. The helical wrap had a right-hand-pitch in bundles 2A and 2B and a left-hand-pitch in bundle 1B. For measurement purposes, thermocouples were embedded in the center of the helical wrap and are represented by the small circles adjacent to the heater cross-section in Figures II-2, II-3, and II-4. The number in the small circle gives the distance from the beginning of the heated zone to the thermocouple. In this study, thermocouples are identified by the rod number to which they are attached, followed by the distance of the thermocouple above the start of the heated zone. For example, the thermocouple on rod 4 at the 21 inch level is designated by 0421.

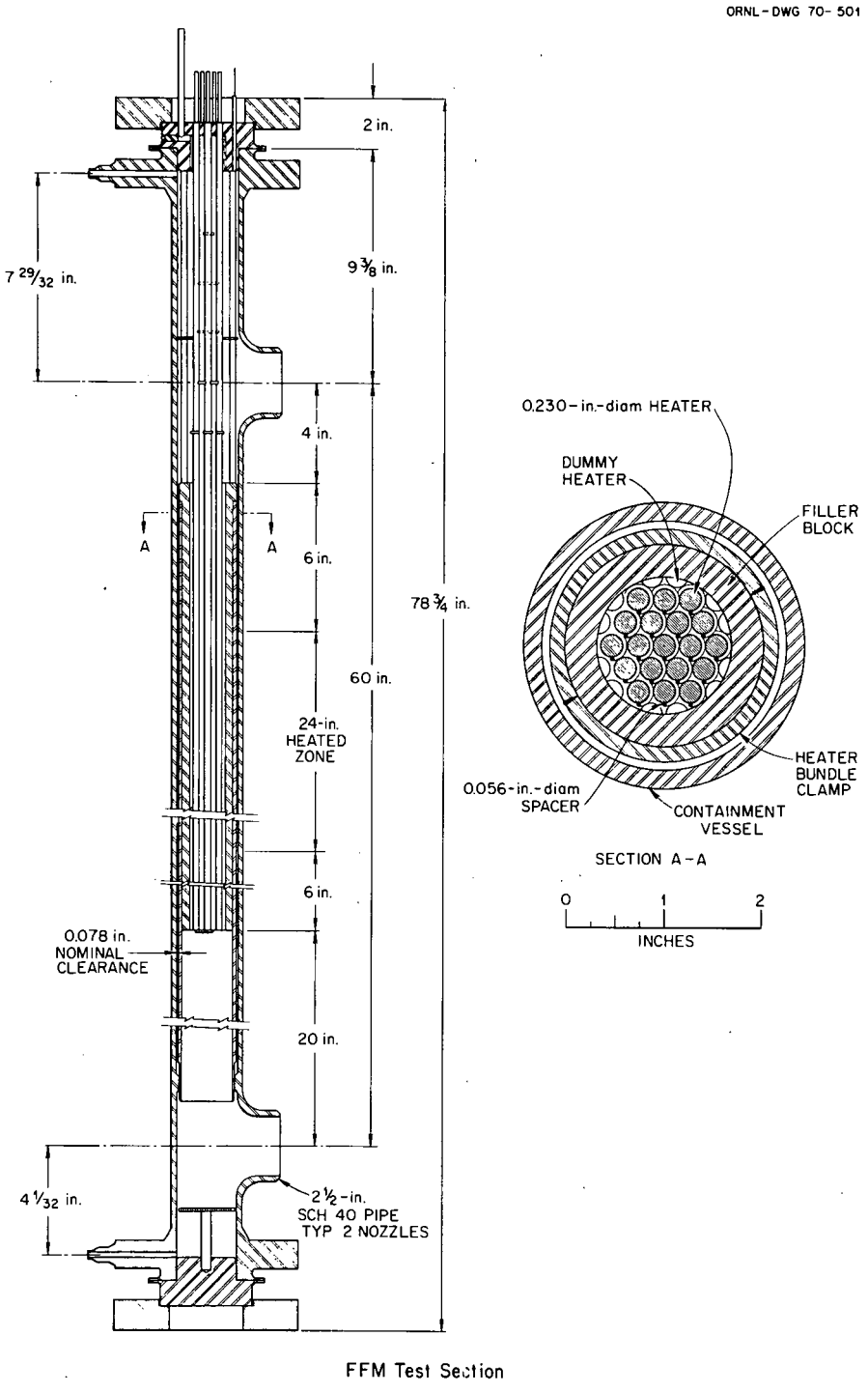

Figure II-1. LMFBR-FFM bundle number 2.

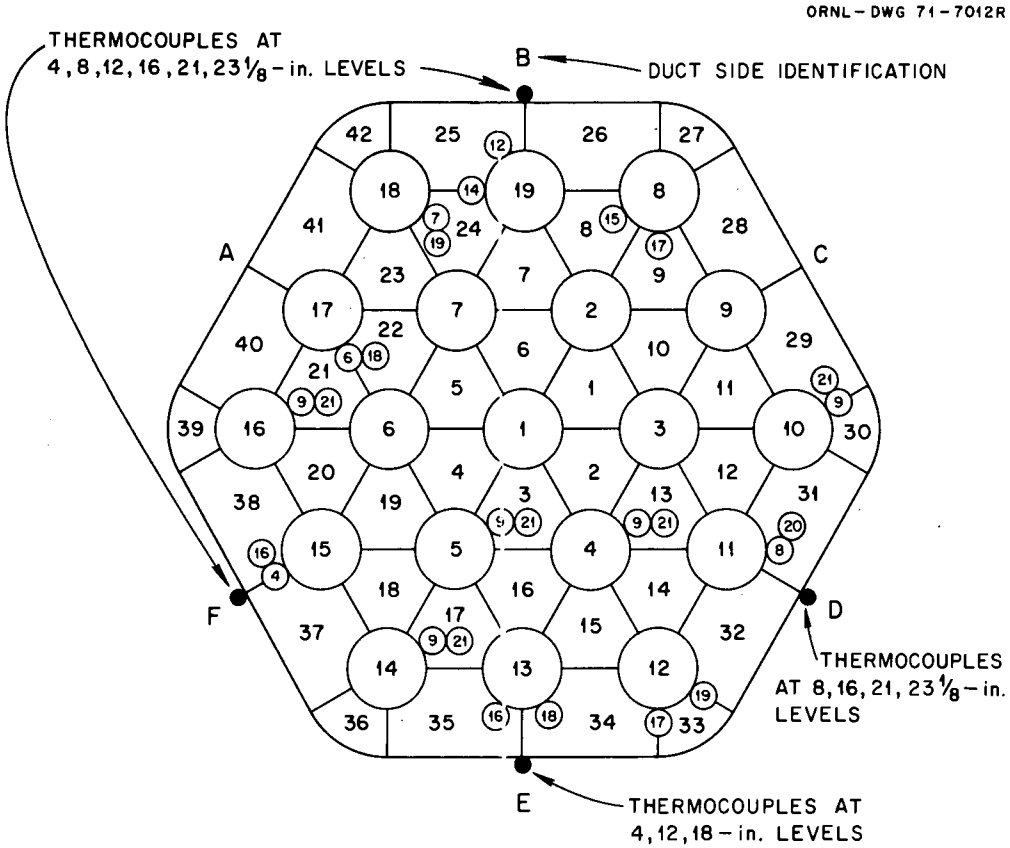

VIEW LOOKING UPSTREAM

LOCATIONS OF UNGROUNDED WIRE-WRAP THERMOCOUPLES. THE SMALL CIRCLES INDICATE THE LOCATION OF THE WRAP FOR EACH JUNCTION AND THE NUMBERS IN THE ROD OPPOSITE THEM INDICATE THE AXIAL POSITIONS.

Figure II-2. FFM bundle 2A.

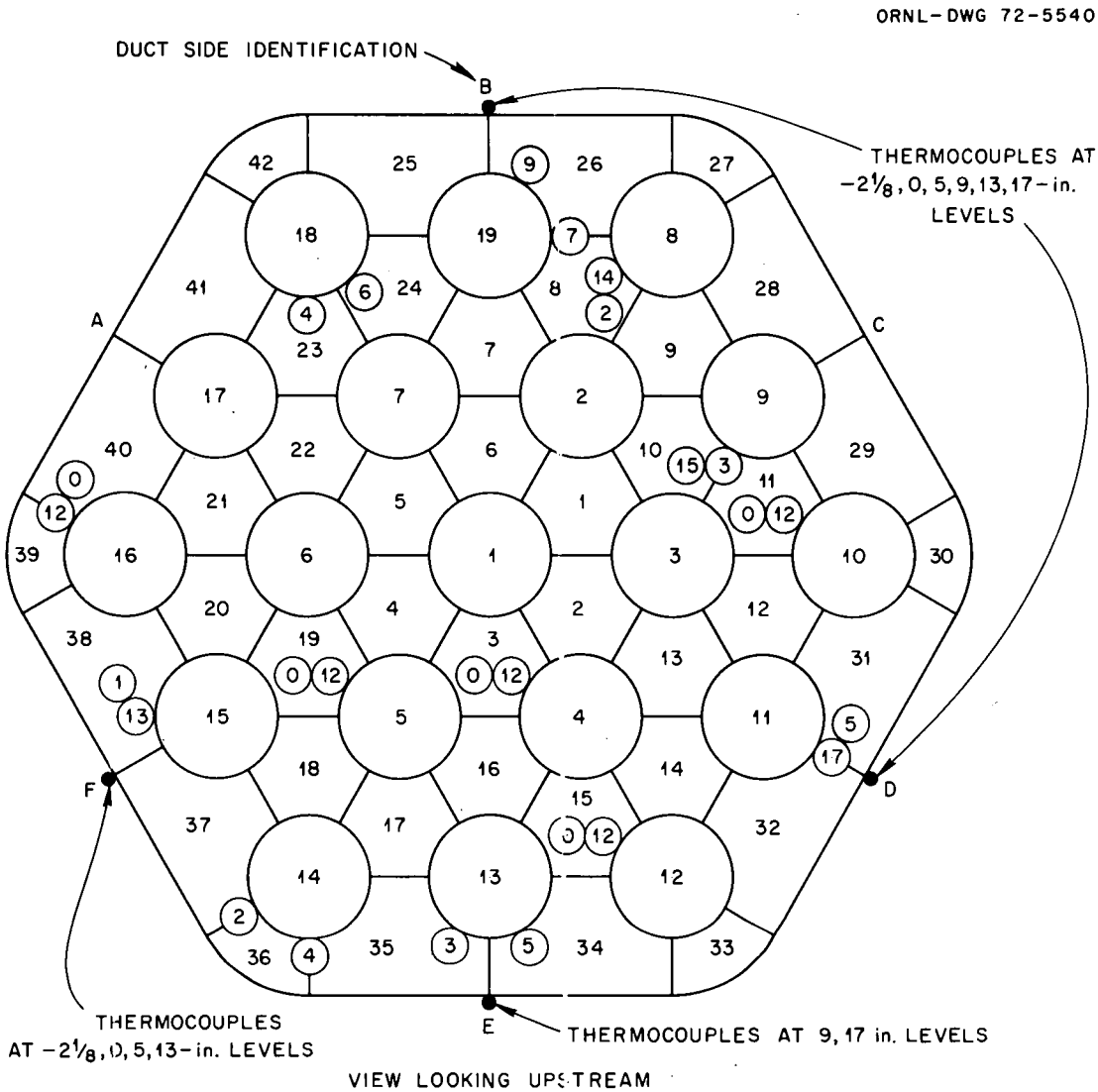

LOCATIONS OF UNGROUNDED WIRE-WRAP THERMOCOUPLES. THE SMALL CIRCLES INDICATE THE LOCATION OF THE WRAP FOR EACH JUNCTION, AND THE NUMBERS IN THE ROD OPPOSITE THEM INDICATE THE AXIAL POSITIONS.

Figure II-3. FFM bundle 2B.

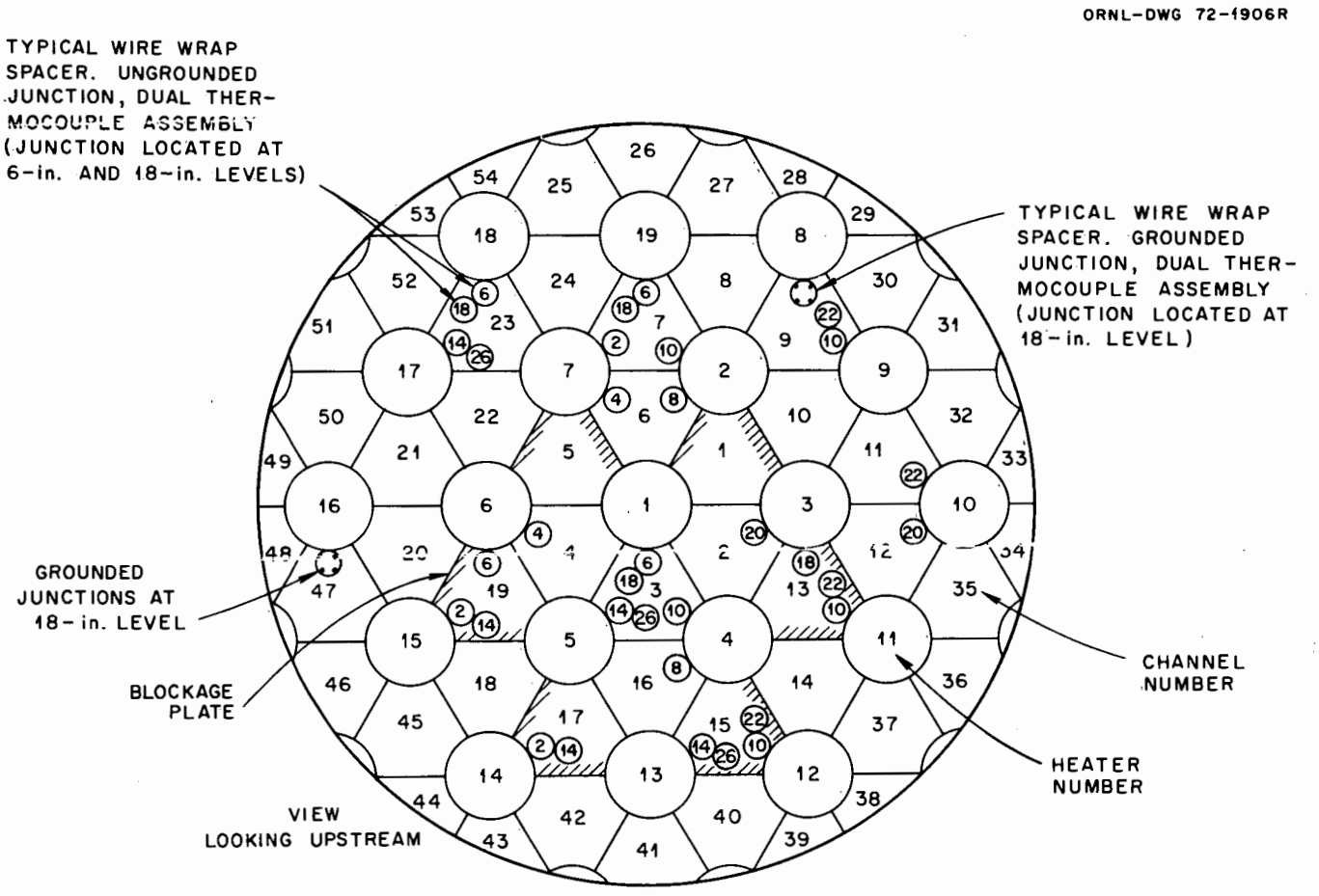

Figure II-4. FFM bundle 1B.

The heating element is located in the center of the rod and has a 0.057 inch diameter nichrome wire coiled into a 0.175 inch outside diameter spiral. The electrical insulation in the rod is high purity boron nitride. The heater sheath is type 304 stainless steel 0.012 inches thick. A schematic diagram of a rod is shown in Figure II-5.

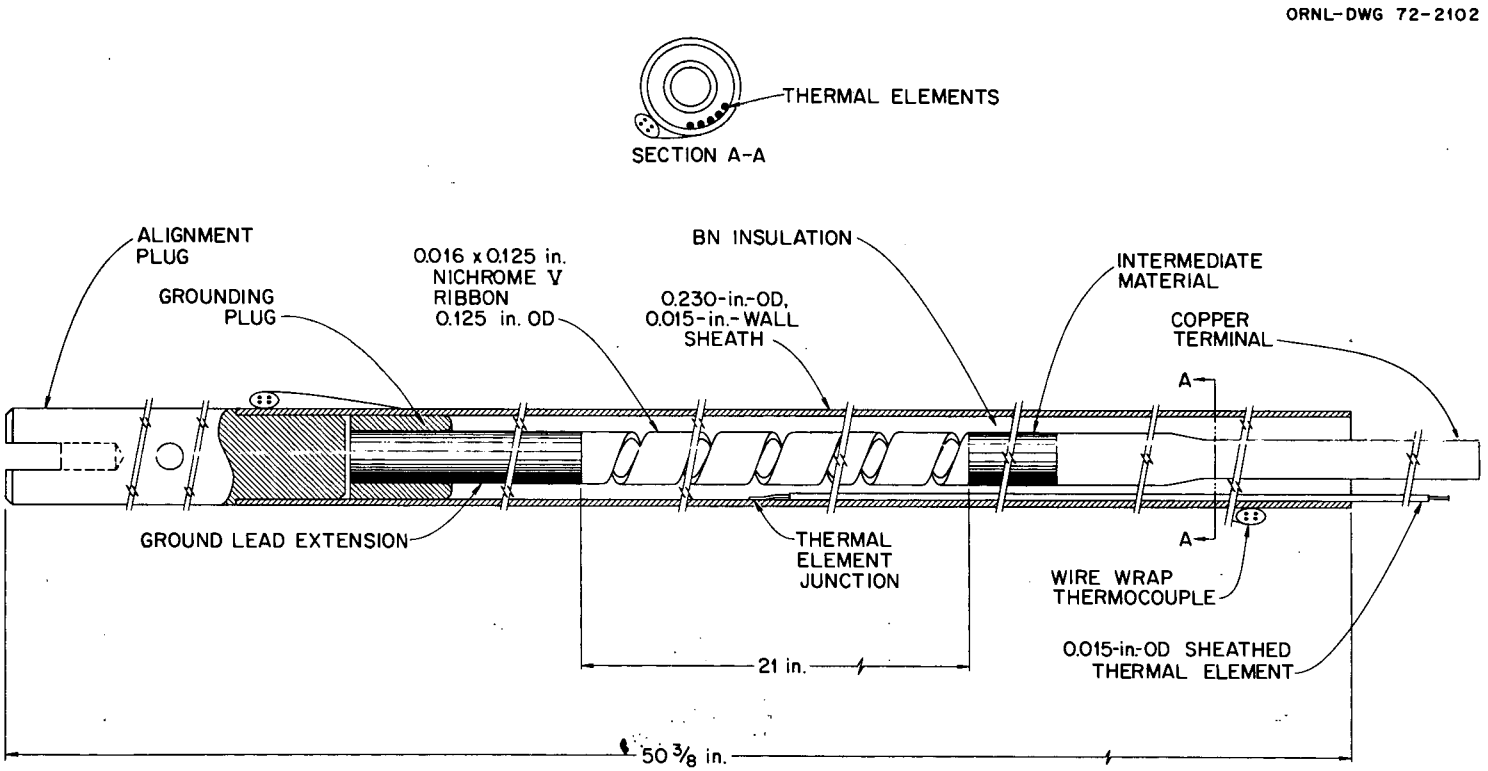

Figure II-5. Prototypic category-II heater to simulate LMFBR fuel pins. Cross section.

CHAPTER III

EXPERIMENTAL PROCEDURE

A number of different testing procedures may be used to obtain experimental information on system dynamics. In this work, frequency response measurements were used. In principle, frequency response tests involve measuring the responses to sinusoidal inputs at selected frequencies. In practice, modern techniques can give equivalent results using nonsinusoidal inputs and Fourier analysis. Frequency response testing with periodic inputs has the advantage that high accuracy can be obtained by repetition of the input through the use of multiple periods of the input.

Frequency response results can be obtained by putting an input into a system and Fourier analyzing the input and output signals. Four steps were followed in the FFM frequency response tests:

1. The input signal was chosen.
2. The system was perturbed by the input signal.*
3. The input signal and the resultant output signal were recorded.*
4. The recorded signals were analyzed.

---

*Mr. D. N. Fry of Oak Ridge National Laboratory performed the experiments.

I. TEST SIGNAL

The test signal used in these experiments was a pseudorandom binary sequence (PRBS).[1] This periodic signal has the important property that a number of harmonics have nearly the same amplitude. This is important since one experiment can give the frequency response over a range of frequencies. The frequency response is specified by the ratio of the amplitude of the output to the amplitude of the input and the phase difference between the input and the output.

The frequency response may be obtained with general, nonsinusoidal, periodic input signals by Fourier analysis. The input and output signals may be expressed as a Fourier series:[2]

$$I(t) = C_k \, e^{jw_k t}$$

$$O(t) = C_k \, e^{jw_k t} \, G(jw_k)$$

where

$w_k = \frac{2k\pi}{T}$,

T = period,

C_k = complex Fourier coefficient, and

$G(jw_k)$ = frequency response.

The input-output cross power spectrum, P_{IO}, and the power spectrum of the input, P_{II}, are given by

$$P_{IO} = G(jw_k)\ C_k C_{-k}$$

$$P_{II} = C_k C_{-k}$$

then the frequency response is

$$G(jw_k) = \frac{P_{IO}}{P_{II}}$$

Thus, the power spectrum of the input and the input-output cross power spectrum will determine the frequency response.

The power spectrum of an N-bit PRBS is given by:[3]

$$P_k = \frac{A^2}{N^2} \qquad \text{for } k = 0$$

$$P = \frac{2(N+1)A^2}{N^2} \quad \frac{(\sin \frac{k\pi}{N})^2}{\left(\frac{k\pi}{N}\right)^2} \qquad \text{for } k \neq 0$$

where

P_k = power in the k^{th} harmonic,

A = signal amplitude, and

k = harmonic number.

For a PRBS signal, the lowest available frequency is the fundamental frequency:

$$f_o = \frac{1}{T} \qquad \text{(Hz)}$$

where

f_o = fundamental frequency (Hz), and

T = period length (sec).

The specification of the highest frequency available is less definite. A practical "rule of thumb," however, is: the harmonic frequency at which the signal power is down to one-half of its maximum power is the highest frequency at which useful information is likely to be obtained. The half-power frequency can be shown to be:[4]

$$f = \frac{0.44}{\Delta t} \qquad \text{(Hz)}$$

where

Δt = time duration of a bit.

It follows that the useful frequency range of a PRBS signal is:

$$\frac{1}{T} \leq f \leq \frac{0.44}{\Delta t} \qquad \text{(Hz)}$$

This expression shows that the low frequency limit depends only on the period, and the high frequency limit depends only on the bit duration.

II. CHOICE OF PRBS SEQUENCE

Before selecting an input signal, one has to determine the frequency range of interest, and the frequency resolution desired in order to concentrate the signal energy in the range of frequencies desired. Previous experiments on the FFM[5] showed that the range of interest is about 0.1 Hz to 3 Hz.

The signal chosen for the tests on bundles 2A and 2B was a 127 bit PRBS with a bit duration of 0.1032 seconds and a period of 13.12 seconds. These values were obtained by adjusting the available settings on equipment and inputs to analysis programs as follows.

1. The data were recorded on a tape recorder at a rate of 1.875 inches per second and played back at a speed of 60 inches per second for a speed up of 32. Since the Beckman 4040 digitizer at ORNL used in these tests has a digitizing rate of 1000 points per second, the real time digitizing rate is $\frac{1000}{32}$ = 31.25 samples per second.

2. The data were analyzed by the computer code CROSSPOW[6] which uses a Fast Fourier Transform technique to Fourier transform the data. The Fast Fourier Transform has to have a data block size of 2^n for integer values of n. In this case, the selected value of n was 11 to give a block size of 2048 points. For the calculated Fast Fourier Transform to be accurate, the record analyzed must consist of an integral number of periods of the signal being transformed. This leads to the following requirements:

$$NT = \frac{(32)(2048)}{1000}$$

where N is an integral number of periods in a data block and T is the period of the signal.

3. It is known that

$$Z\Delta t_{bit} = T \quad \text{so}$$

$$\Delta t_{bit} = \frac{T}{Z} = \frac{T}{127} \quad \text{or}$$

$$\Delta t_{bit} = \frac{(32)(2048)}{(1000)(127)(N)} \qquad \text{(sec)}$$

The number of periods (N) was arbitrarily selected to be five so $\Delta t_{bit} = 0.1032$ seconds and $T = 13.11$ seconds. The bit duration and period chosen gave a useful frequency range of:

$$0.076 \leq f \leq 4.26 \qquad \text{(Hz)}$$

The test signal for use in bundle 1B was different because a new, special purpose Fourier analyzer (a Hewlett-Packard 5451A Fourier Analyzer) was available. This eliminated the 1000 samples per second digitizing rate restriction in earlier tests which used the Beckman 4040 digitizer.

The signal chosen for the tests on bundle 1B was a 127 bit PRBS with a bit duration of 0.1575 seconds and a period of 20 seconds. The data from these tests were handled as follows:

1. The data were recorded on a tape recorder at a rate of 1.875 inches per second and played back at a rate of 3.75 inches per second for a speed up of 2.

2. The period was selected to be 20 seconds so

$$\Delta t_{bit} = \frac{20}{127} = 0.1575 \text{ seconds}$$

The bit duration and period give a useful frequency range of:

$$0.5 \leq f \leq 2.8 \qquad \text{(Hz)}$$

III. SIGNAL INPUT

Figure III-1 shows the flow diagram for the input signal. The PRBS signal was generated by a Hewlett-Packard 3722A signal generator. From the signal generator the signal went to the appropriate heater control circuit (only a single heater was used in each test) and then to the Silicon Controlled Rectifier (SCR) which controlled the power to the heaters. The timer was used to set the period of the PRBS accurately. A Transitor Specialties INC. Universal Counter model 361 was used to measure the period.

IV. SIGNAL OUTPUT

The flow diagram for the output signal is shown in Figure III-2. The junction box was the terminal point for all of the thermocouples. Six different signals left the junction box and went to six Princeton Applied Research 113 preamplifiers. The output signals from the amplifiers and the input signal were recorded on a Sanborn 3907A FM tape recorder. An oscilloscope was used during the tests to observe

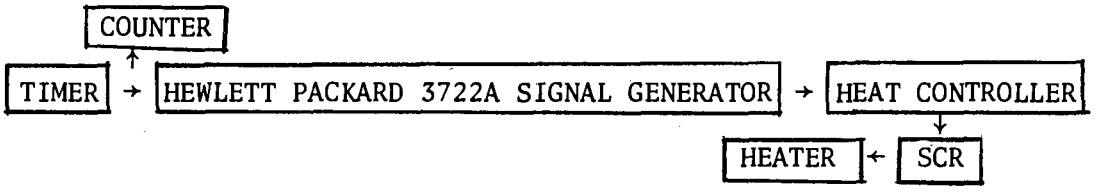

Figure III-1. Flow diagram for the input signal.

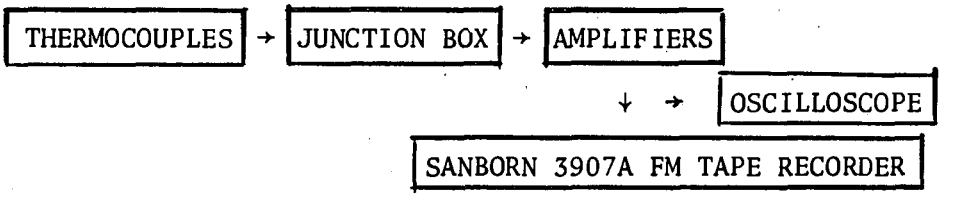

Figure III-2. Flow diagram for the output signal.

the output signal from the amplifiers so that they could be adjusted if necessary. Typical input and output signals are shown in Figure III-3.

V. DATA ANALYSIS

The flow diagram for the data analysis for bundles 2A and 2B is shown in Figure III-4. The Beckman 4040 analog-to-digital converter was used to digitize the experimental data and write the results on a digital tape. This digital record was used as the input data for the computer program CROSSPOW.[6] This code uses the Fast Fourier Transform technique to Fourier transform the input and output signals and thus derive the power spectrum of the input signal and the cross power spectrum of the input and output signals. The frequency response at each frequency of analysis is found by dividing the cross power spectrum by the input power spectrum.

The flow diagram for the data analysis for bundle 1B is shown in Figure III-5. A Hewlett-Packard 5451A Fourier Analyzer uses a Fast Fourier Transform algorithm to Fourier transform the input and output signals. The frequency response is again found by dividing the cross power spectrum by the input power spectrum.

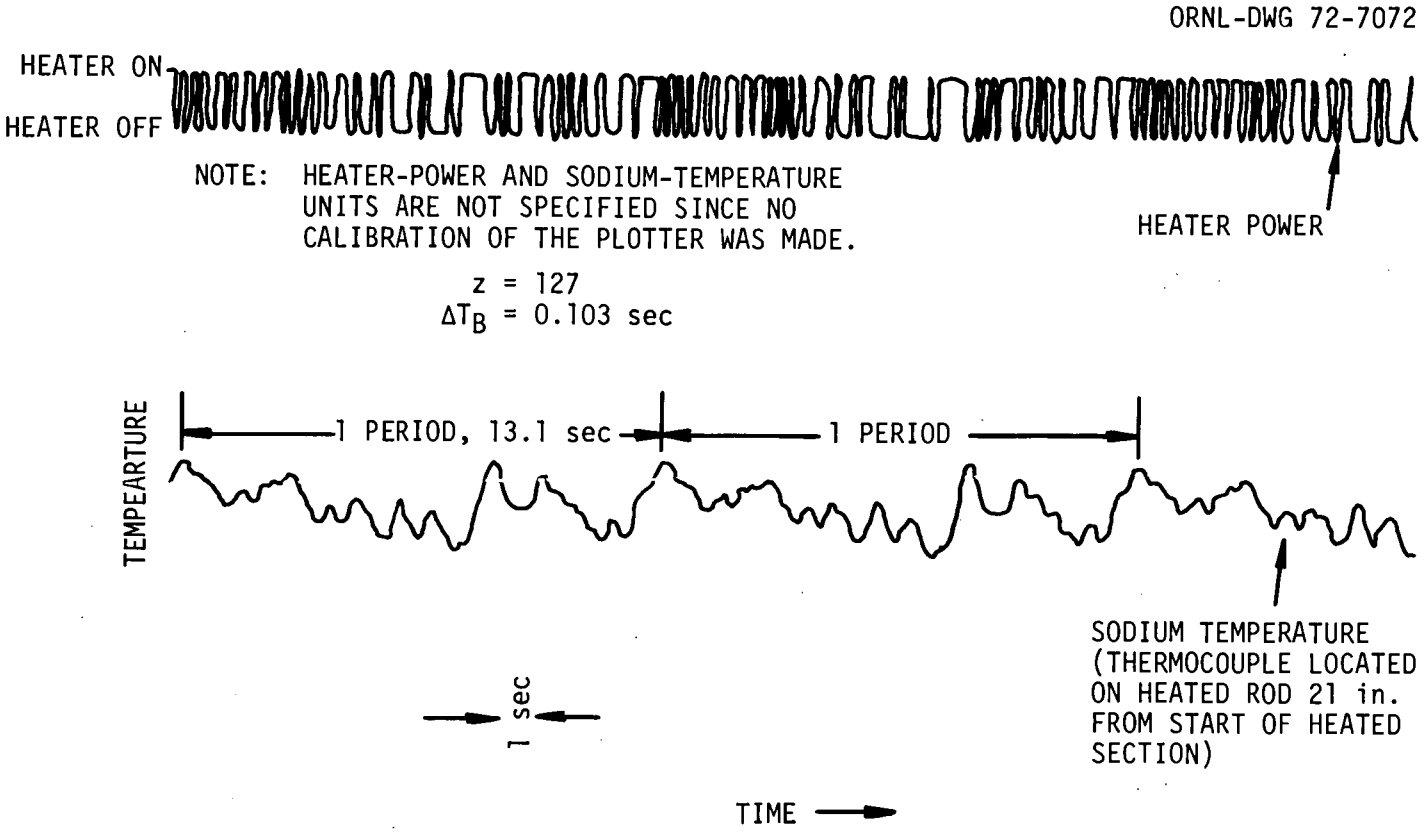

Figure III-3. Heater-power and sodium-temperature response in FFM frequency-response test.

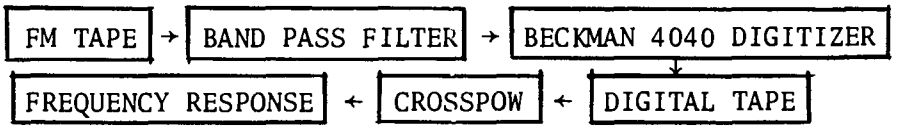

Figure III-4. Flow diagram for data analysis for bundles 2A and 2B.

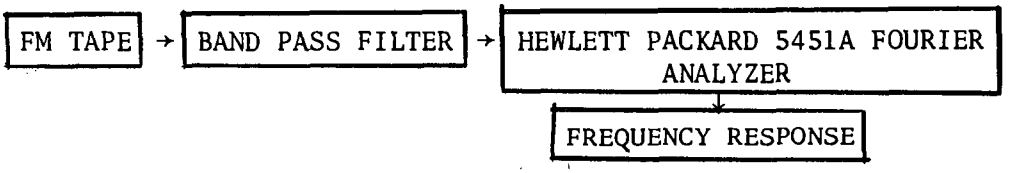

Figure III-5. Flow diagram for data analysis for bundle 1B.

CHAPTER IV

THEORETICAL RESULTS

The objective of the dynamic tests on the FFM was to provide information on flow and heat transfer in the bundle. To help understand the experimental results, simplified theoretical models were developed for well mixed flow and slug flow which were taken as the likely extremes of flow conditions that actually exist in the bundle. The theoretical models were not intended to predict the detailed behavior of the FFM so only the trends of the theoretical results were observed. Both models simulate only a single pin and the coolant in an assumed channel around the pin, thus omitting the important effects of the wire wraps on inter-channel mixing. These simplifications restrict the use of the model results to application as an aid to understanding rather than as a predictor of detailed, quantitative behavior. In both models the coefficients which were used are shown in Table I. The accuracy of the values in Table I is not a major concern since only trends were of interest.

I. WELL MIXED MODEL

The well mixed model assumes that fluid mixes in the direction of flow. Figure IV-1 shows a schematic representation of the simple simulation used in this study. The model simulates one rod and the fluid around the rod. The model has two axial sections for the fluid and two axial sections for the solid. The assumptions in this model were:

TABLE I

COEFFICIENT VALUES USED IN THE THEORETICAL MODELS

	Outside Diameter of Stainless Steel	0.0192	ft
	Inside Diameter of Stainless Steel	0.0165	ft
ρ_1	Density of Boron Nitride	125.0	lb/ft^3
C_1	Specific Heat of Boron Nitride	0.418	Btu/lb°F
k_1	Thermal Conductivity of Boron Nitride	0.0025	Btu/sec°F ft
ρ_2	Density of Heating Element	312.5	lb/ft^3
C_2	Specific Heat of Heating Element	0.1	Btu/lb°F
k_2	Thermal Conductivity of Heating Element	0.0025	Btu/sec°F ft
ρ_3	Density of Stainless Steel	500.0	lb/ft^3
C_3	Specific Heat of Stainless Steel	0.1	Btu/lb°F
k_3	Thermal Conductivity of Stainless Steel	0.0034	Btu/sec°F ft
h_{film}	Film Heat Transfer Coefficient	8.33	$Btu/sec°F\ ft^2$
H	Effective Heat Transfer Coefficient	0.34	$Btu/sec°F\ ft^2$

NOTE: $$H = \frac{1}{\frac{1}{4k_1} + \frac{\ln(r_2/r_1)}{2k_2} + \frac{\ln(r_3/r_2)}{2k_3} + \frac{1}{2r_3 h_{film}}} \times \frac{1}{2r_3}$$

where

subscript 1 refers to the heating element,
subscript 2 refers to the boron nitride,
subscript 3 refers to the cladding,
H = effective heat transfer coefficient,
k = thermal conductivity,
r = radius,
C = specific heat, and
h_{film} = film heat transfer coefficient.

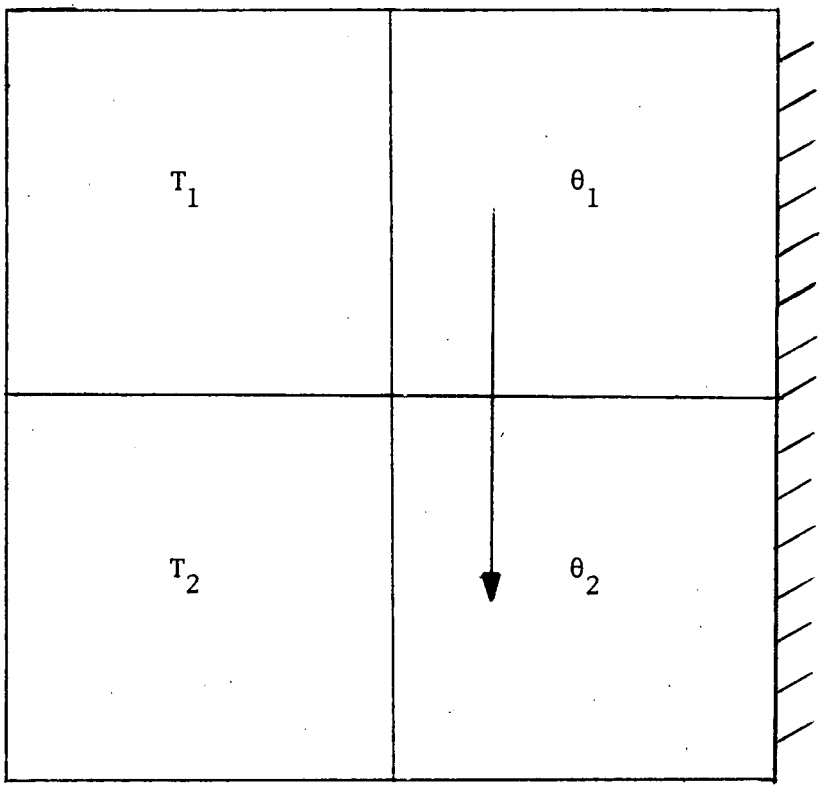

Figure IV-1. Well mixed model schematic.

1. No conduction occurs in the fluid.
2. No axial heat conduction occurs in the solid or fluid.
3. Well mixed fluid exists in each lump.
4. Treating a whole section as a single lump is valid.

The equations that describe the model are:

$$(MC)_{solid} \frac{dT_1}{dt} = P_1 - HA(T_1 - \theta_1) \quad (1)$$

$$(MC)_{solid} \frac{dT_2}{dt} = P_2 - HA(T_2 - \theta_2) \quad (2)$$

$$(MC)_{liquid} \frac{d\theta_1}{dt} = HA(T_1 - \theta_1) - WC(\theta_1 - \theta_{in}) \quad (3)$$

$$(MC)_{liquid} \frac{d\theta_2}{dt} = HA(T_2 - \theta_2) - WC(\theta_2 - \theta_1) \quad (4)$$

where

M	= mass	(lb)
W	= mass flow rate	(lb/sec)
P_i	= heat generation rate in section i	(Btu/sec)
A	= heat transfer surface area	(ft^2)
H	= effective heat transfer coefficient (includes film resistance and internal rod resistance)	(Btu/sec °F ft^2)
t	= time	(sec)
C	= specific heat	(Btu/lb °F)
T_i	= temperature of solid in section i	(°F)
θ_i	= temperature of liquid in section i	(°F)

Standard procedures (7) were followed to obtain the following transfer functions from equations 1 through 4:

$$\frac{\delta\theta_1(s)}{\delta P_1(s)} = \frac{ca}{s^2 + (b + c + \frac{1}{R})s + \frac{b}{R}} \tag{5}$$

$$\frac{\delta\theta_2(s)}{\delta P_2(s)} = \frac{ca(s^2 + (b + c + \frac{2}{R})s + \frac{2b}{R})}{(s^2 + \frac{b}{R} + (b + c + \frac{1}{R})s)^2} \tag{6}$$

$$\frac{\delta\theta_2(s)}{\delta\theta_1(s)} = \frac{s^2 + (b + c + \frac{2}{R})s + \frac{2b}{R}}{s^2 + (b + c + \frac{1}{R})s + \frac{b}{R}} \tag{7}$$

where

$b = \frac{(HA)}{(MC)_{solid}}$,

$R = \frac{(WC)}{(MC)_{liquid}}$,

$a = \frac{1}{(MC)_{solid}}$,

$c = \frac{(HA)}{(MC)_{liquid}}$,

P_1 = heat generation rate in section 1,

P_2 = heat generation rate in section 2, and

δ denotes deviation from steady state.

These transfer functions were chosen since the form of the experimental frequency response is (fluid temperature)/(power).

The frequency response for θ_1 was found by substituting $j\omega$ (ω is the angular frequency) for s in equation 5 and carrying out the complex arithmetic. Similarly, the frequency response for θ_2 was found by substituting $j\omega$ for s in equation 6. Typical frequency response results obtained with the well mixed model are shown in Figures IV-2 and IV-3.

As will be seen in subsequent sections, it is enlightening to consider the ratio of the frequency response gains obtained for two different observation points at a given flow or for a given observation point at two different flows. This is because these gain ratios emphasize the differences between well mixed flow and slug flow. Figure IV-4 shows the ratio, (frequency response gain for θ_2)/(frequency response gain for θ_1) computed by the well mixed model at a flow rate of 54 gallons per minute (GPM). The phase difference is shown in Figure IV-5. Figure IV-6 shows the ratio, (frequency response gain at 54 GPM)/(frequency response gain at 10 GPM) computed by the well mixed model at θ_1. The phase difference for this case is shown in Figure IV-7.

It may be noted that the calculated results show that the gain ratios computed by the well mixed model approach unity monotonically as the frequency increases. The physical basis for this may be understood if one notes that the temperature changes for thermocouples on or near heated rods are due to two causes: heat swept to the thermocouple from upstream mainly by convection, and heat added in the vicinity of the thermocouple and carried to the thermocouple mainly by conduction. To a first approximation, both of these processes behave like first order lags. However, for the FFM, the break frequency for the

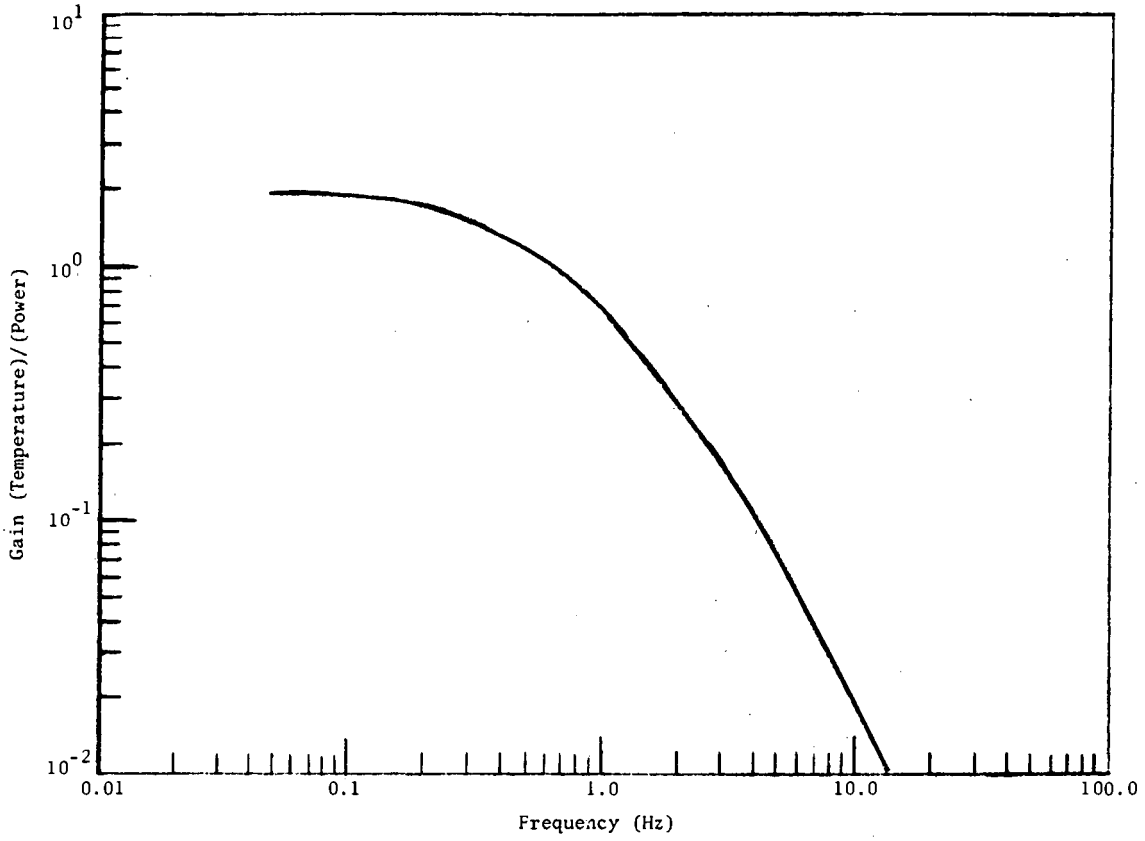

Figure IV-2. Frequency response gain computed by the well mixed model for $\delta\theta_1/\delta P$ at 54 GPM.

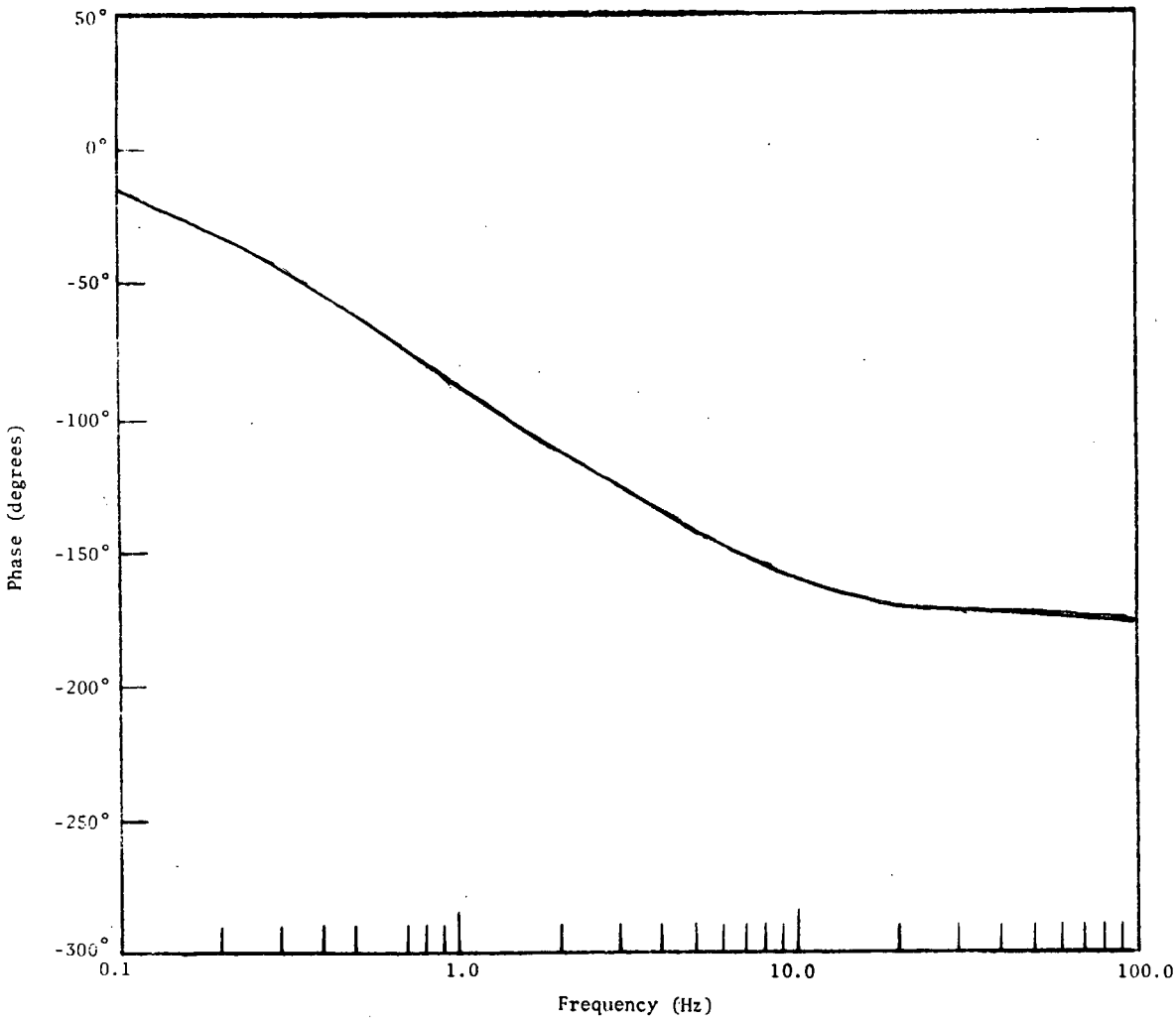

Figure IV-3. Frequency response phase computed by the well mixed model for $\delta\theta_1/\delta P$ at 54 GPM.

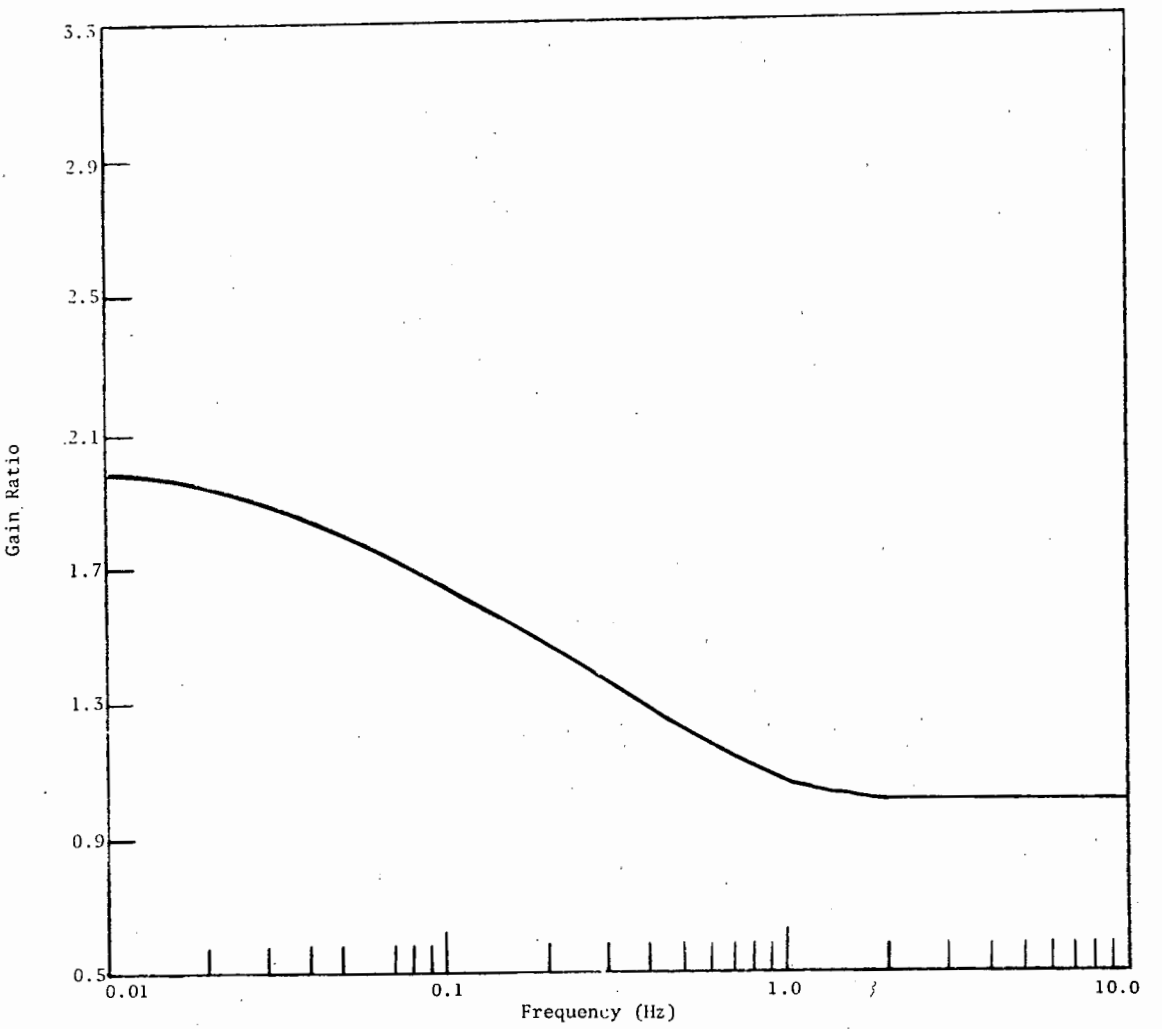

Figure IV-4. Gain ratios, (gain at θ_2)/(gain at θ_1), computed by the well mixed model at 54 GPM.

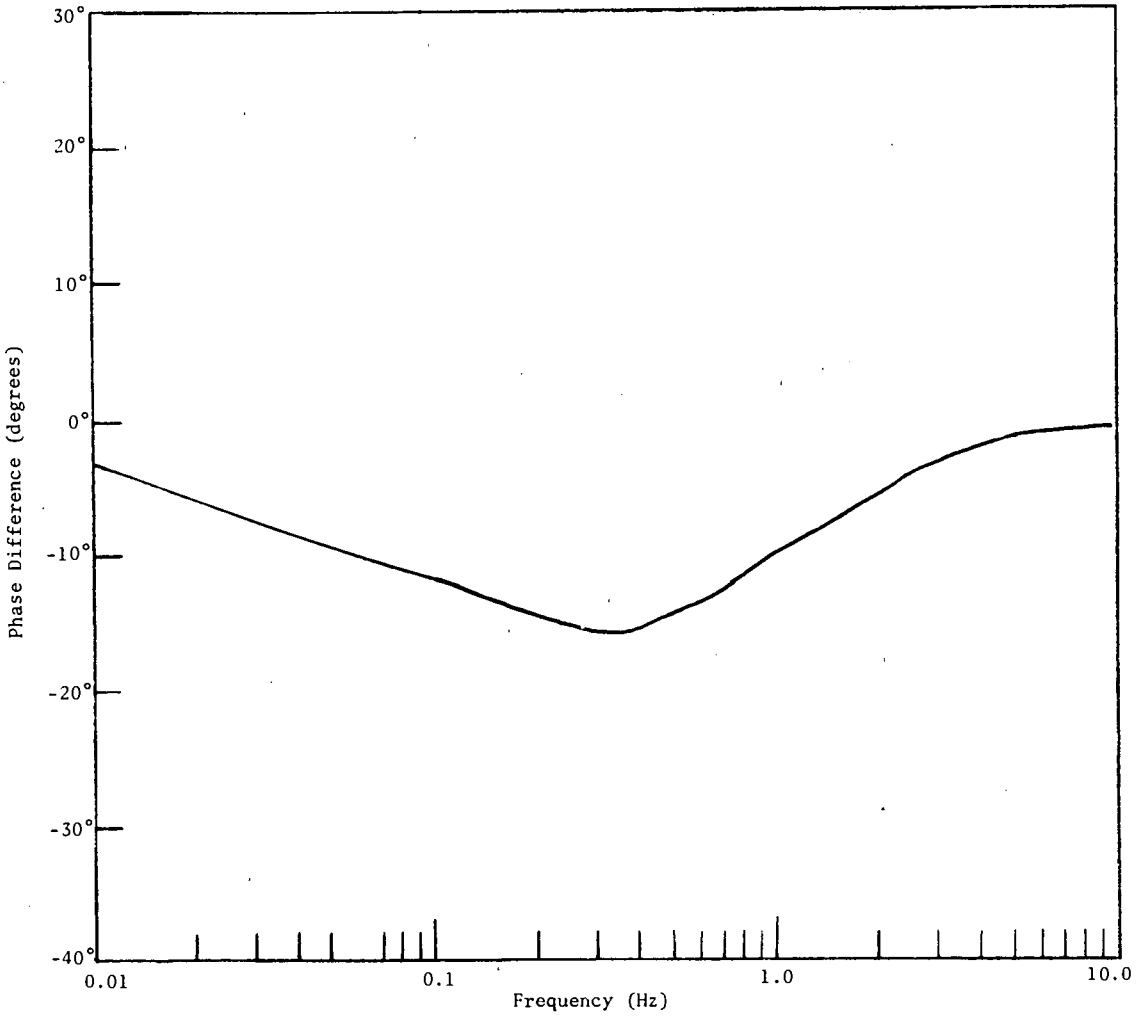

Figure IV-5. Phase differences, (phase at θ_2)-(phase at θ_1), computed by the well mixed model at 54 GPM.

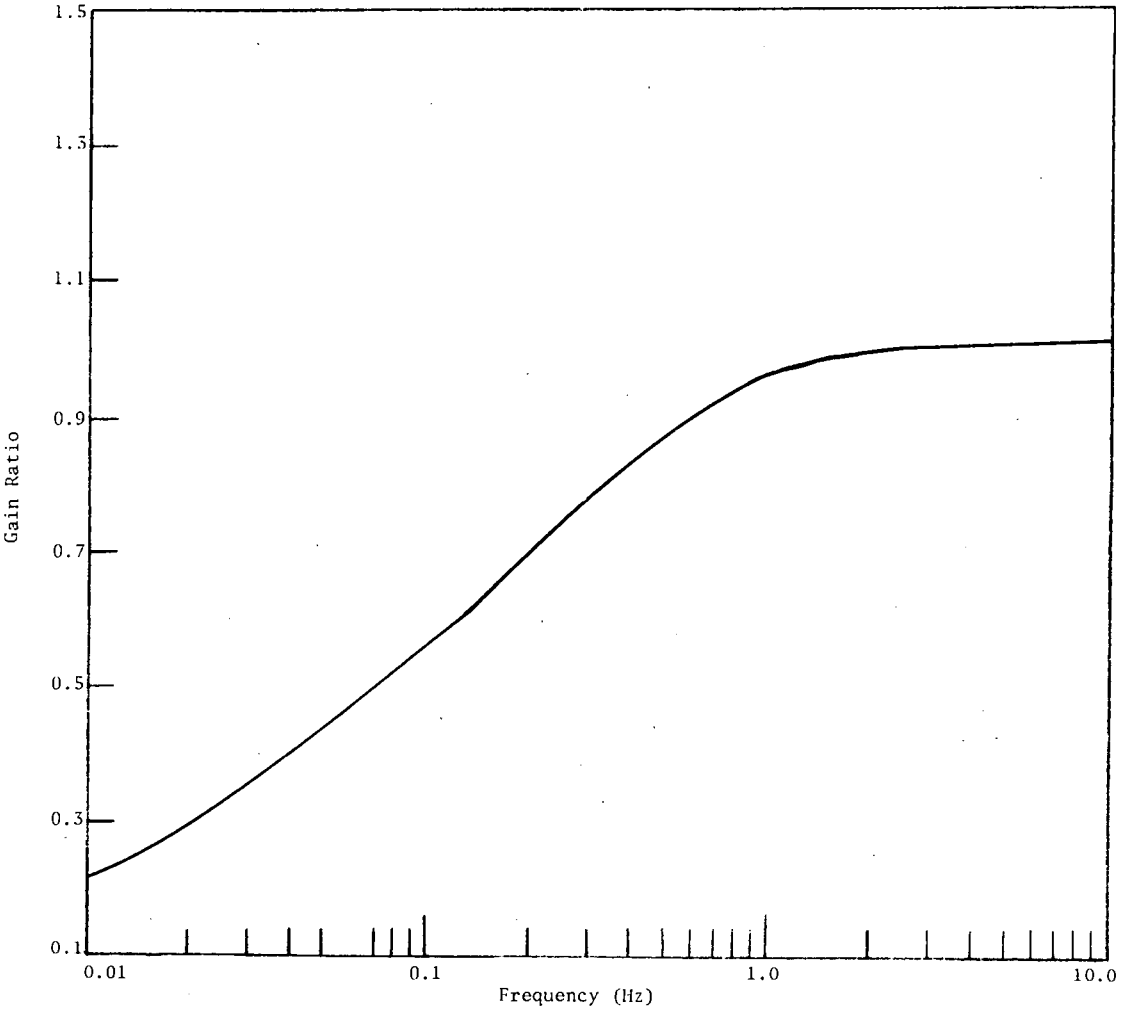

Figure IV-6. Gain ratios, (gain at 54 GPM)/(gain at 10 GPM), computed by the well mixed model at θ_1.

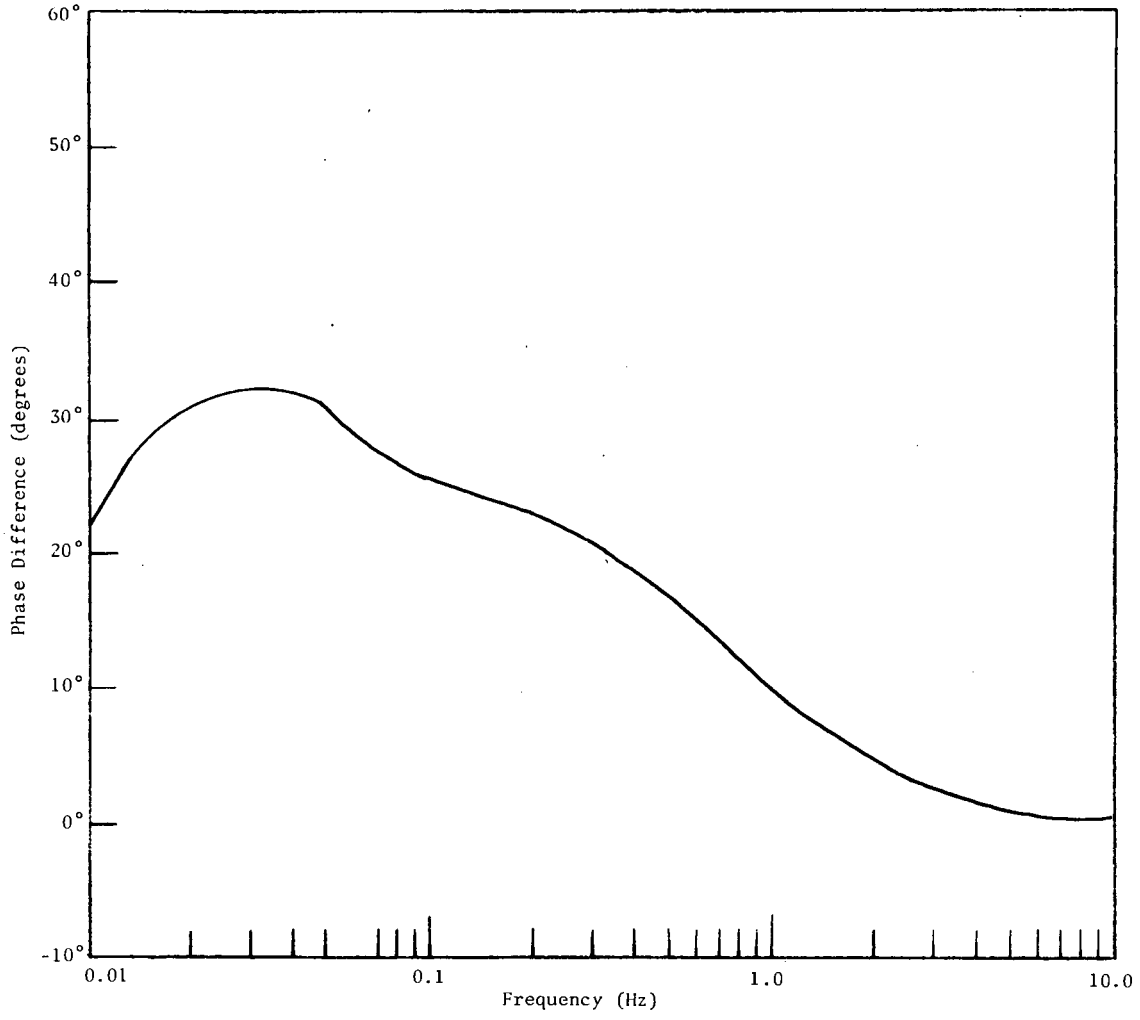

Figure IV-7. Phase differences, (phase at 54 GPM)-(phase at 10 GPM), computed by the well mixed model at θ_1.

conduction process is higher than the break frequency for the convection process. Thus, at high frequencies, the response is dominated by the conduction mechanism. Since this is an effect that is the same for any axial position, the gains for fluid temperature approach the same value at high frequencies at all axial positions.

II. SLUG FLOW MODEL

The slug flow model was used to solve for the frequency response of the fluid at selected axial positions. The model simulates one rod and the fluid in an assumed channed around the rod. This model assumed:

1. Coolant is single phase, slug flow.
2. The axial heat conduction is negligible in both the solid and the liquid.
3. The physical and heat transfer properties of all materials are independent of temperature.
4. The temperature of the solid is a function of time and axial and radial positions.
5. The temperature of the fluid is a function of time and axial position.

In this model, the basic equations are the heat conduction equation in the solid and the heat convection equation for the fluid. The equations are:

$$(\rho c)_i \frac{\partial T_i}{\partial t} = K_i \nabla^2 T_i + Q_i \qquad (i = 1,2,3) \qquad (8)$$

$$\frac{\partial \theta}{\partial t} + U \frac{\partial \theta}{\partial x} = b(T_3 - \theta) \qquad (9)$$

where

i = 1 is the heating element,

i = 2 is the boron nitride,

i = 3 is the cladding,

T_i = temperature in heater, boron nitride, of cladding, (°F)

θ = temperature in fluid, (°F)

Q = heat generation rate per unit volume, (Btu/sec ft^3)

ρ = density, (lb/ft^3)

K = thermal conductivity, (Btu/sec°F ft)

$b = \frac{(h_{film} A)}{Mc}$, ($sec^{-1}$)

U = velocity of fluid, (ft/sec)

c = specific heat, (Btu/lb°F)

M = mass, (lb)

h_{film} = film heat transfer coefficient, (Btu/sec°F ft^2)

A = area, (ft^2)

x = axial position, (ft)

t = time, (sec)

r = radial position, and (ft)

$\nabla^2 = \frac{\partial^2}{\partial r^2} + \frac{1}{r} \frac{\partial}{\partial r}$.

The boundary conditions are:

$$\frac{\partial T_1}{\partial r} = 0 \qquad \text{at } r = 0$$

$$K_1 \frac{\partial T_1}{\partial r} = K_2 \frac{\partial T_2}{\partial r} \qquad \text{at } r = a$$

$$K_2 \frac{\partial T_2}{\partial r} = K_3 \frac{\partial T_3}{\partial r} \qquad \text{at } r = b$$

$$K_3 \frac{\partial T_3}{\partial r} = h_{film} (\theta - T_o) \qquad \text{at surface}$$

$$T_1 = T_2 \qquad \text{at } r = a$$

$$T_2 = T_3 \qquad \text{at } r = b$$

where

a = radius of the heating element,

b = radius of the boron nitride,

c = radius of the cladding, and

T_o = surface temperature of the cladding.

Transfer functions may be obtained from these equations and boundary conditions. Fluid temperature to power frequency response results for this model were computed by the computer code FOURC.[8] Typical results obtained with the slug flow model appear in Figures IV-8, IV-9, IV-10, and IV-11. A significant feature of these results is the crossing of the gain curves for two different thermocouples at a given flow rate or for a single thermocouple at two different flow rates. This crossing effect does not occur with the well mixed model, and therefore is a

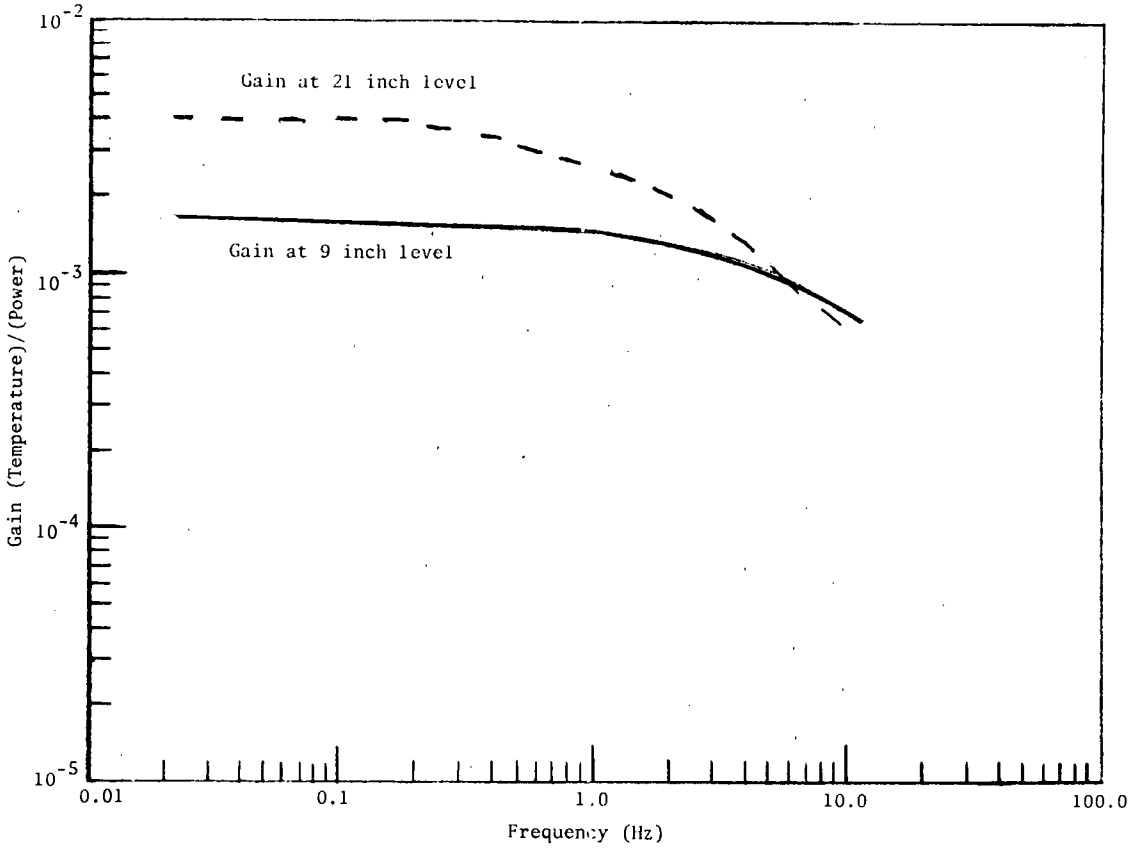

Figure IV-8. Frequency response gains computed by the slug flow model at the 9 inch and 21 inch level at 54 GPM.

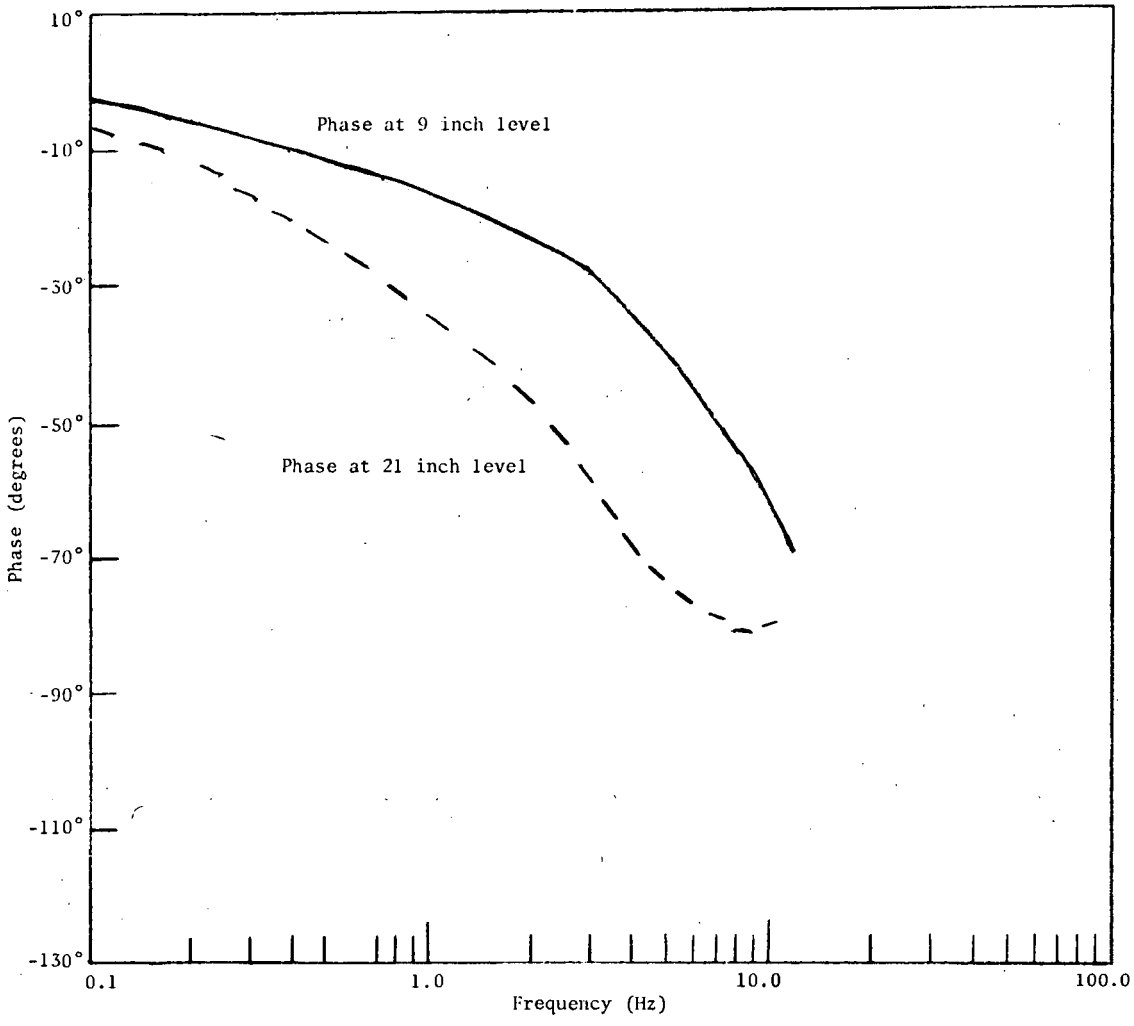

Figure IV-9. Frequency response phases computed by the slug flow model at the 9 inch and 21 inch level at 54 GPM.

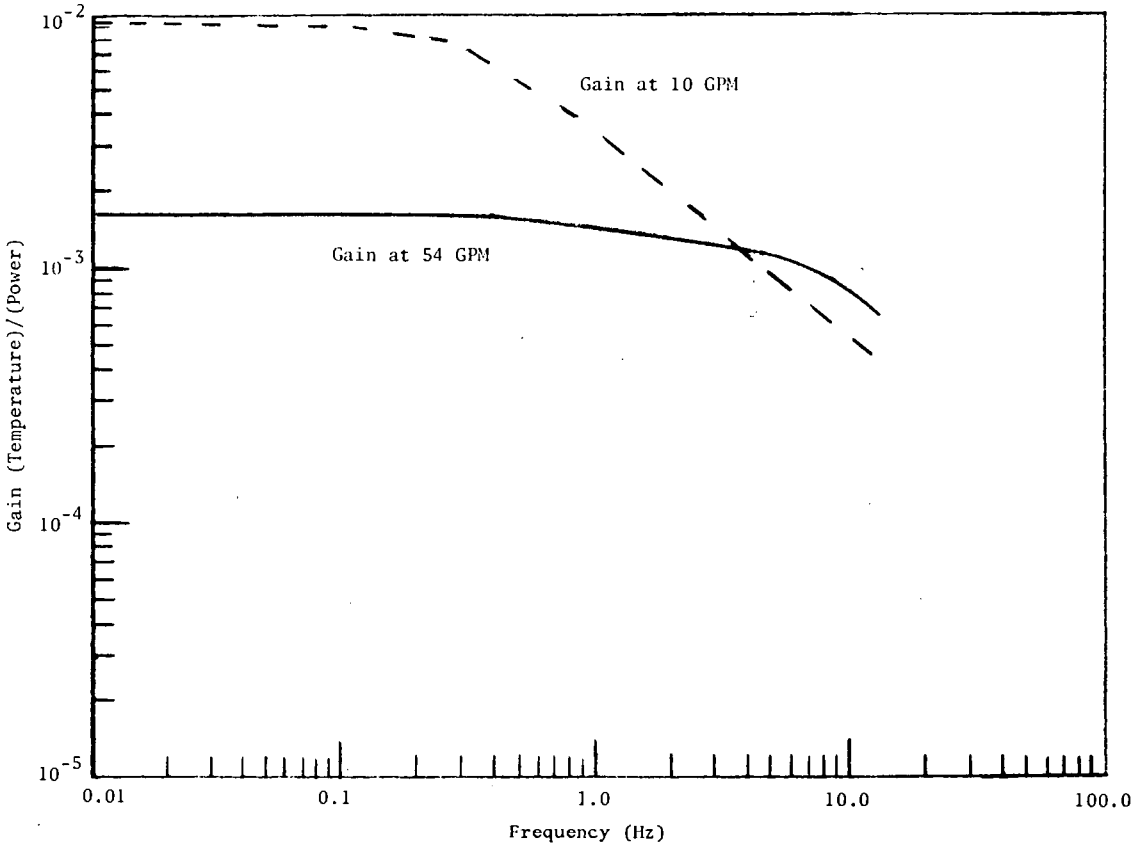

Figure IV-10. Frequency response gains computed by the slug flow model at the 9 inch level at 10 GPM and 54 GPM.

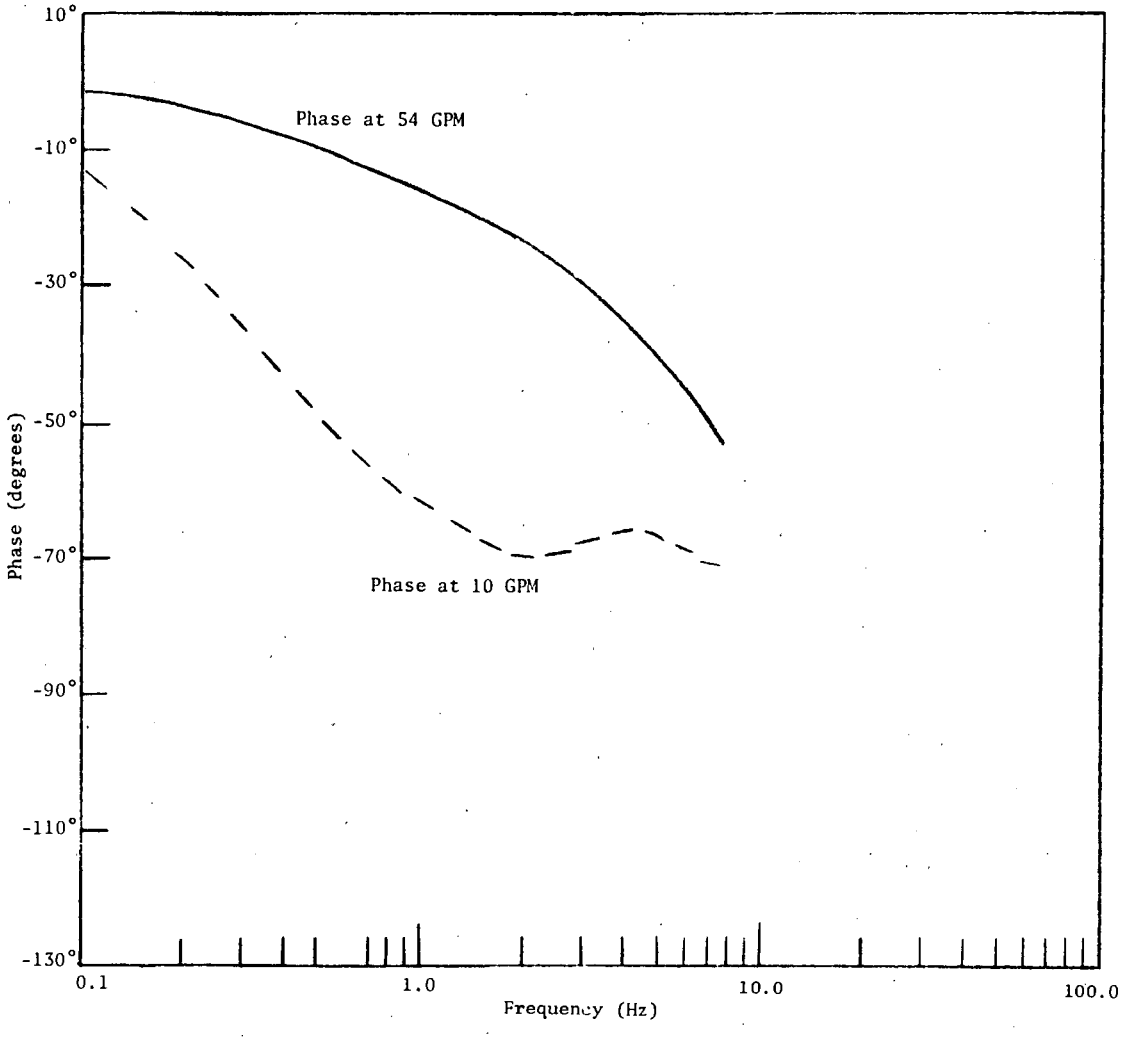

Figure IV-11. Frequency response phases computed by the slug flow model at the 9 inch level at 10 GPM and 54 GPM.

phenomenon that may be exploited to distinguish between slug flow and well mixed flow in interpretation of experimental results.

This crossing is emphasized if the ratio of the two gain curves is plotted. This way of presenting the results has been adopted here and in the interpretation of the experimental results in Chapter V. The gain ratios which were computed by the well mixed model were also computed by the slug flow model. Figure IV-12 shows the ratio, (frequency response gain at the 21 inch level)/(frequency response gain at the 9 inch level), computed by the slug flow model at 54 GPM. Phase difference results are shown in Figure IV-13. Figure IV-14 shows the ratio, (frequency response gain at 54 GPM)/(frequency response gain at 10 GPM), computed by the slug flow model at the 9 inch level. Figure IV-15 shows the phase difference for this case.

The oscillations in the gain ratios computed by the slug flow model will be called ringing. The frequency at which ringing occurs depends on the flow rate and the position in the bundle. For example, as the flow rate increases the ringing occurs at higher frequencies, and as the position moves down the bundle the ringing occurs at lower frequencies.

The physical reason for the ringing is that as a fluid volume element moves through the bundle it is affected by a modulated heat input that is high in some parts of the bundle and low in other parts of the bundle. If the power is oscillating at f Hertz and T is the time for a volume element to reach the observation point, then the number of half cycles in heater oscillation experienced in reaching the

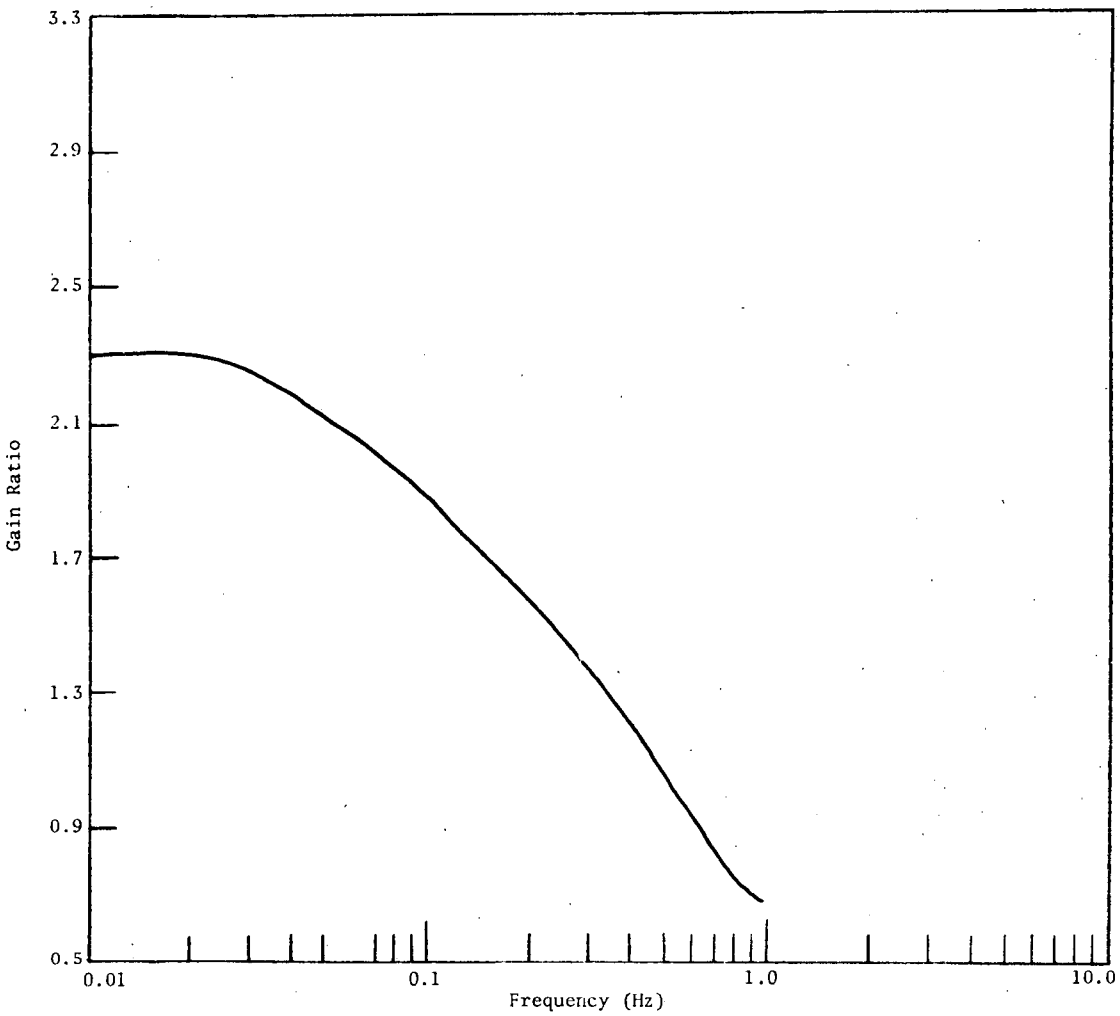

Figure IV-12. Gain ratios, (gain at the 21 inch level)/(gain at the 9 inch level), computed by the slug flow model at 54 GPM.

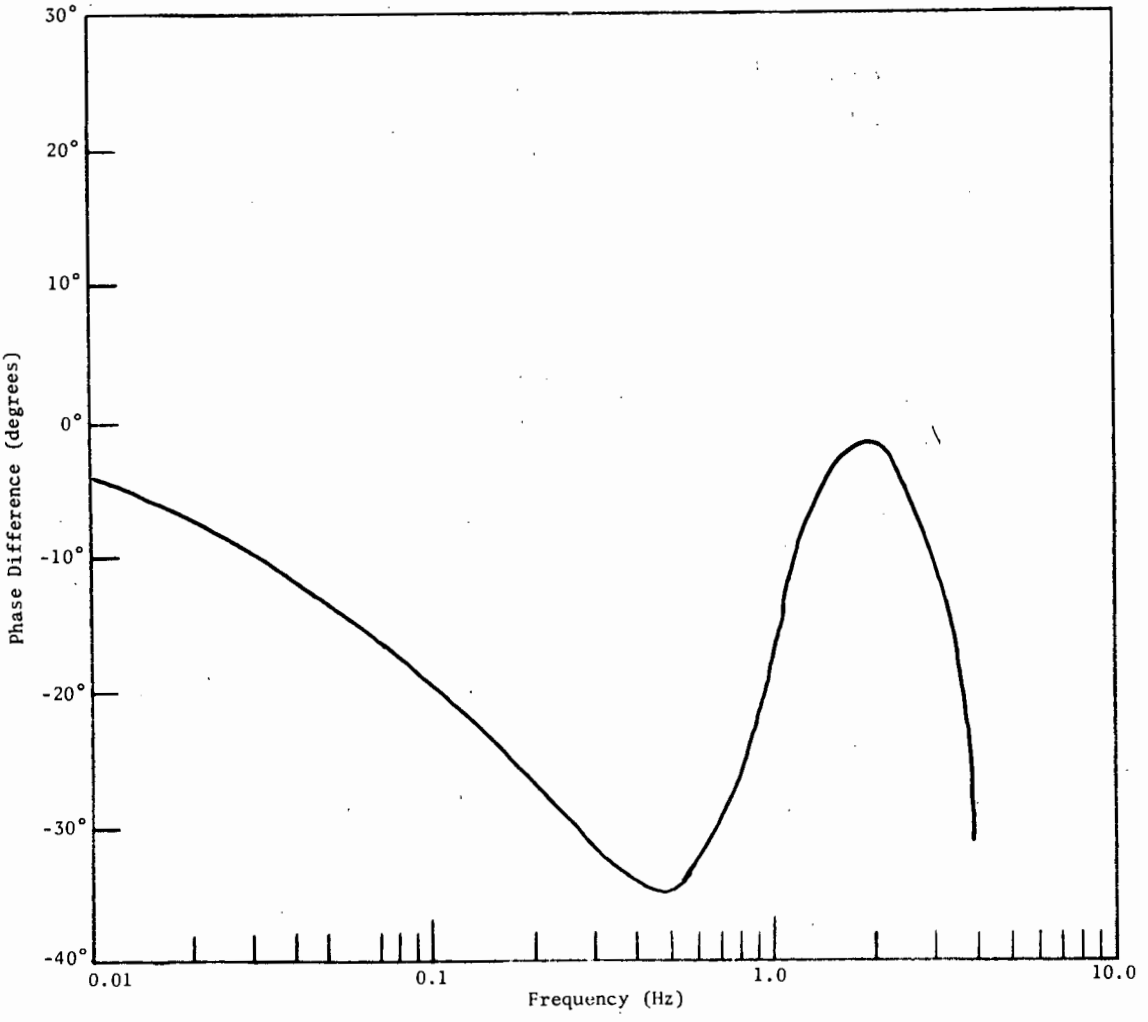

Figure IV-13. Phase differences, (phase at the 21 inch level)-(phase at the 9 inch level), computed by the slug flow model at 54 GPM.

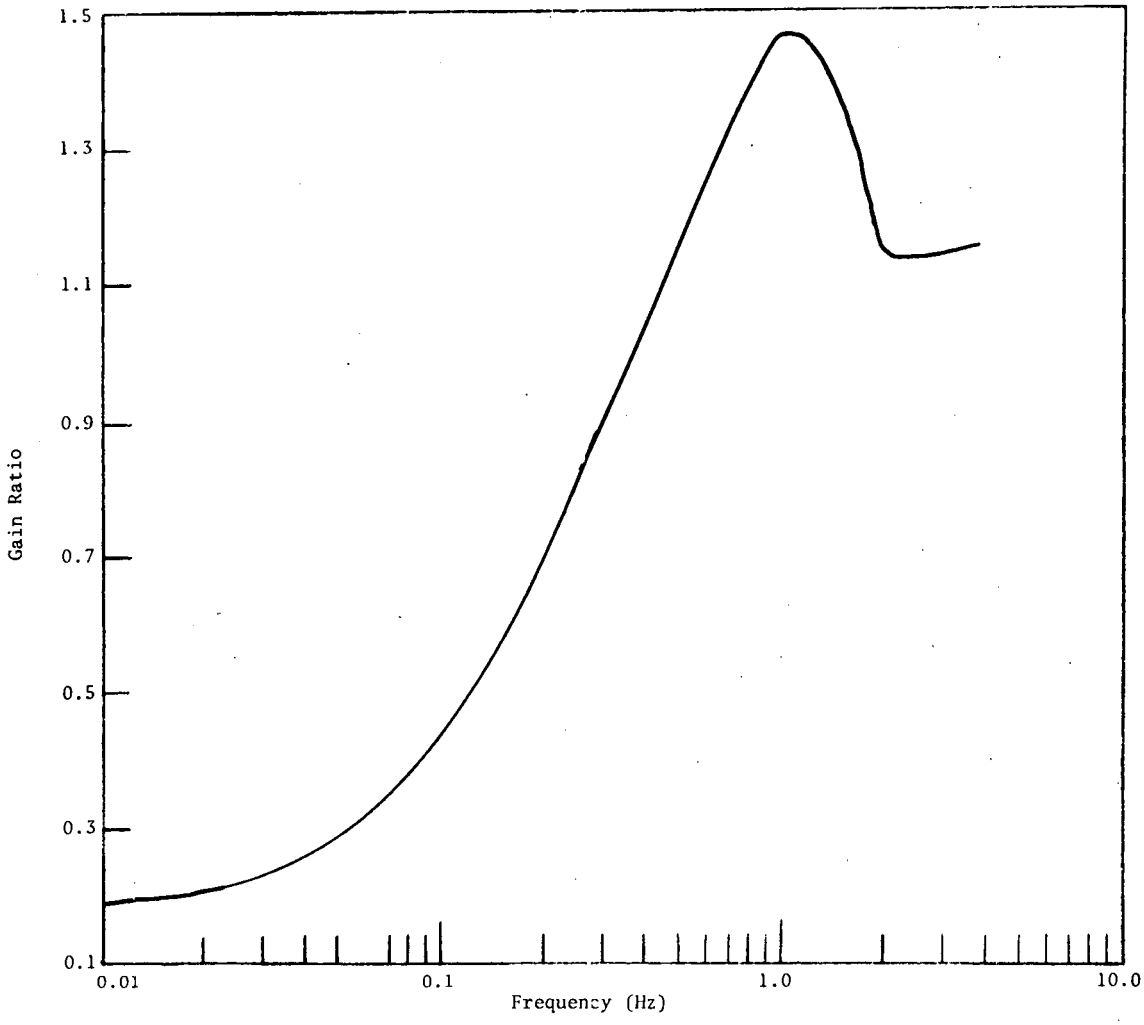

Figure IV-14. Gain ratios, (gain at 54 GPM)/(gain at 10 GPM), computed by the slug flow model at the 9 inch level.

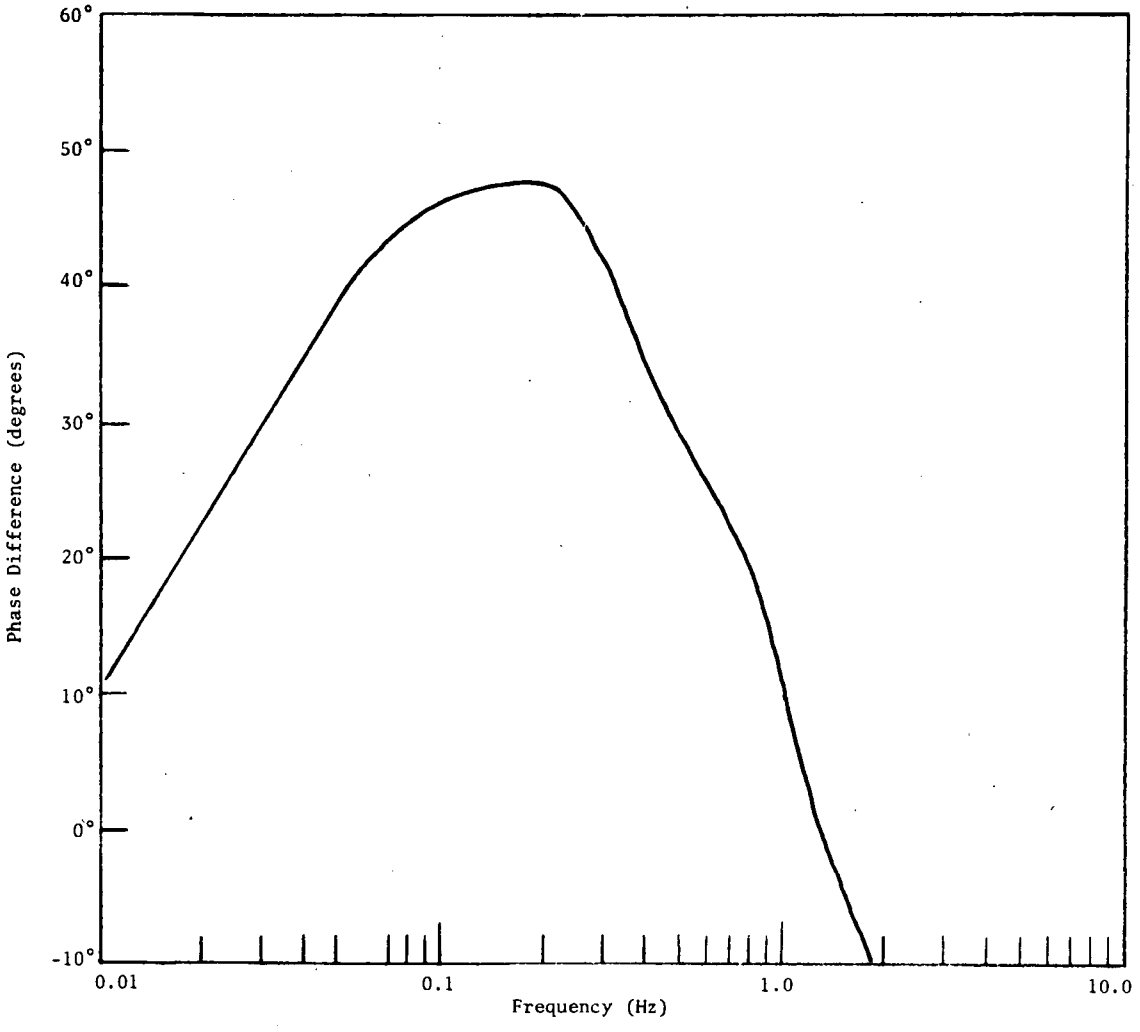

Figure IV-15. Phase differences, (phase at 54 GPM)-(phase at 10 GPM), computed by the slug flow model at the 9 inch level.

observation point is 2fT. The total heat input will be the integral of the modulated heat input along the channel. The maximum of this integral occurs when 2fT is an odd number and a minimum occurs when 2fT is an even number. These maximum and minimum points give the ringing seen in the gain ratios of the slug flow model.

A significant difference between the well mixed model results and the slug flow model results is that the gain ratios computed by the well mixed model approach unity monotonically while the gain ratios computed by the slug flow model show oscillations. These differences in trends indicate that it may be possible to use gain ratios to interpret experimental results and distinguish between well mixed flow and slug flow.

Of course, the analysis presented here does not prove conclusively that the presence or absence of ringing is a sure indicator of the flow characteristics. However, the analysis coupled with the physical argument give evidence that this is a plausible explanation for experimentally observed ringing.

CHAPTER V

EXPERIMENTAL RESULTS

Experimental frequency responses were obtained using the methods described in Chapter III. All of the experimental results in this thesis involved power modulation to only one rod at a time. Thermocouples located in wire wraps on a simulated fuel rod measure a temperature somewhere between the rod temperature and the fluid temperature. In this work, it will be assumed that the thermocouples measure fluid temperature, and the frequency response will be given as (fluid temperature)/(power). A typical experimental (fluid temperature)/(power) frequency response is shown in Figures V-1 and V-2.

The experimental results will be presented in two forms:

1. vector diagrams
2. gain ratios

In both cases, only selected results will be discussed. Additional results are in the appendix for possible future use by other workers.

I. VECTOR DIAGRAMS

The gain of the experimental frequency response is the ratio of the amplitude of the fluid temperature to the amplitude of the heater power. Thus, the gain is proportional to the fluid temperature change and hence to the fluid energy change that would accompany a heater power change. It is important to note that as the frequency decreases the frequency

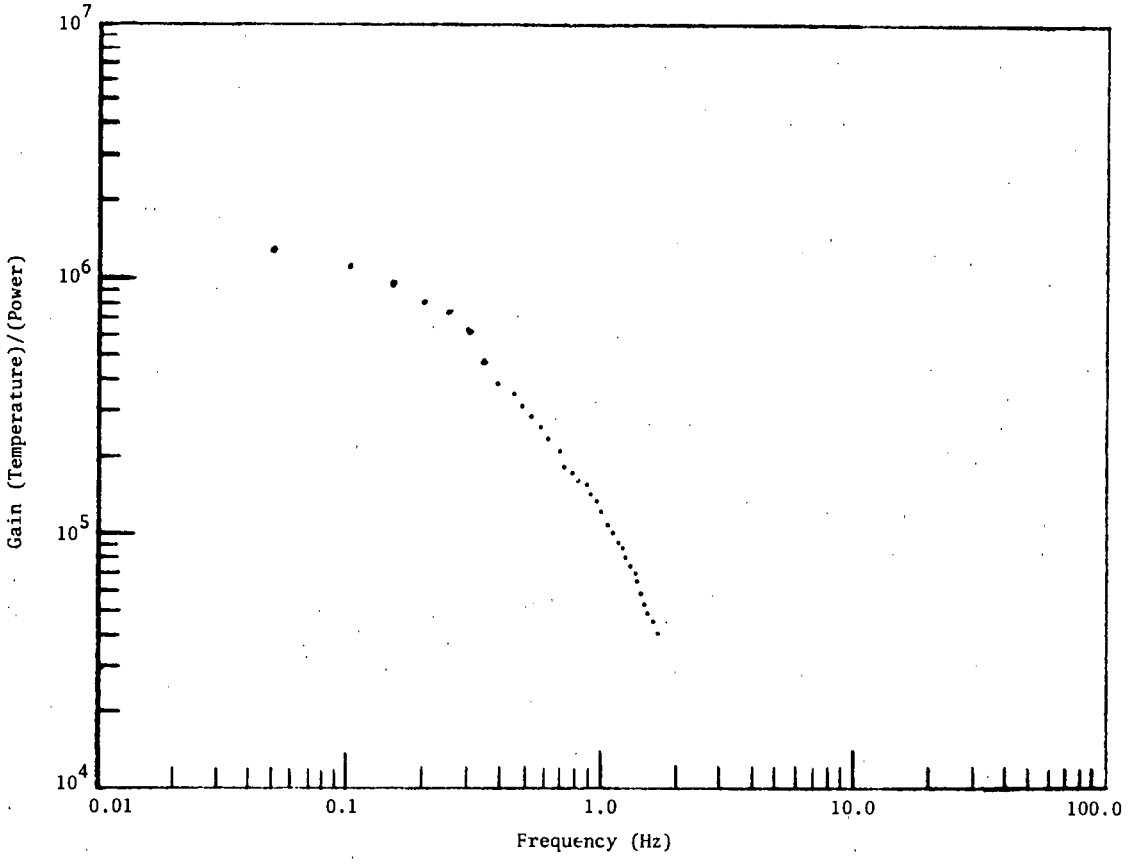

Figure V-1. Bundle 1B, gain for thermocouple 0118 with rod 1 heated at 10 GPM.

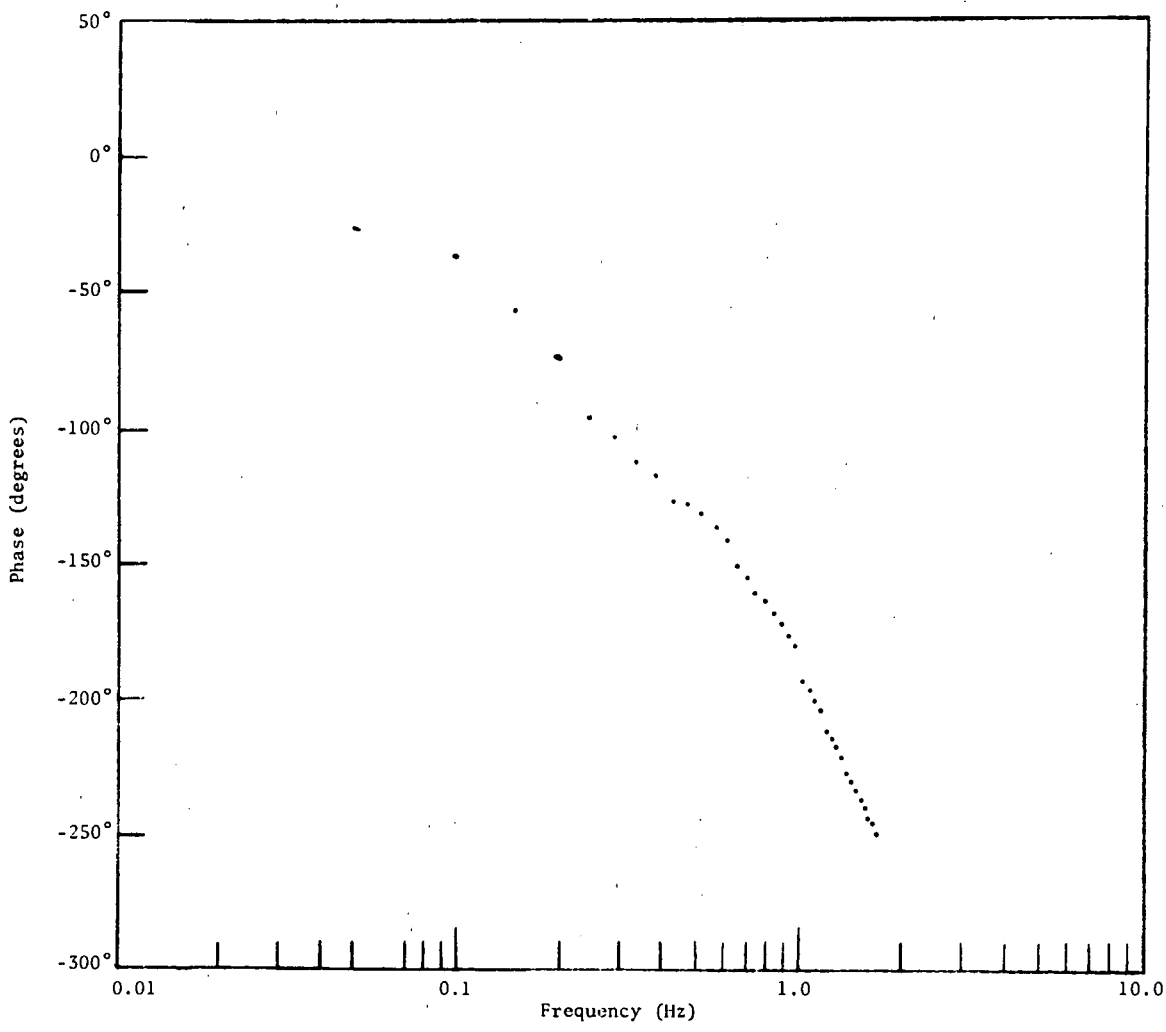

Figure V-2. Bundle 1B, phase for thermocouple 0118 with rod 1 heated at 10 GPM.

response amplitude goes to a constant value that equals the value at zero frequency. The gain at zero frequency is numerically equal to the change in response that would be reached asymptotically following a step input. This can be shown by considering a system with a transfer function, G(s), and a unit step input (whose Laplace transform is 1/s). The Laplace transform of the output is

$$\delta O(s) = G(s) \frac{1}{s} \quad .$$

The final value theorem may be used to give

$$\delta O(t)_{t=\infty} = \lim_{s \to o} s \delta O(s) = G(o) \quad .$$

Thus, the asymptotic temperature response that would be obtained following a step change in power to an FFM rod may be obtained by observing the value of the low frequency gain. This may be preferable to actually using a step change because the accuracy of the low frequency gain may be made as great as required by using more periods of the periodic input signal in the test. Since the fluid termperature change is proportional to the fluid energy change, the low frequency gain may be interpreted as the change in energy flowing to the fluid at the measurement point due to a change in the power supplied to a selected rod.

The steady state gains are presented in vector diagrams which show the steady state gains at a particular level for various heater-thermocouple combinations. The steady state gain at a thermocouple is

represented by a vector from the heated rod to the rod on which the thermocouple is mounted. The length of the solid line is proportional to the energy flow from the whole length of the heated rod to the measurement point. A dashed continuation of the line is used to show clearly the destination of the vector. If the entire line between two rods is dashed, it signifies that the steady state gain is too small to be shown on the scale used. For example, in Figure V-3 the steady state (fluid temperature)/(power) gain at thermocouple 0421 with rod 5 heated is 2.5×10^5 and is represented by a vector 5 units long from rod 5 to rod 4. (The units are (output volts)/(input volts). No attempt was made to change the units to (degrees)/(watts), but all cases are consistent.) Note that the gain at thermocouple 0421 is due to the energy input along the length of rod 5. The purpose of the vector diagrams is to show the energy flow from the total length of a heated rod to a selected thermocouple.

Typical vector diagrams for bundle 2A are shown in Figures V-3 and V-4. No general trends are seen in these figures because measurements were made for too few heater-thermocouple pairs.

Typical vector diagrams for bundle 2B are shown in Figures V-5 and V-6. Figure V-5 shows that the vector from rod 15 to rod 4 is larger than the vector from rod 4 to rod 5 even though the distance between the thermocouple and the heated rod is larger in the first case. Figure V-6 shows that the steady state gain at thermocouple 0412 with rod 11 heated is very small compared to the steady state gain at thermocouple 0412 with rod 5 heated. These examples show that the steady state gain is

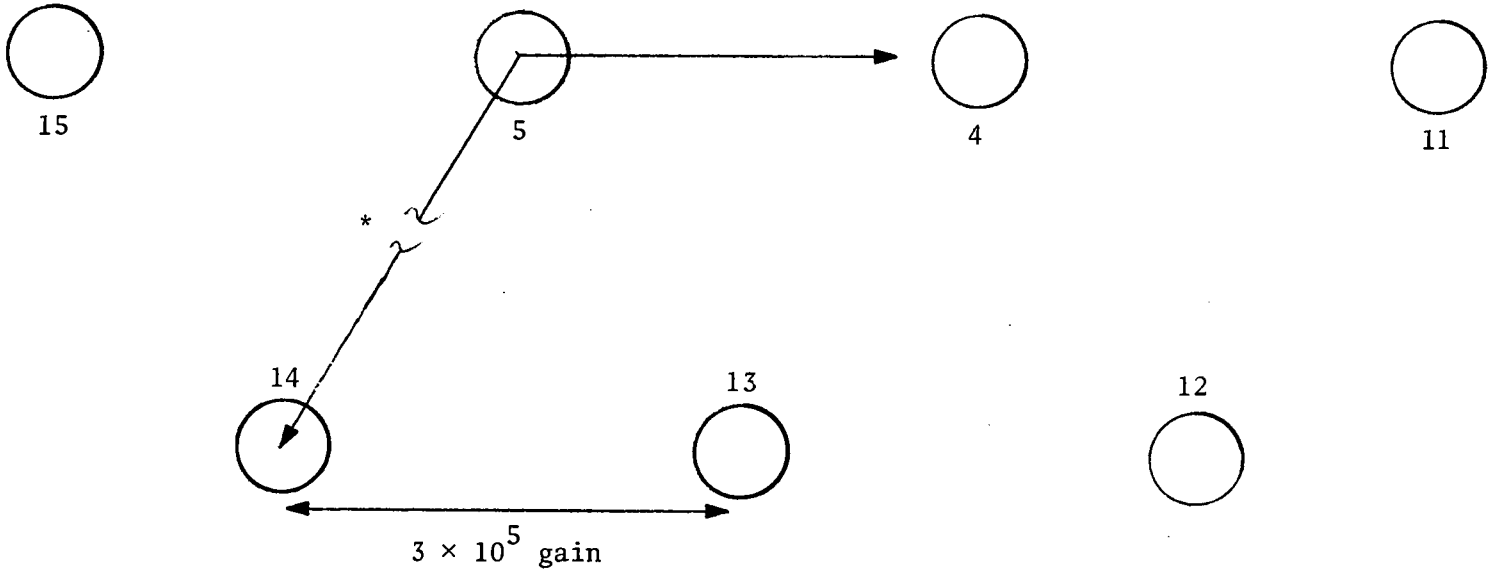

*The gain at thermocouple 1421 with rod 5 heated is 4.15×10^5.

Figure V-3. Bundle 2A, vector diagram at 10 GPM at the 21 inch level.

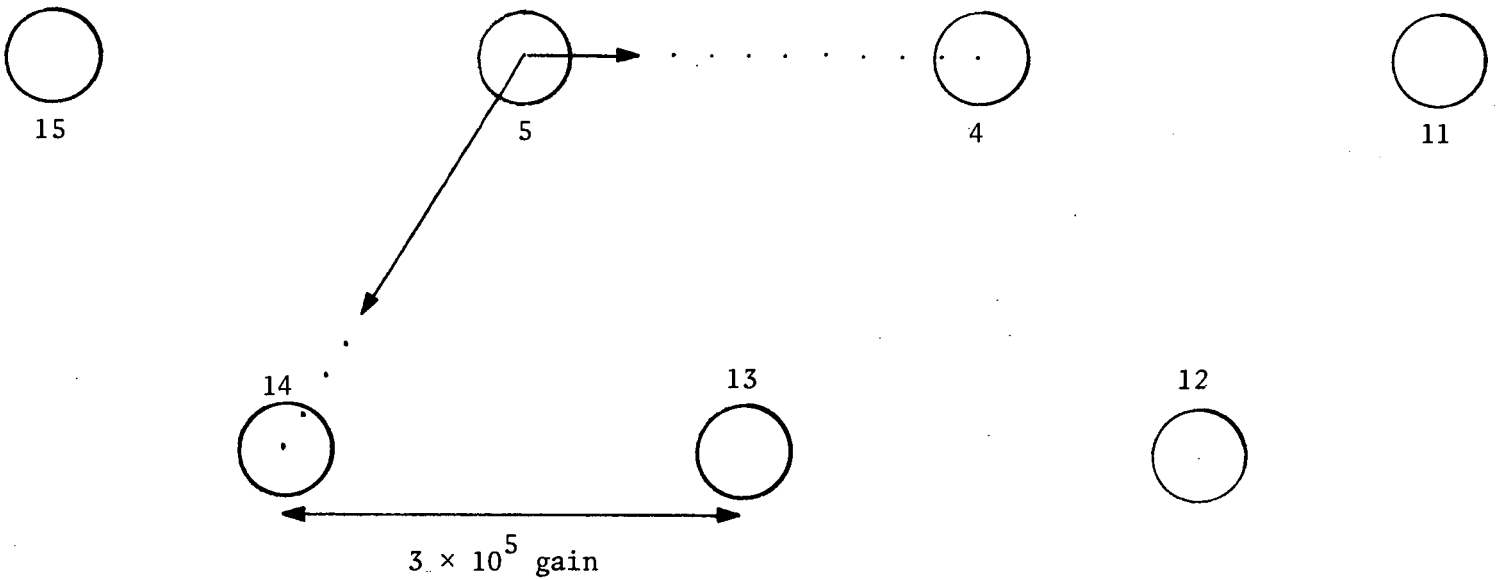

Figure V-4. Bundle 2A, vector diagram at 10 GPM at the 9 inch level.

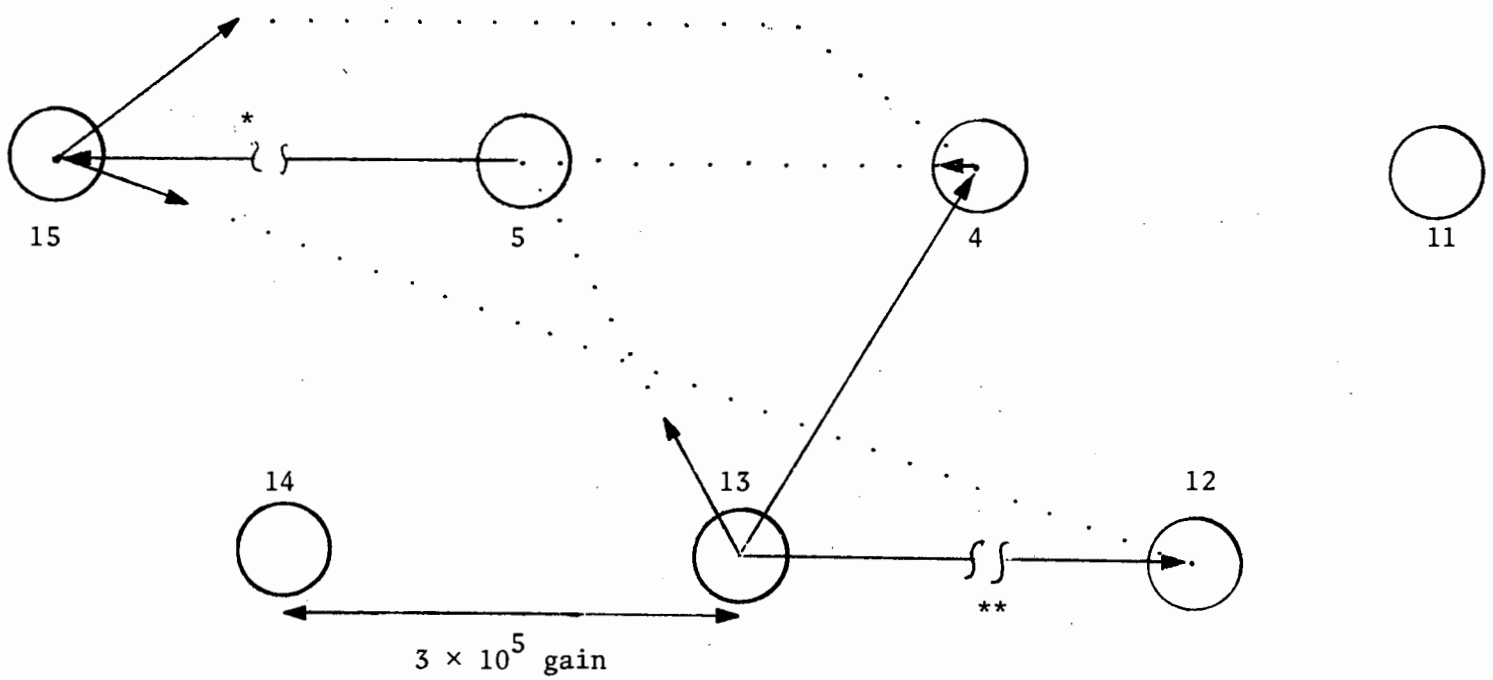

*The gain at thermocouple 0512 with rod 15 heated is 9.1×10^5.

**The gain at thermocouple 1212 with rod 13 heated is 6.0×10^5.

Figure V-5. Bundle 2B, vector diagram at 10 GPM at the 12 inch level.

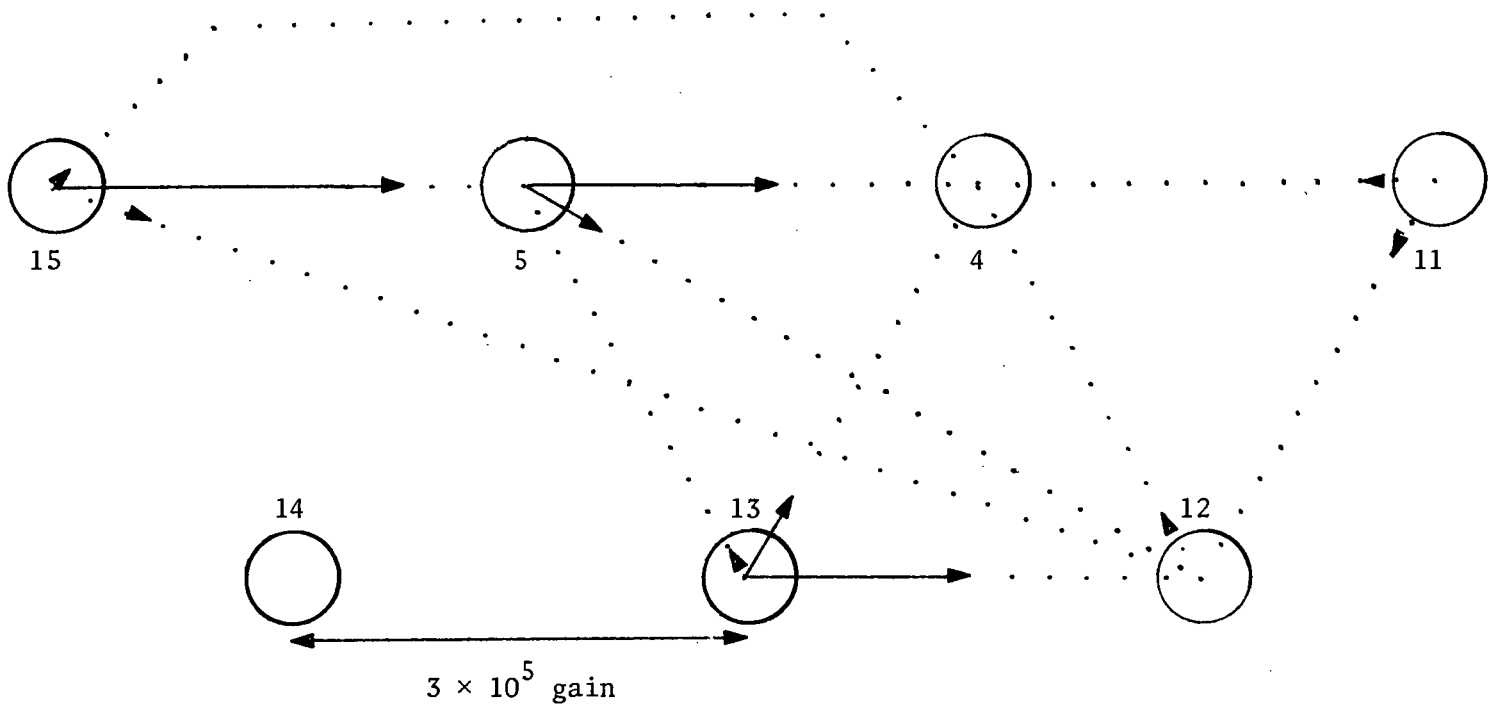

Figure V-6. Bundle 2B, vector diagram at 54 GPM at the 12 inch level.

much larger if the thermocouple is to the right of the heated rod. It is thought that this is due to an edge swirl in the counterclockwise direction which would carry the fluid from left to right for positions in the lower part of the bundle (as drawn in the bundle schematics shown in this thesis).

Figures V-7 and V-8 show vector diagrams for bundle 1B. No general trend is observed in these figures. It is thought that no trends were seen because the dummy rods around the periphery of the bundle (see Figure II-4, page 7) decreased the edge swirl seen in the interior of the bundle.

In summary, the vector diagrams show that an edge swirl is present in bundles with smooth edges and no edge swirl is present in bundles without smooth edges. Additional diagrams are shown in Figures A-1 to A-37 in Appendix A.

The vector diagram concept should be very useful for studying bundle flow patterns in cases where enough thermocouples are available to provide detailed energy flow maps.

II. GAIN RATIOS

The experimental results may also be presented in the form of gain ratios. Previously it has been shown that it may be possible to use gain ratios to distinguish between well mixed flow and slug flow. The gain ratios, (gain at thermocouple 0521)/(gain at thermocouple 0509), are shown in Figure V-9. Figure V-10 shows the phase differences between thermocouples 0521 and 0509. A point to note is that the experimental

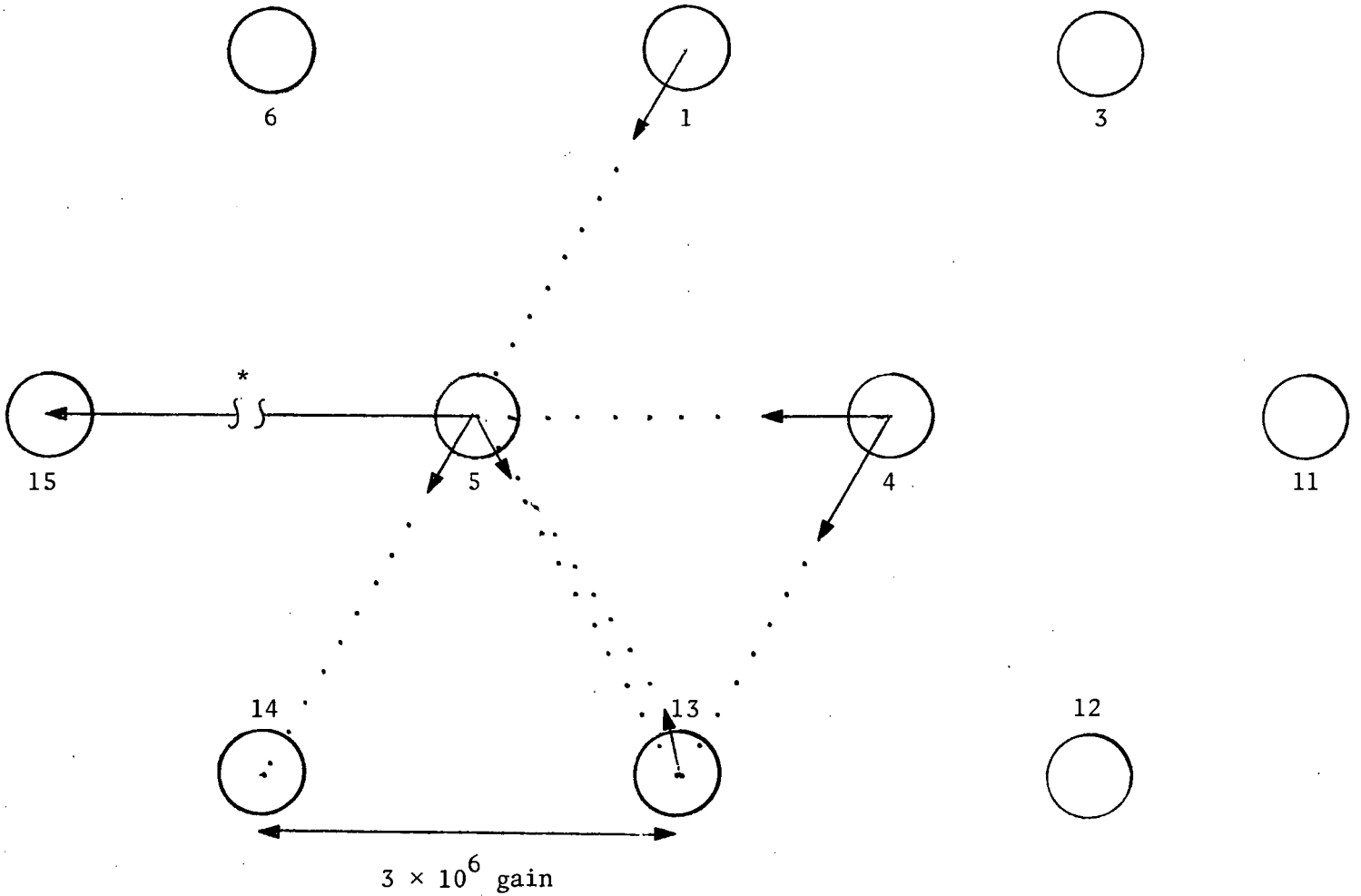

*The gain at thermocouple 1512 with rod 5 heated is 9.64×10^6.

Figure V-7. Bundle 1B, vector diagram at 10 GPM at the 14 inch level.

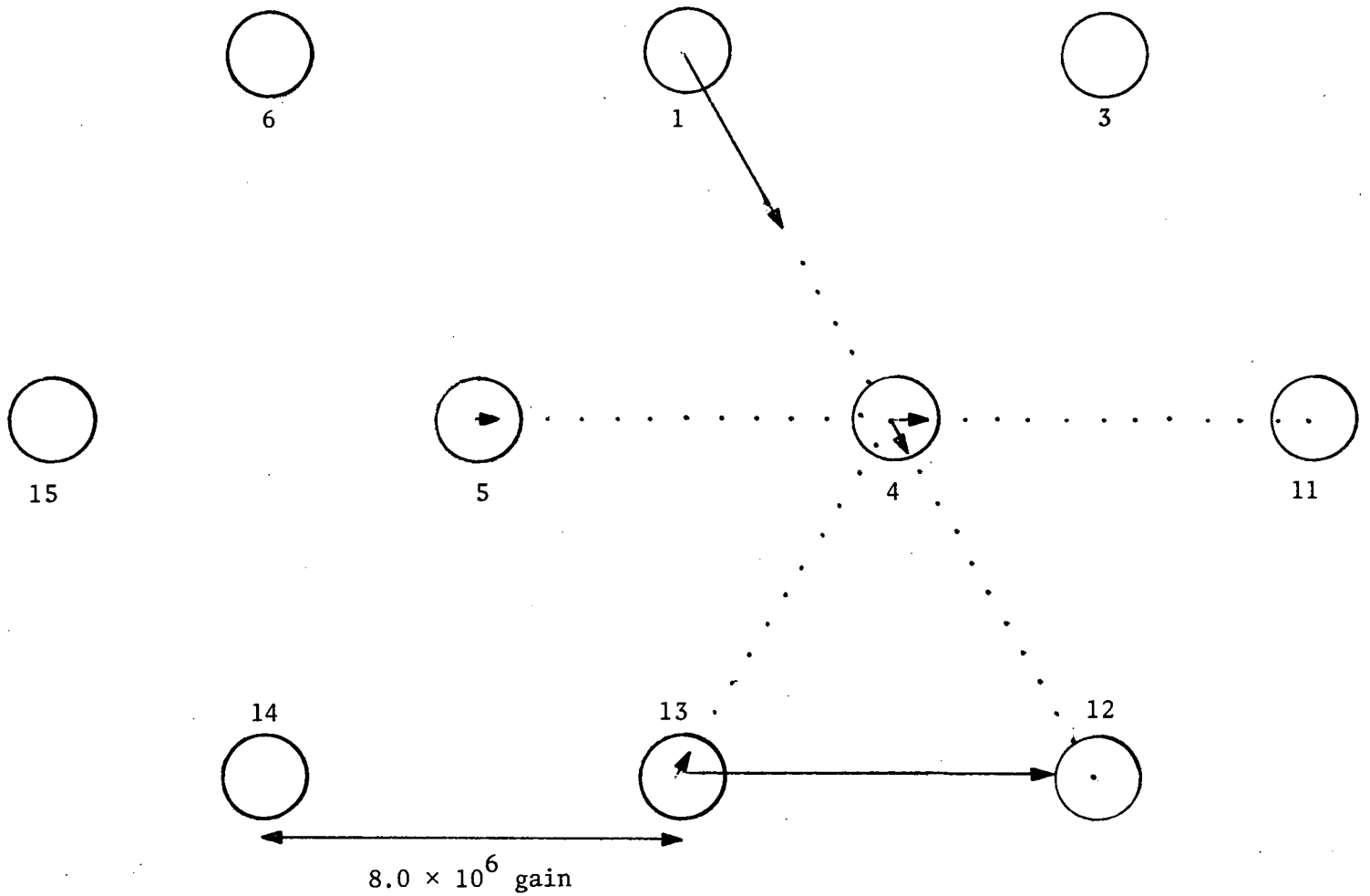

Figure V-8. Bundle 1B, vector diagram at 10 GPM at the 10 inch level.

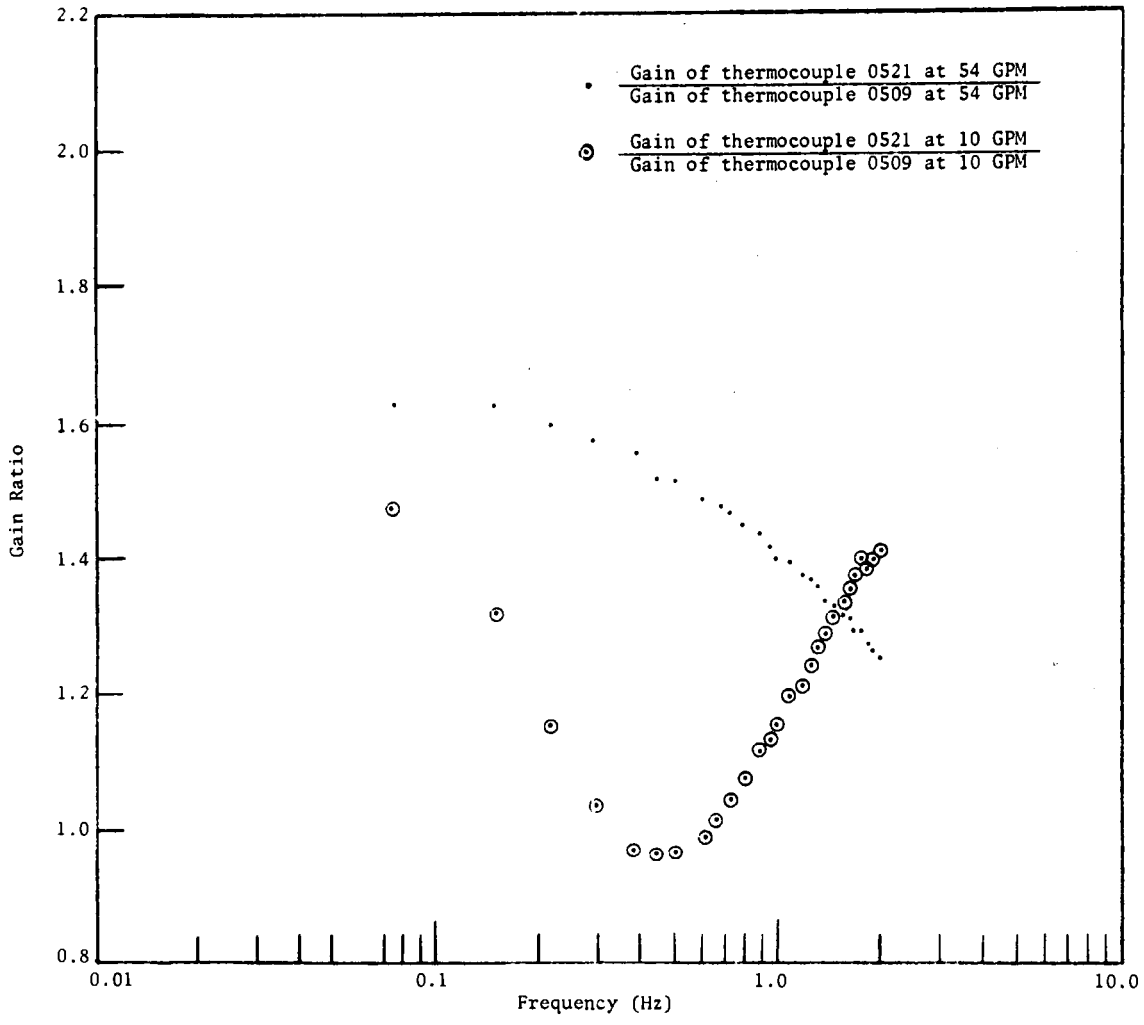

Figure V-9. Bundle 2A, gain ratios with rod 5 heated at 54 GPM and 35 GPM.

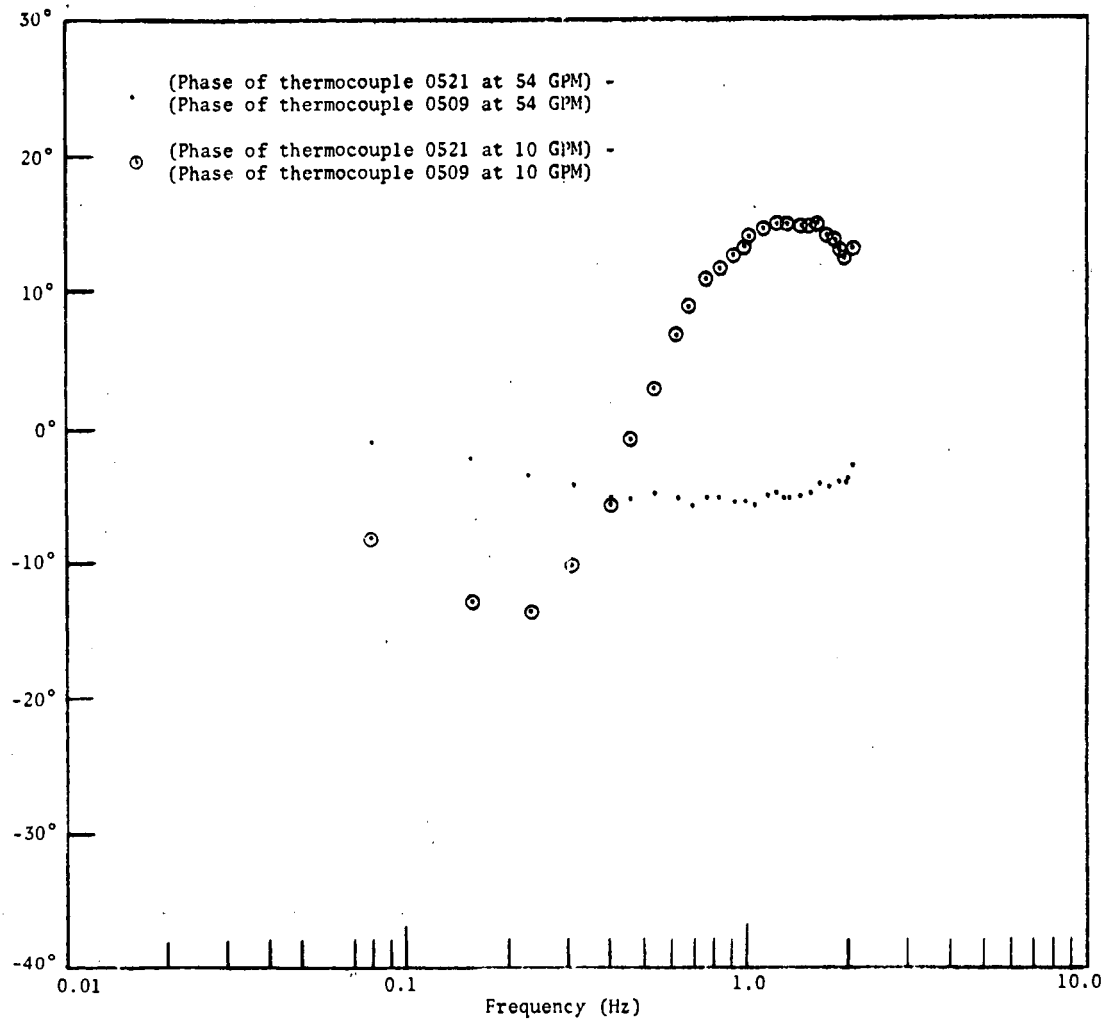

Figure V-10. Bundle 2A, phase differences with rod 5 heated at 54 GPM and 10 GPM.

results show a positive phase shift at higher frequencies. A possible reason for this effect is that thermocouple 0509 has a lower break frequency than thermocouple 0521. At this time experimental data on thermocouple response is not available so the gain ratios that involve two different thermocouples with slight, but unknown differences in response cannot be interpreted.

The thermocouple response problem can be eliminated if one considers the gain of a single thermocouple at two different flow rates. For this reason the gain ratios, (gain at a selected flow rate)/(gain at flow rate 10 GPM), will be used to present the data.

The gain ratios for bundle 2A are shown in Figures V-11 through V-13. Figure V-11 shows the gain ratios for thermocouple 0509 and rod 5 heated. This figure has ringing similar to that seen in the results of the slug flow model. Figure V-12 shows the gain ratios for thermocouple 0521 and rod 5 heated. This case has no ringing. The gain ratios for thermocouple 1421 and rod 5 heated are shown in Figure V-13. The gain ratios show ringing similar to the ringing in Figure V-11.

The gain ratios for bundle 2B are shown in Figures V-14 through V-16. Figure V-14 shows the gain ratios for thermocouple 0412 and rod 4 heated. No ringing is seen in this figure. The gain ratios for thermocouple 0512 with rod 15 heated are shown in Figure V-15. Ringing is seen in this figure. No ringing is seen in Figure V-16 which shows the gain ratios for thermocouple 1212 and rod 4 heated.

Figures V-17 through V-20 show the gain ratios of the thermocouples on the heated rod in bundle 1B. These figures show that at the beginning

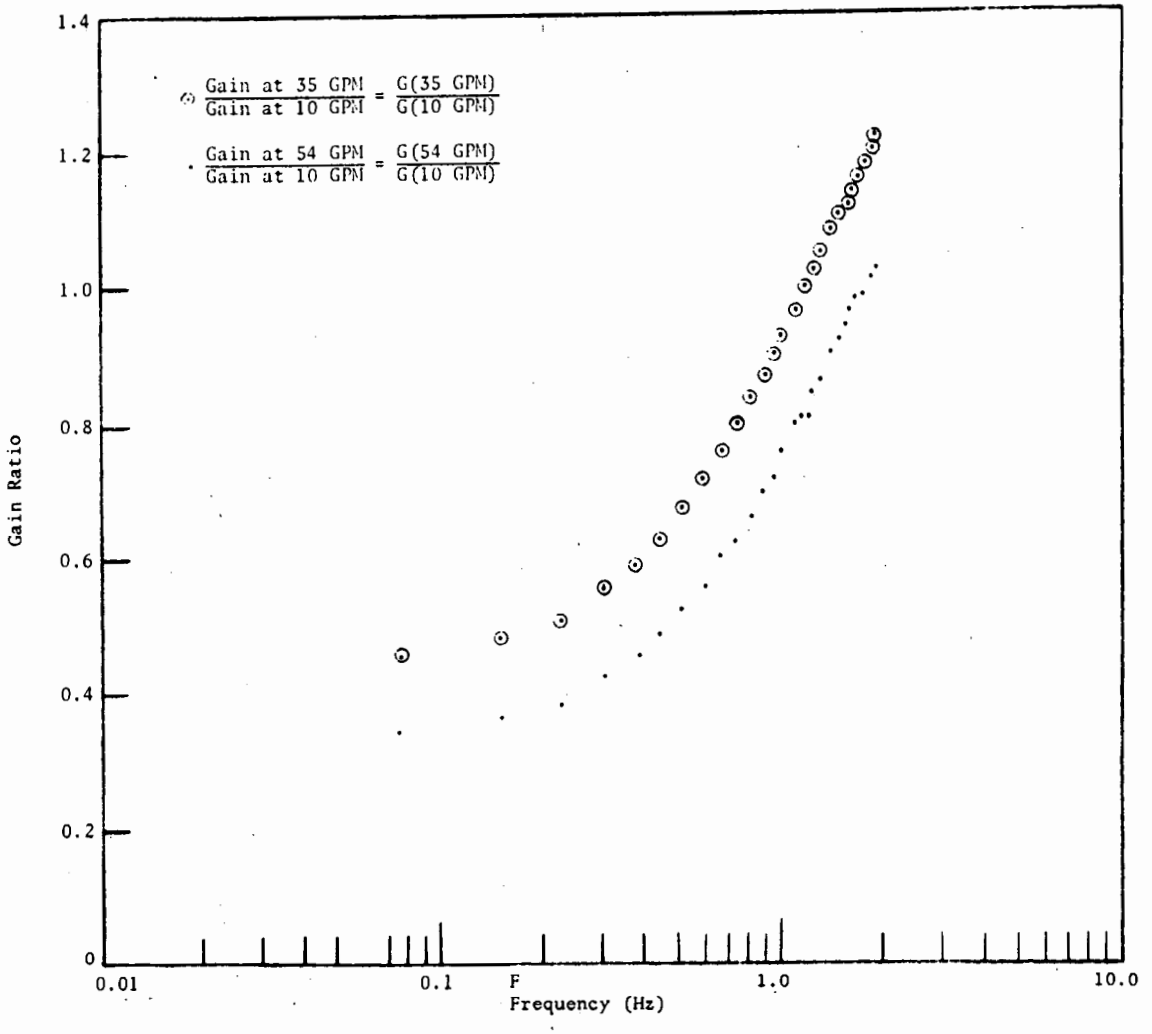

Figure V-11. Bundle 2A, gain ratios for thermocouple 0509 with rod 5 heated.

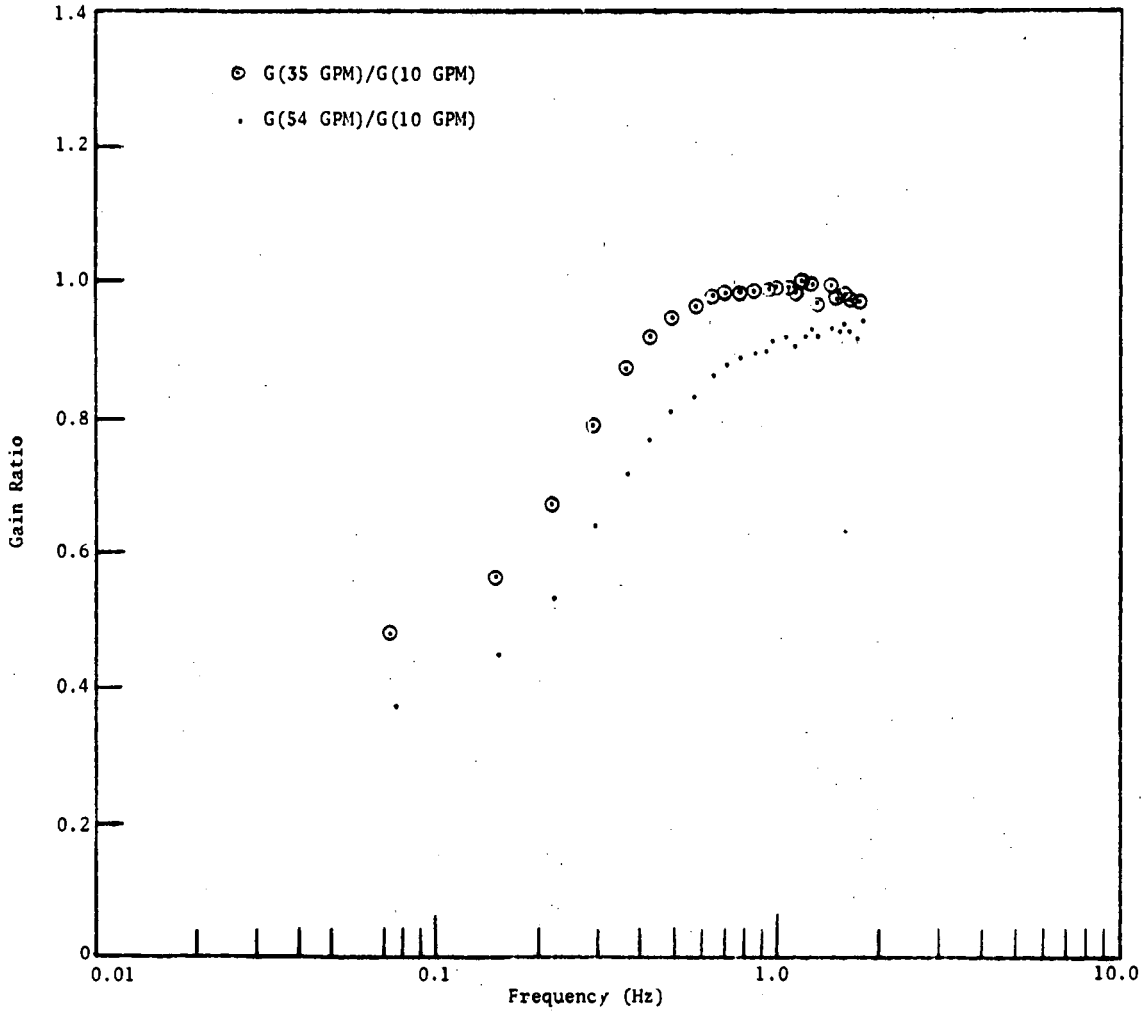

Figure V-12. Bundle 2A, gain ratios for thermocouple 0521 with rod 5 heated.

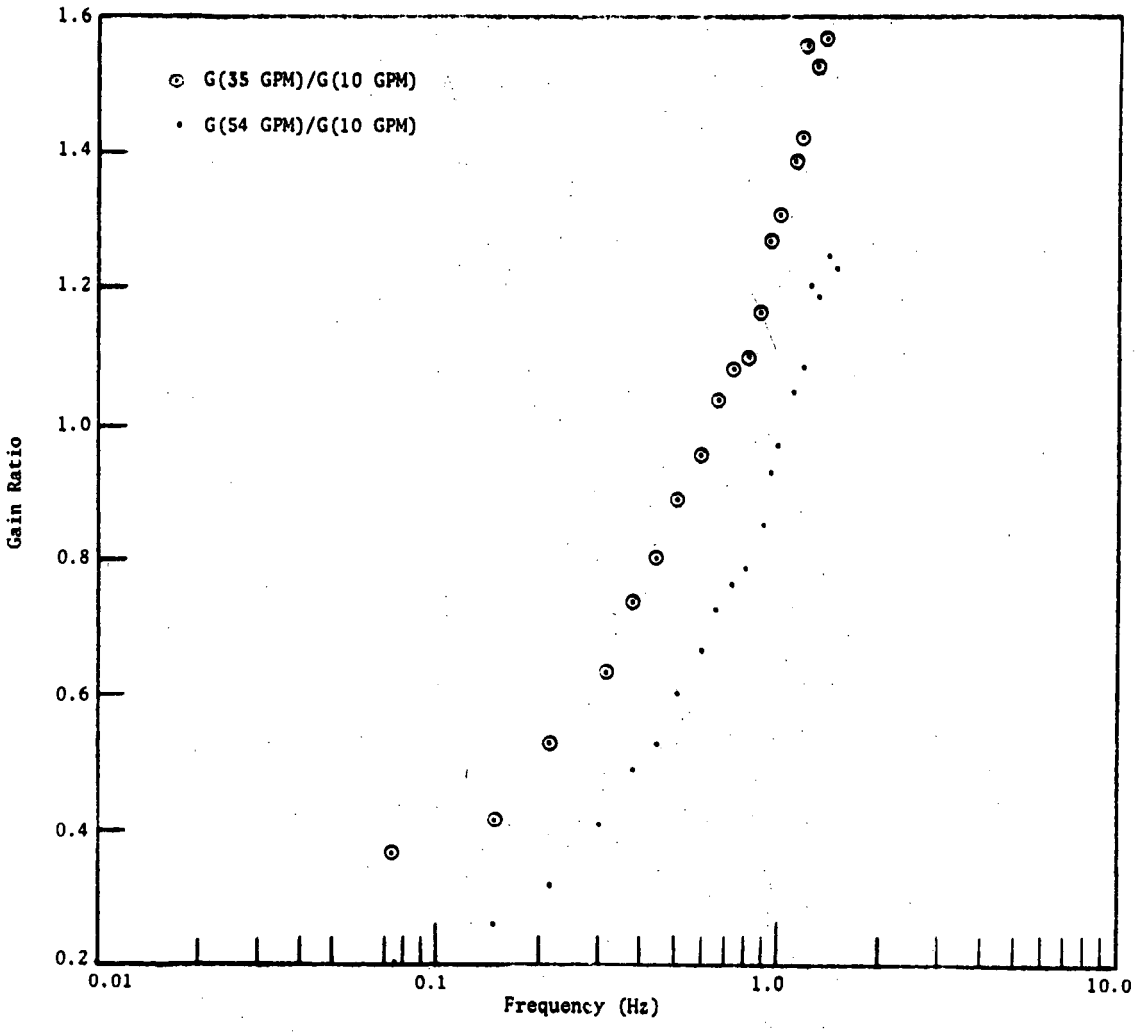

Figure V-13. Bundle 2A, gain ratios for thermocouple 1421 with rod 5 heated.

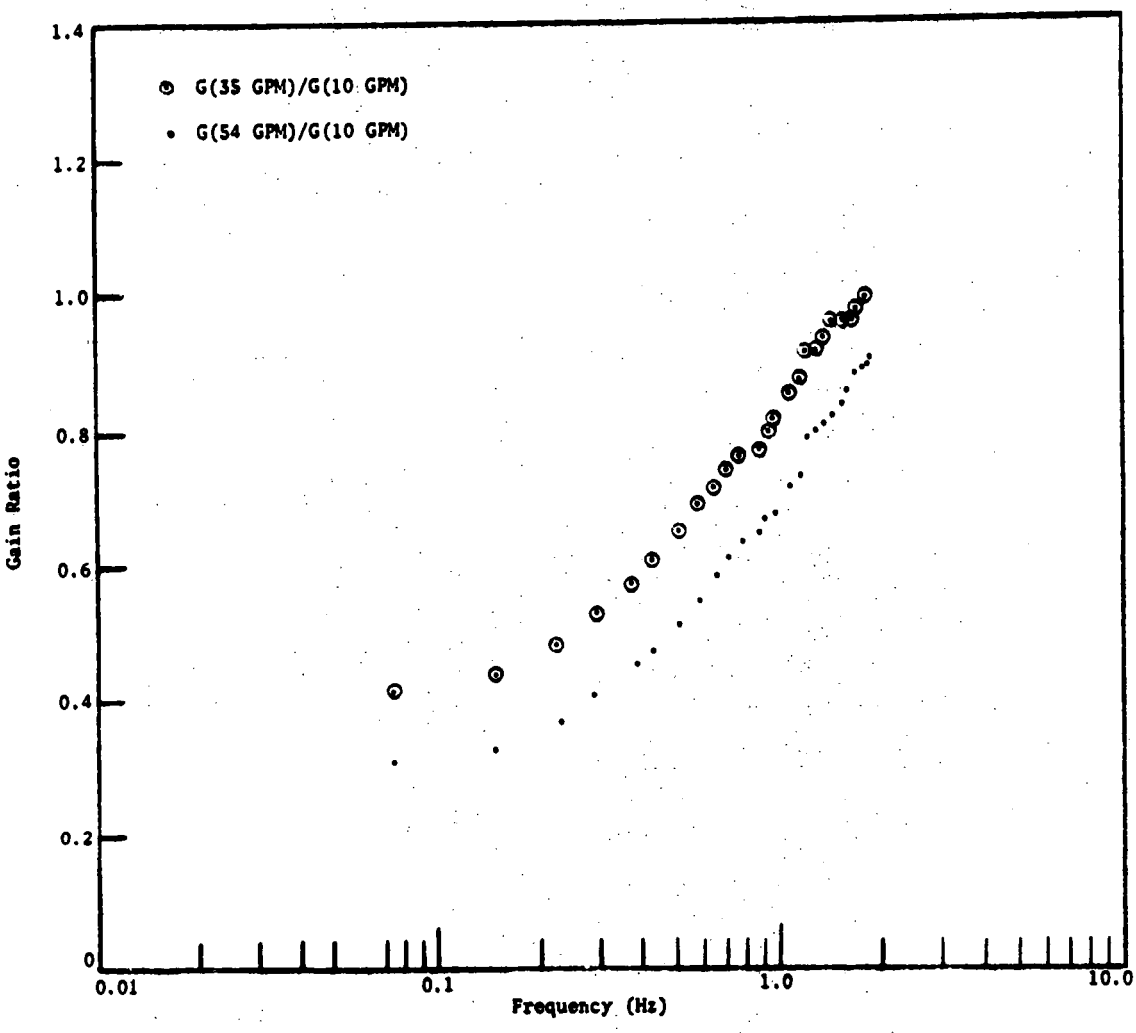

Figure V-14. Bundle 2B, gain ratios for thermocouple 0412 with rod 4 heated.

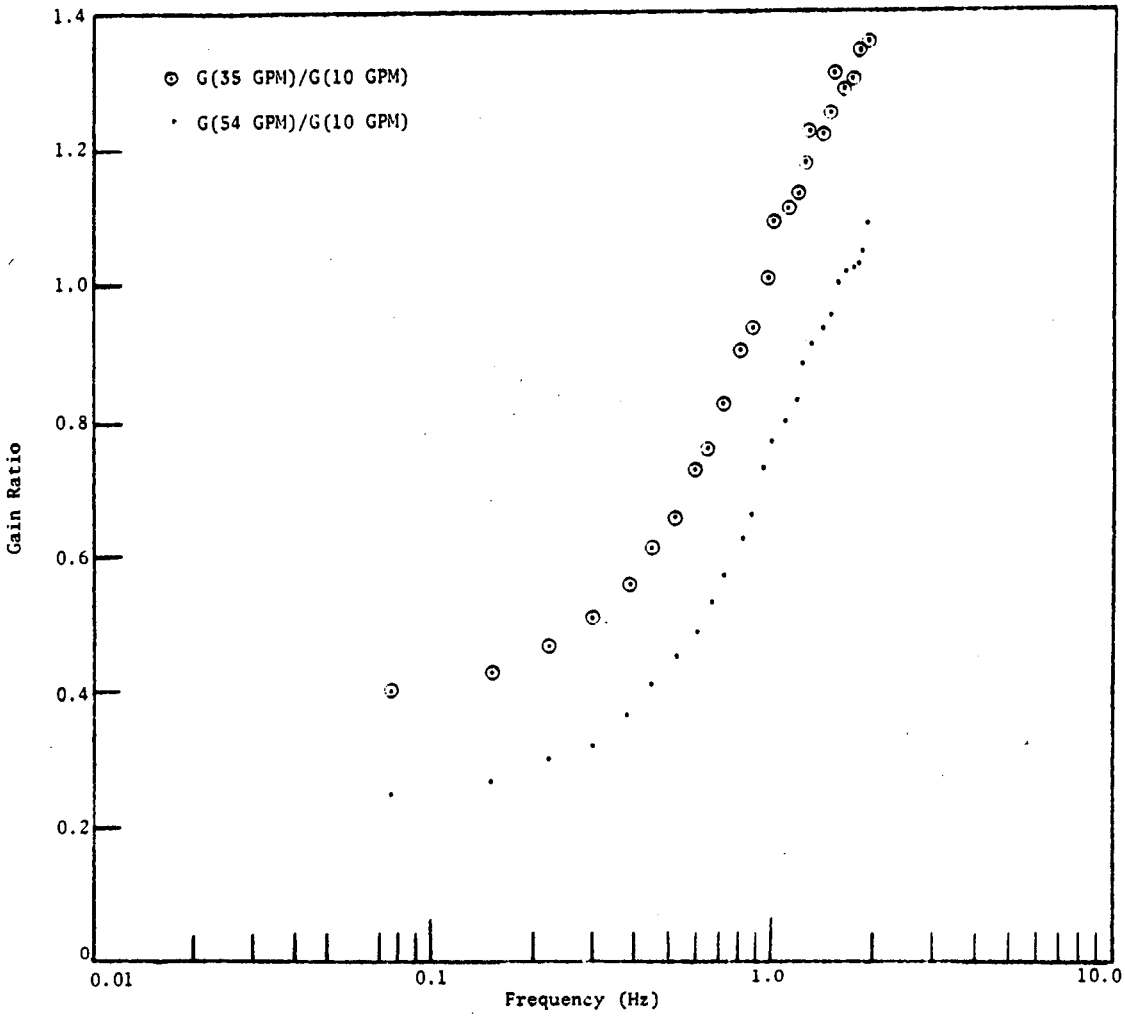

Figure V-15. Bundle 2B, gain ratios for thermocouple 0512 with rod 15 heated.

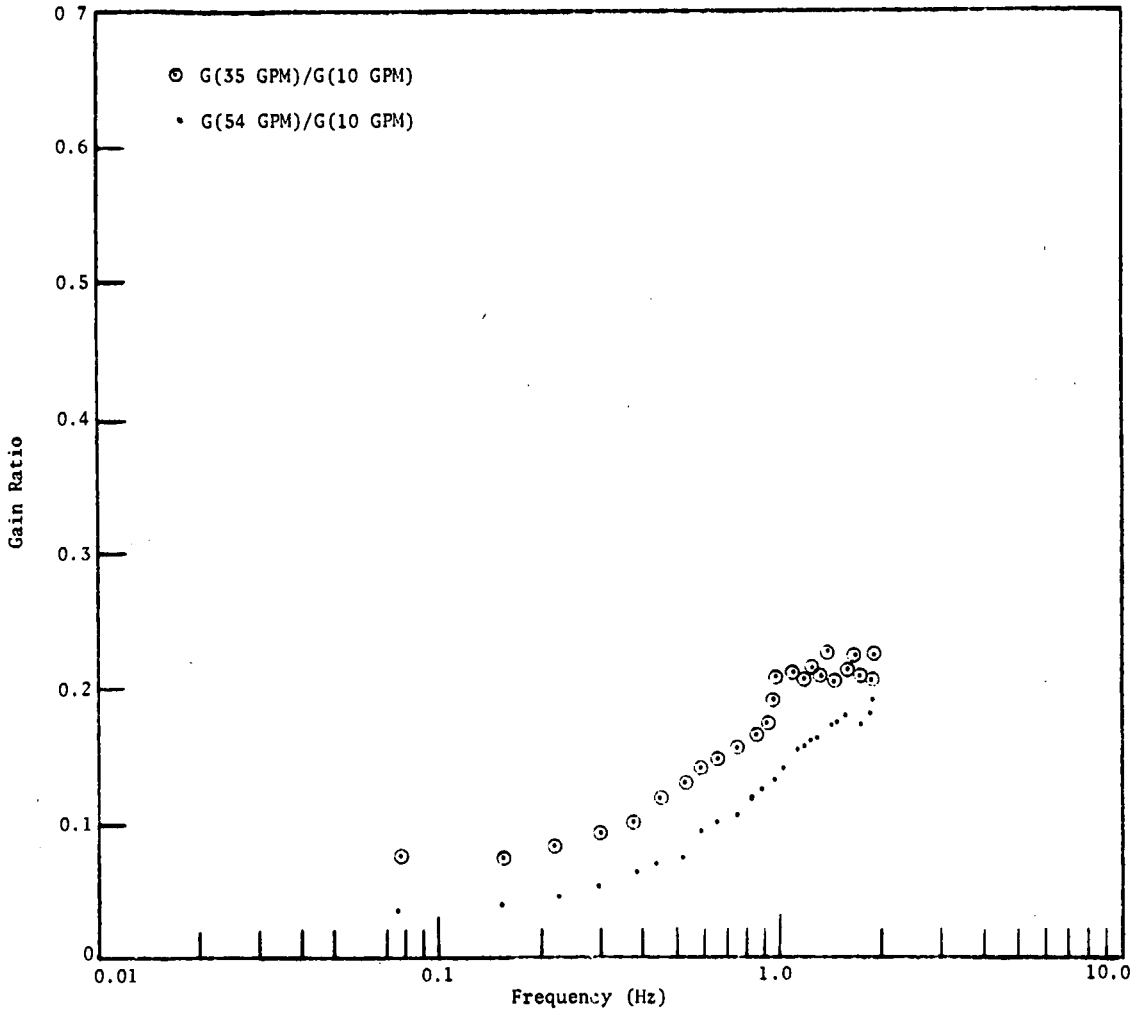

Figure V-16. Bundle 2B, gain ratios for thermocouple 1212 with rod 4 heated.

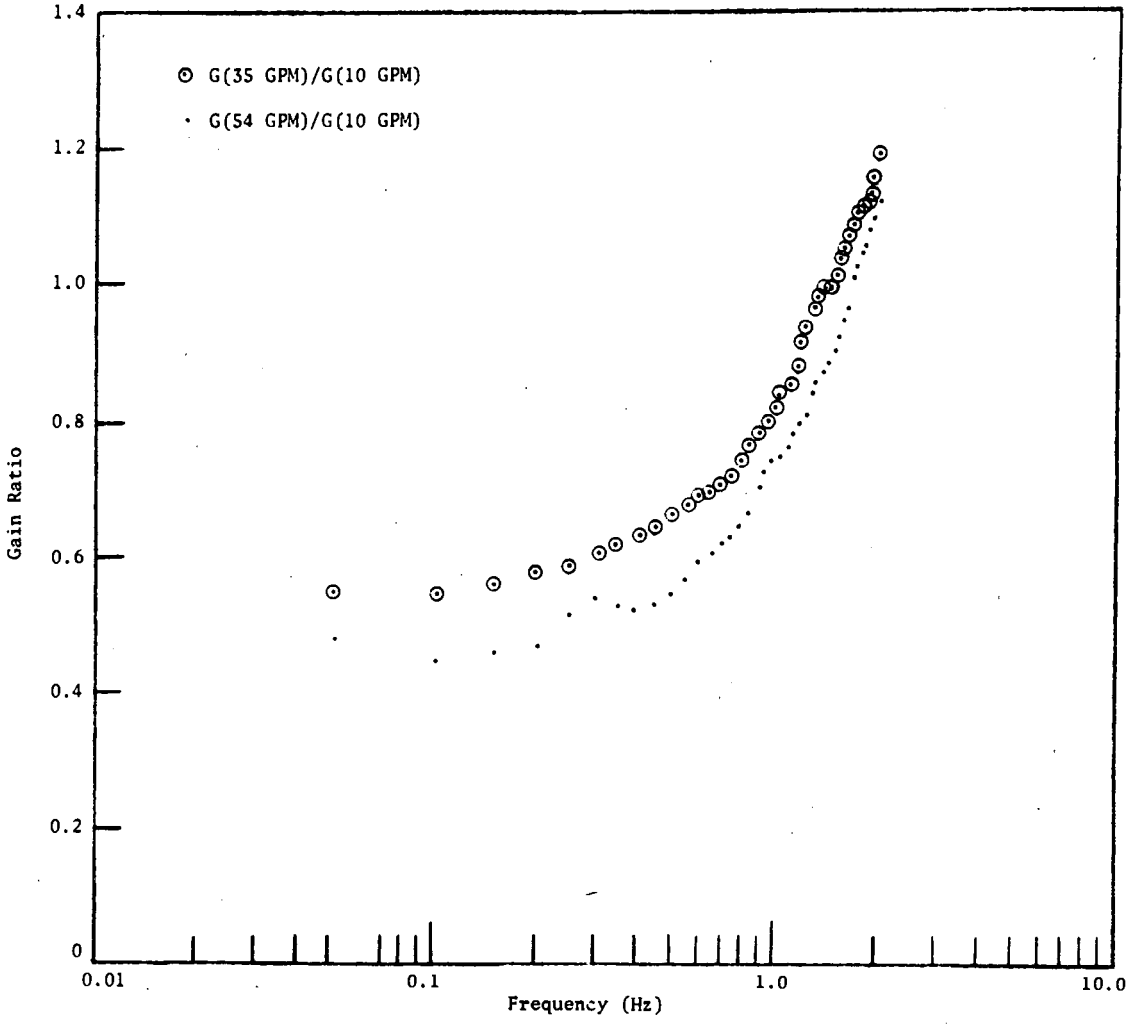

Figure V-17. Bundle 1B, gain ratios for thermocouple 0106 with rod 1 heated.

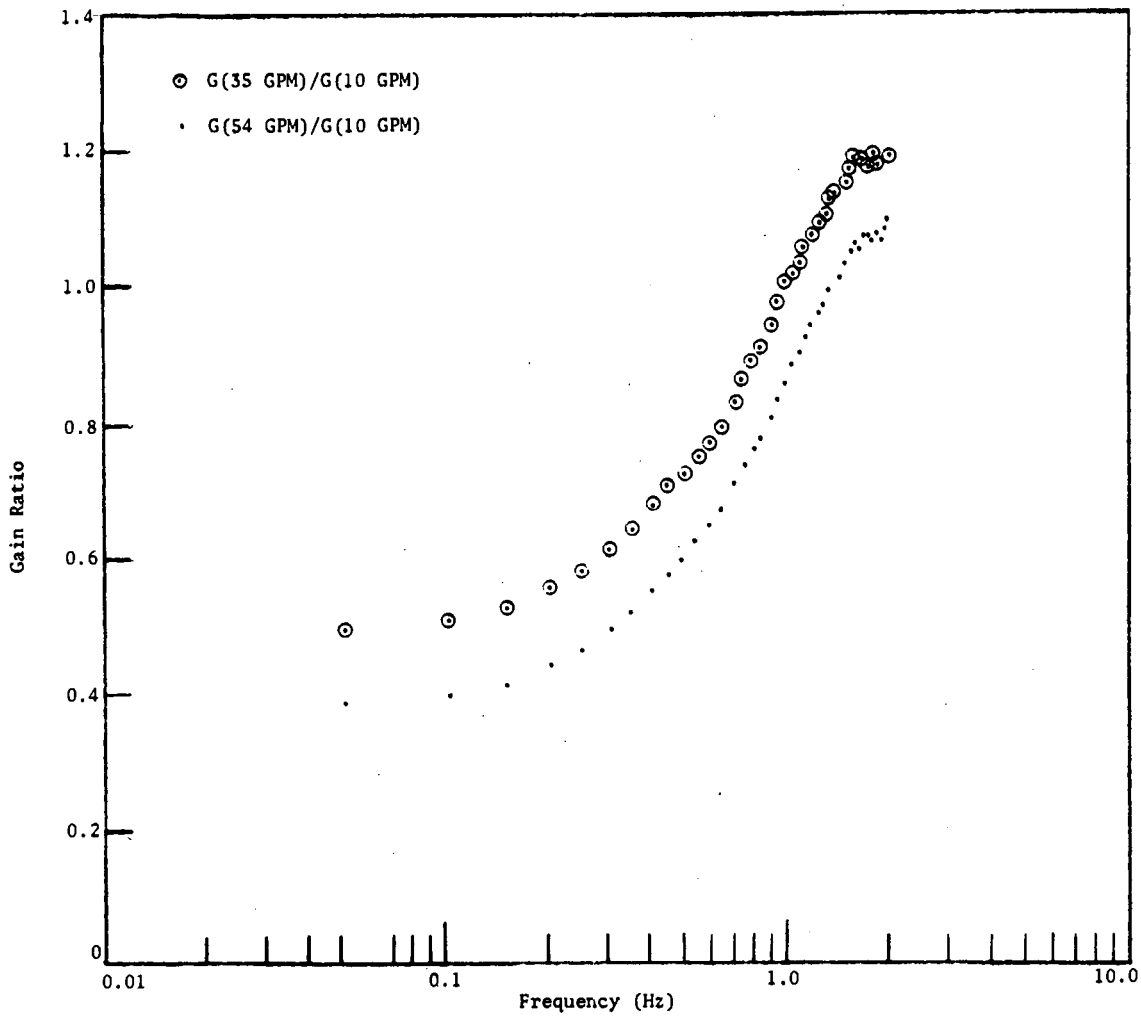

Figure V-18. Bundle 1B, gain ratios for thermocouple 0410 with rod 4 heated.

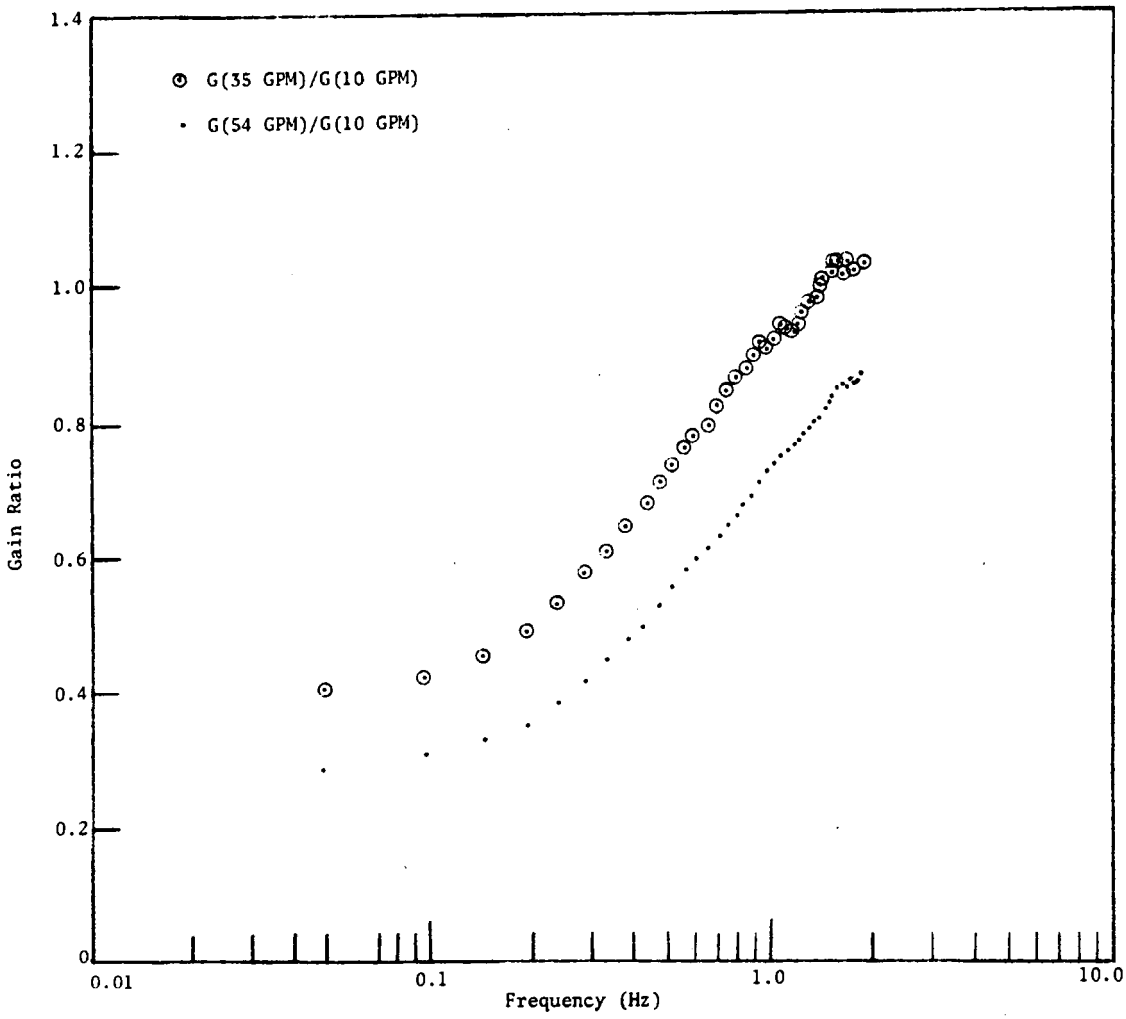

Figure V-19. Bundle 1B, gain ratios for thermocouple 0514 with rod 5 heated.

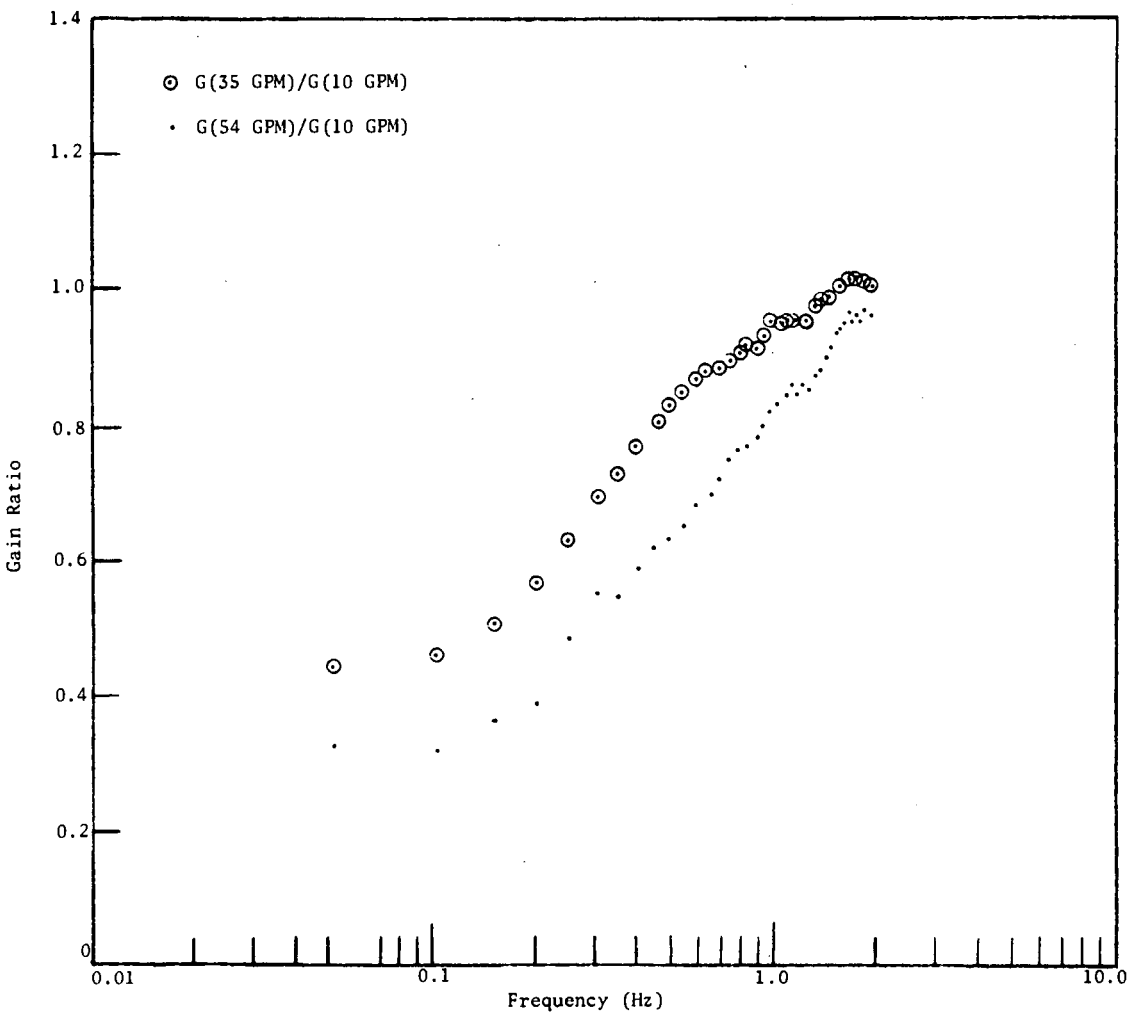

Figure V-20. Bundle 1B, gain ratios for thermocouple 0118 with rod 1 heated.

of the heated section the gain ratios have ringing and as the position of the thermocouple moves down the bundle the ringing decreases. For example, Figure V-17 shows the gain ratios for thermocouple 0106 with rod 1 heated, and Figure V-20 shows the gain ratios for thermocouple 0118 with rod 1 heated. The gain ratios at the 6 inch level show ringing while the gain ratios at the 18 inch level show no ringing. Some typical gain ratios from thermocouples not on the heated rod are shown in Figures V-21 through V-24. The gain ratios in Figures V-21 and V-22 show ringing while the gain ratios in Figures V-23 and V-24 show no ringing.

In summary, the gain ratios from thermocouples on the heated rod have ringing if the thermocouple is close to the beginning of the heated section and the ringing decreases as the thermocouple position approaches the end of the heated section. The gain ratios from thermocouples not on the heated rod do not show this trend. Additional gain ratios are shown in Figures B-1 through B-34 in Appendix B.

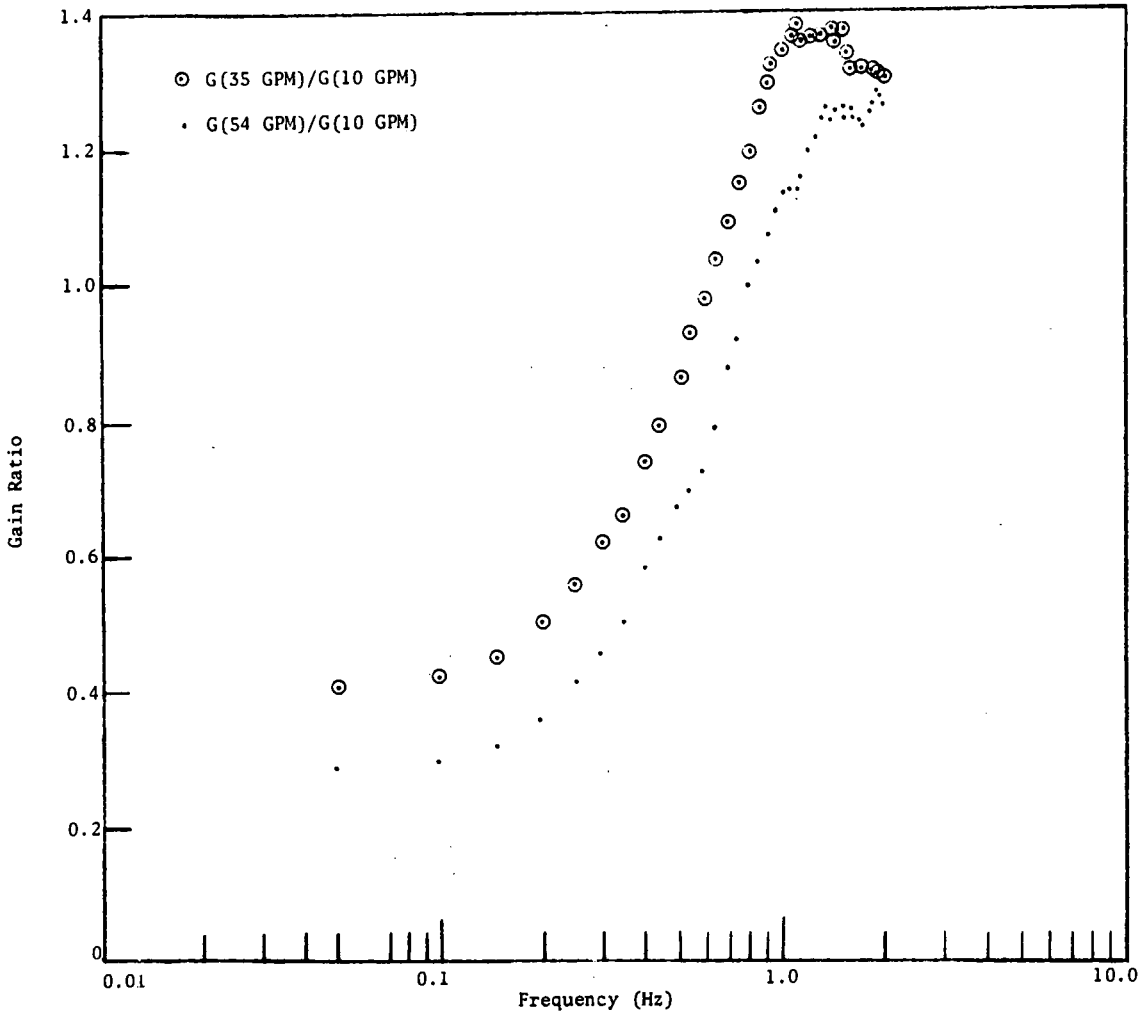

Figure V-21. Bundle 1B, gain ratios for thermocouple 0514 with rod 1 heated.

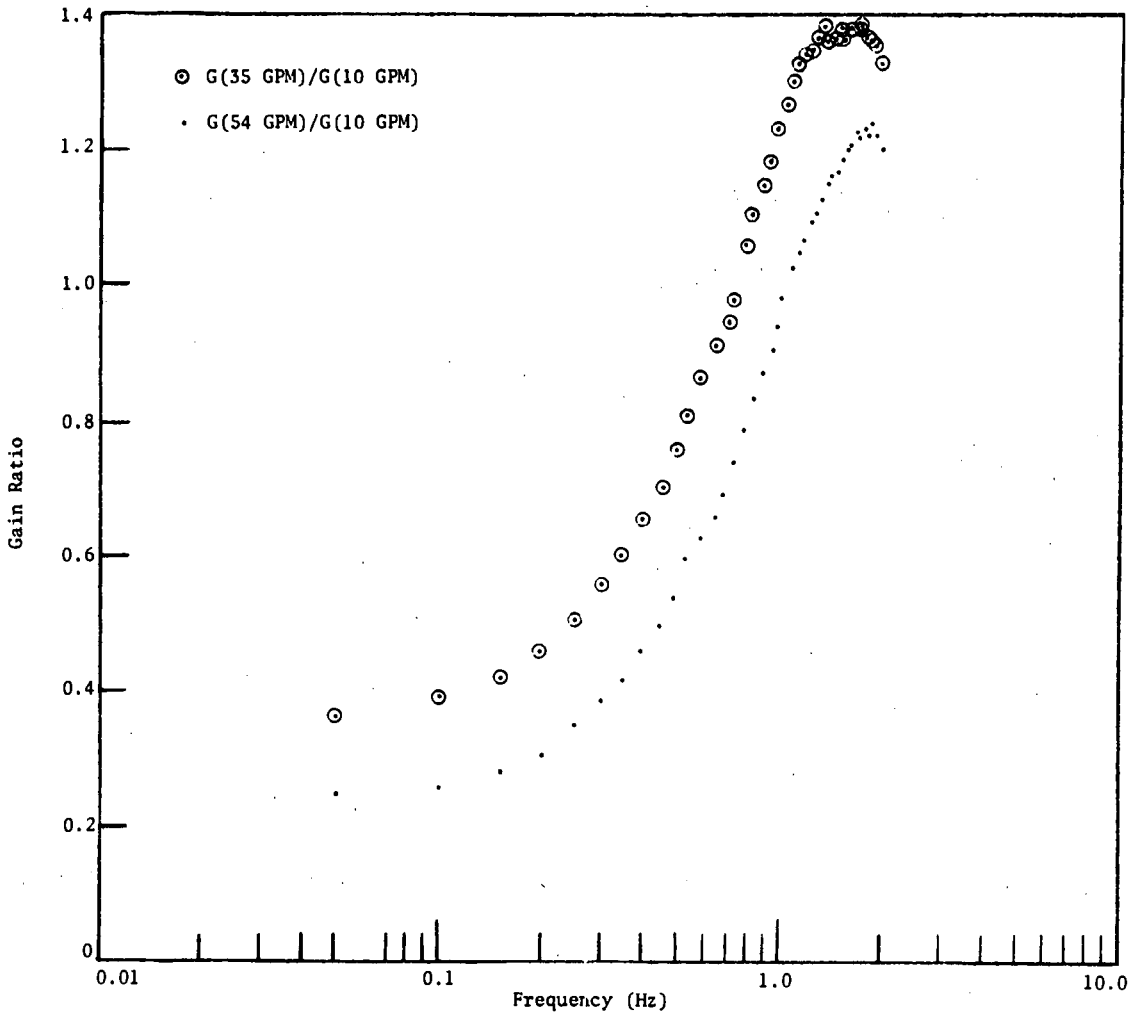

Figure 22. Bundle 1B, gain ratios for thermocouple 1514 with rod 5 heated.

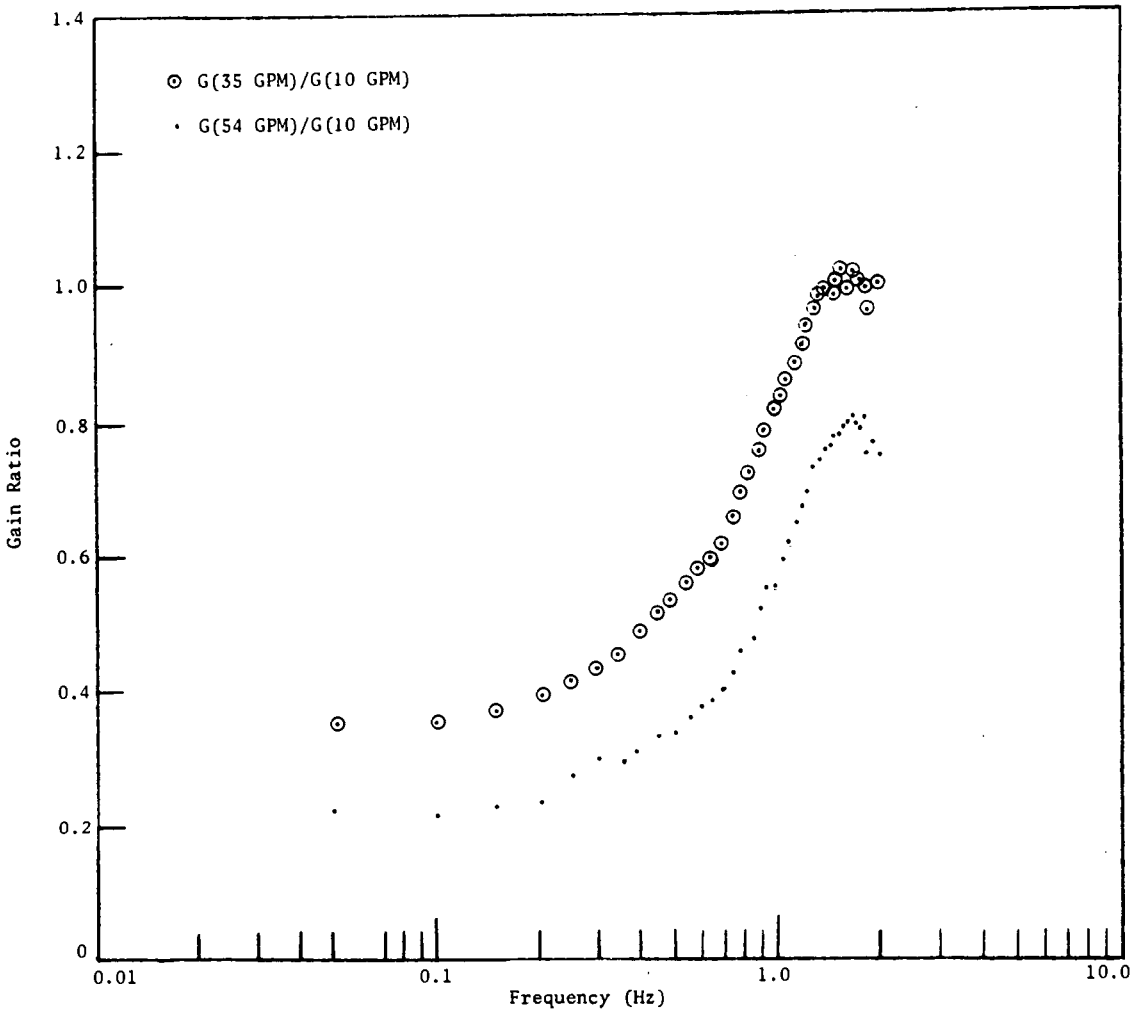

Figure 23. Bundle 1B, gain ratios for thermocouple 0410 with rod 1 heated.

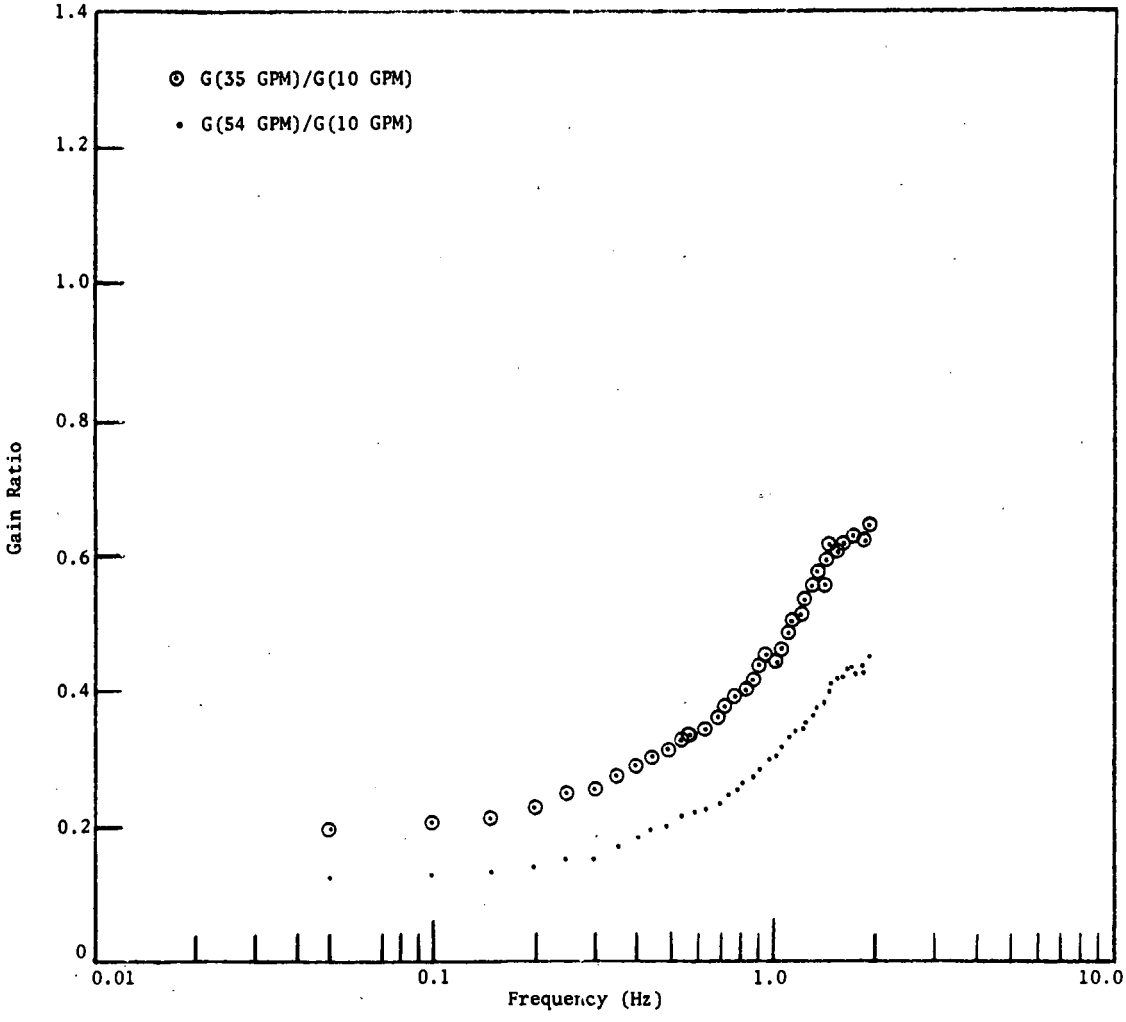

Figure V-24. Bundle 1B, gain ratios for thermocouple 0410 with rod 5 heated.

CHAPTER VI

INTERPRETATION OF EXPERIMENTAL RESULTS

I. VECTOR DIAGRAMS

No general trends were seen in the vector diagrams for bundle 2A since measurements were made for too few heater-thermocouple pairs.

The general trend observed in the vector diagrams for bundle 2B was that the vector length was larger if the vector direction was counterclockwise. It is thought that this trend is due to an edge swirl in the counterclockwise direction. This would aid counterclockwise energy flow and hinder clockwise energy flow. Therefore, vector lengths would be larger in the direction of the edge swirl.

The edge swirl is produced by the wire wraps on the outside rods since each wire wrap sweeps the fluid in the counterclockwise direction. Since the edge of the can is smooth, a swirl is established. The edge swirl has also been seen in other experiments on the FFM.[9]

No general energy flow trend was observed in the vector diagrams of bundle 1B. It is thought that no trends were seen because of the dummy rods around the periphery of the bundle whose purpose was to simulate an infinite bundle. Therefore, the effect of the edge swirl would be small or nonexistent in the interior of the bundle, and energy flow would not be aided by the edge swirl.

II. GAIN RATIOS

The physical reasoning in Section II of Chapter IV indicates that a plausible explanation of the ringing of the gain ratios is slug flow effects, and that well mixed flow causes the gain ratios to approach unity monotonically as the frequency increases. This implies that a plausible argument is that if the experimental gain ratios have ringing, it is an indication of predominant slug flow, and if the experimental gain ratios monotonically approach one as the frequency increases, it is an indication of predominant well mixed flow.

To interpret the experimental gain ratios, the gain ratios will be divided into two groups. First, gain ratios from thermocouples on the heated rod will be presented, and then gain ratios from thermocouples not on the heated rod will be presented. Table II shows that the gain ratios from thermocouples on the heated rod had a general pattern (see Figures V-17 through V-20, pages 67 through 70). If the thermocouple was close to the beginning of the heated section, the gain ratios had ringing similar to the slug flow model. As the position of the thermocouple moved down the bundle, the gain ratios had less ringing and became more like the gain ratios of the well mixed model. The interpretation of this trend is that at the entrance of the bundle there was predominant slug flow, and as the coolant moved through the bundle, mixing increased until there was predominant mixed flow.

The gain ratios from thermocouples not on the heated rod do not show the same trend. Table III shows that gain ratios similar to

TABLE II

GAIN RATIOS FROM THERMOCOUPLES ON THE HEATED ROD

Heated Rod Number	Thermocouple	Figure Number	Description of Gain Ratios
1	0106	V-17	Gain ratios show ringing similar to slug flow model
4	0410	V-18	Gain ratios show less ringing than Figure V-17
5	0514	V-19	Gain ratios exceed unity slightly, no ringing
1	0118	V-20	Gain ratios approach unity similar to well mixed model

TABLE III

GAIN RATIOS FROM THERMOCOUPLES NOT ON THE HEATED ROD

Heated Rod Number	Thermocouple	Figure Number	Description of Gain Ratios
1	0514	V-21	Gain ratios show ringing similar to slug flow model
1	0410	V-23	Gain ratios approaches unity similar to well mixed model
5	1514	V-22	Gain ratios show ringing similar to slug flow model
5	0410	V-24	Gain ratios do not reach unity

both theoretical models are seen throughout the bundle. For example, Figures V-21 and V-22, pages 72 and 73, show that gain ratios from thermocouples 0514 and 1514 are similar to the gain ratios of the slug flow model while Figures V-23 and V-24, pages 74 and 75, show that gain ratios from thermocouple 0410 are similar to the gain ratios of the well mixed model. A possible explanation for this is that the wire wrap on the heated rod affects the gain ratios seen at an adjacent rod.

If the wire wrap on the heated rod is responsible for the type of gain ratios seen at an adjacent rod, it is reasonable to expect that identical heated rod to thermocouple geometries would have similar gain ratios. For example, the combination of thermocouple 0318 with rod 1 heated has the same geometry as thermocouple 1918 with rod 18 heated. Figures VI-1 and VI-2 compare the gain ratios of identical thermocouple to heated rod geometries. As the figures show, the gain ratios are very similar. This agreement is not seen in all cases. For example, the gain ratios in Figure VI-3 show no agreement even though the geometries are identical. The only explanation at this time for Figure VI-3 is that the results from thermocouple 1414 may be affected by edge effects which change the gain ratios.

Further support of the postulated explanation of the effect of the wire wraps on the gain ratios can be obtained from the results of thermocouples which are symmetric with respect to two heated rods. If the wire wrap on the heated rod does influence the results, the gain ratios from a thermocouple and a heated rod would be expected to differ with the gain ratios from the same thermocouple and a different heated rod

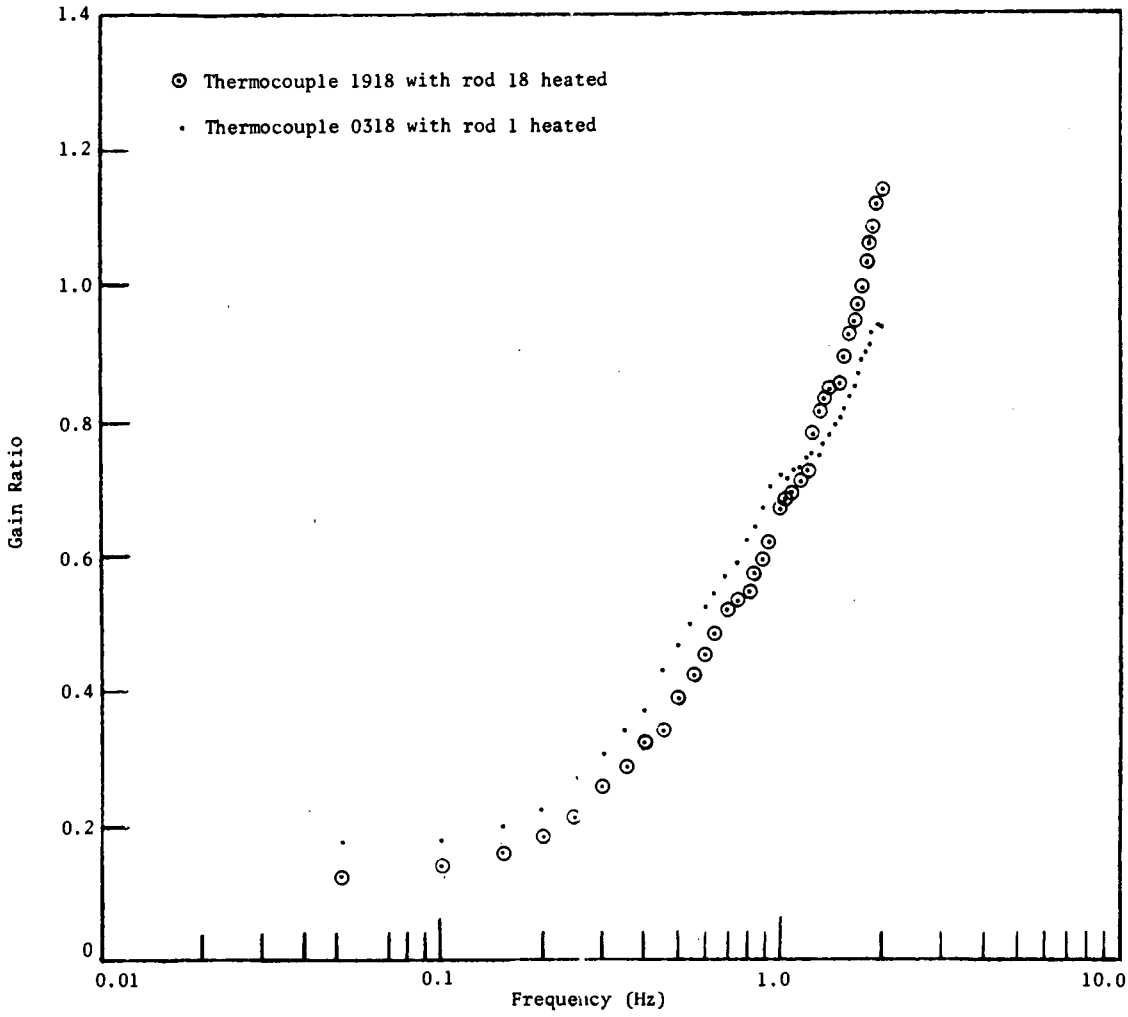

Figure VI-1. A comparison of the gain ratios, G(54 GPM)/G(10 GPM), from thermocouples 0318 and 1918.

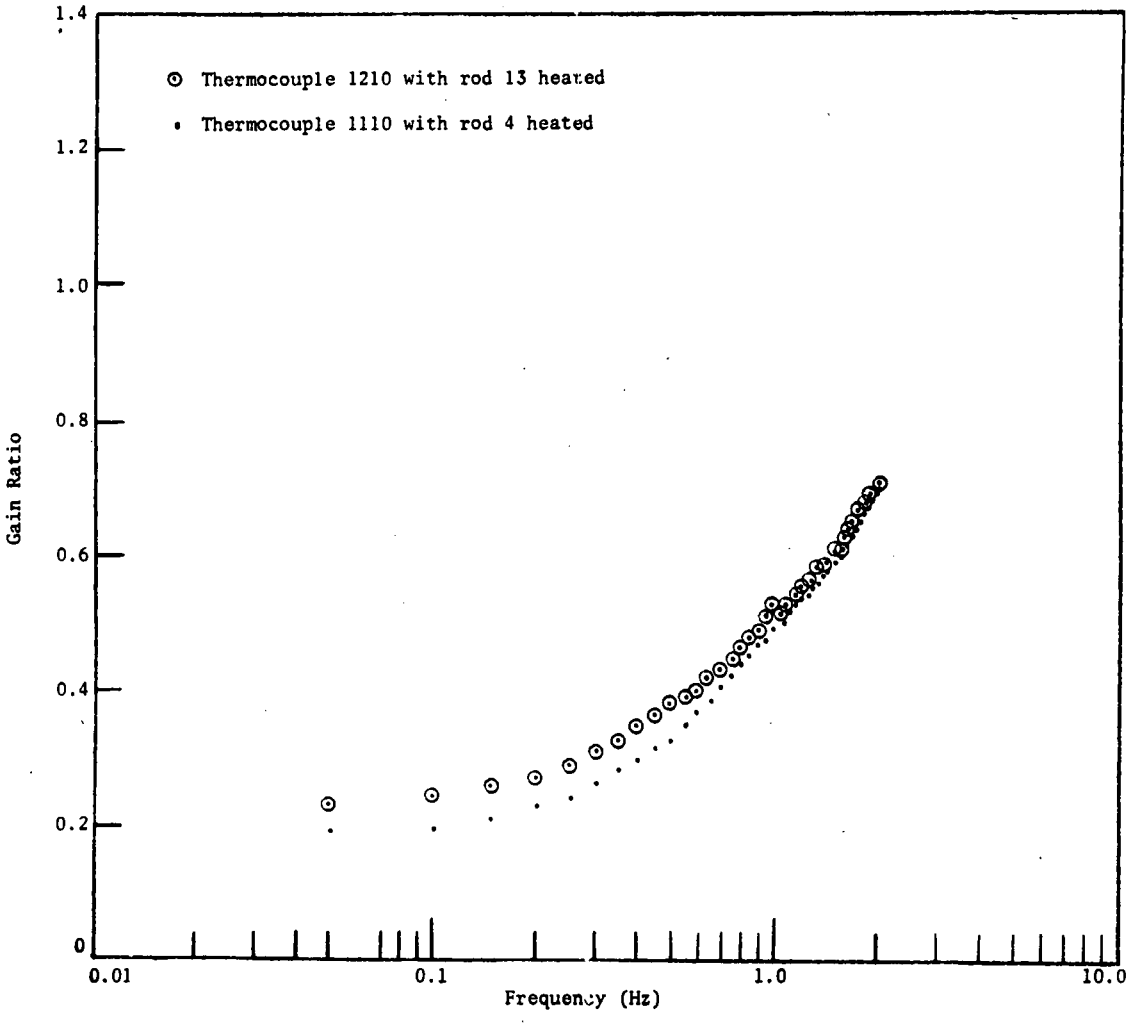

Figure VI-2. A comparison of the gain ratios, G(54 GPM)/G(10 GPM), from thermocouples 1210 and 1110.

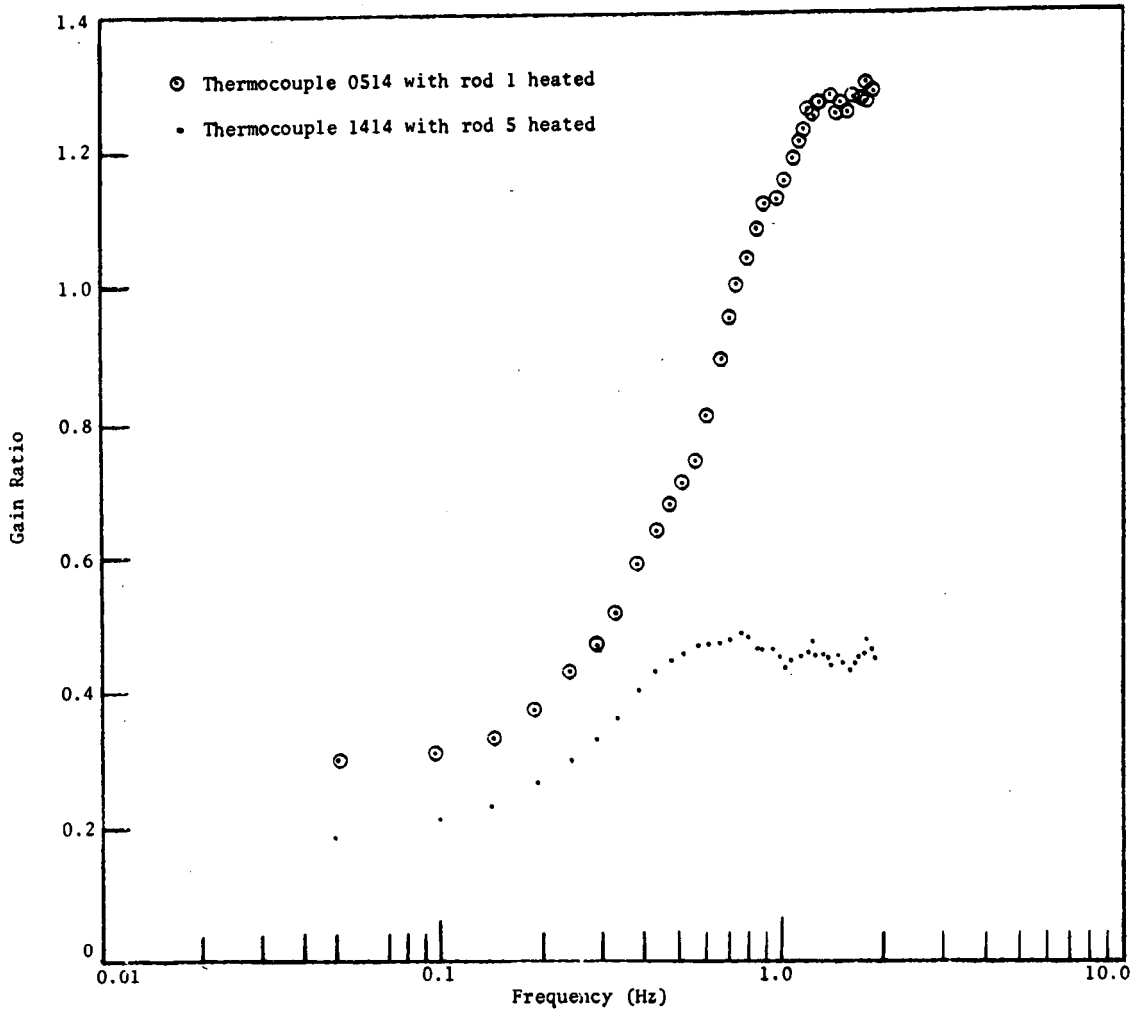

Figure VI-3. A comparison of the gain ratios, G(54 GPM)/G(10 GPM), from thermocouples 0514 and 1414.

since the orientation between the wire wraps and the thermocouple is different. As an example, thermocouple 0118 is symmetric with respect to rods 4 and 5. Figure VI-4 shows that ringing is seen when rod 5 is heated, and no ringing is seen when rod 4 is heated. Since the results are different, they support the theory that the wire wrap on the heated rod affects the results from a thermocouple on an adjacent rod.

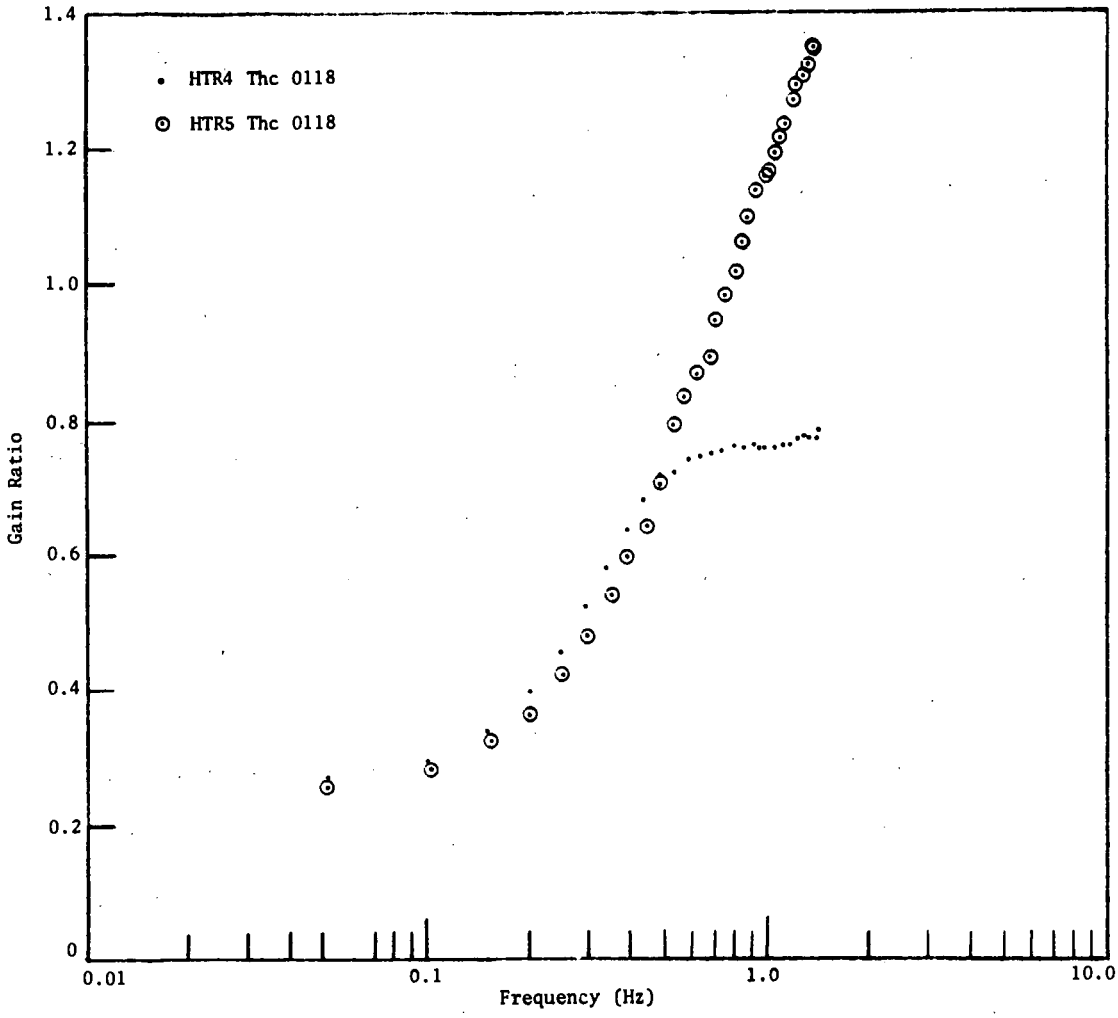

Figure VI-4. Bundle 1B, gain ratios, G(54 GPM)/G(10 GPM), for thermocouple 0118.

CHAPTER VII

CONCLUSIONS AND RECOMMENDATIONS

This study presents the experimental data from dynamic tests on the FFM and a preliminary interpretation of the experimental data. All of the information from the dynamic tests is not yet fully interpreted and more work is needed to fully understand the experimental data.

This work has furnished a new experimental technique and interpretation procedure based on vector diagrams that appears to have the capability of providing useful information on energy flow patterns in LMFBR fuel bundles. Full realization of this technique will require further testing with larger numbers of thermocouples and development of more rigorous theoretical models that would allow more detailed comparisons between theory and experiment.

The objective of the dynamic tests was to provide information on flow and heat transfer in the FFM bundles. To help understand the experimental results, two simplified theoretical models were developed. As a result a method was developed for distinguishing between slug flow and well mixed flow. This capability can be further evaluated in interpreting future experimental results.

Future FFM bundles would give a more complete picture of fluid and heat flow if the bundle contained more thermocouples. If more thermocouples were on the heated rod, the type of flow through the bundle would be shown better.

The following additional work is recommended:

1. Interpret the phase differences as well as the gain ratios.
2. Apply the techniques developed in this study to blocked bundles.
3. Obtain the frequency response of the thermocouples so that the gain ratio (Gain of thermocouple 1)/(Gain of thermocouple 2) can be interpreted.
4. Develop more rigorous theoretical models that include inter-channel mixing.
5. Evaluate the possible advantages of tests in which more than one heated rod is used.

LIST OF REFERENCES

1. Kerlin, T. W., "The Pseudo-Random Binary Signal for Frequency Response Testing," USAEC Report ORNL-TM-1662, Oak Ridge National Laboratory (1966).

2. Kerlin, T. W., Nuclear Engineering Department, University of Tennessee, Knoxville, personal communication with the author.

3. Kerlin, T. W., "The Pseudo-Random Binary Signal for Frequency Response Testing," USAEC Report ORNL-TM-1662, Oak Ridge National Laboratory (1966).

4. Kerlin, T. W., "Methods for Frequency Response Measurements in Power Reactors," Dynamics of Nuclear Systems, Hetrick, D. L. (ed.), 320 (1972).

5. Kerlin, T. W., Nuclear Engineering Department, University of Tennessee, Knoxville, personal communication with the author.

6. Kryter, R. C., "Application of the Fast Fourier Transform Algorithm to On-Line Reactor Diagnosis," IEEE Transactions Nuclear Science, NS-16(1), 210-17 (February 1969).

7. Schultz, M. A., Control of Nuclear Reactors and Power Plants, 2nd ed. (New York, 1961).

8. Chen, A. T., Unpublished Notes, Nuclear Engineering Department, University of Tennessee, Knoxville, Tennessee.

9. Fontana, M. H. and Wantland, J. L. and Parsley, L. F., "ORNL Nuclear Safety Research and Development Program Bimonthly Report for March-April 1972," USAEC Report ORNL-TM-3831, Oak Ridge National Laboratory, 8-12.

APPENDIX A

EXPERIMENTAL DATA IN THE FORM OF VECTOR DIAGRAMS

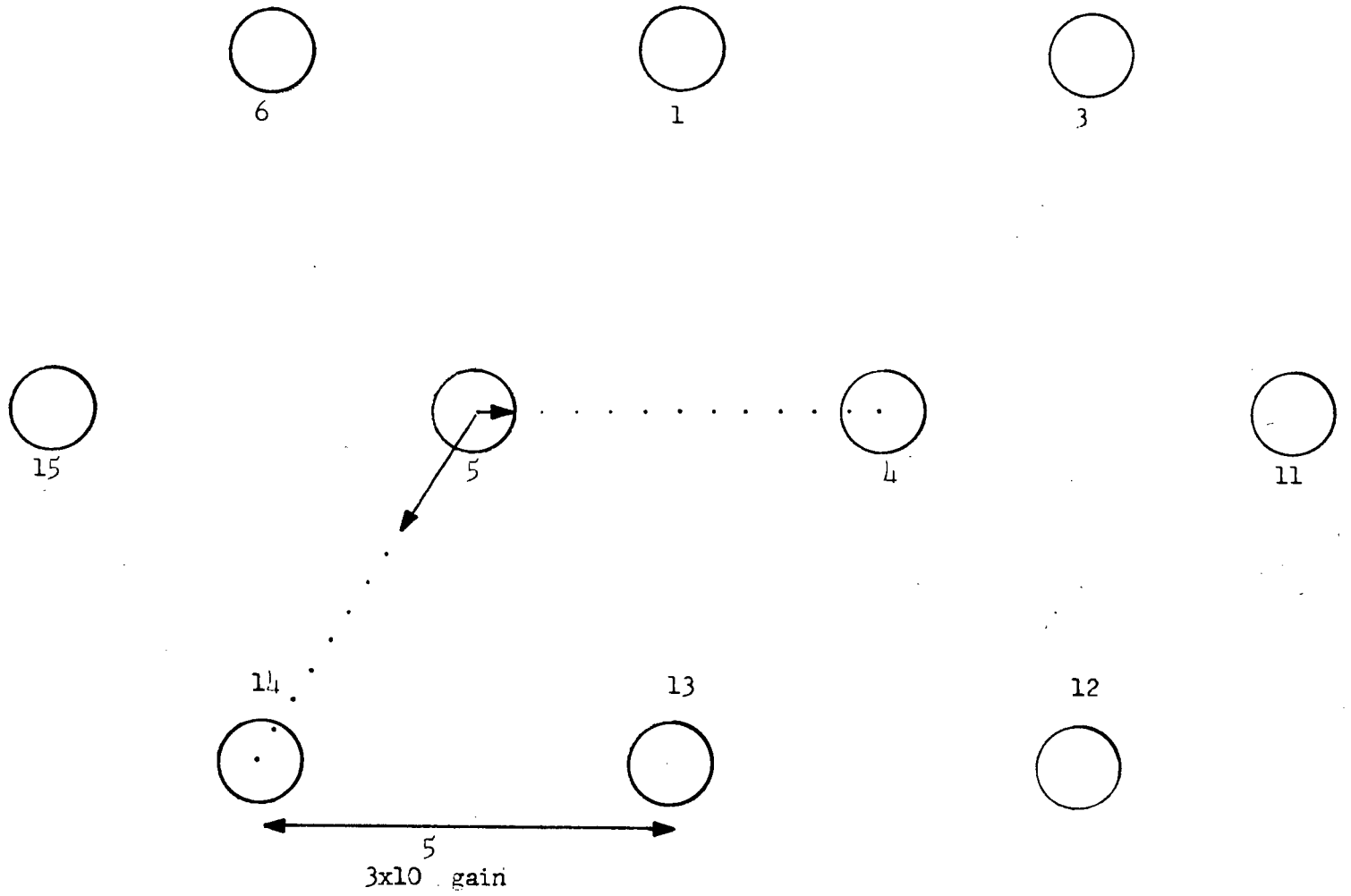

Figure A-1. Vector diagram for bundle 2A at the 9 inch level at 20 GPM.

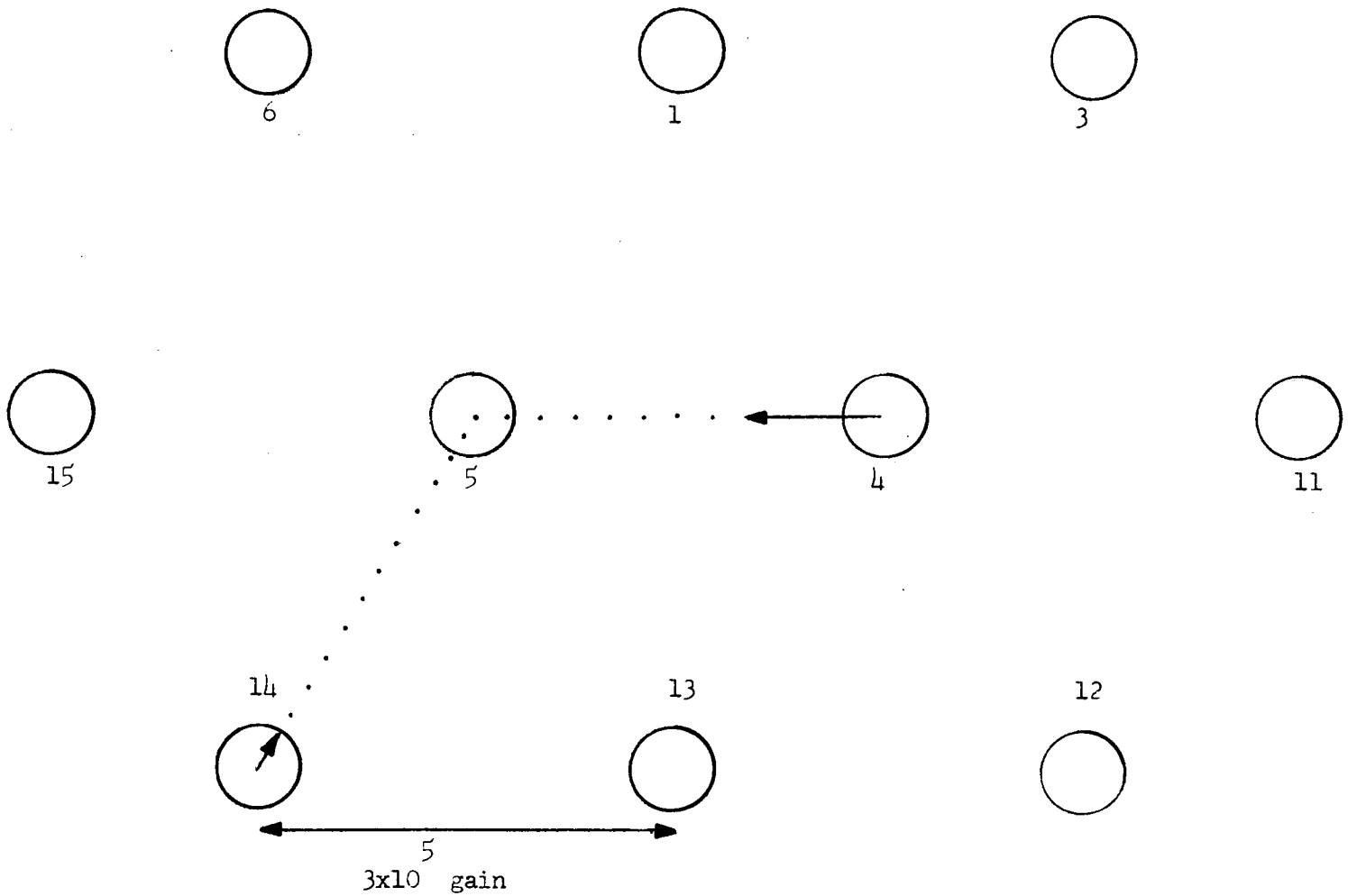

Figure A-2. Vector diagram for bundle 2A at the 9 inch level at 54 GPM.

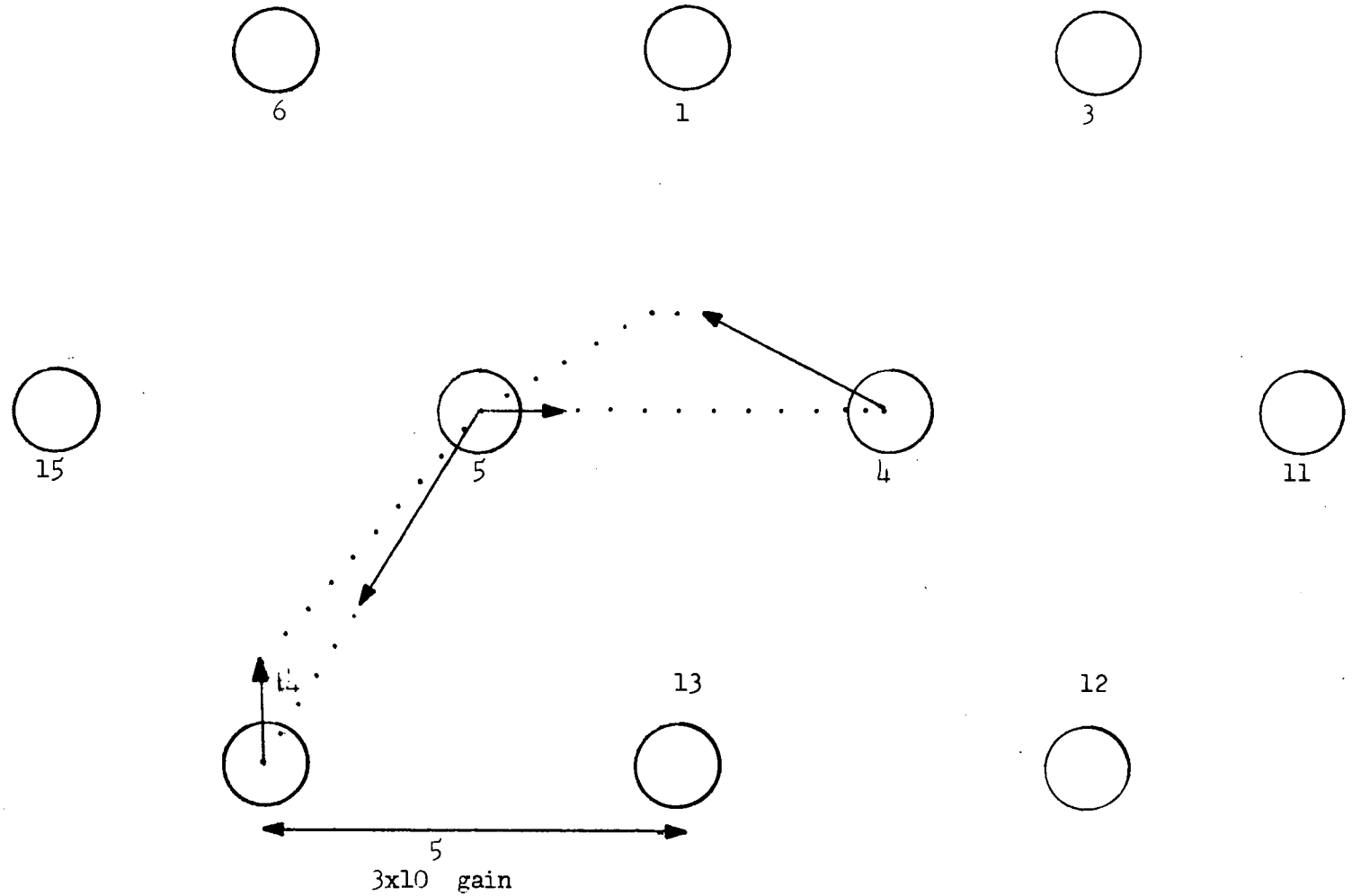

Figure A-3. Vector diagram for bundle 2A at the 21 inch level at 35 GPM.

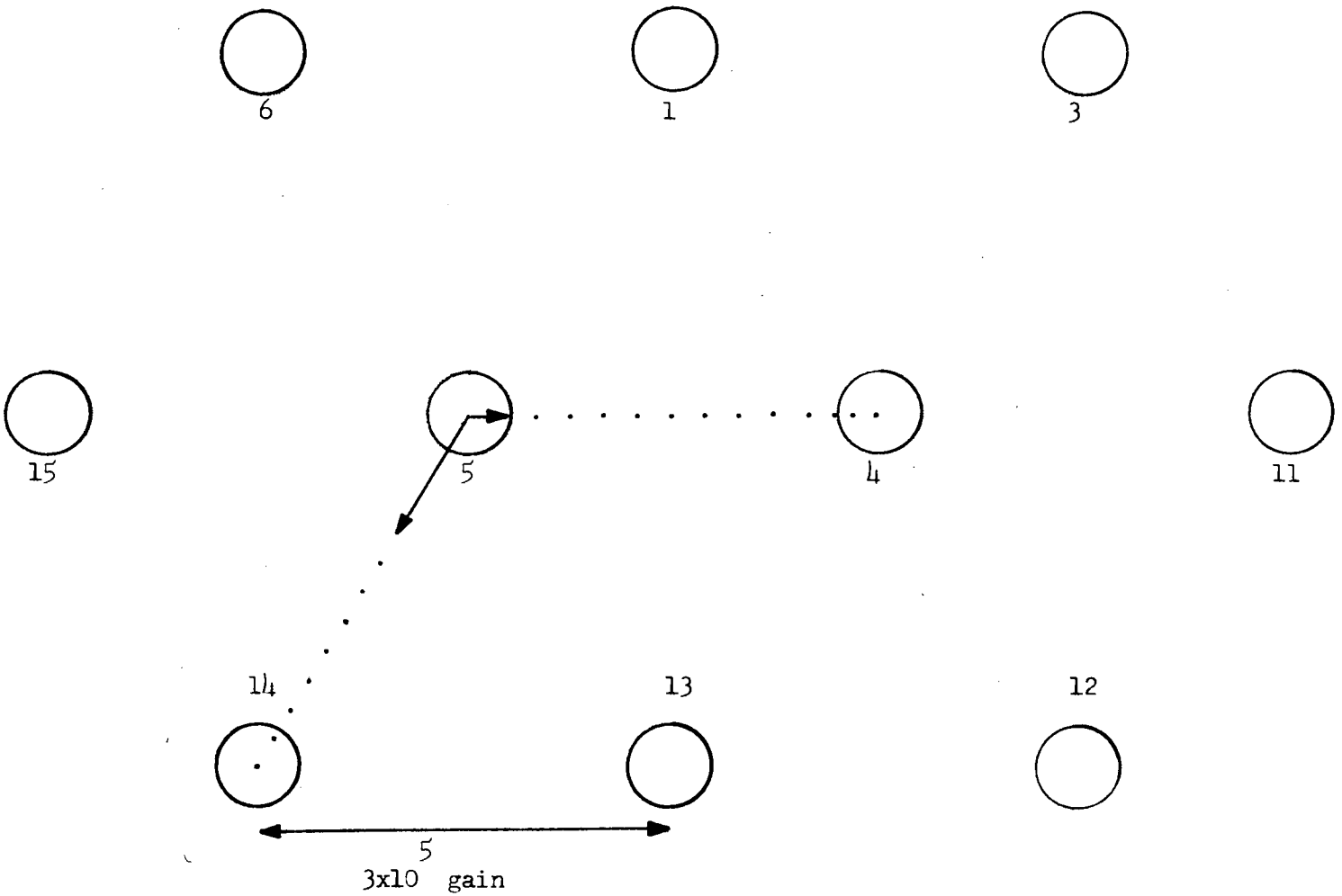

Figure A-4. Vector diagram for bundle 2A at the 21 inch level at 54 GPM.

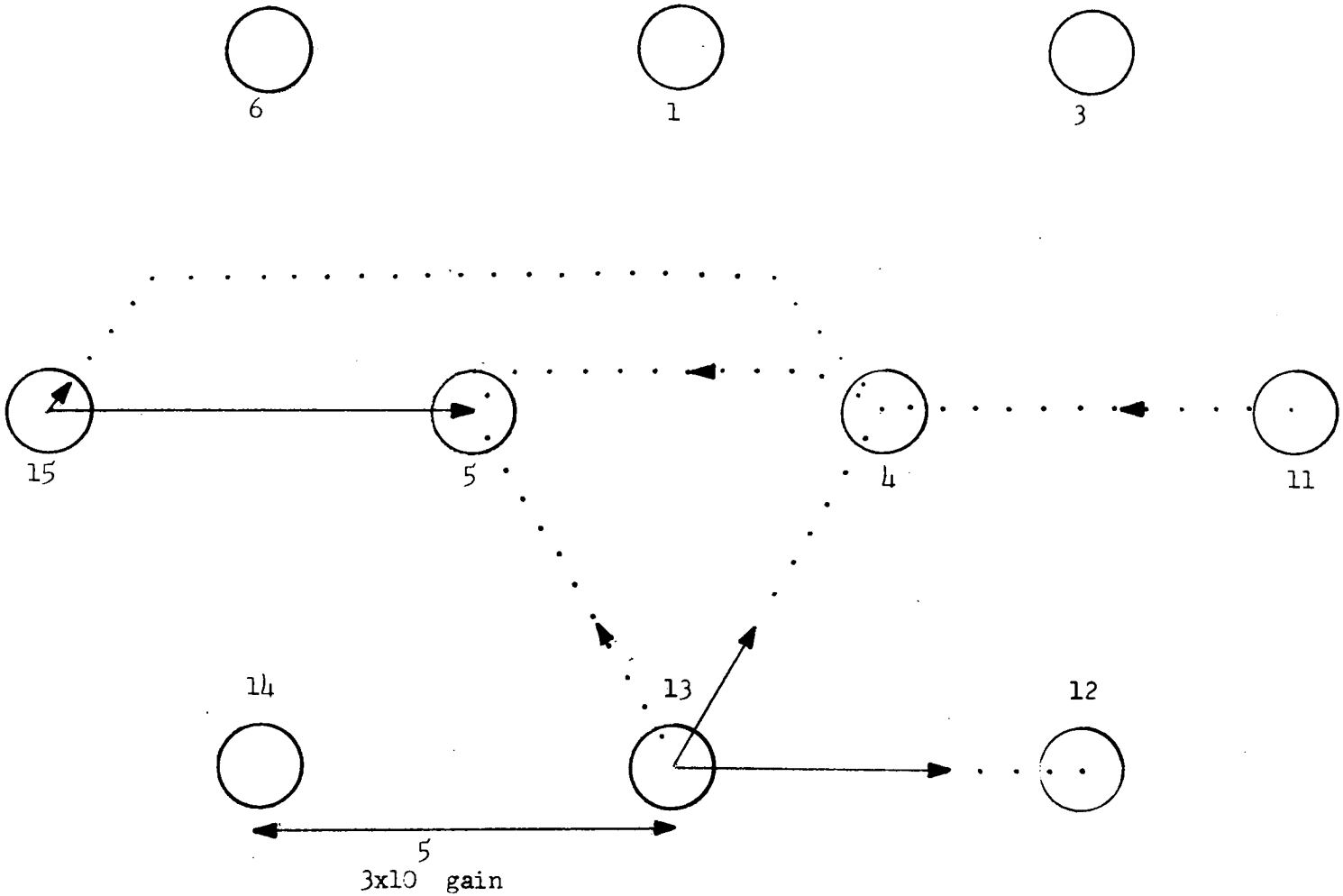

Figure A-5. Vector diagram for bundle 2B at the 12 inch level at 35 GPM.

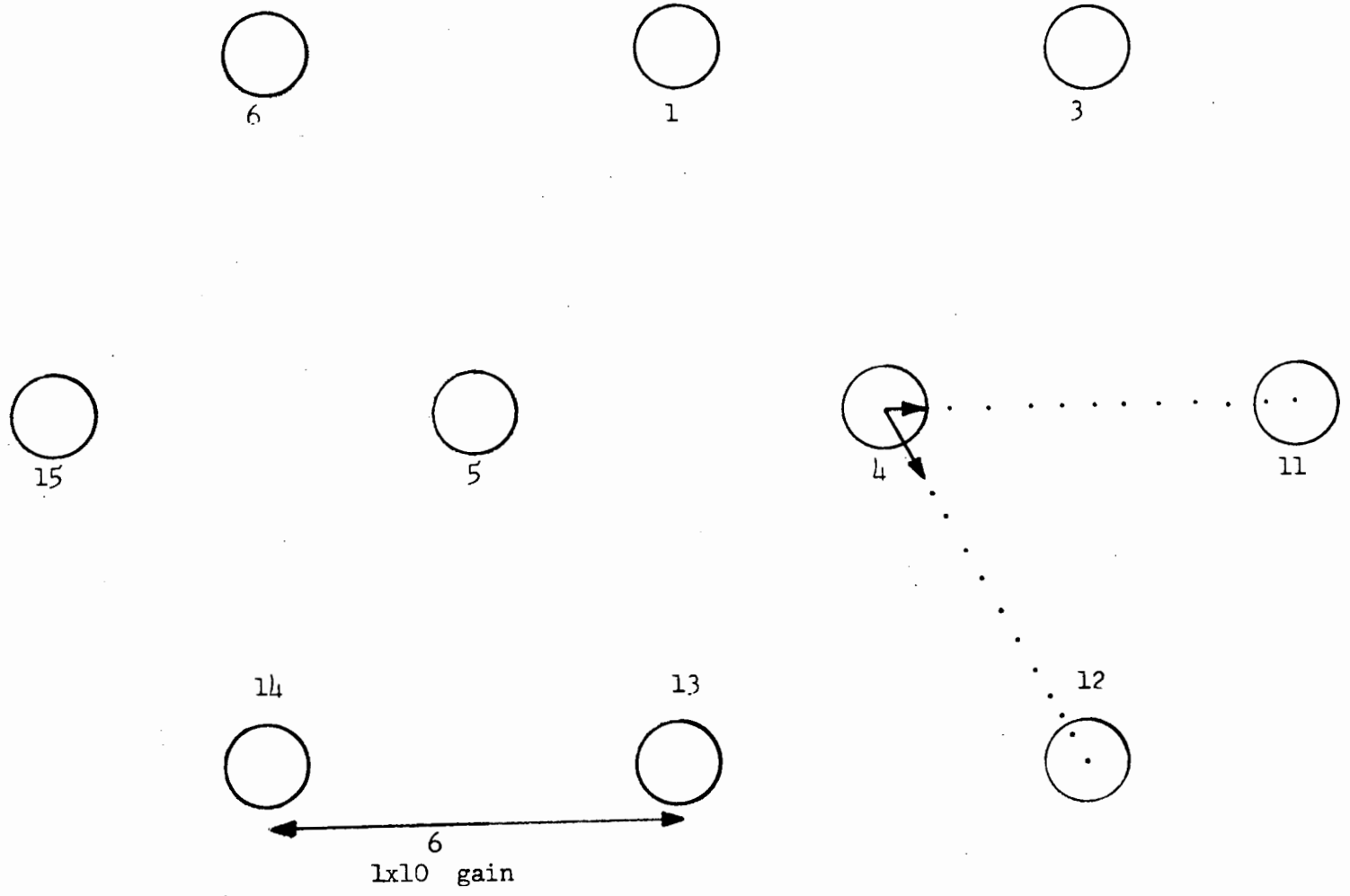

Figure A-6. Vector diagram for bundle 1B at the 22 inch level at 54 GPM.

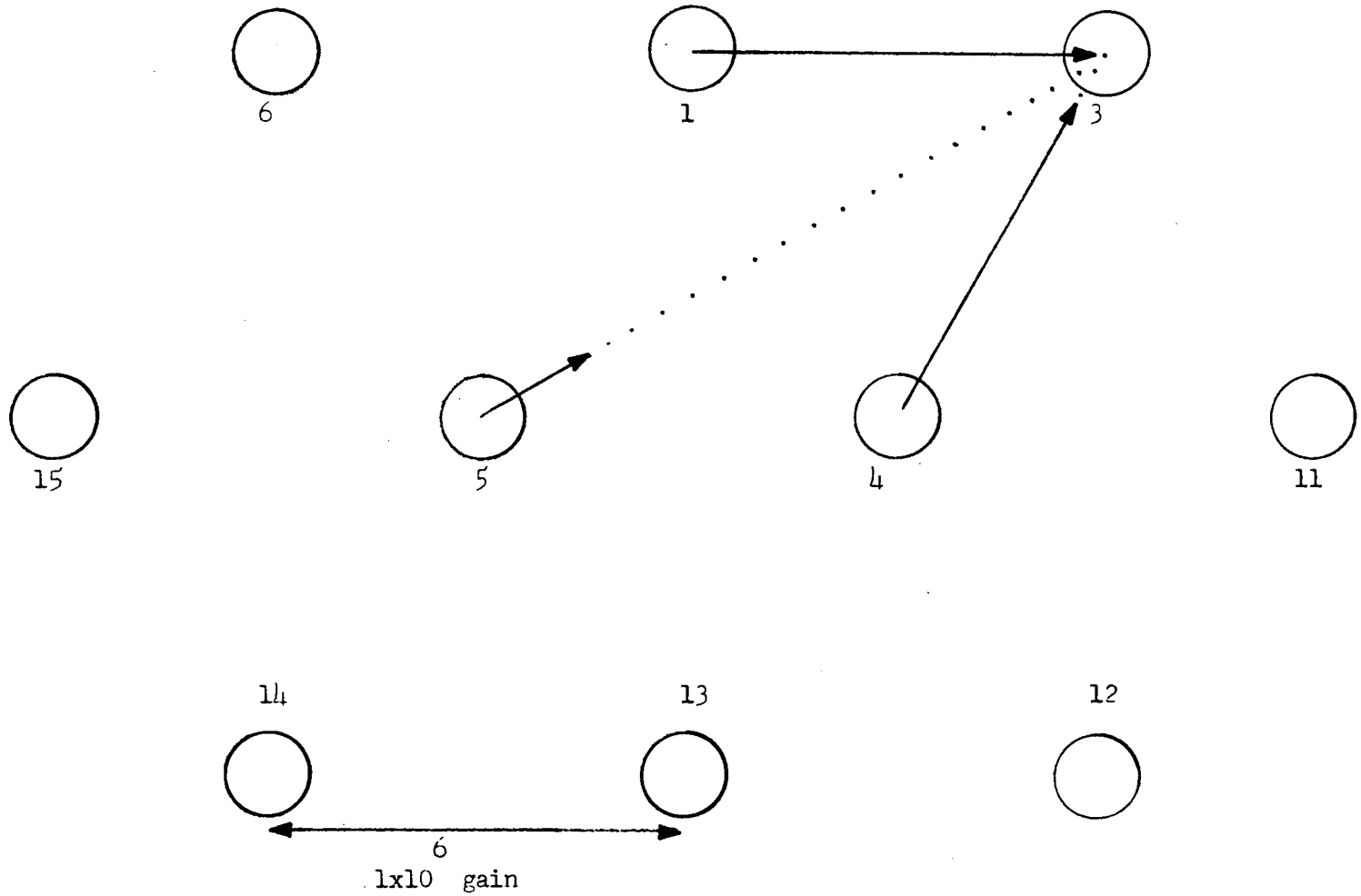

Figure A-7. Vector diagram for bundle 1B at the 20 inch level at 10 GPM.

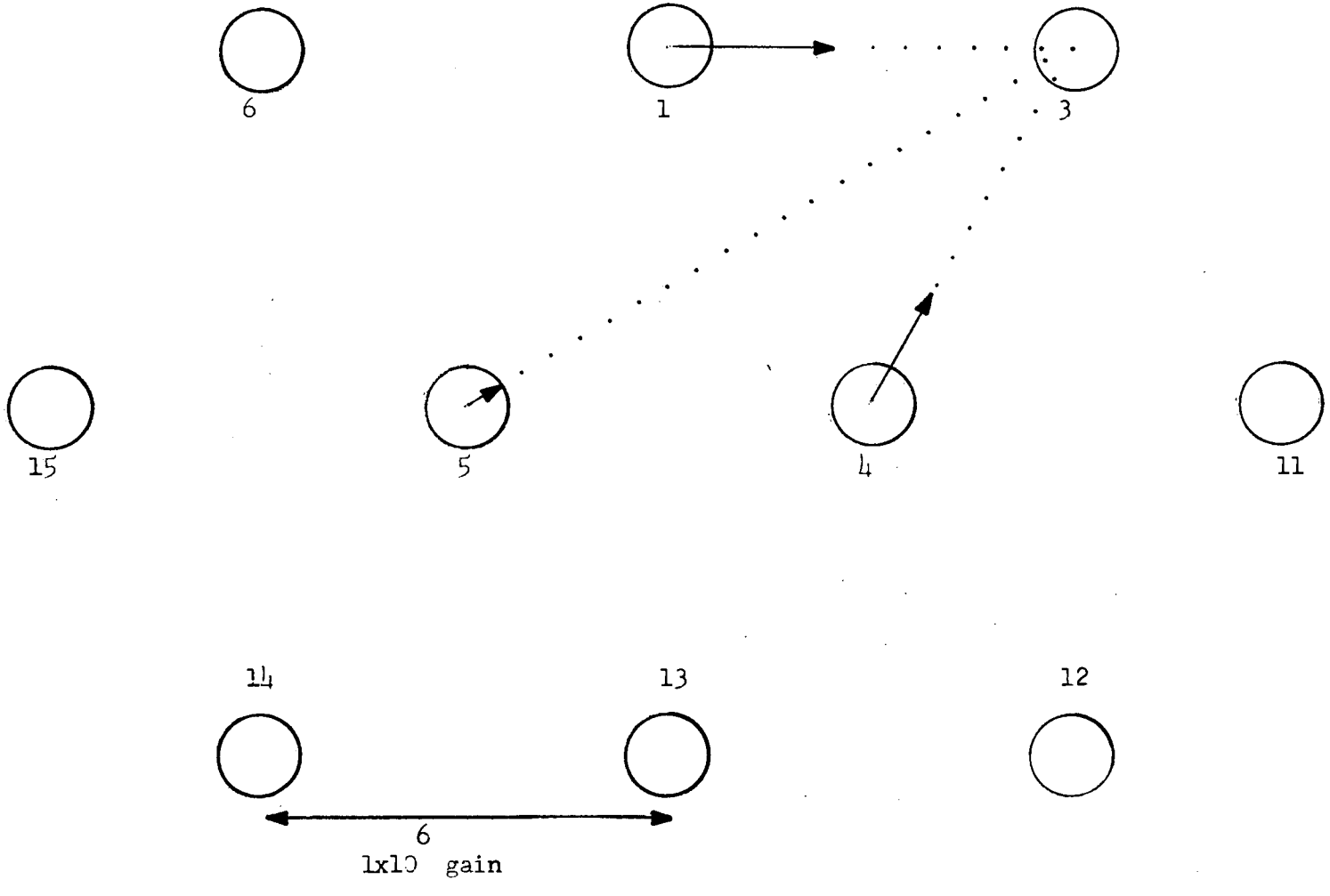

Figure A-8. Vector diagram for bundle 1B at the 20 inch level at 35 GPM.

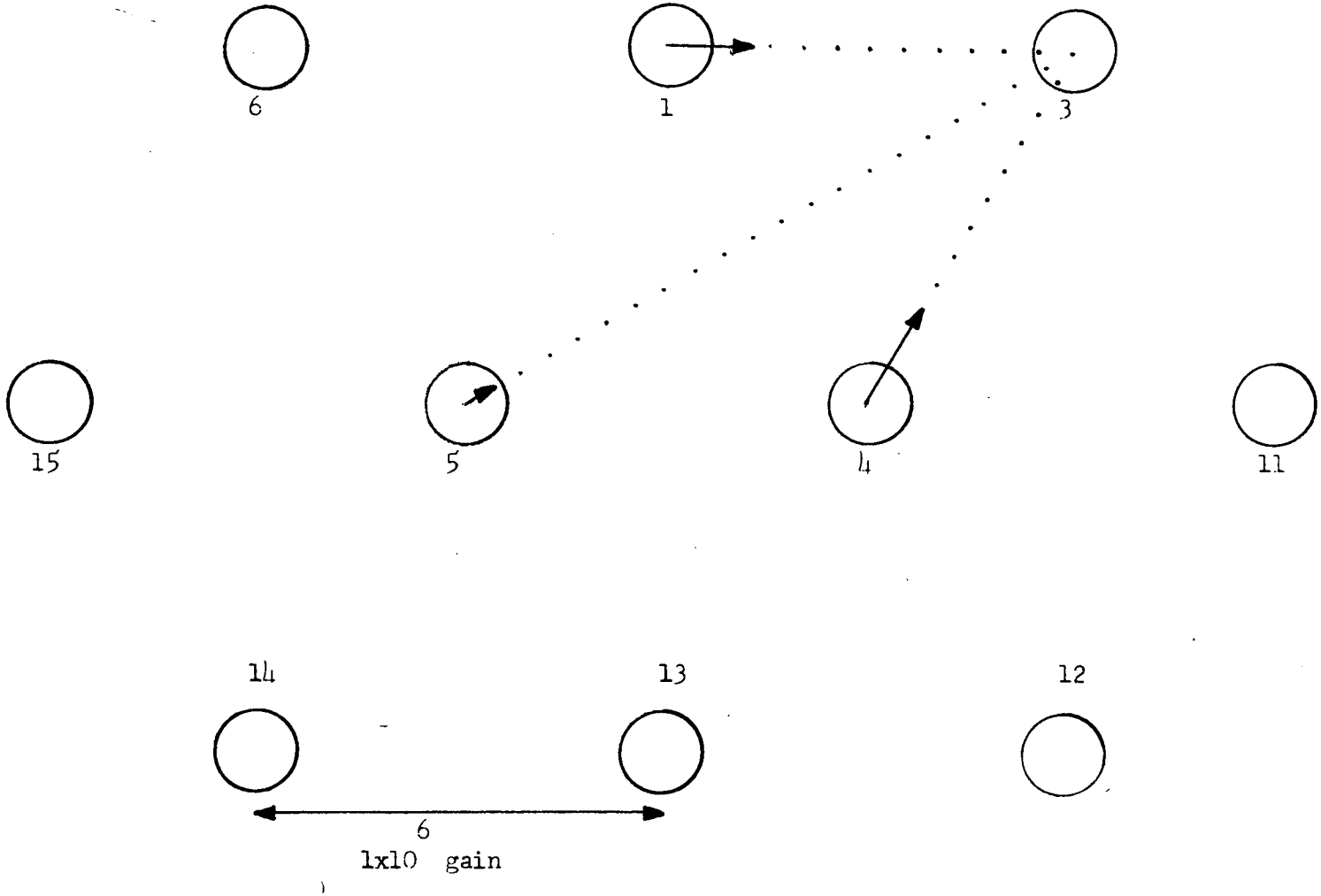

Figure A-9. Vector diagram for bundle 1B at the 20 inch level at 54 GPM.

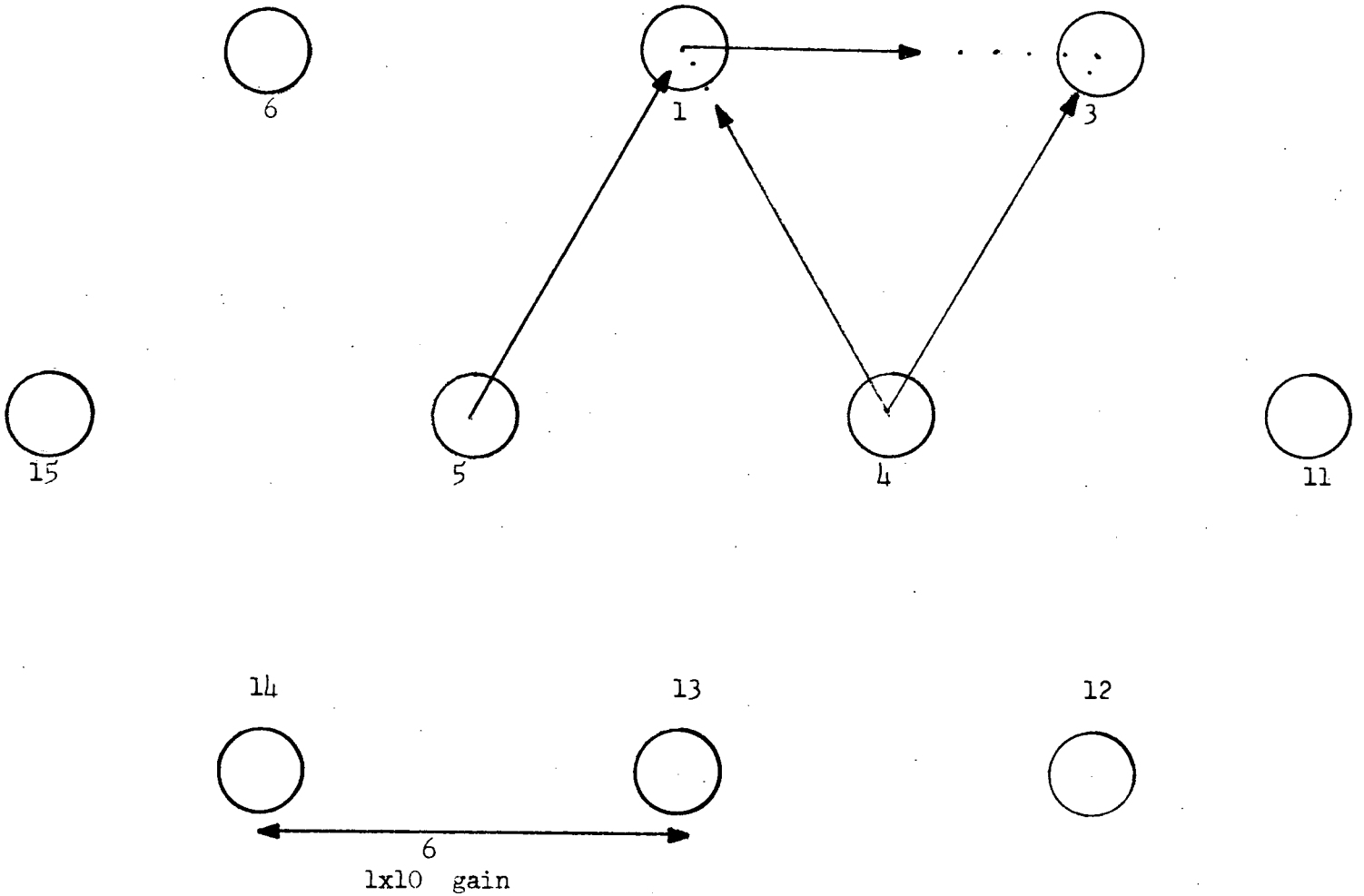

Figure A-10. Vector diagram for bundle 1B at the 18 inch level at 10 GPM.

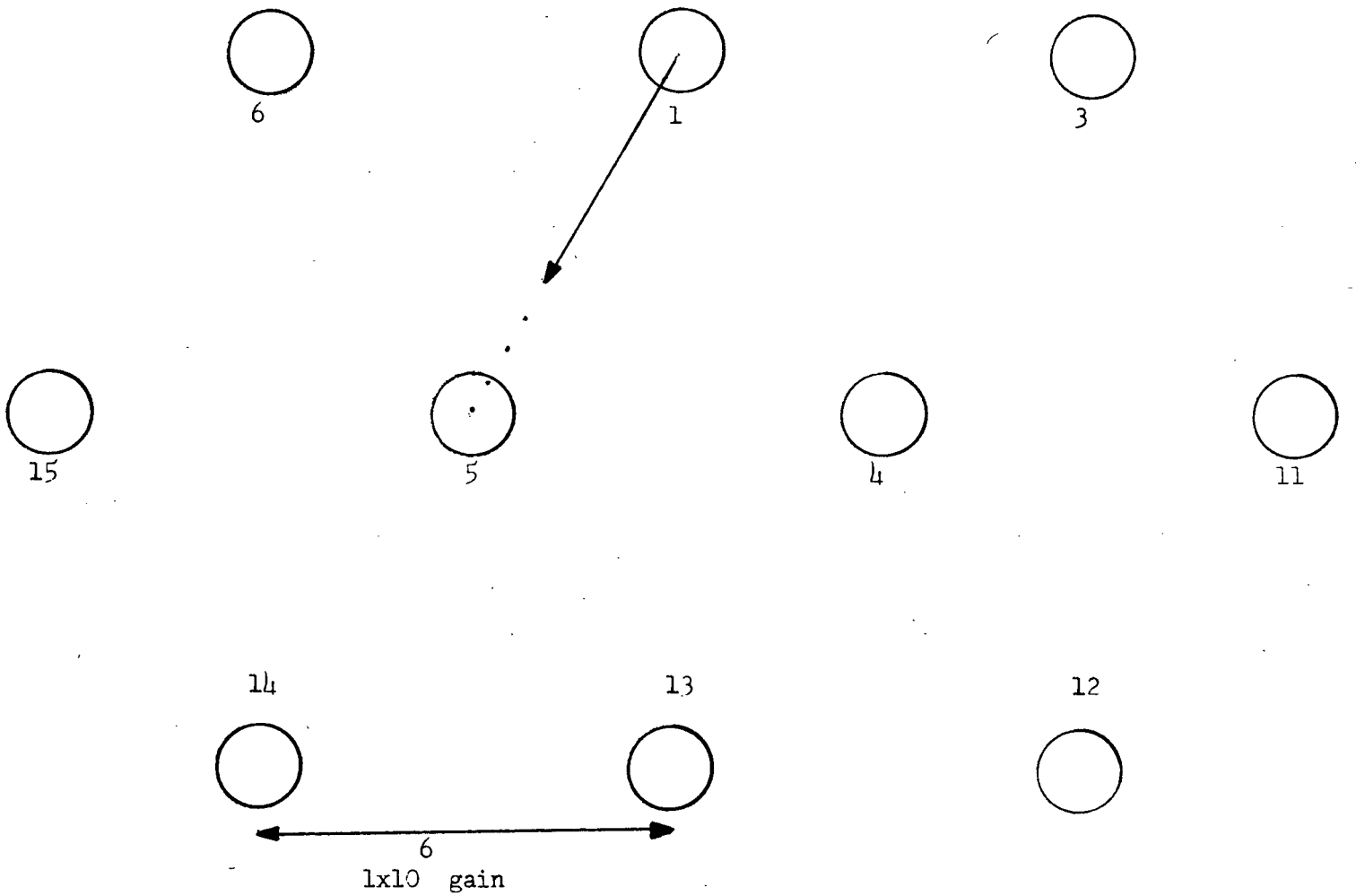

Figure A-11. Vector diagram for bundle 1B at the 26 inch level at 10 GPM.

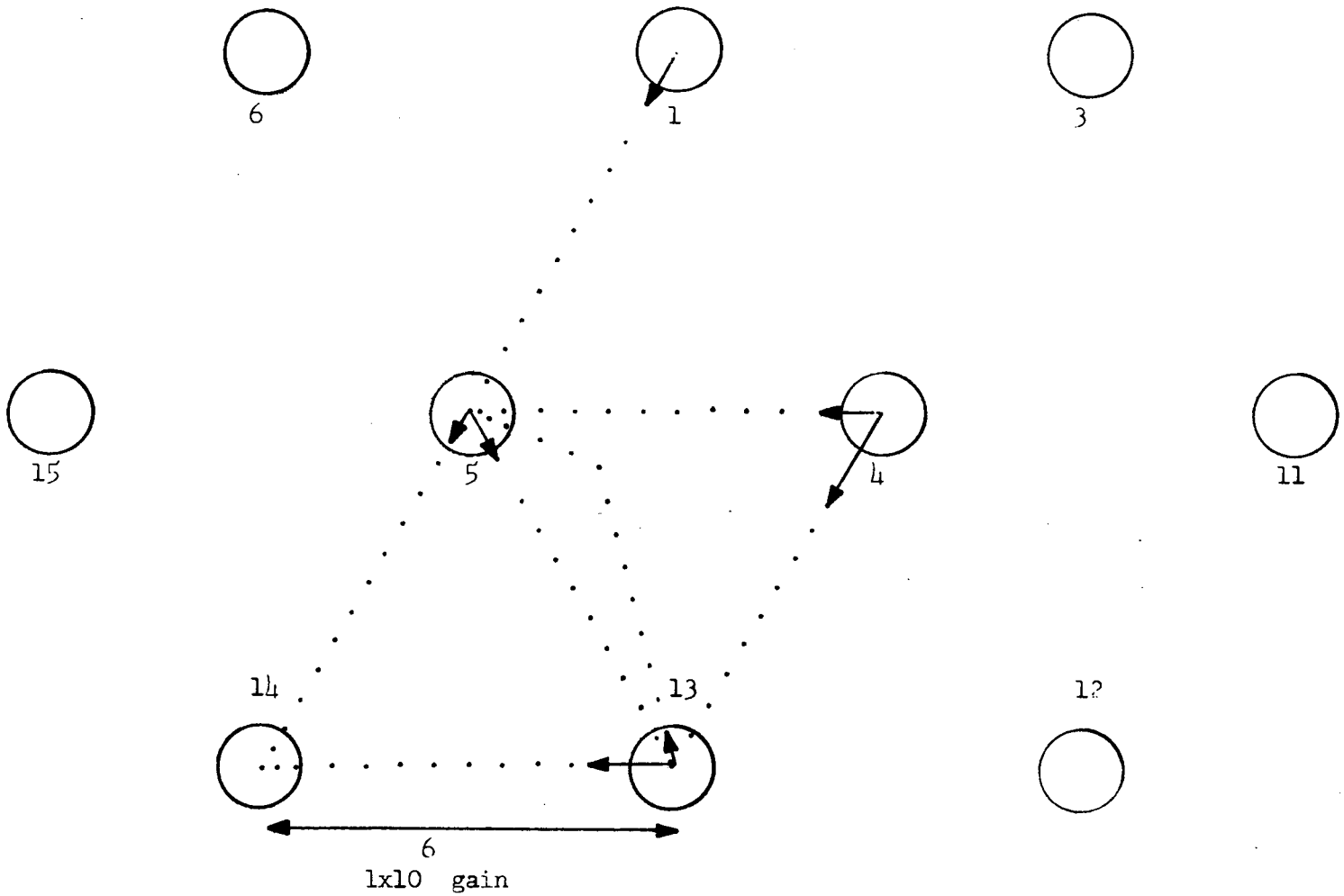

Figure A-12. Vector diagram for bundle 1B at the 14 inch level at GPM.

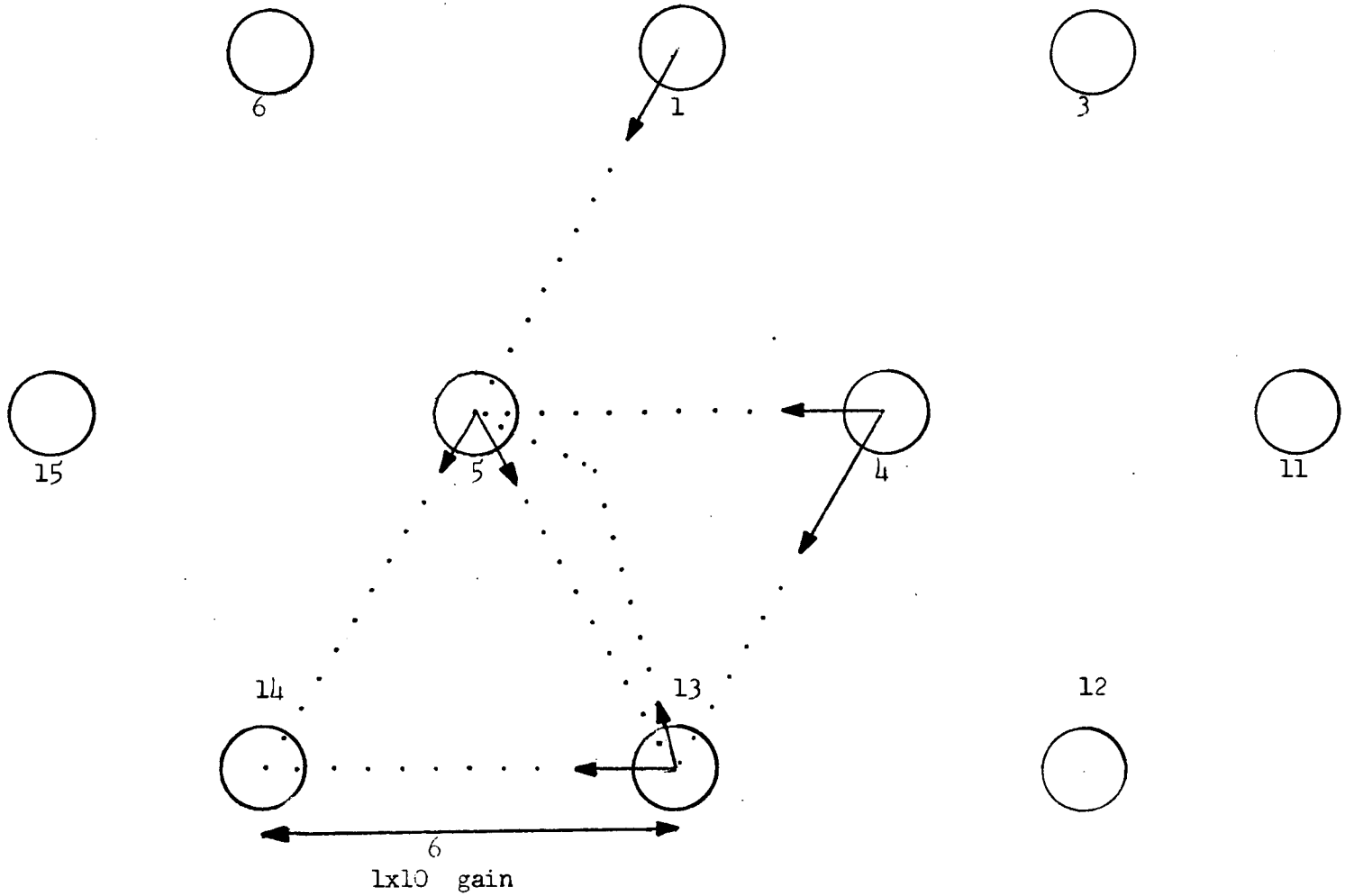

Figure A-13. Vector diagram for bundle 1B at the 14 inch level at 35 GPM.

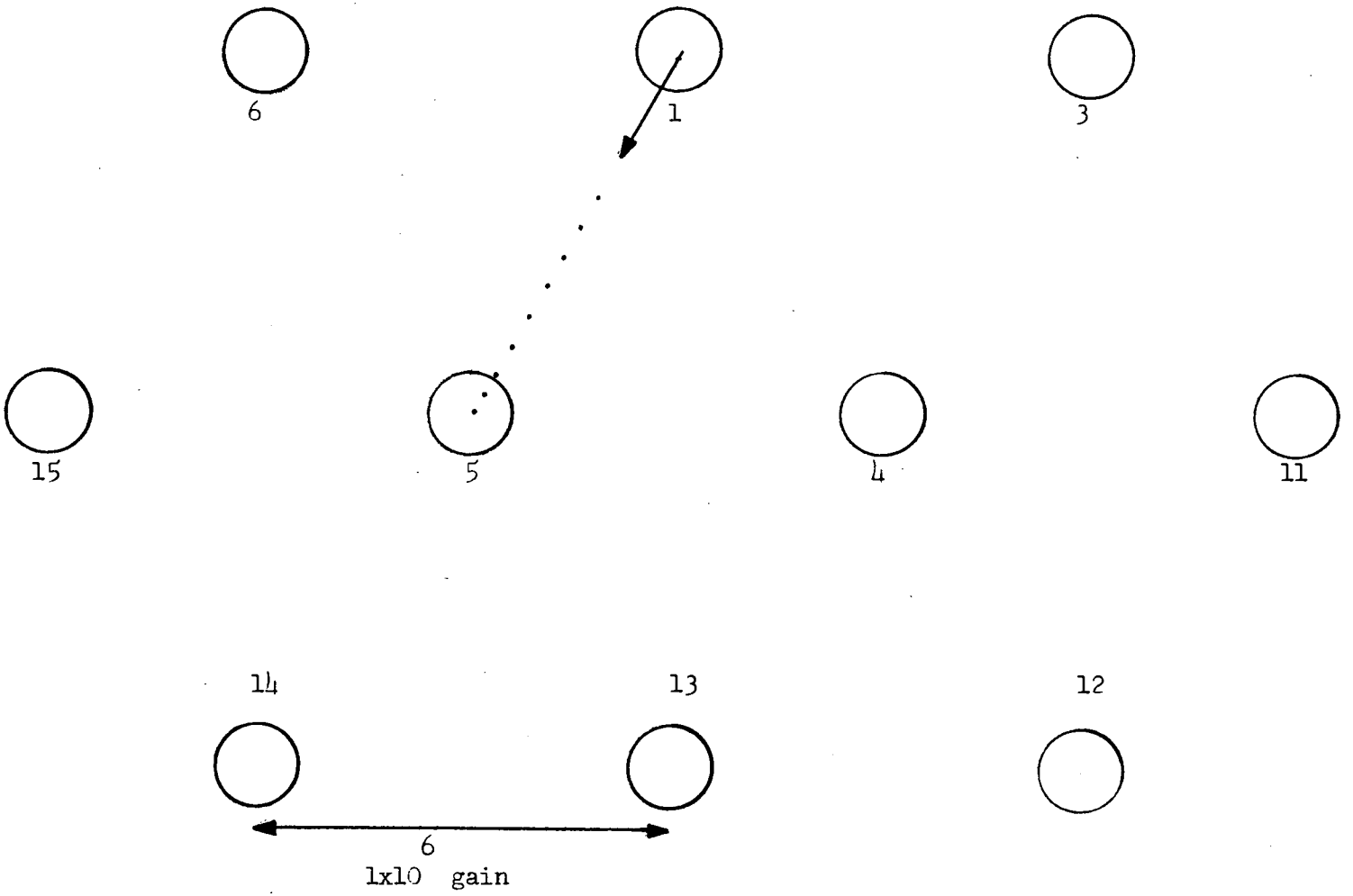

Figure A-14. Vector diagram for bundle 1B at the 26 inch level at 35 GPM.

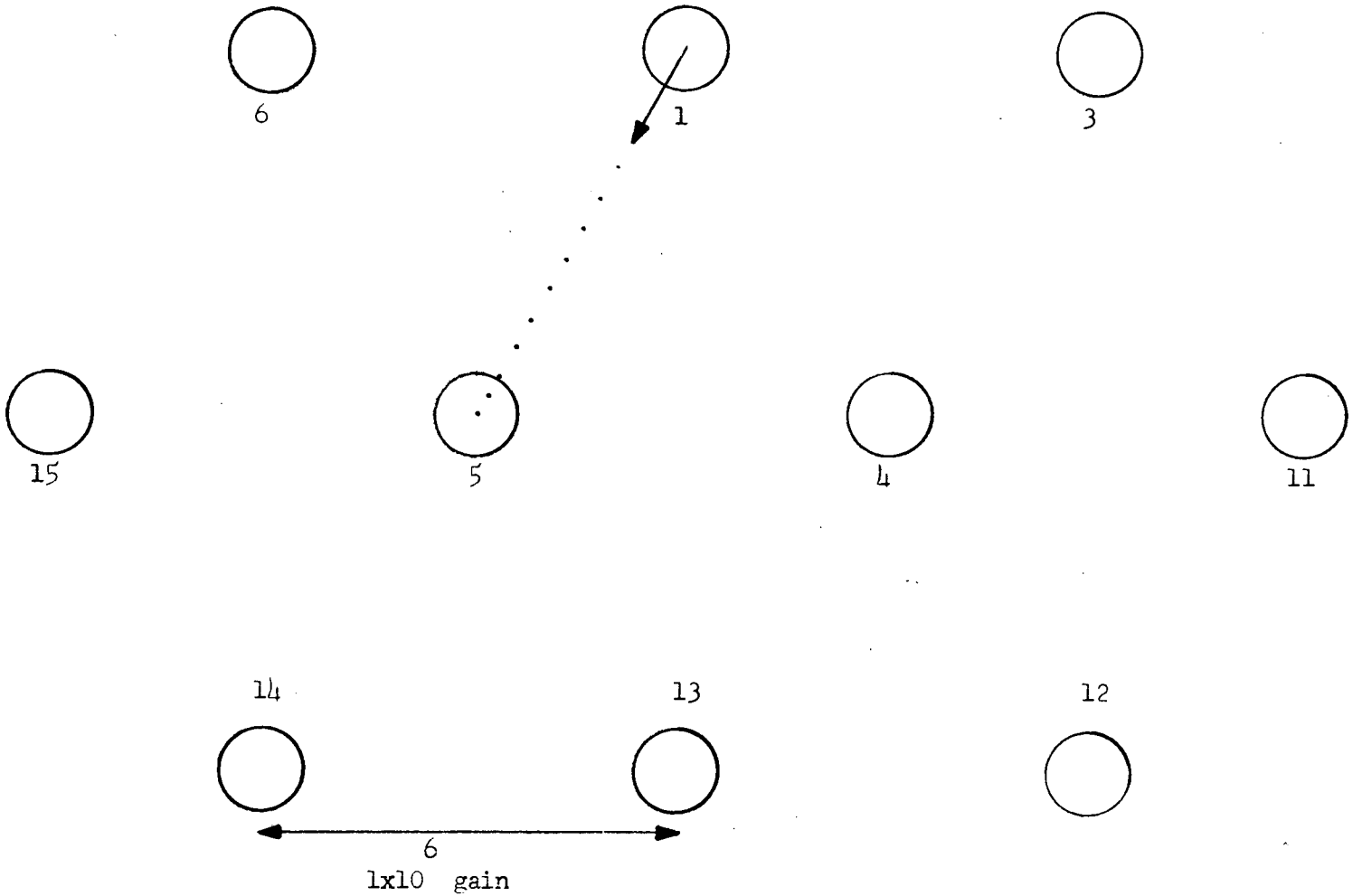

Figure A-15. Vector diagram for bundle 1B at the 26 inch level at 54 GPM.

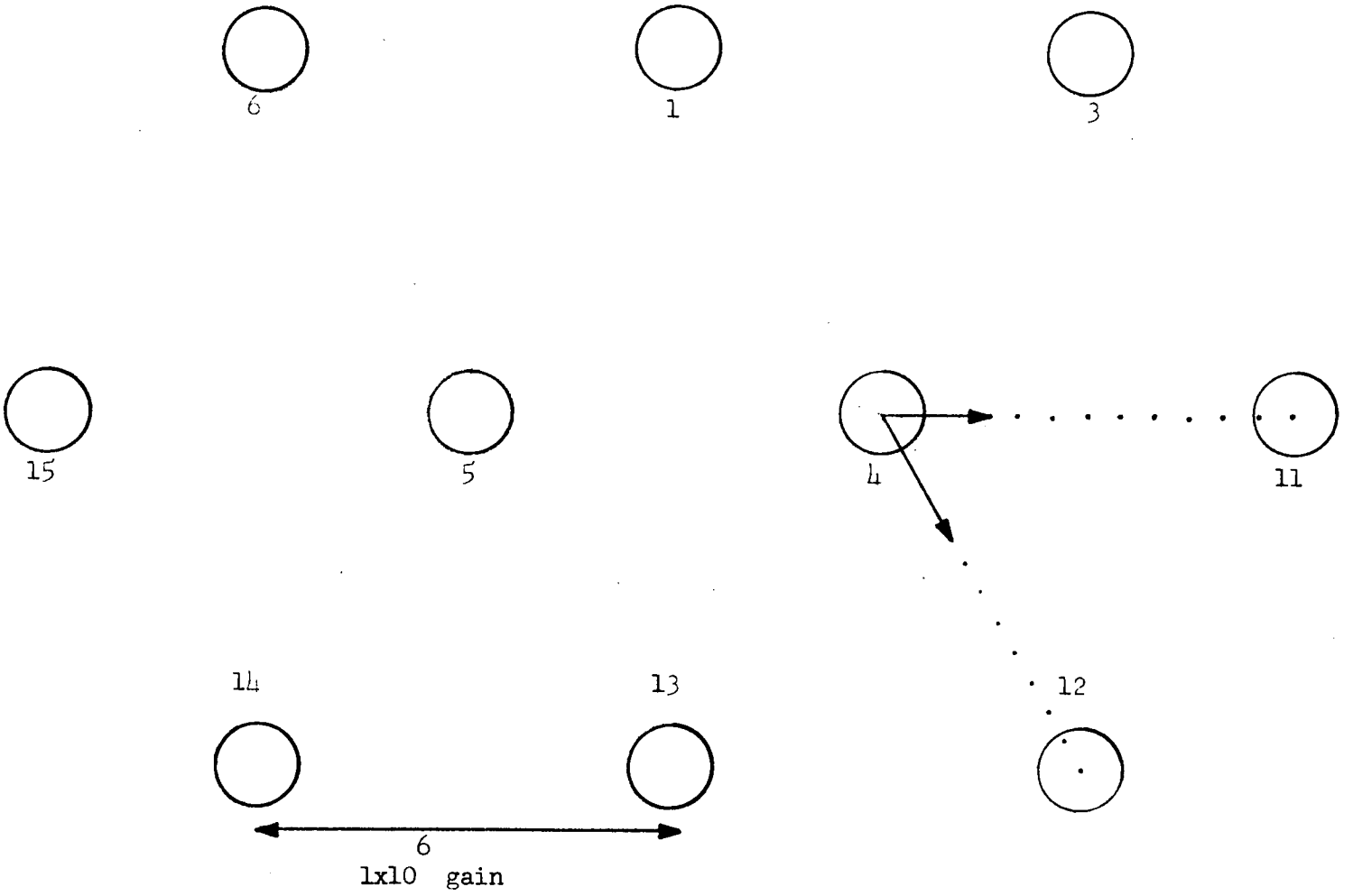

Figure A-16. Vector diagram for bundle 1B at the 22 inch level at 35 GPM.

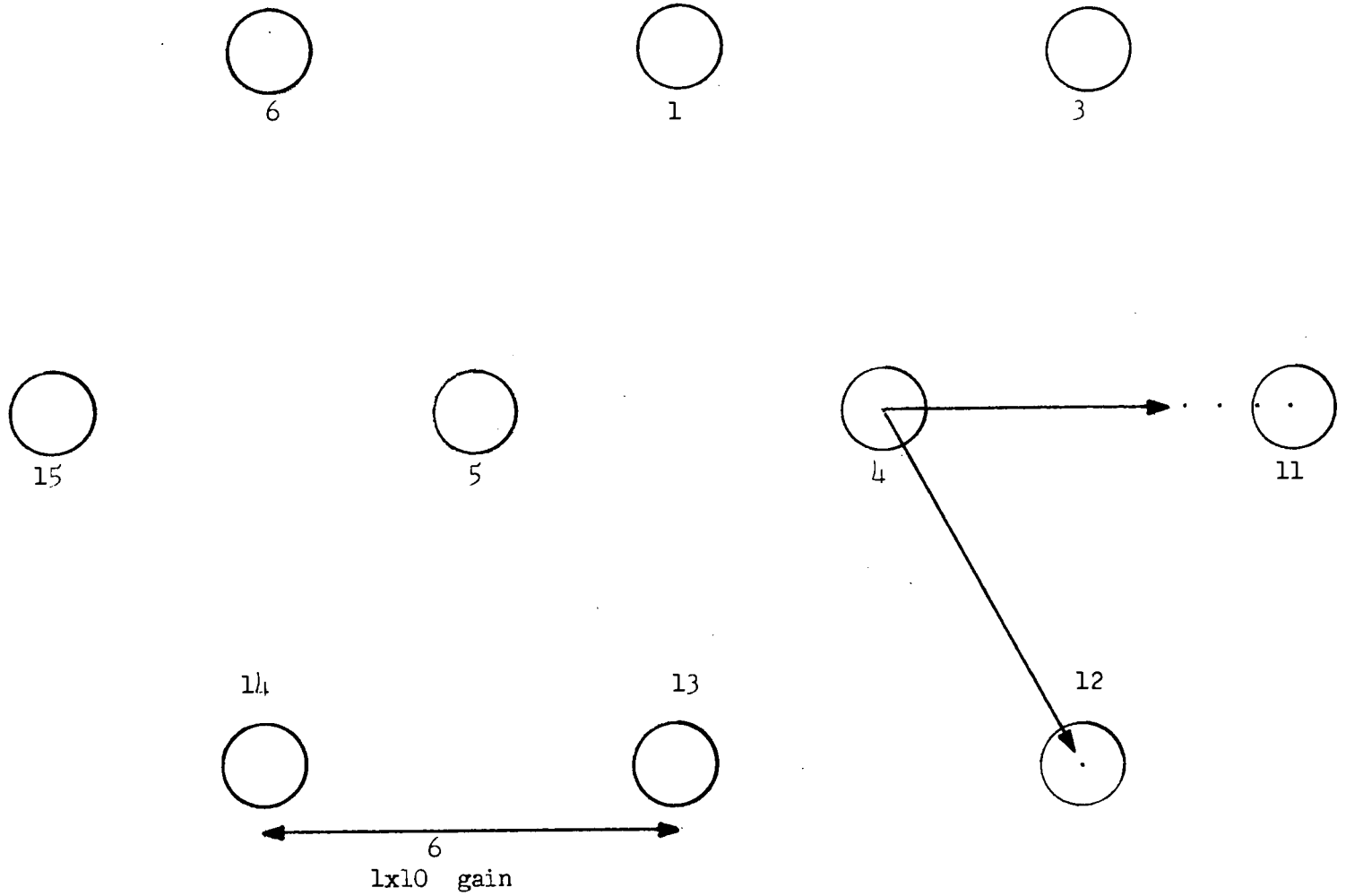

Figure A-17. Vector diagram for bundle 1B at the 22 inch level at 10 GPM.

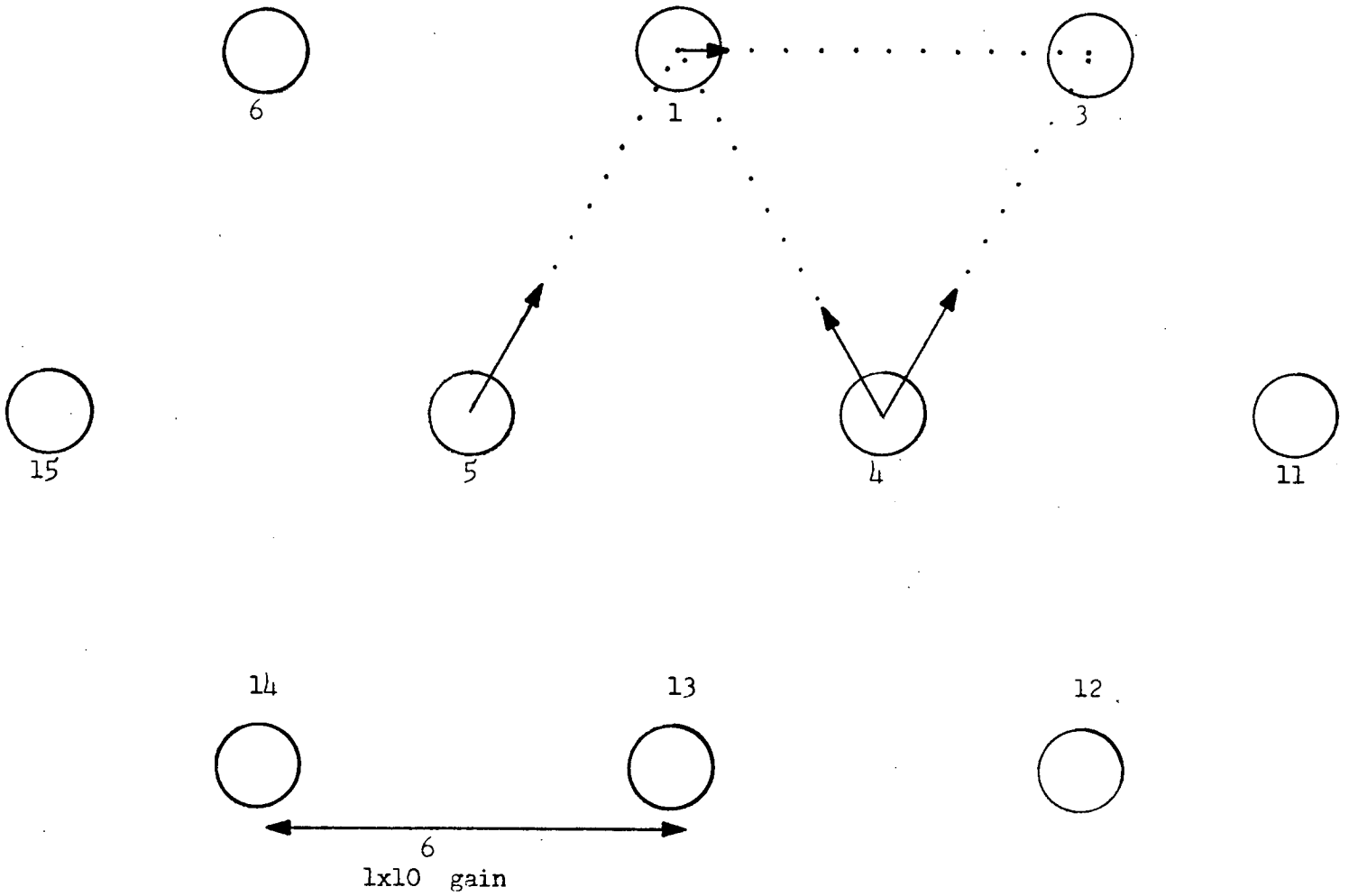

Figure A-18. Vector diagram for bundle 1B at the 18 inch level at 35 GPM.

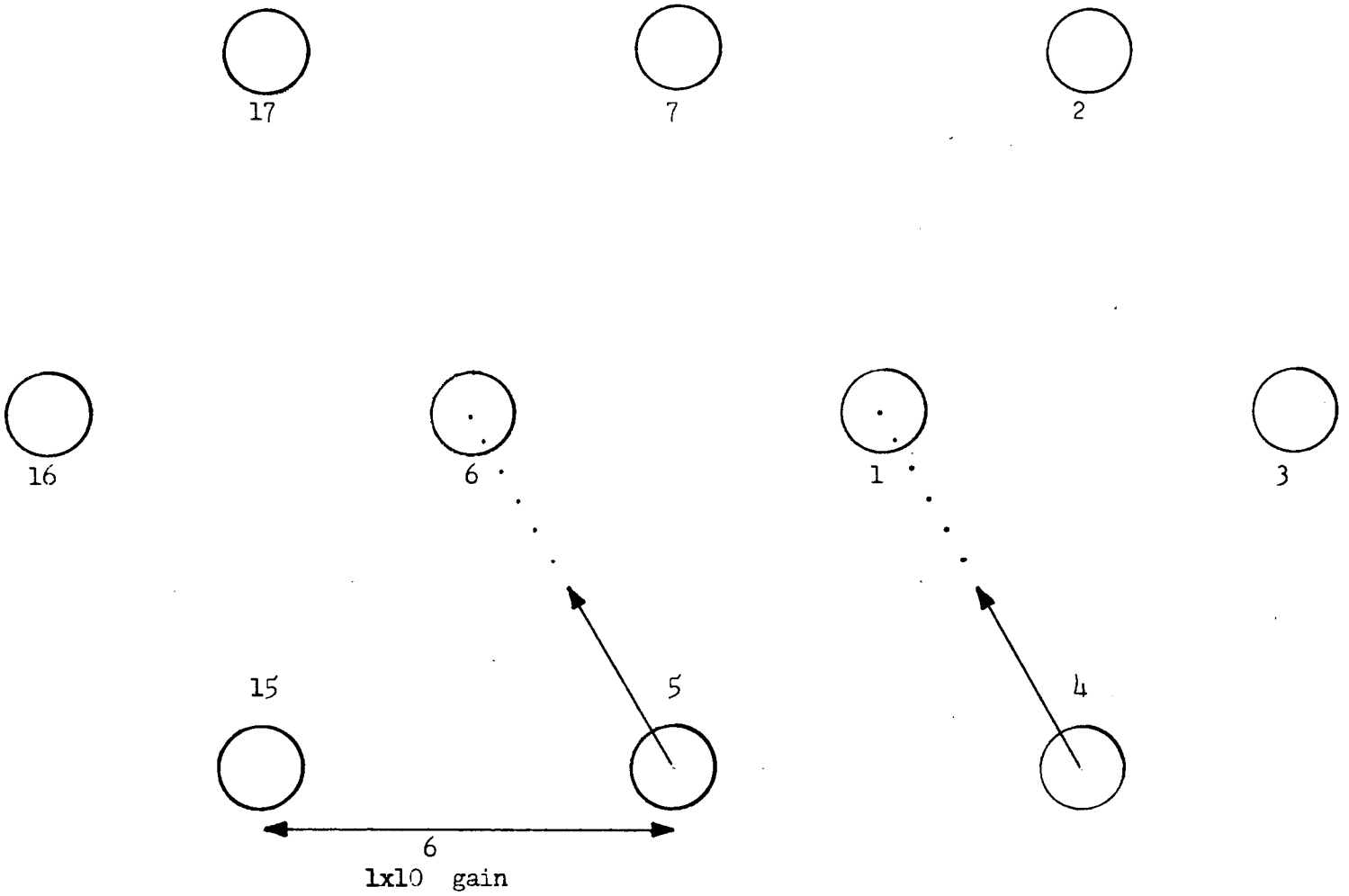

Figure A-19. Vector diagram for bundle 1B at the 6 inch level at 10 GPM.

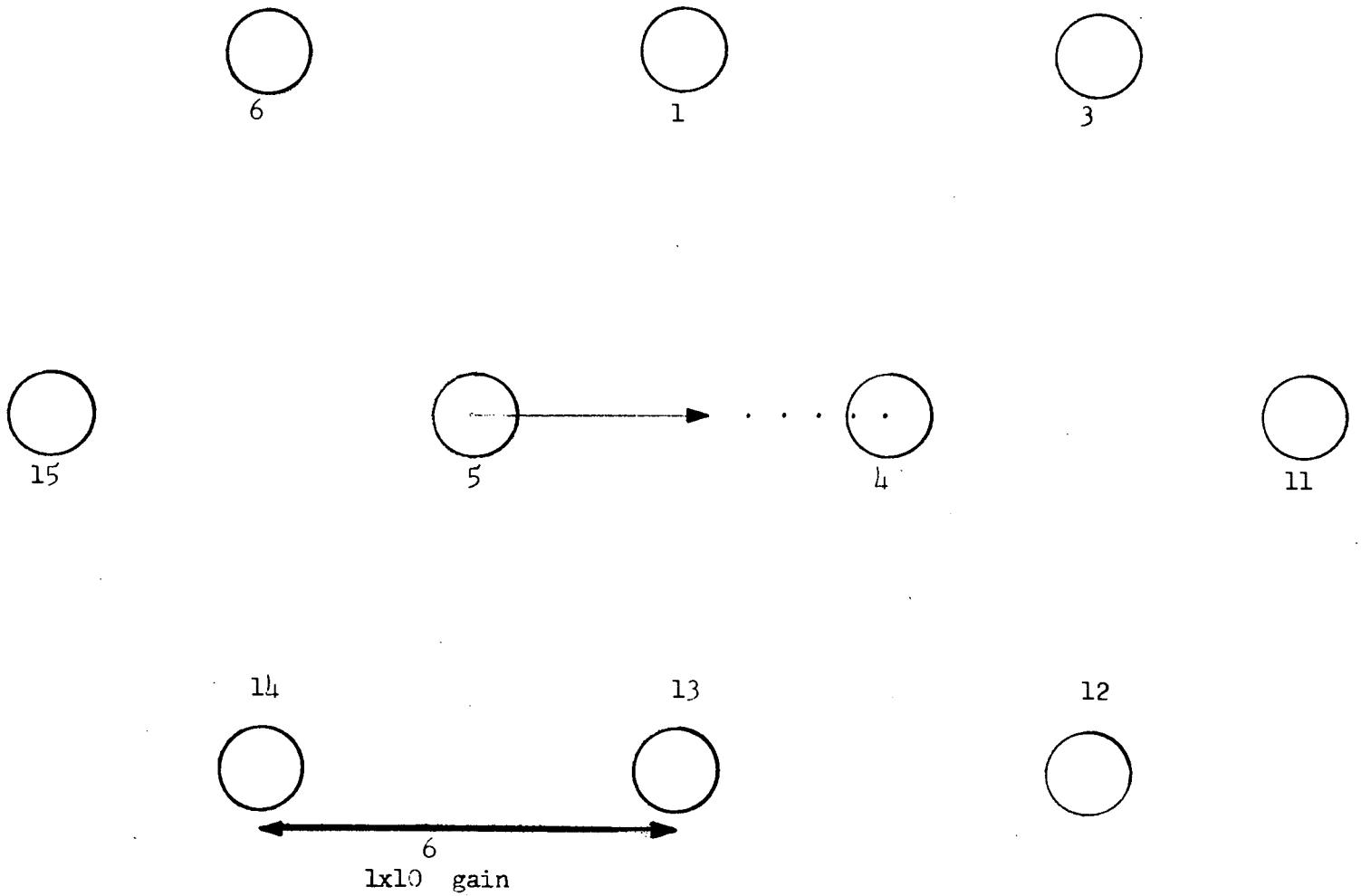

Figure A-20. Vector diagram for bundle 1B at the 8 inch level at 10 GPM.

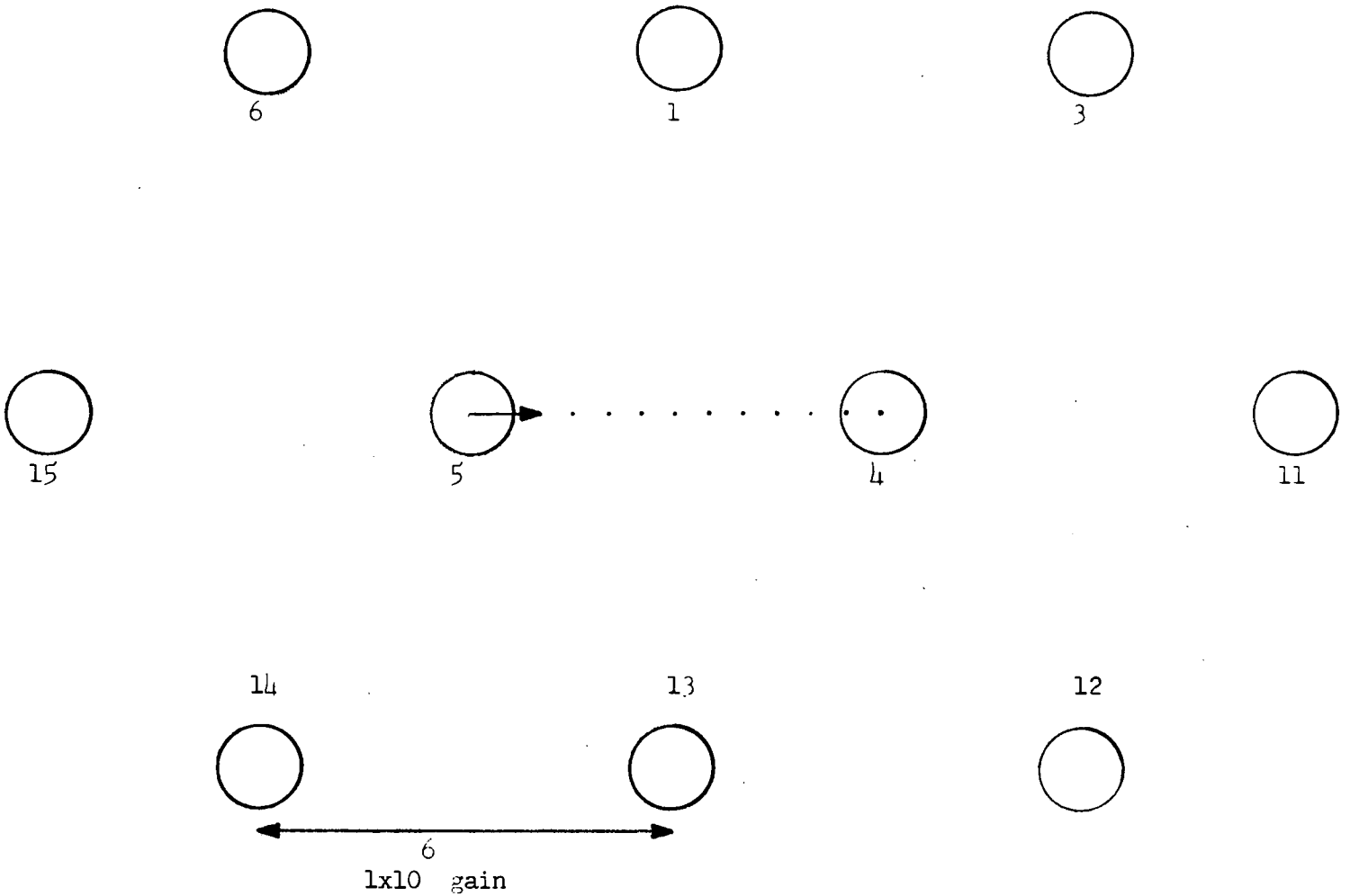

Figure A-21. Vector diagram for bundle 1B at the 8 inch level at 35 GPM.

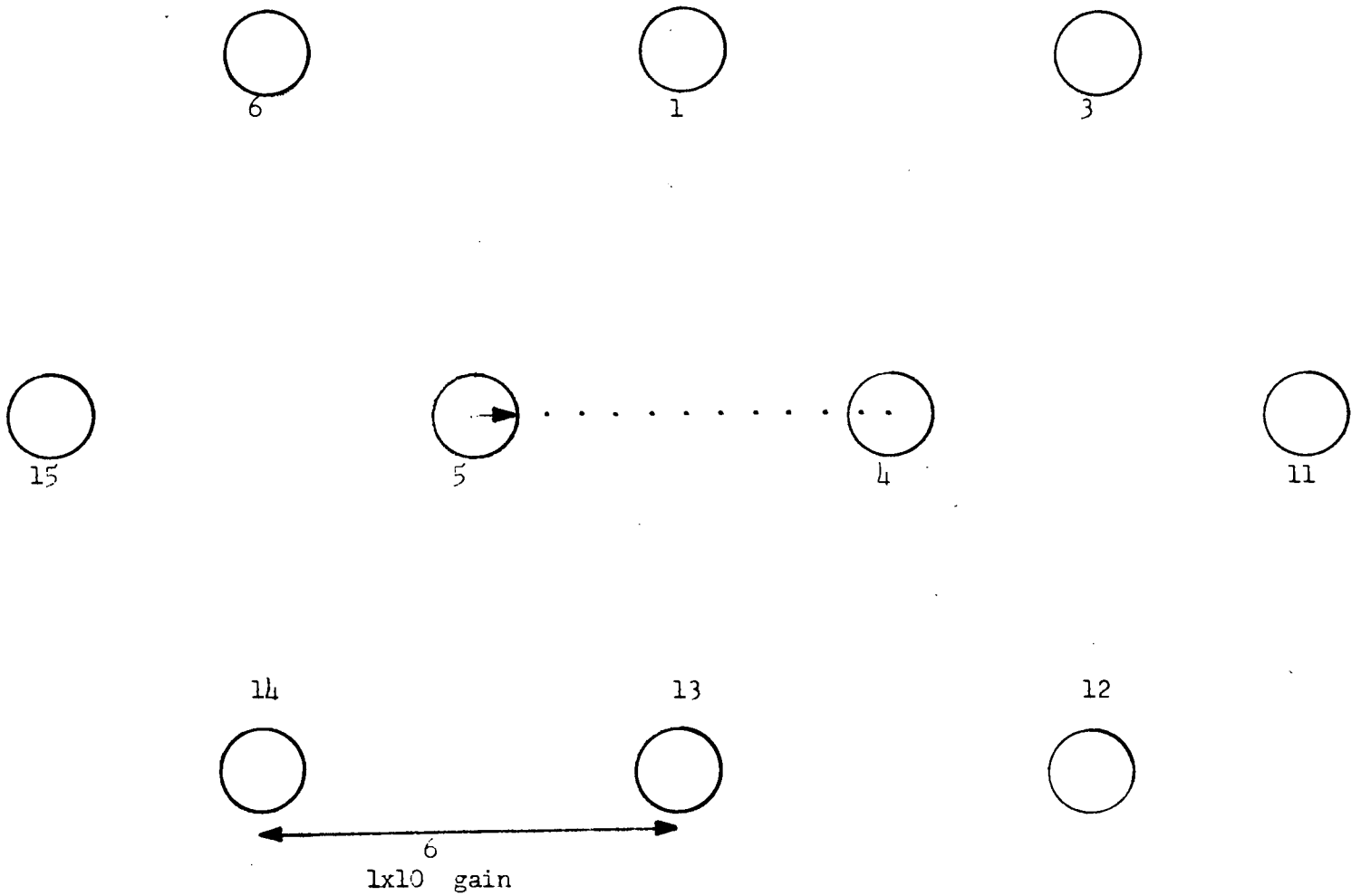

Figure A-22. Vector diagram for bundle 1B at the 8 inch level at 54 GPM.

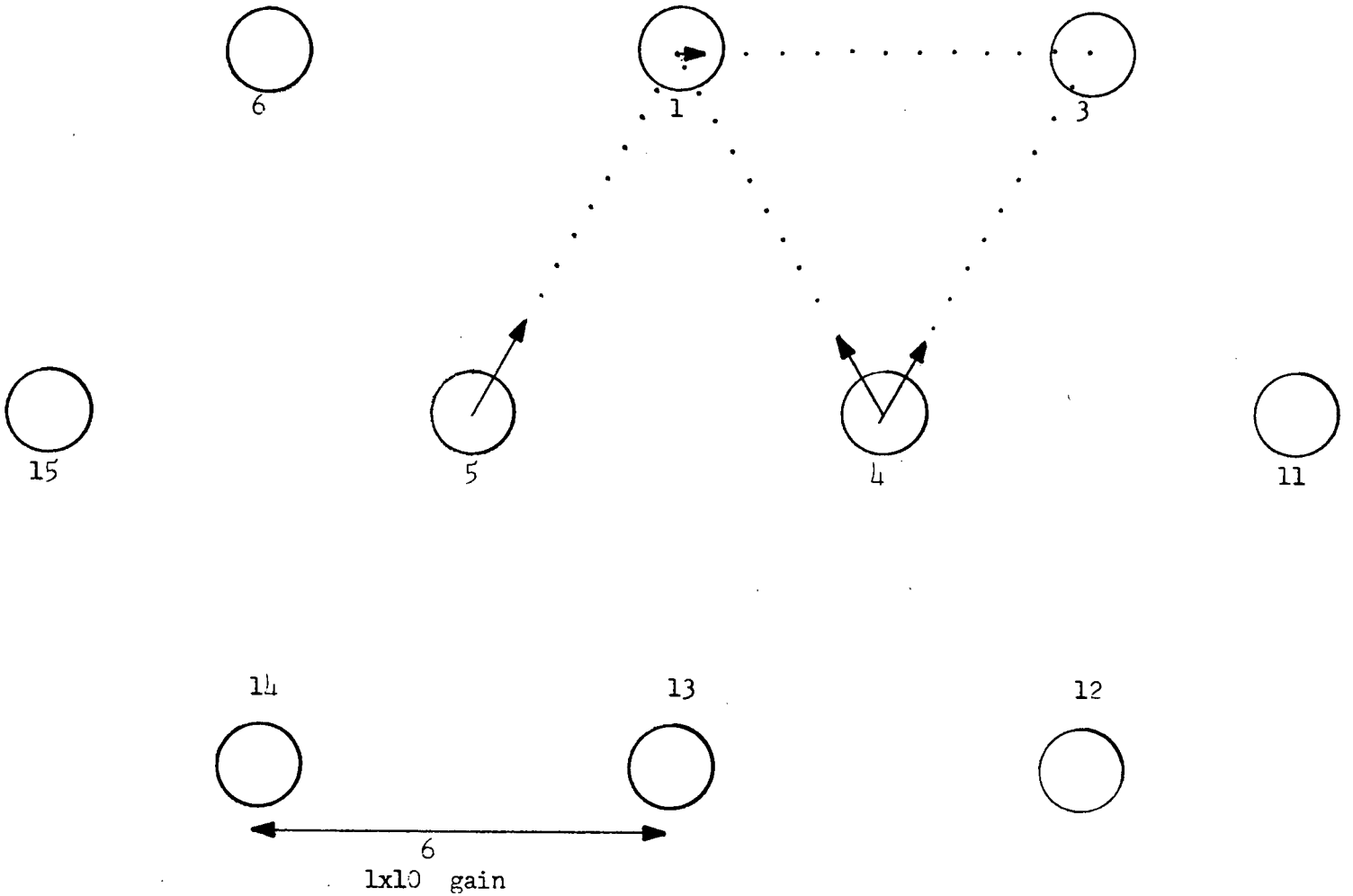

Figure A-23. Vector diagram for bundle 1B at the 18 inch level at 54 GPM.

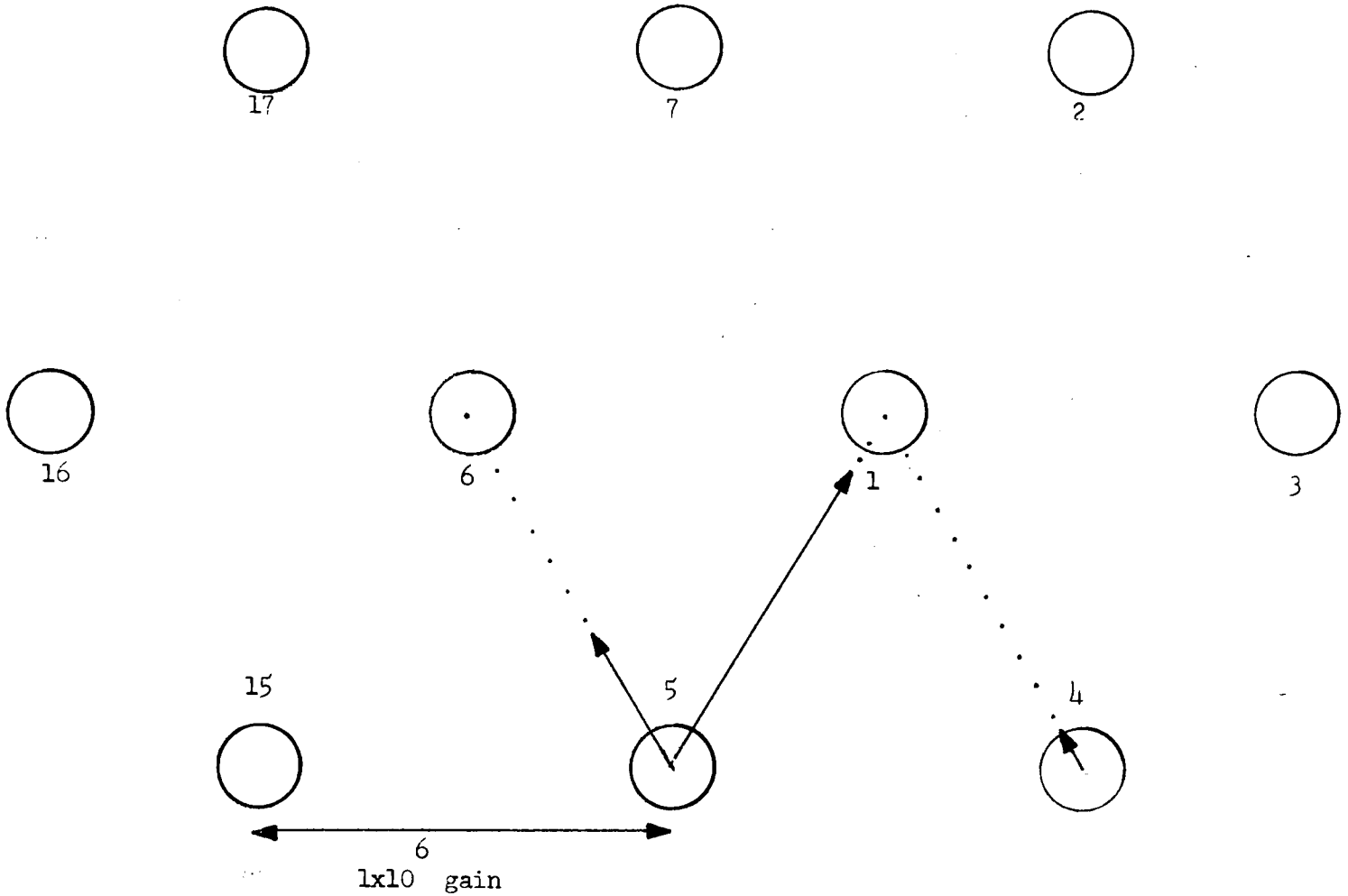

Figure A-24. Vector diagram for bundle 1B at the 6 inch level at 35 GPM.

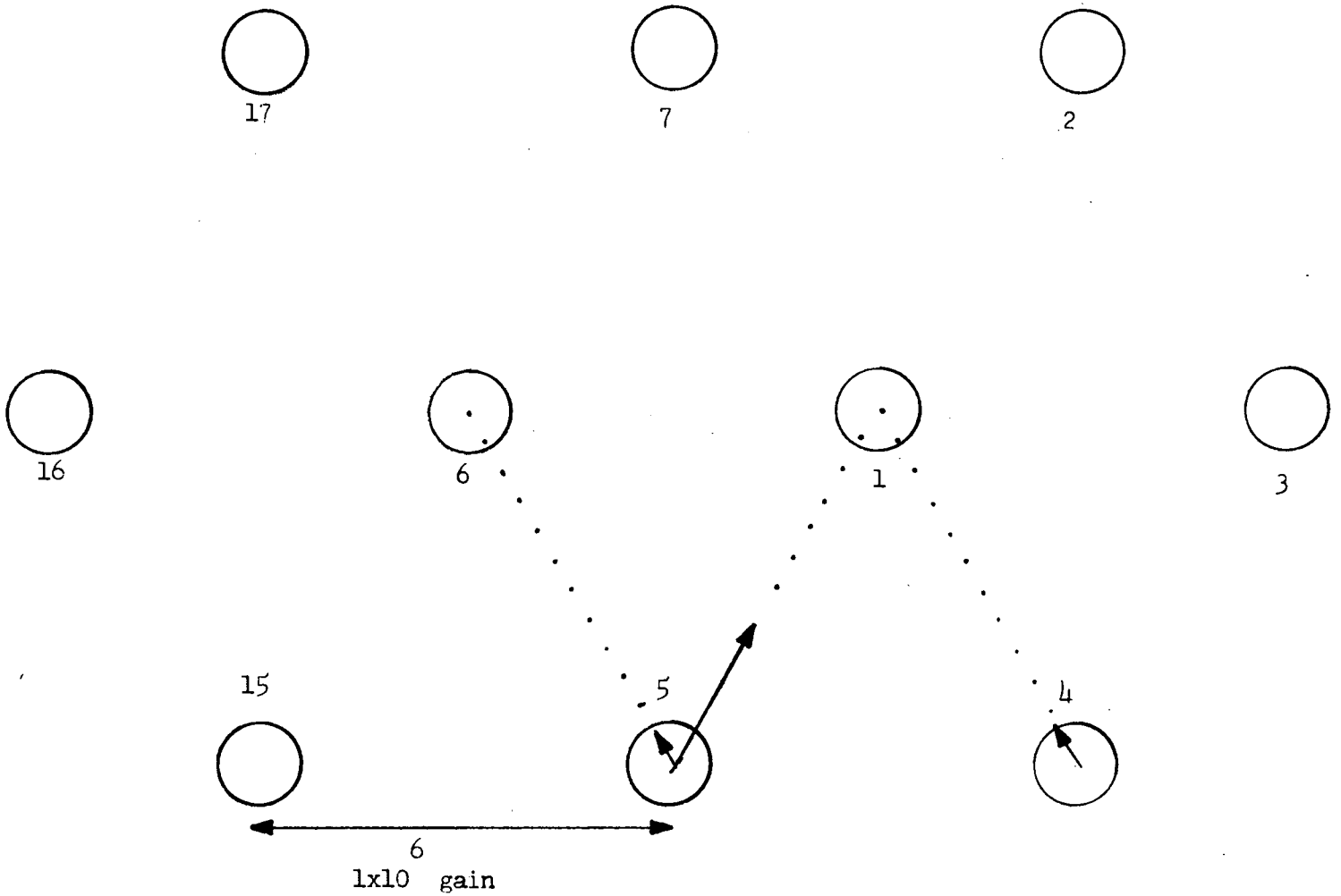

Figure A-25. Vector diagram for bundle 1B at the 6 inch level at 54 GPM.

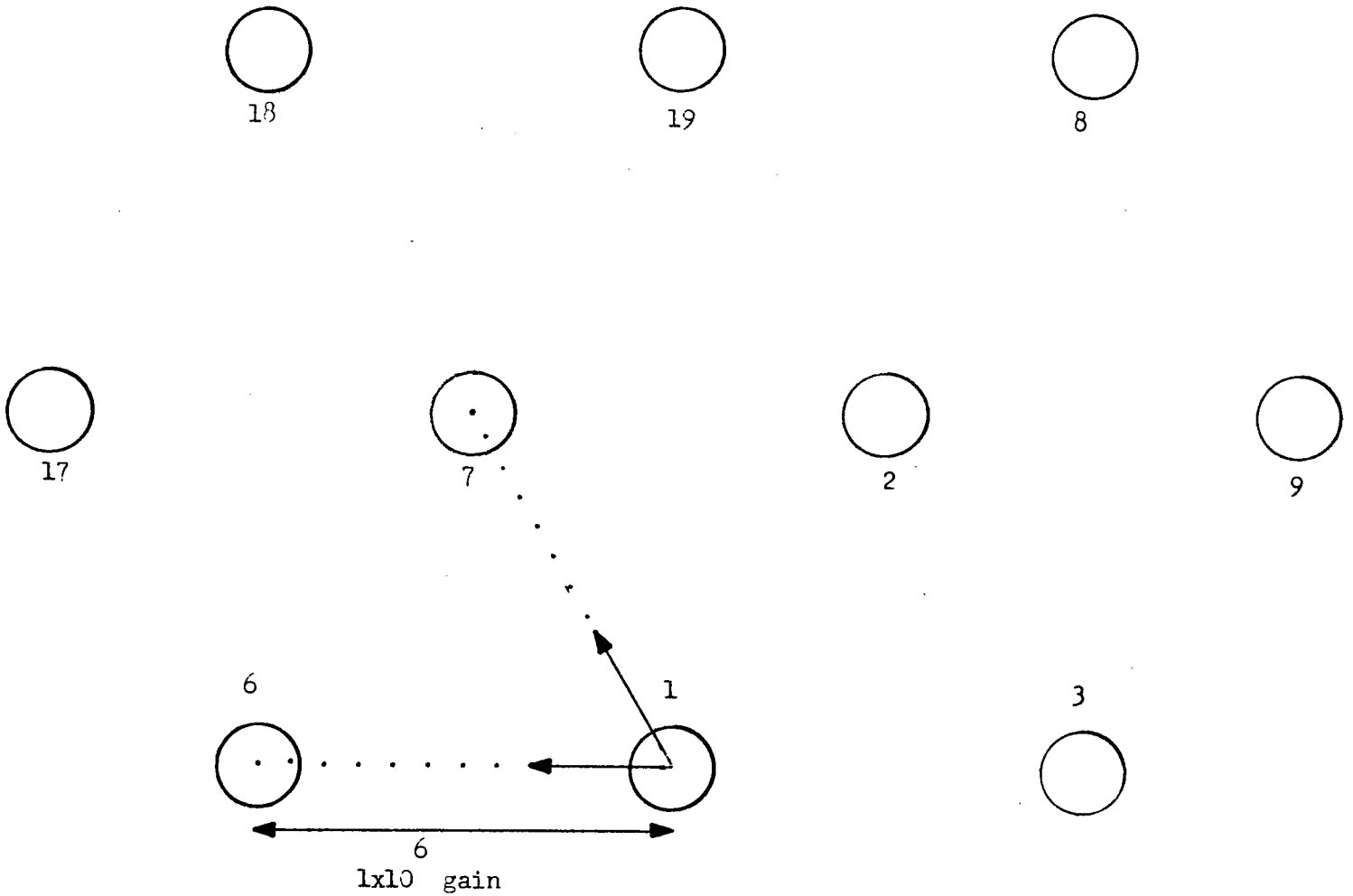

Figure A-26. Vector diagram for bundle 1B at the 4 inch level at 10 GPM.

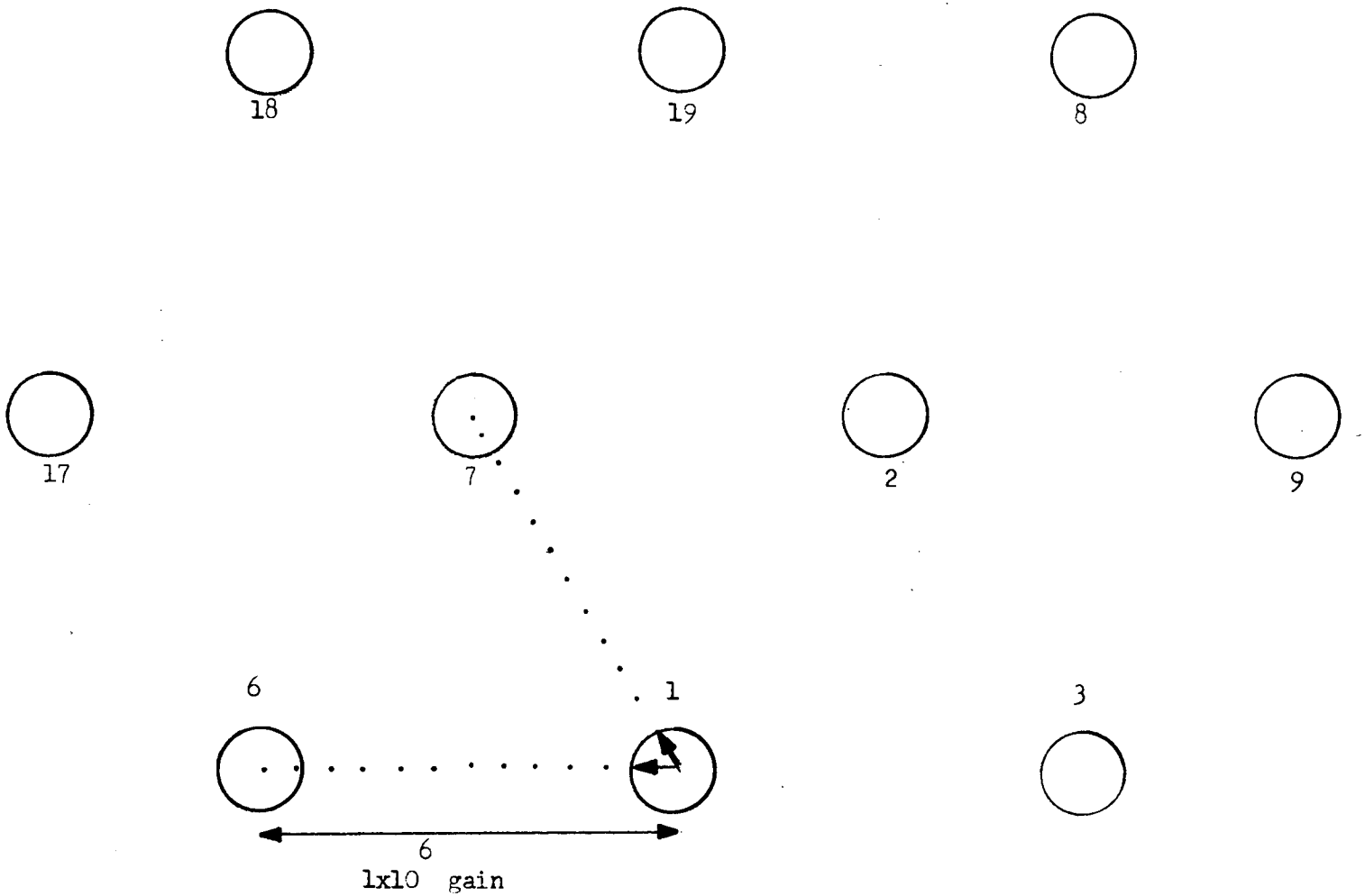

Figure A-27. Vector diagram for bundle 1B at the 4 inch level at 35 GPM.

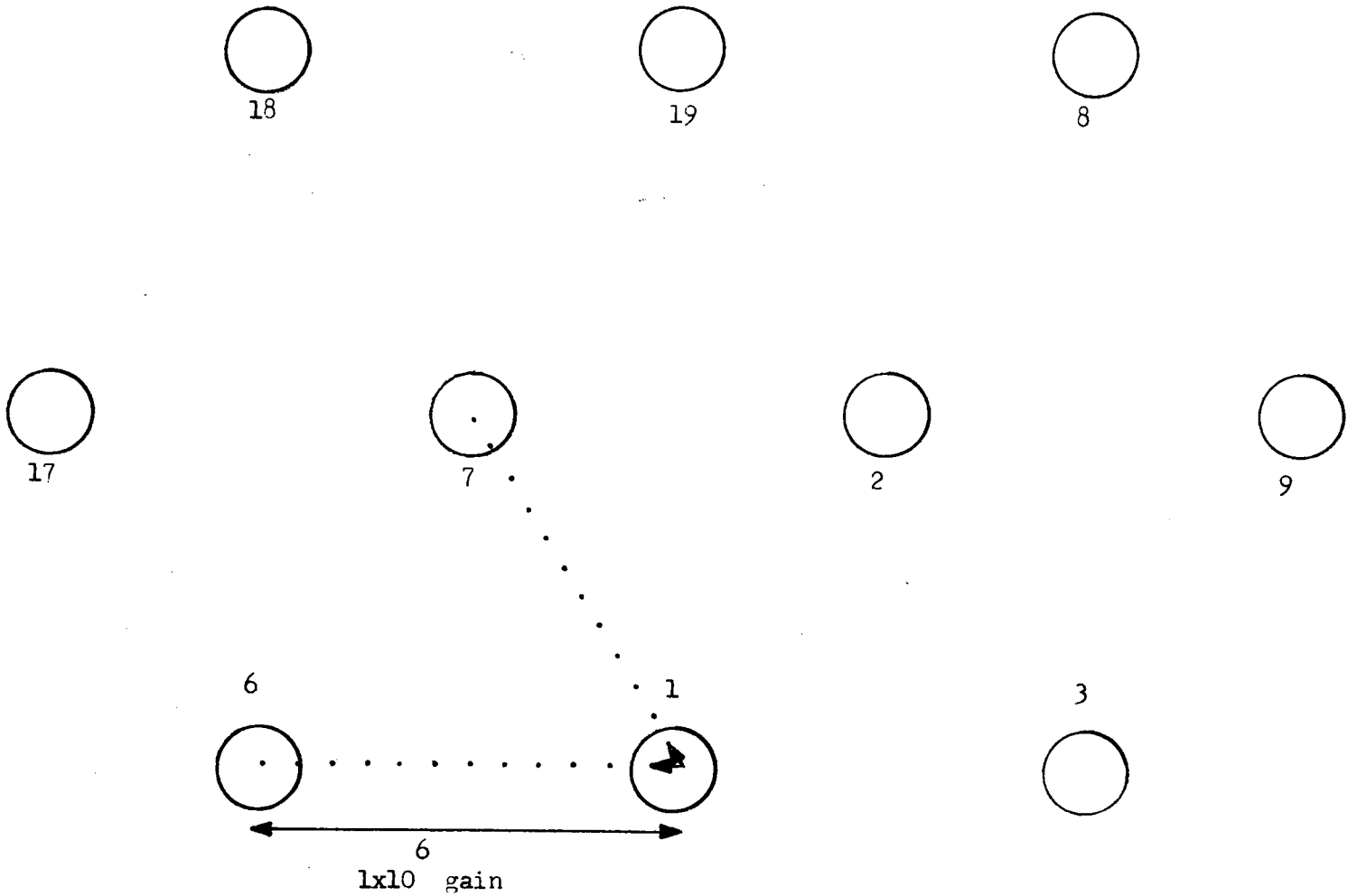

Figure A-28. Vector diagram for bundle 1B at the 4 inch level at 54 GPM.

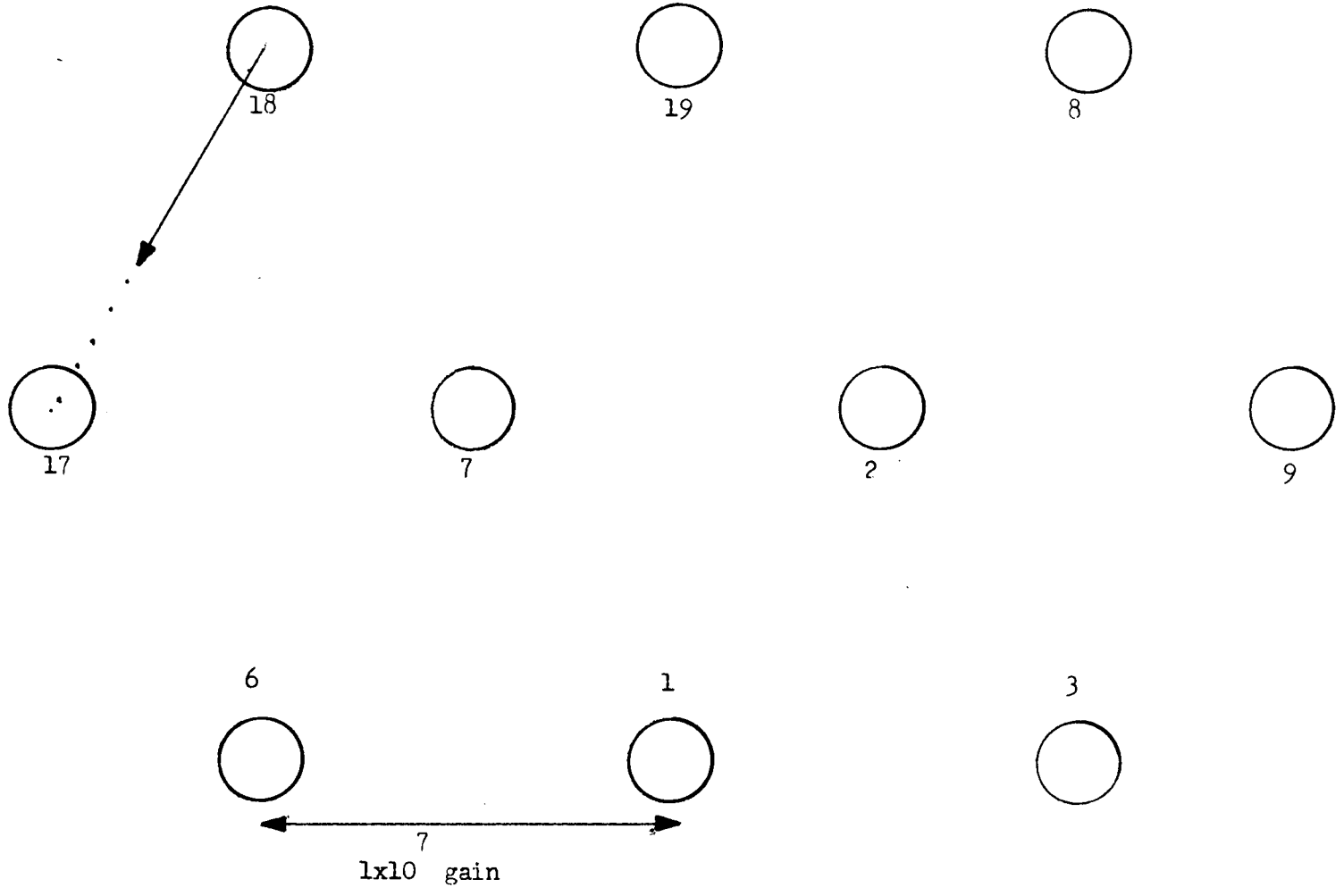

Figure A-29. Vector diagram for bundle 1B at the 14 inch level at 10 GPM.

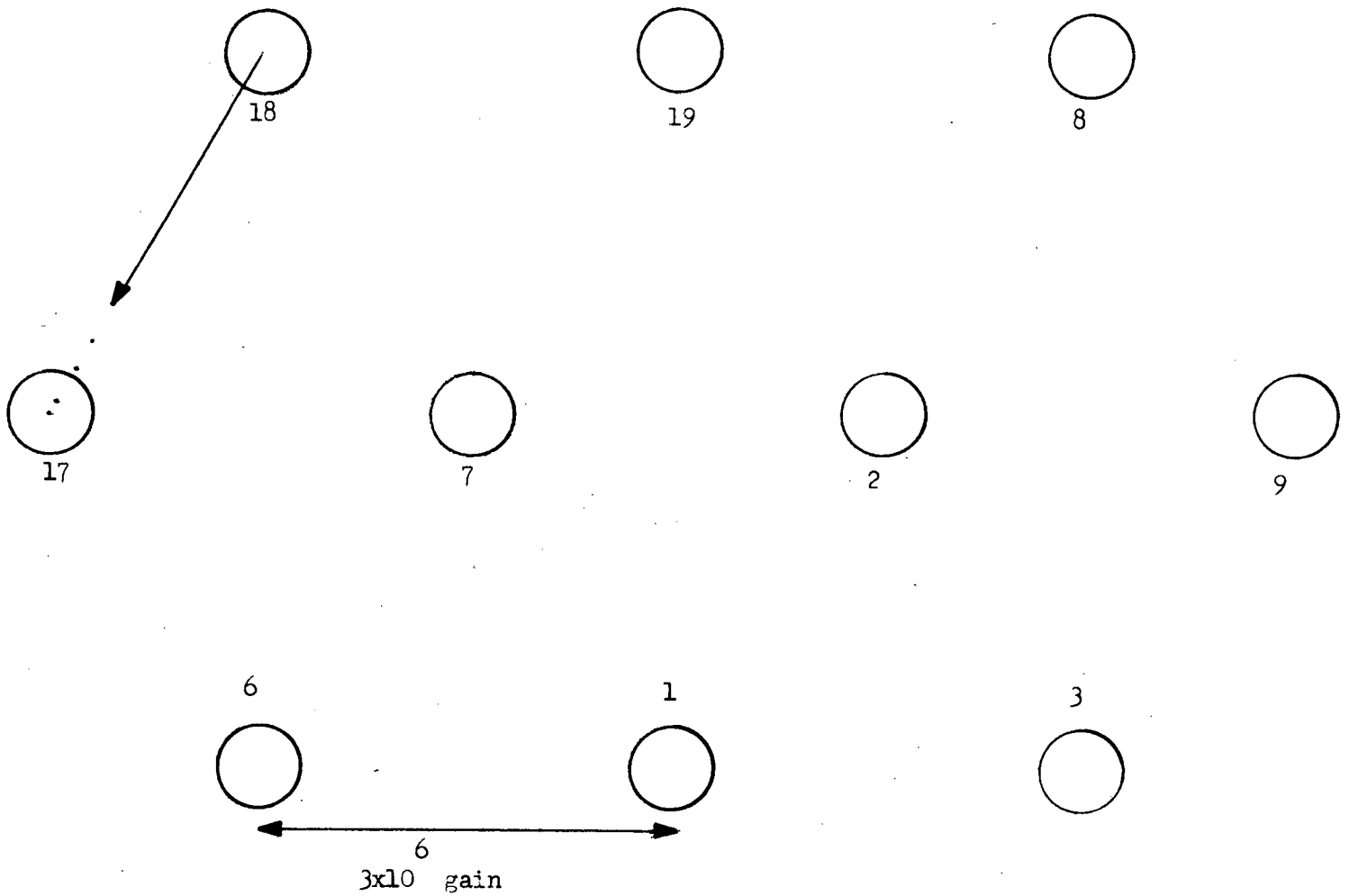

Figure A-30. Vector diagram for bundle 1B at the 14 inch level at 35 GPM.

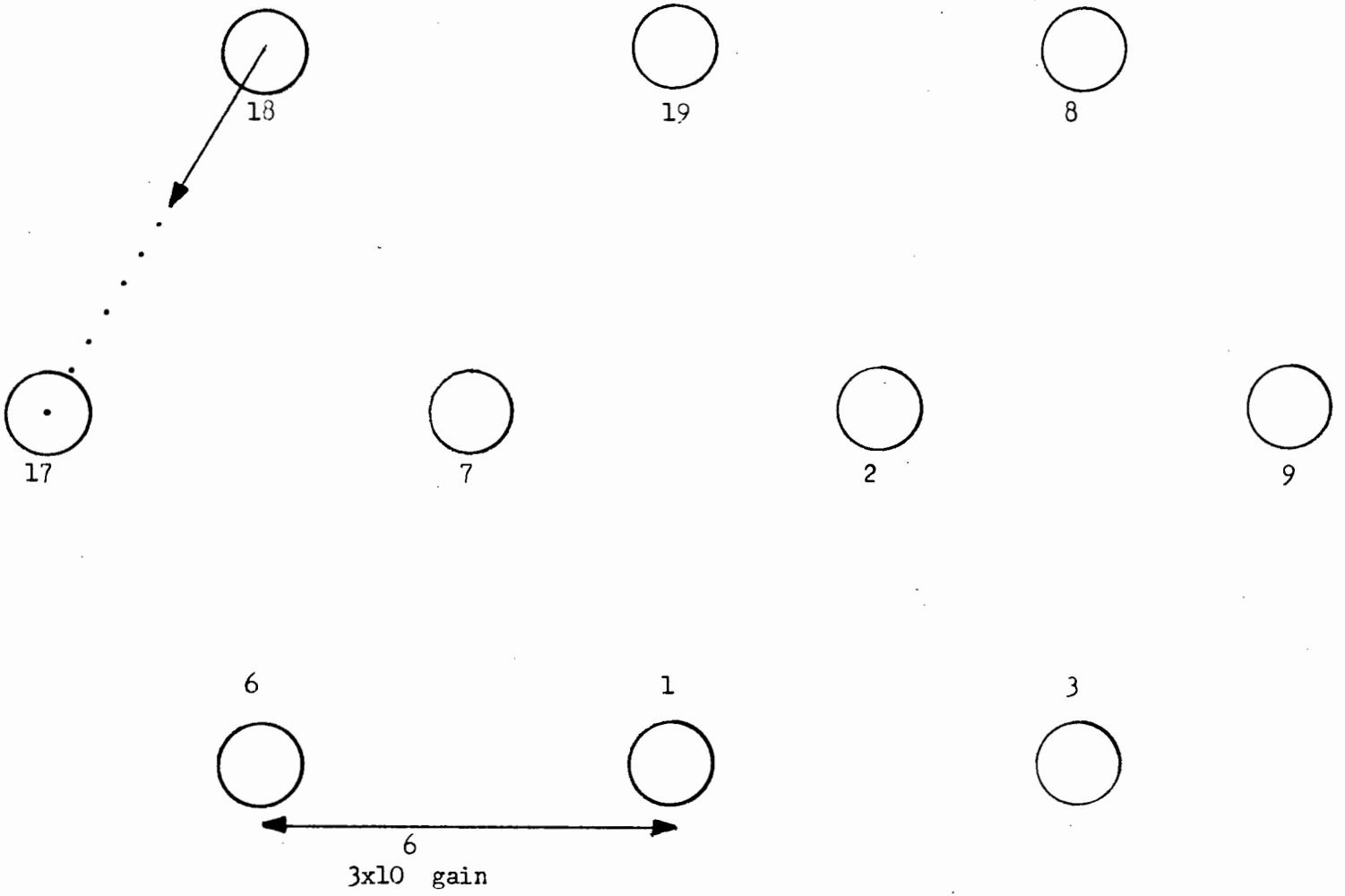

Figure A-31. Vector diagram for bundle 1B at the 14 inch level at 54 GPM.

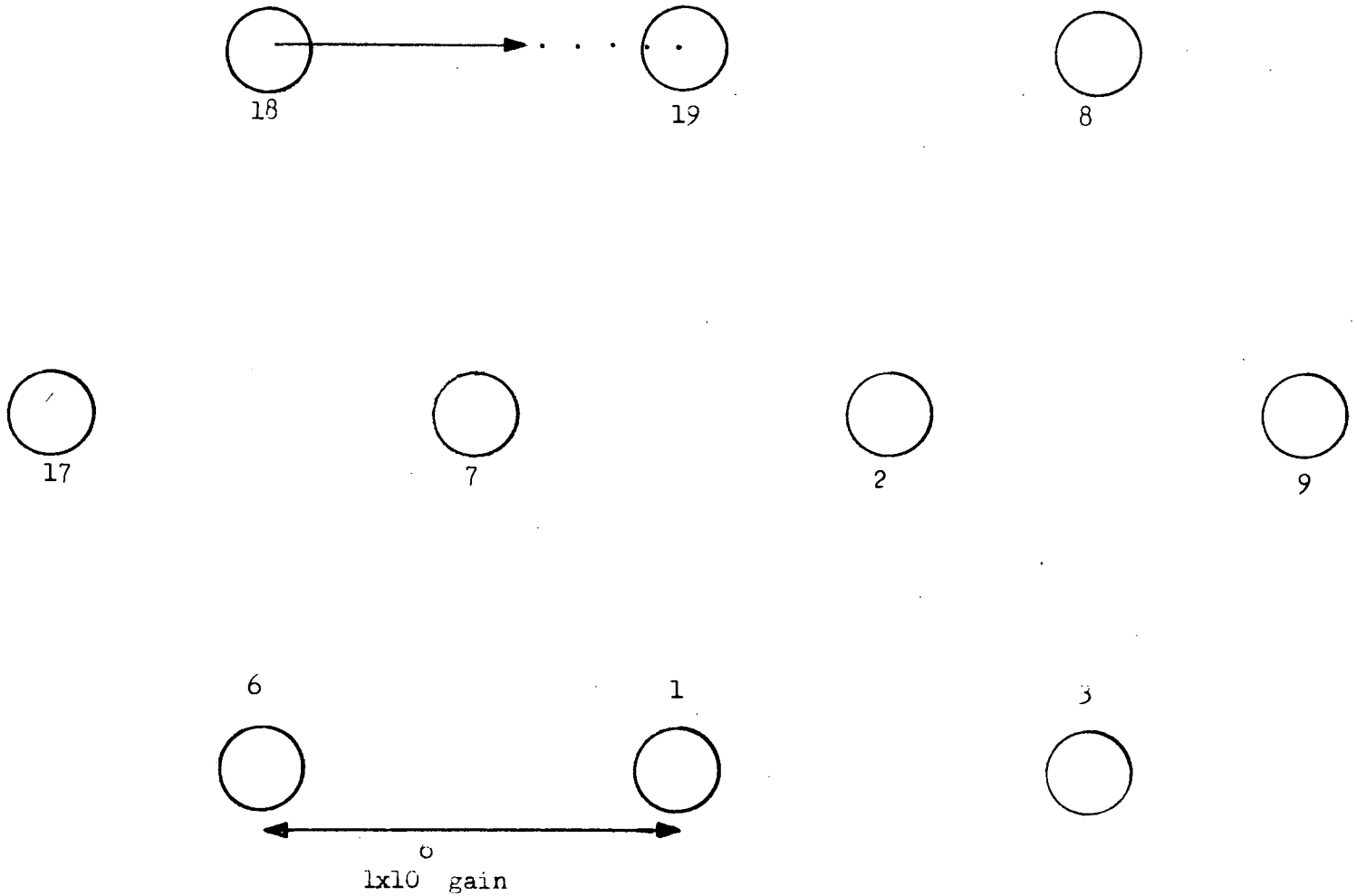

Figure A-32. Vector diagram for bundle 1B at the 18 inch level at 10 GPM.

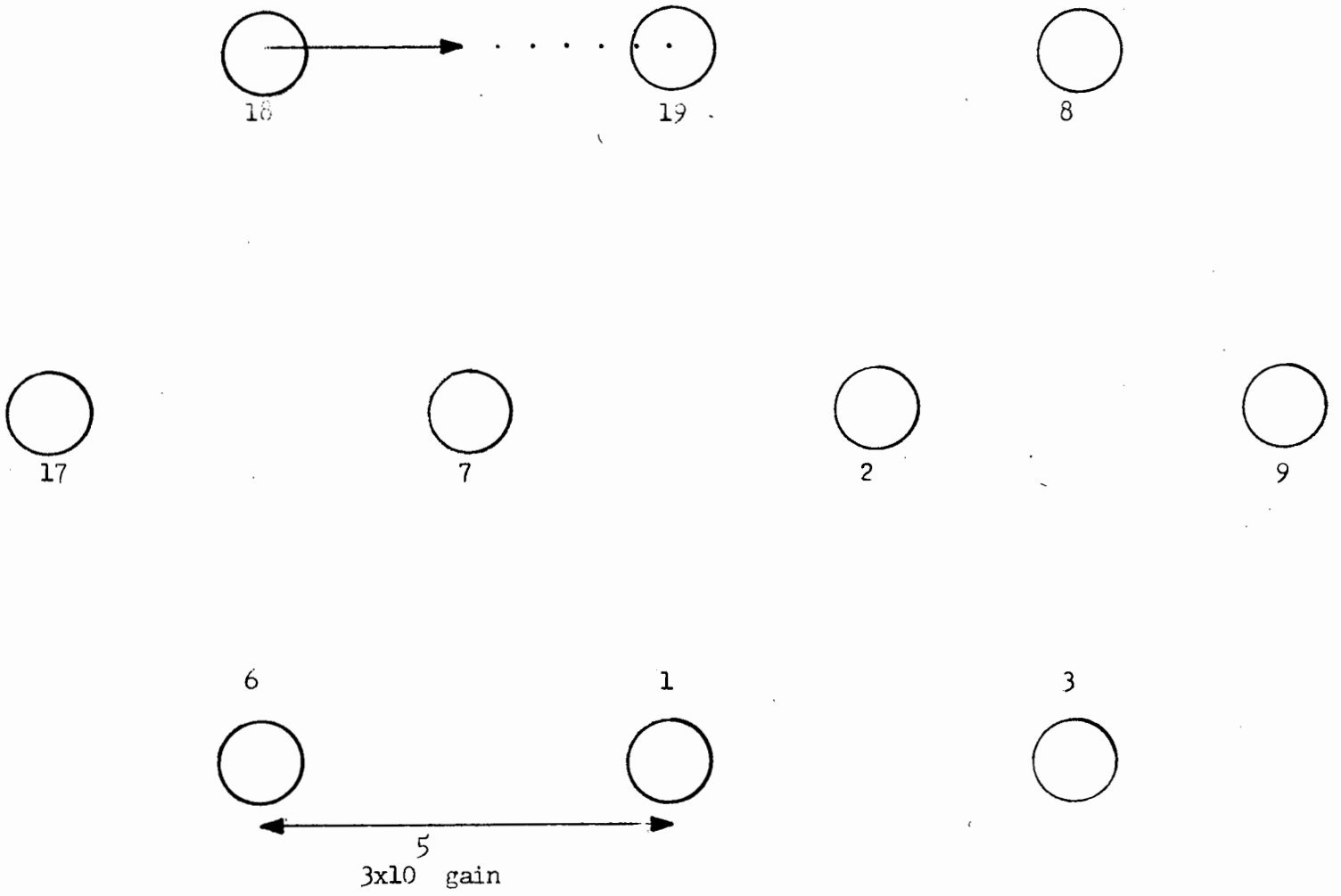

Figure A-33. Vector diagram for bundle 1B at the 18 inch level at 35 GPM.

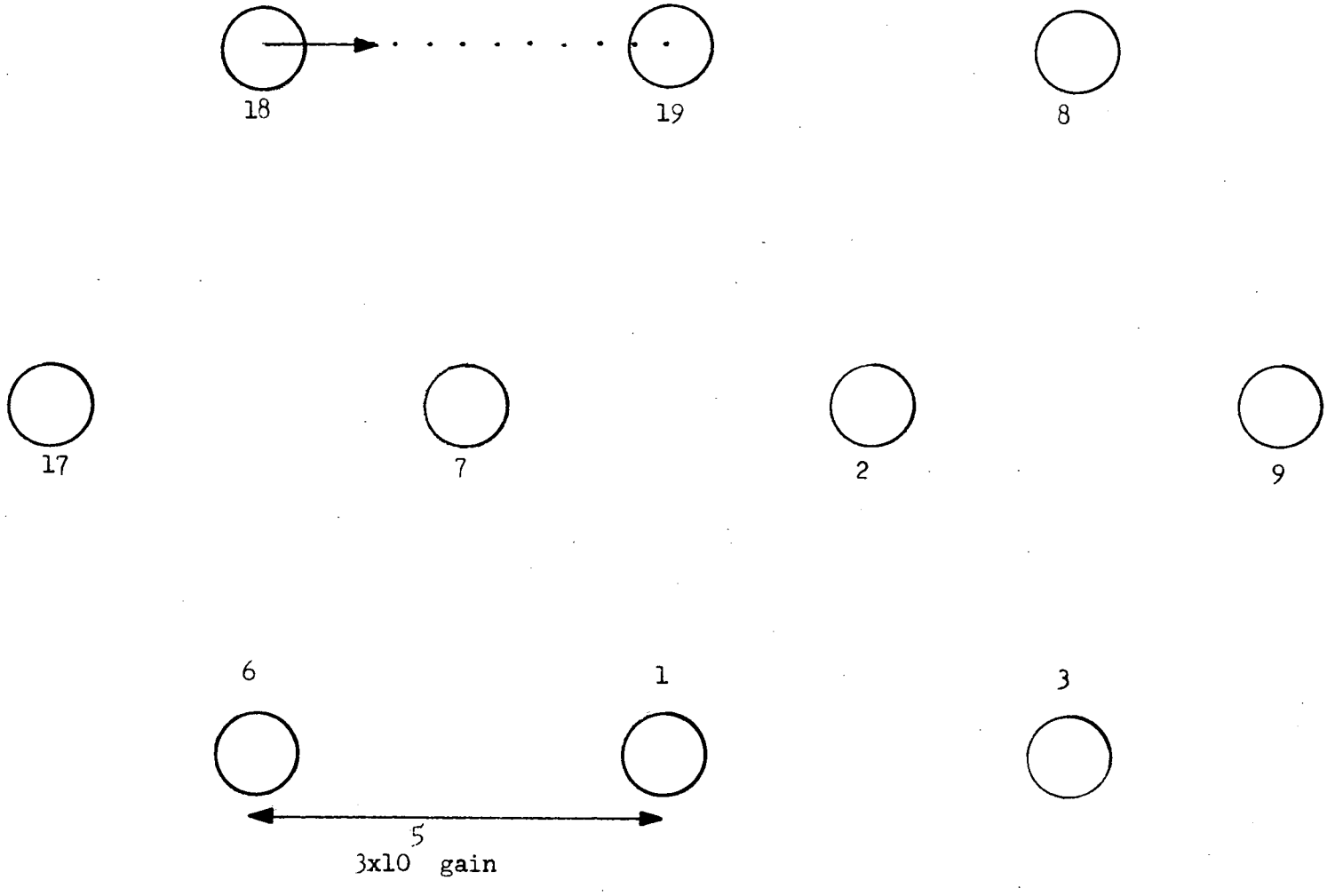

Figure A-34. Vector diagram for bundle 1B at the 18 inch level at 54 GPM.

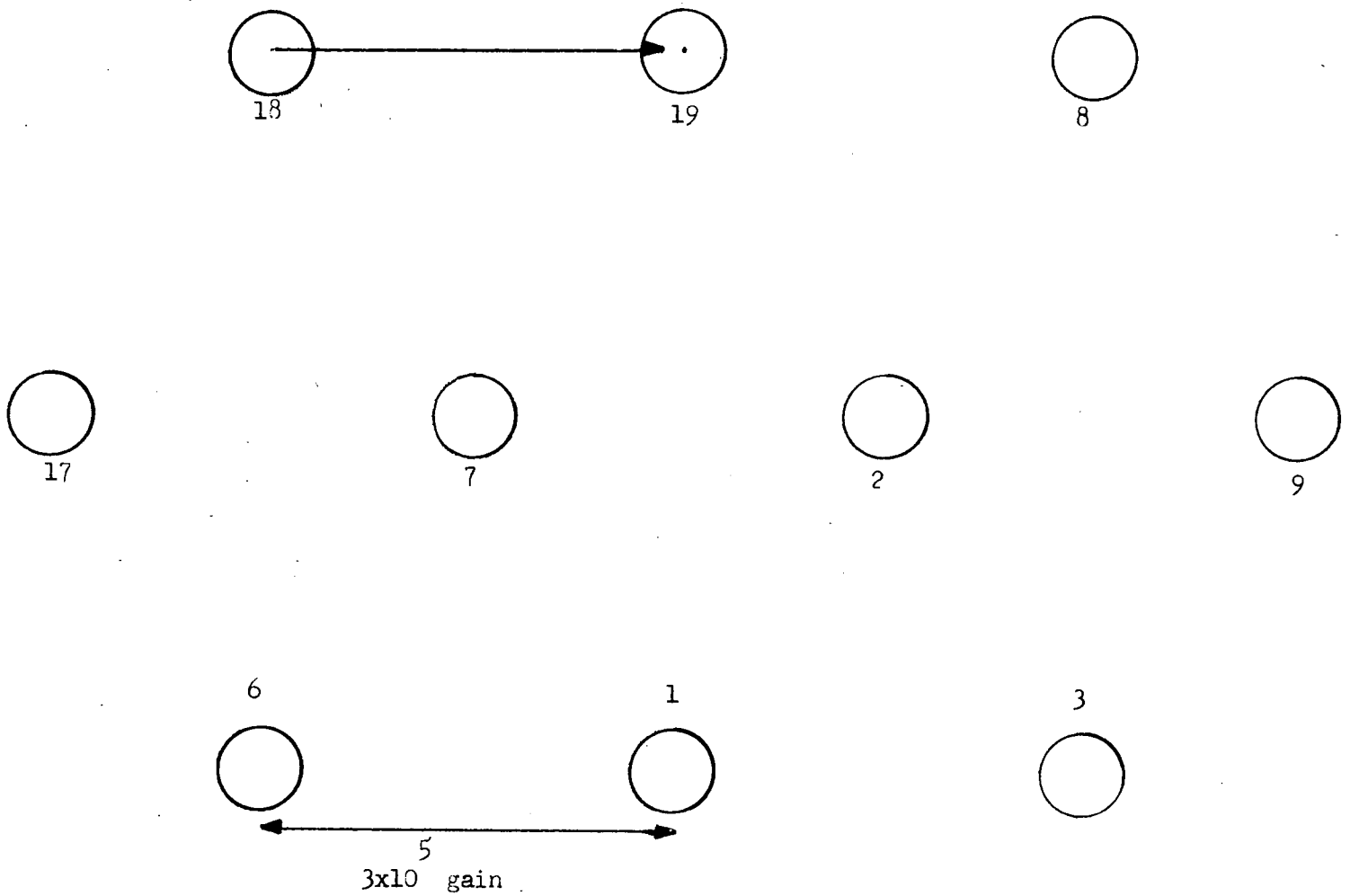

Figure A-35. Vector diagram for bundle 1B at the 6 inch level at 10 GPM.

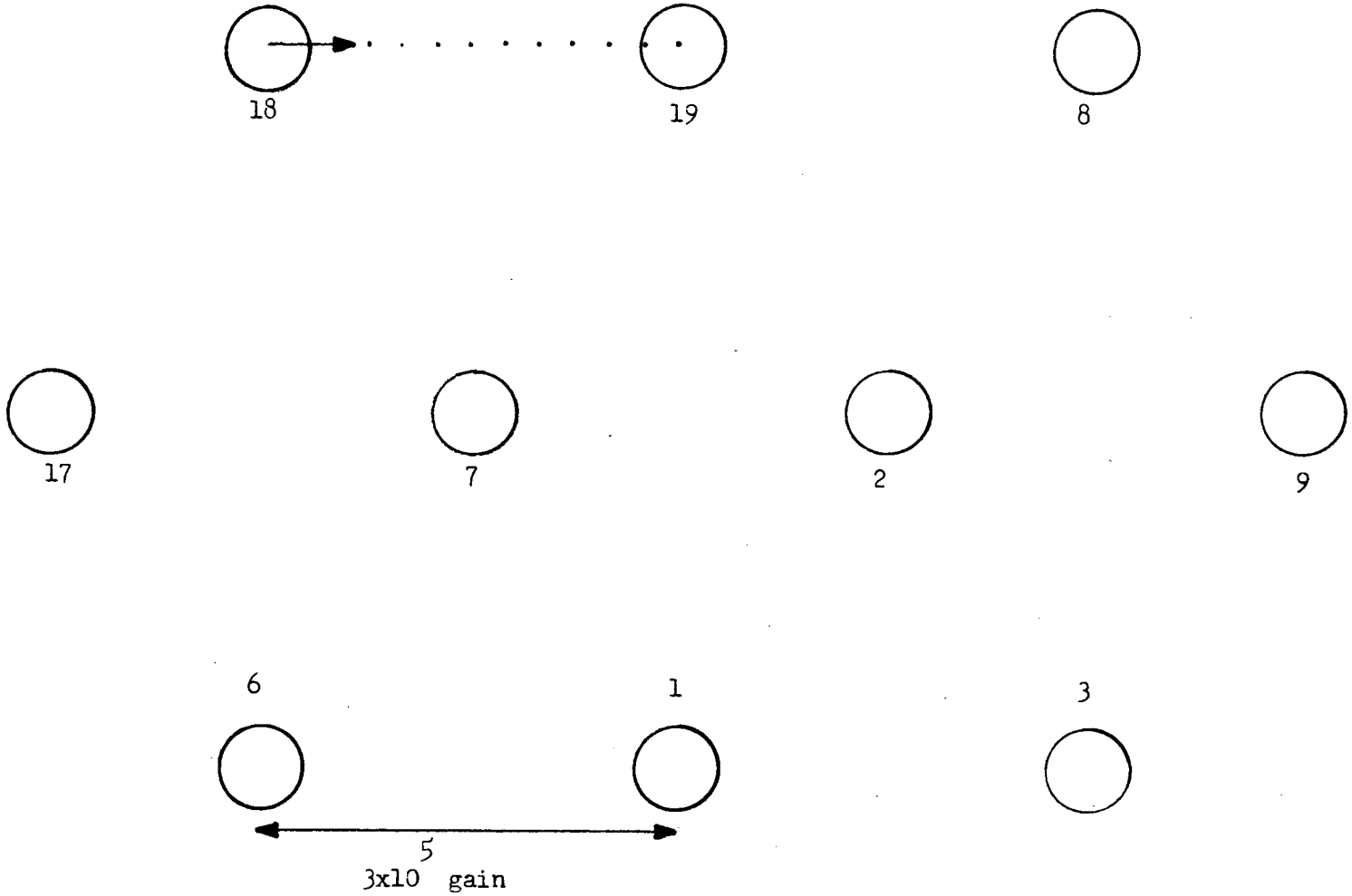

Figure A-36. Vector diagram for bundle 1B at the 6 inch level at 35 GPM.

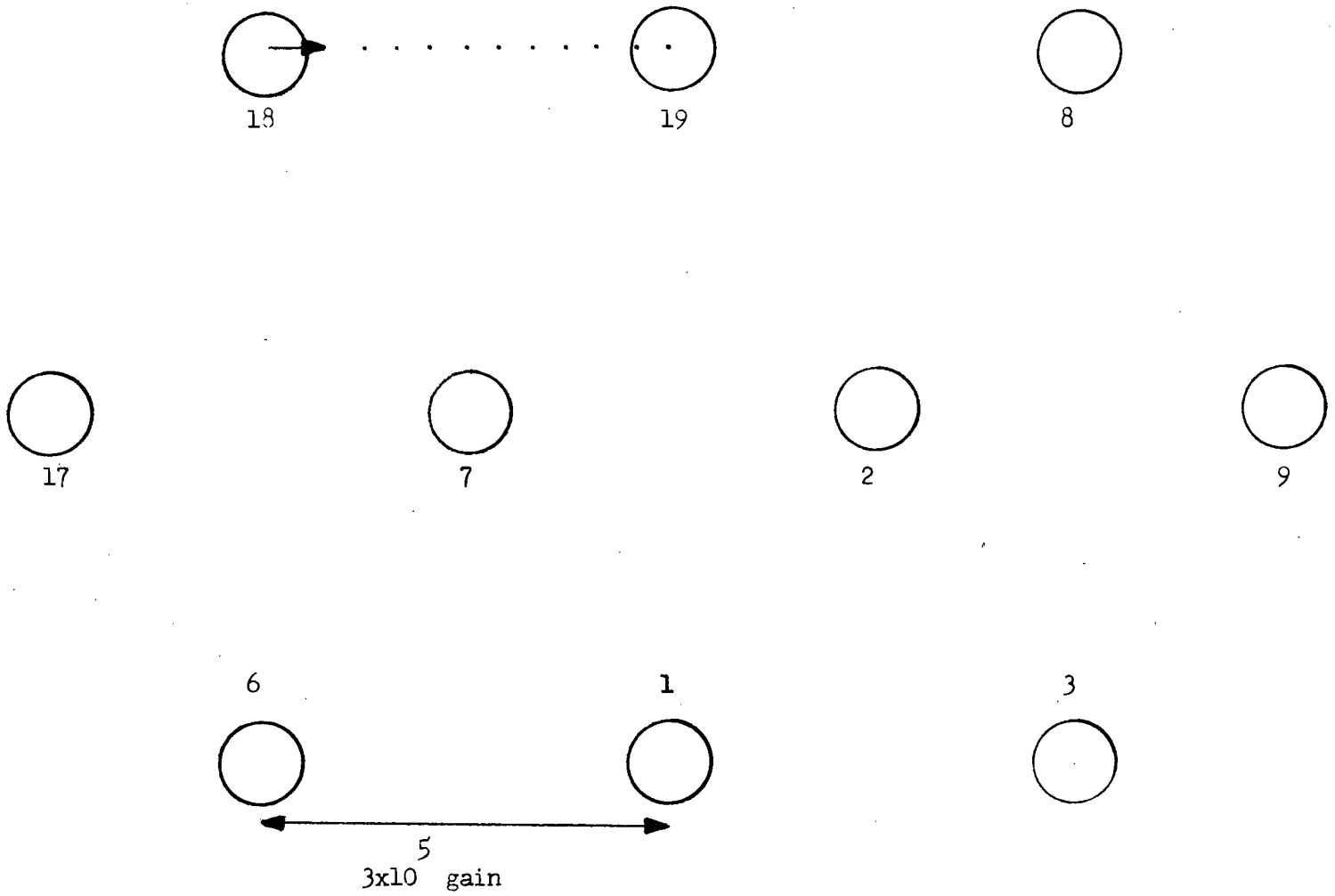

Figure A-37. Vector diagram for bundle 1B at the 6 inch level at 54 GPM.

APPENDIX B

EXPERIMENTAL DATA IN THE FORM OF GAIN RATIOS

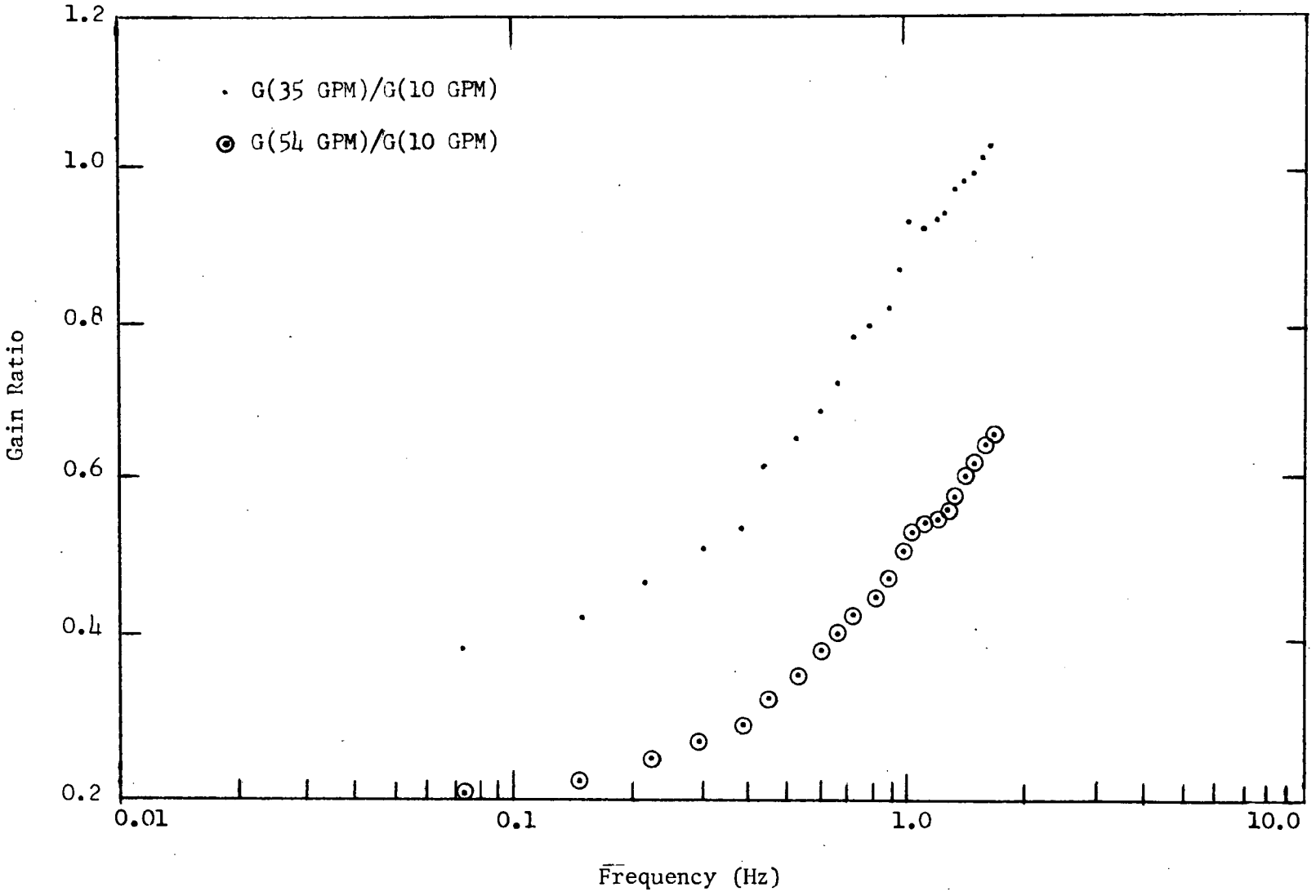

Figure B-1. Bundle 2B, gain ratios for thermocouple 1212 with rod 13 heated.

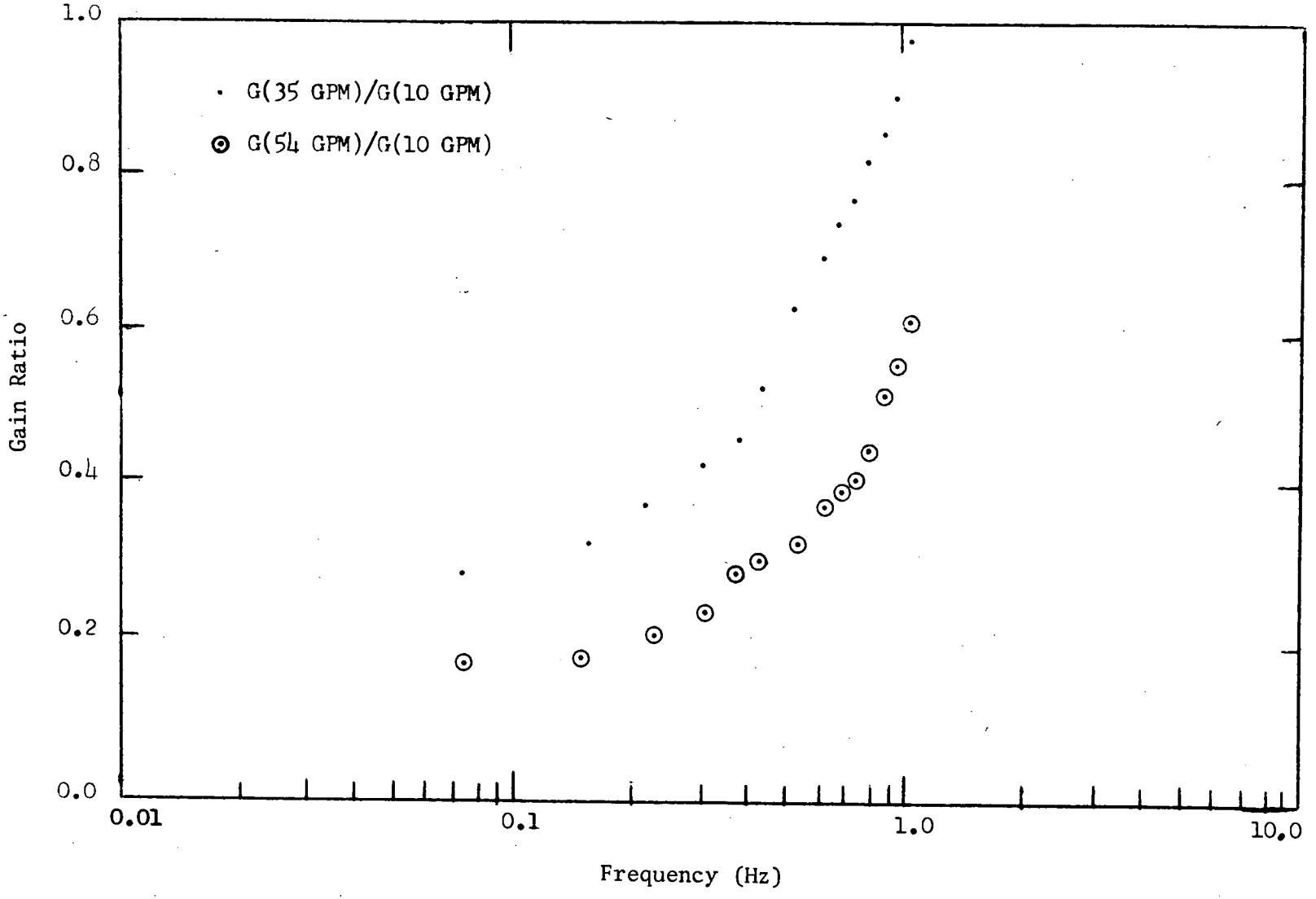

Figure B-2. Bundle 2B, gain ratios for thermocouple 0412 with rod 13 heated.

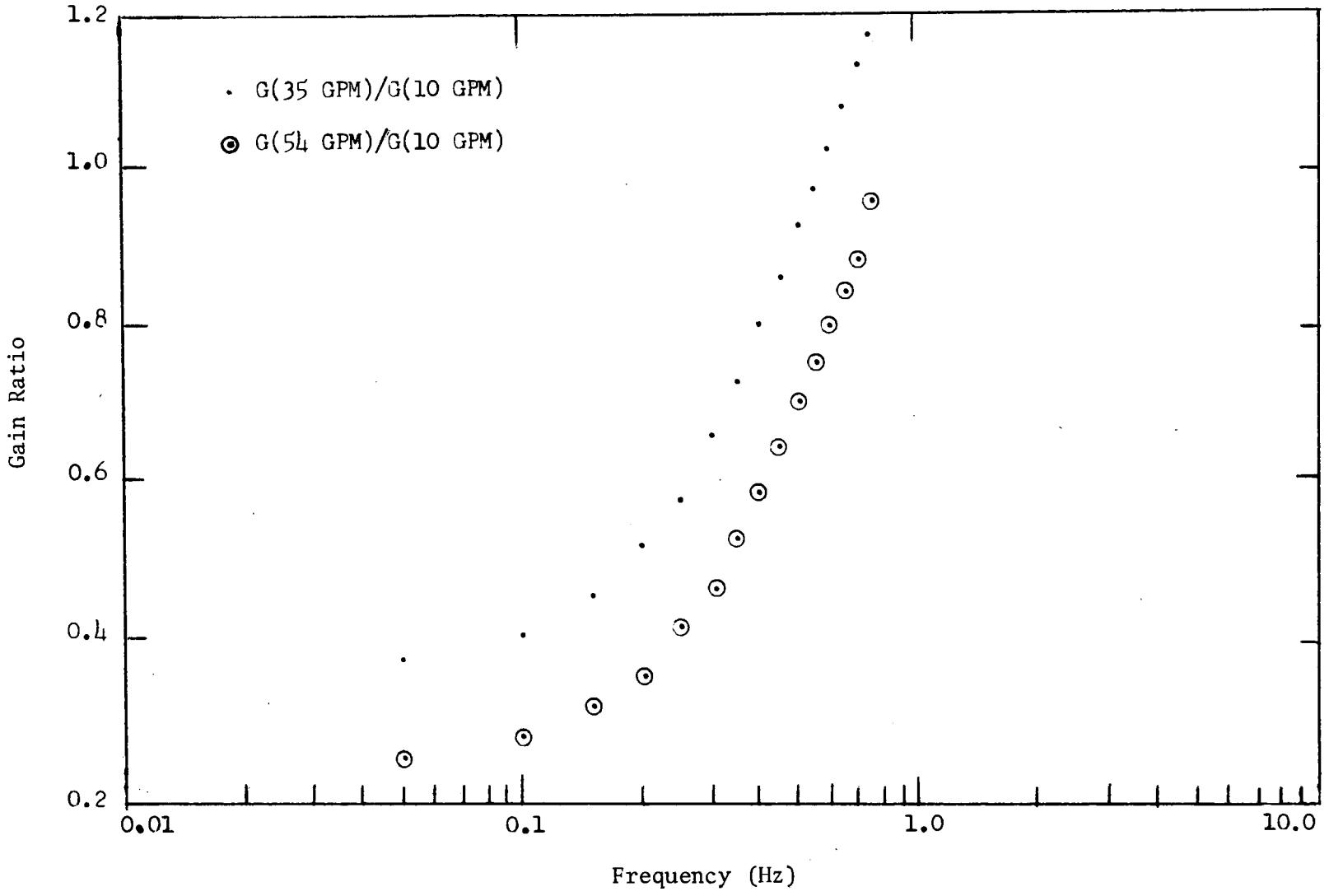

Figure B-3. Bundle 1B, gain ratios for thermocouple 0118 with rod 5 heated.

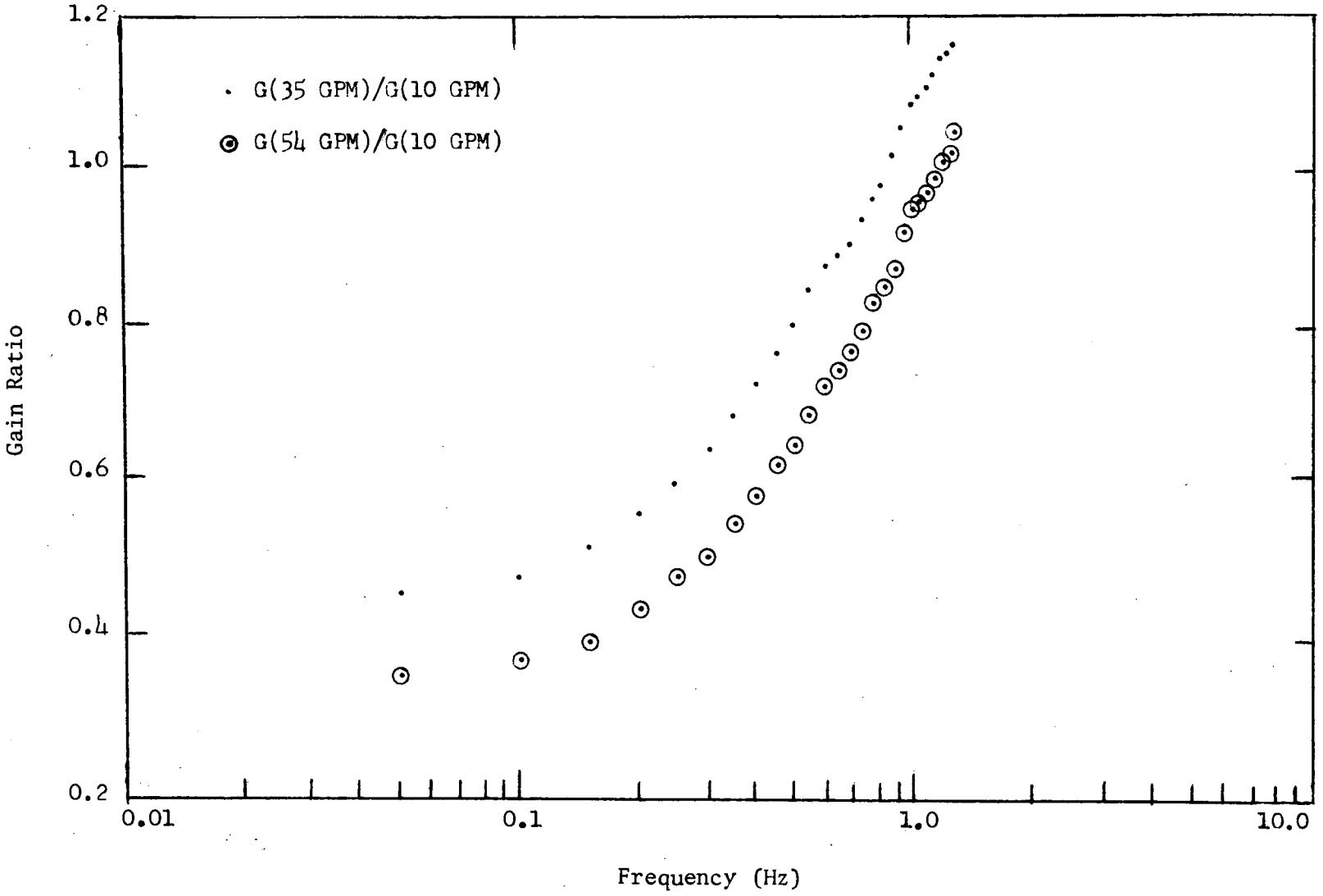

Figure B-4. Bundle 1B, gain ratios for thermocouple 1314 with rod 13 heated.

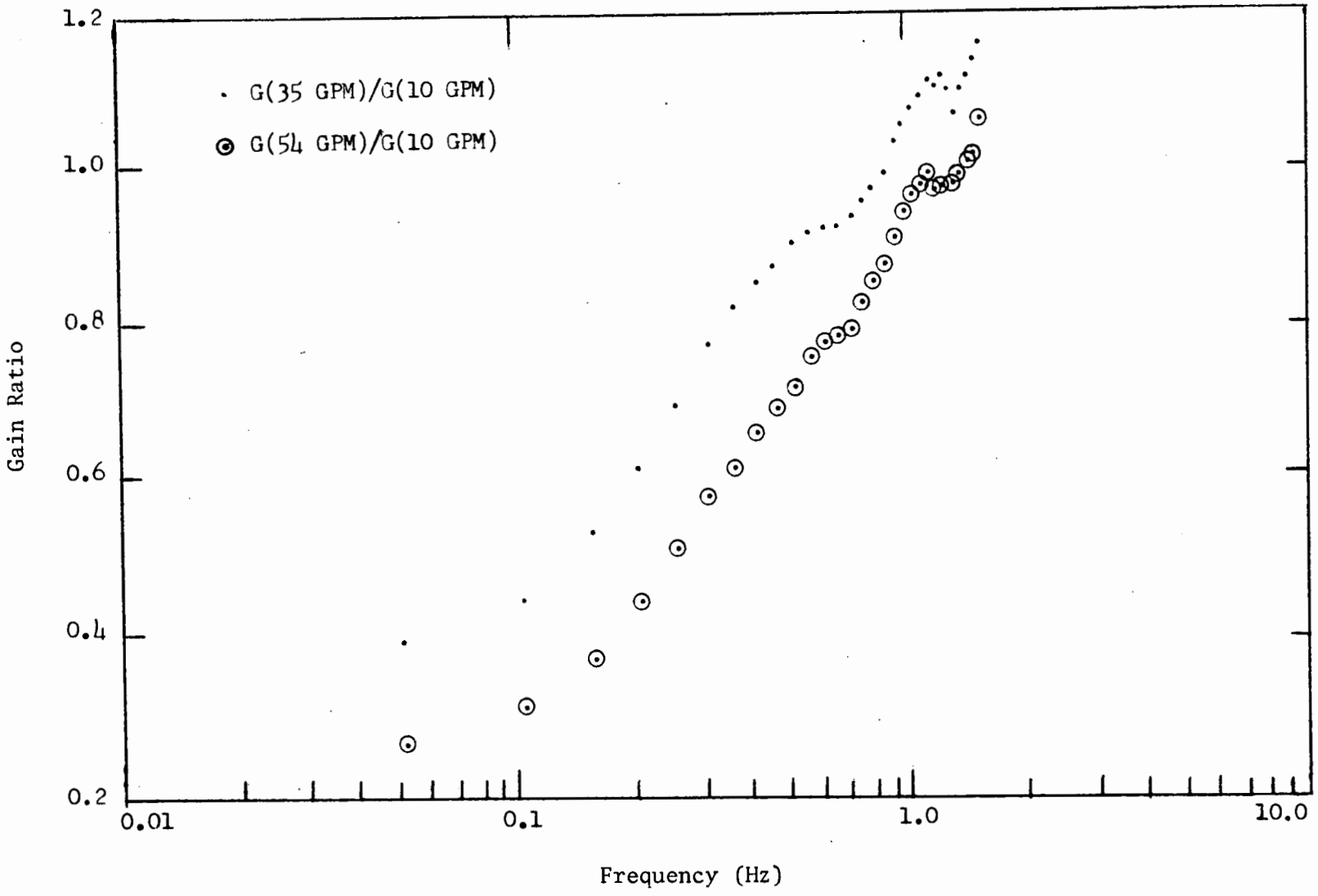

Figure B-5. Bundle 1B, gain ratios for thermocouple 1326 with rod 13 heated.

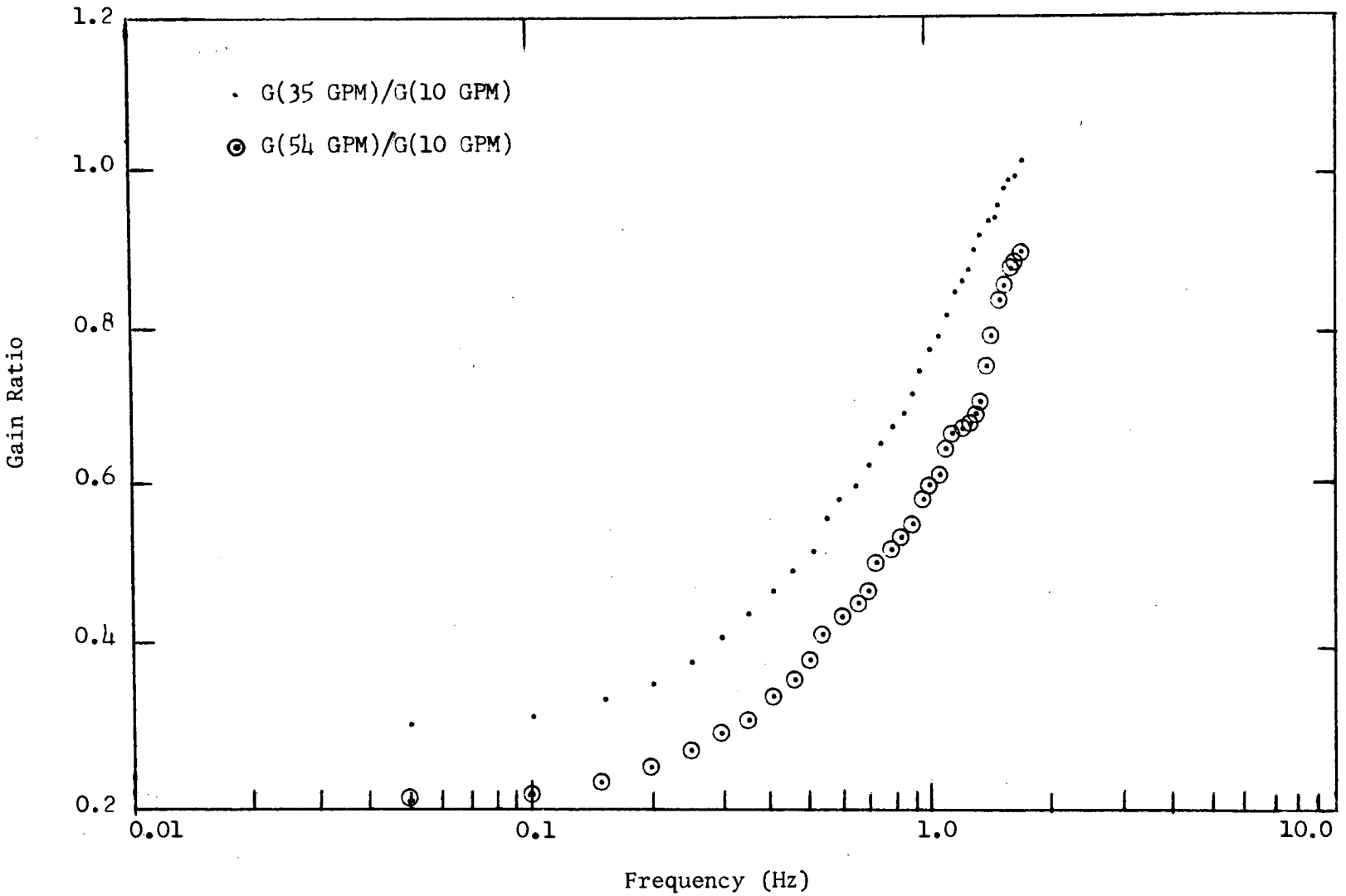

Figure B-6. Bundle 1B, gain ratios for thermocouple 0410 with rod 13 heated.

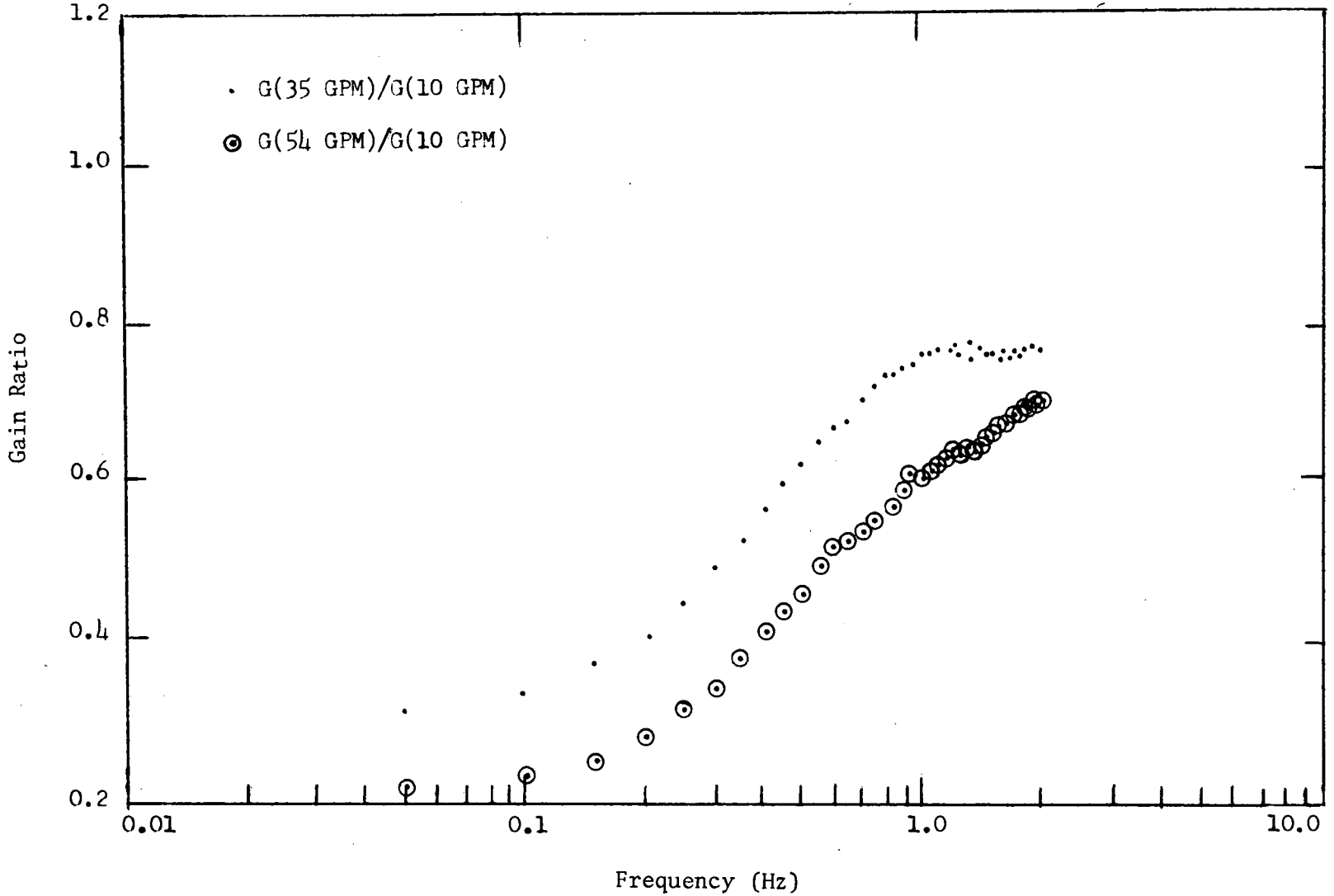

Figure B-7. Bundle 1B, gain ratios for thermocouple 1714 with rod 18 heated.

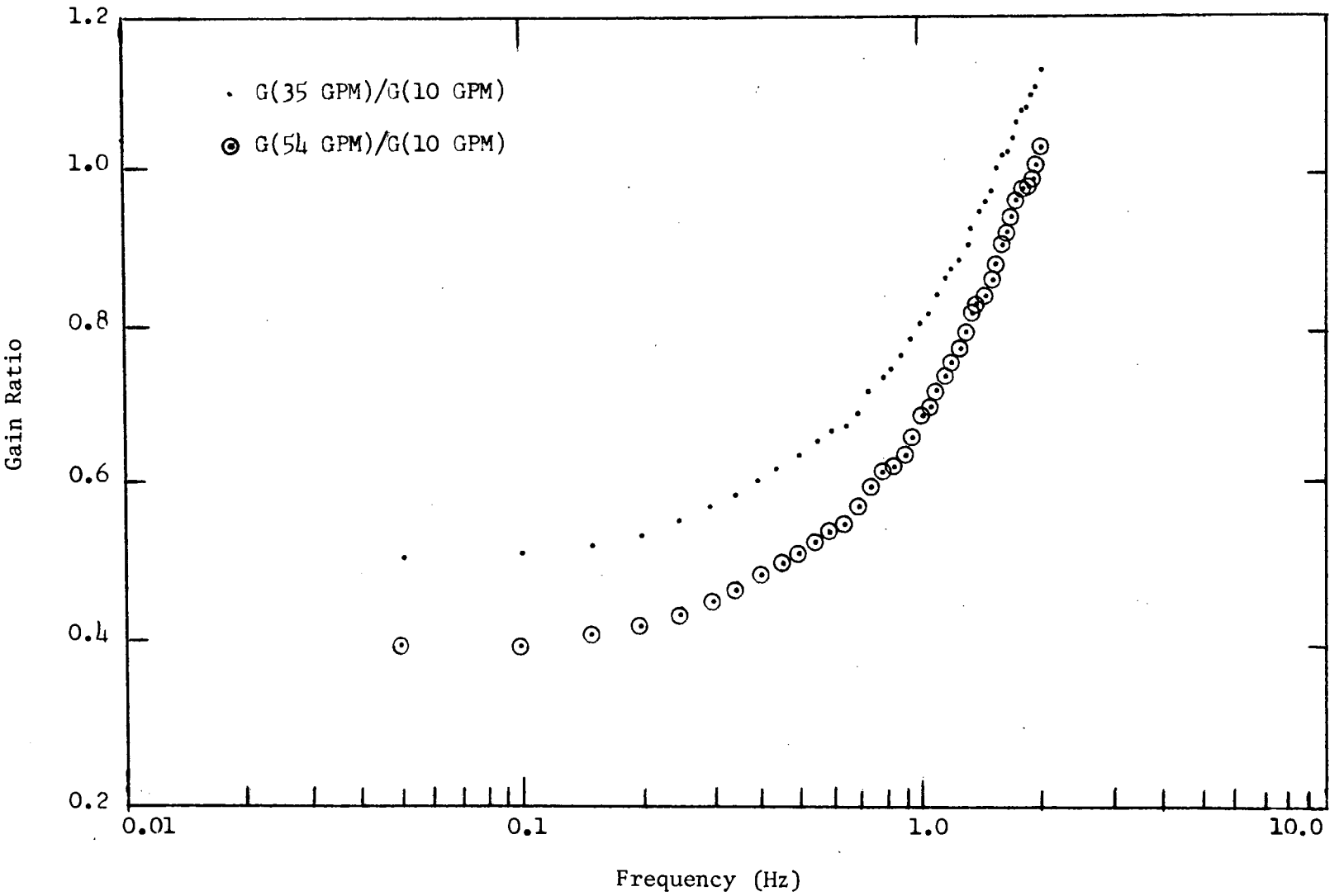

Figure B-8. Bundle 1B, gain ratios for thermocouple 1806 with rod 18 heated.

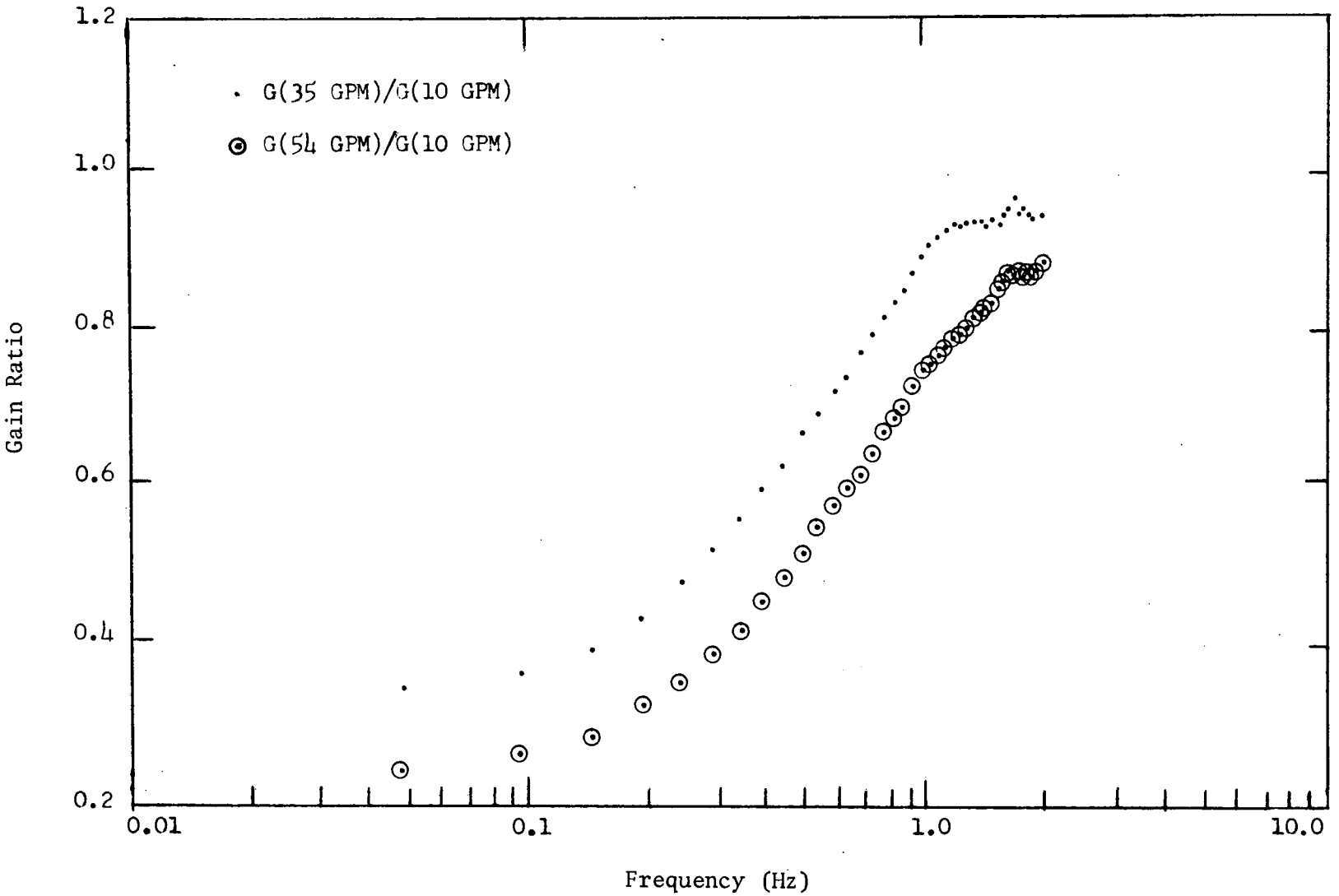

Figure B-9. Bundle 1B, gain ratios for thermocouple 1414 with rod 13 heated.

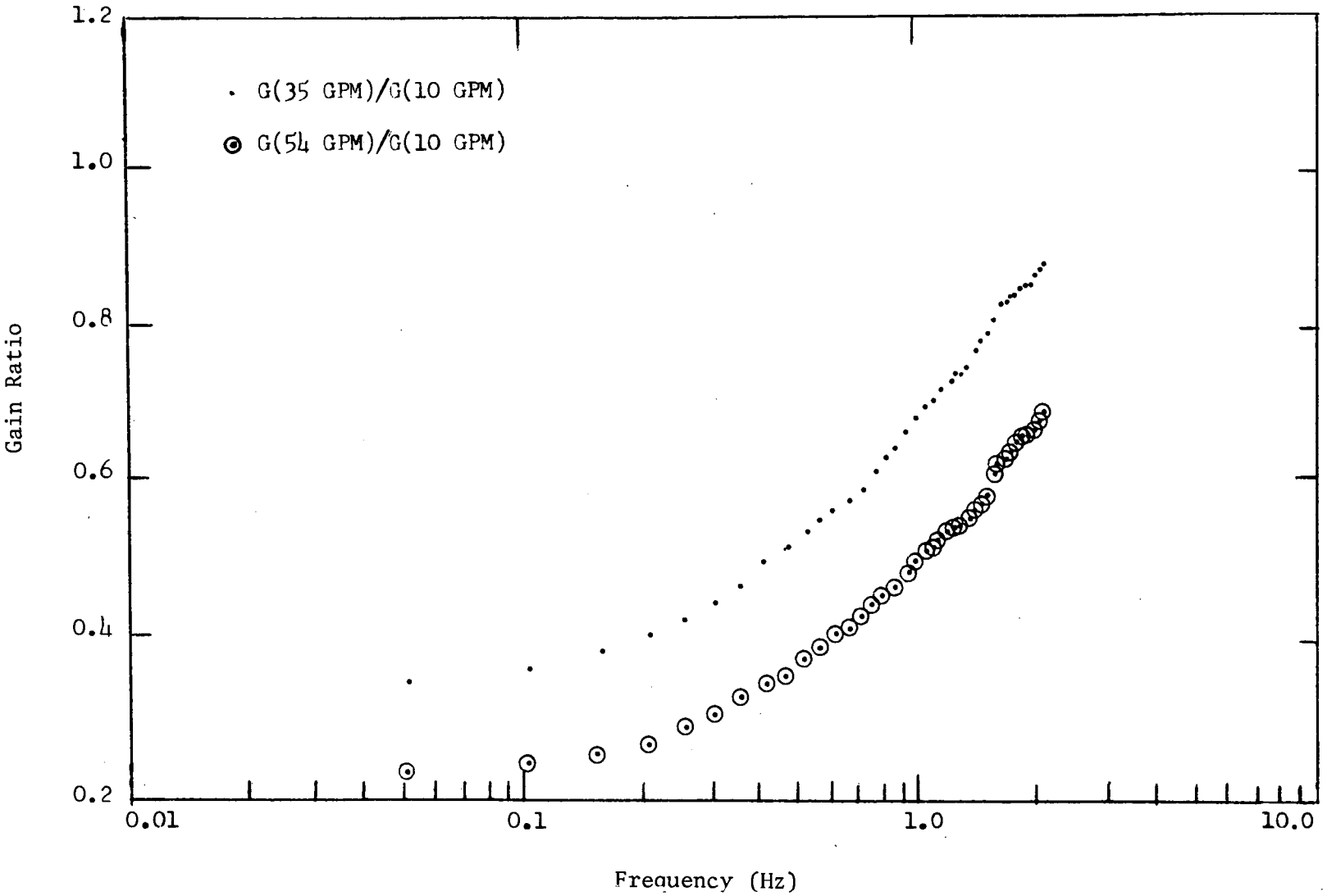

Figure B-10. Bundle 1B, gain ratios for thermocouple 1210 with rod 13 heated.

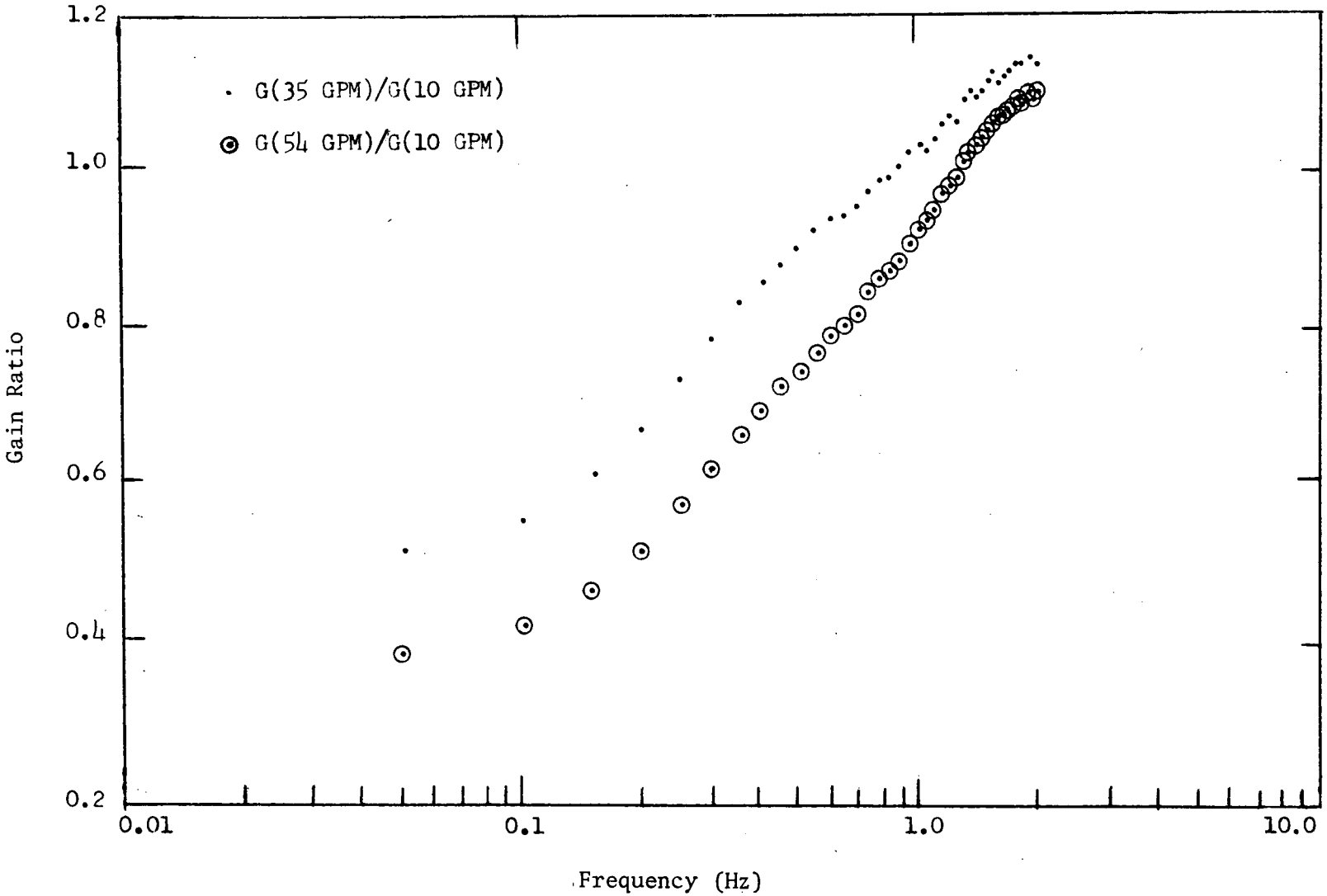

Figure B-11. Bundle 1B, gain ratios for thermocouple 1818 with rod 18 heated.

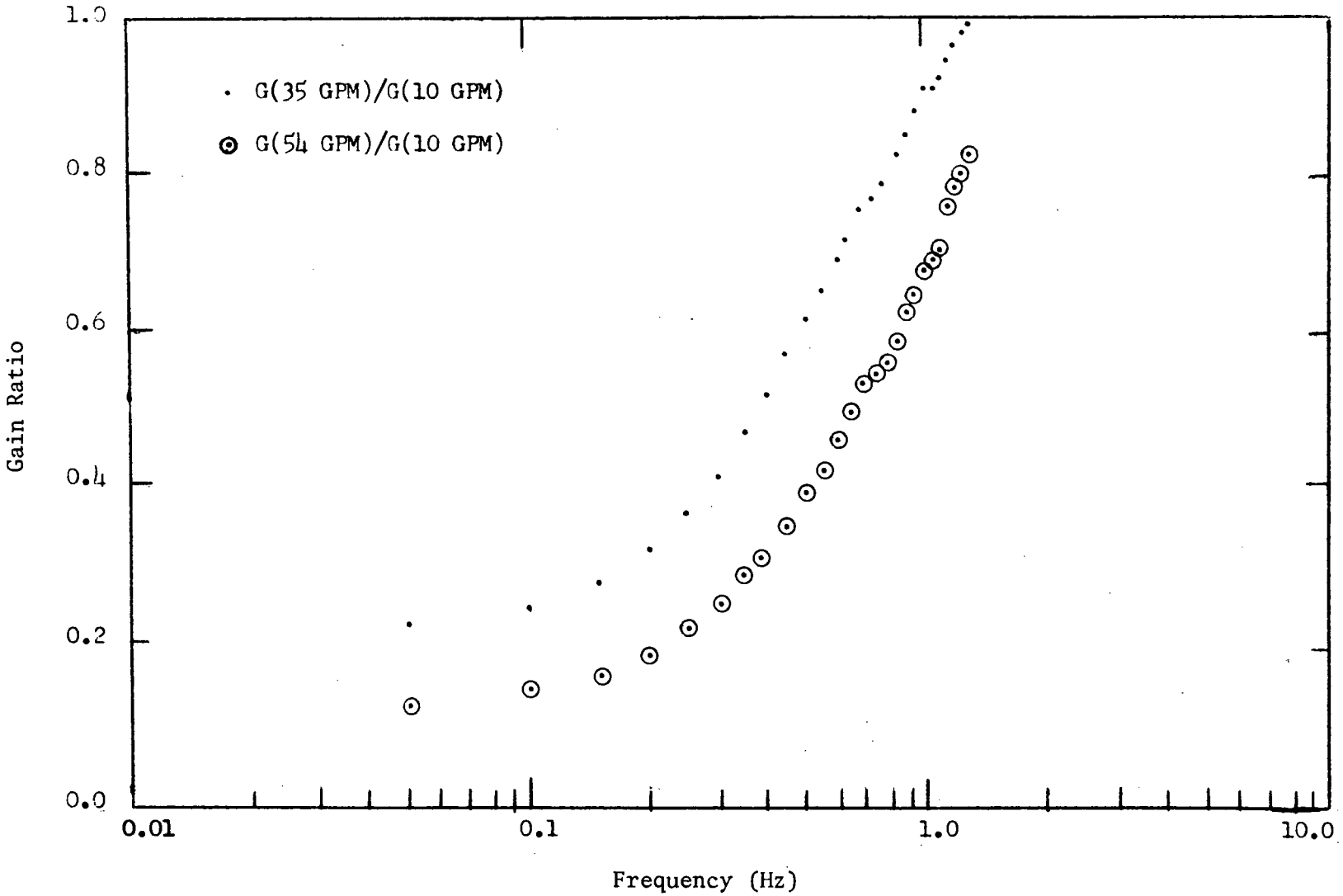

Figure B-12. Bundle 1B, gain ratios for thermocouple 1918 with rod 18 heated.

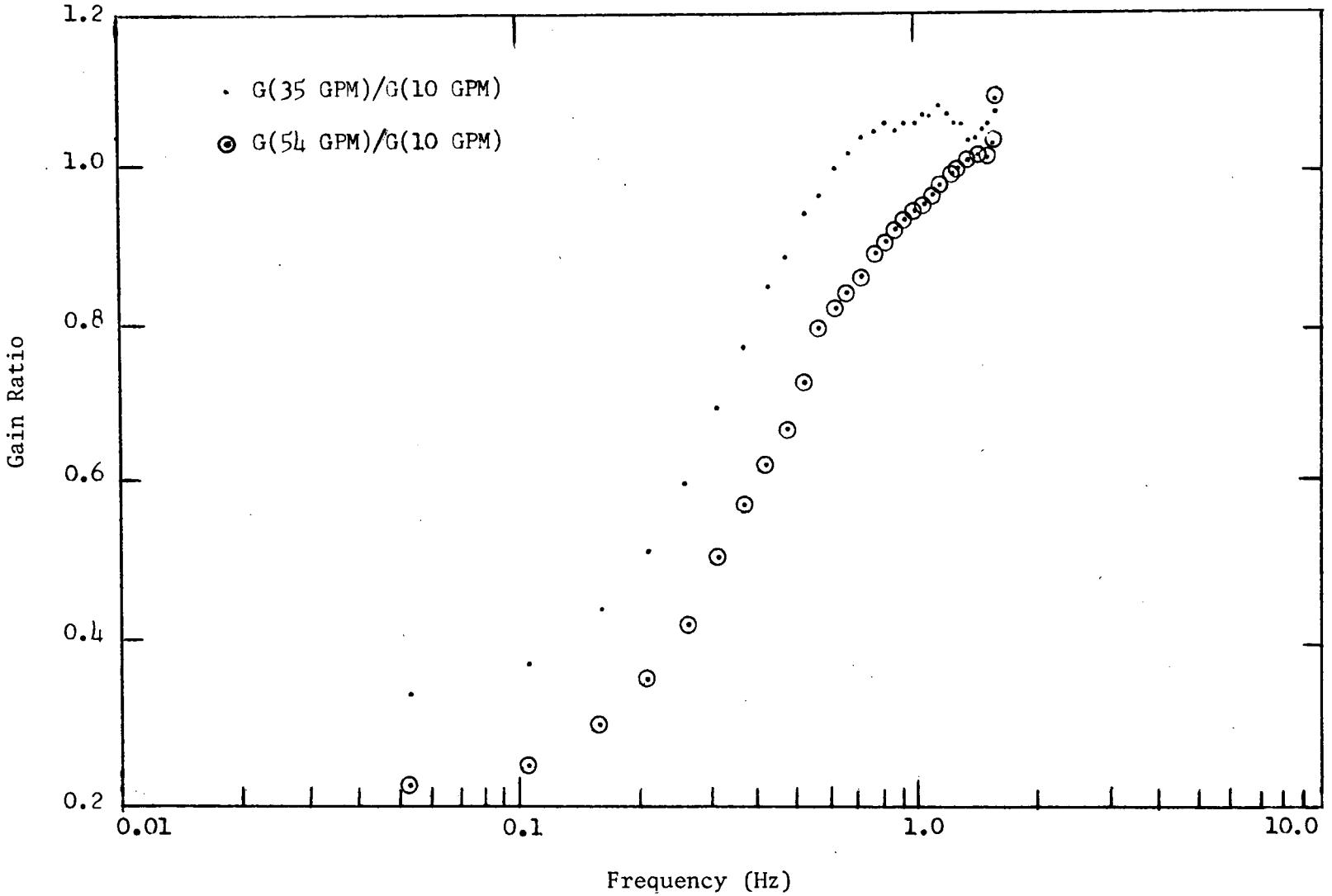

Figure B-13. Bundle 1B, gain ratios for thermocouple 1122 with rod 4 heated.

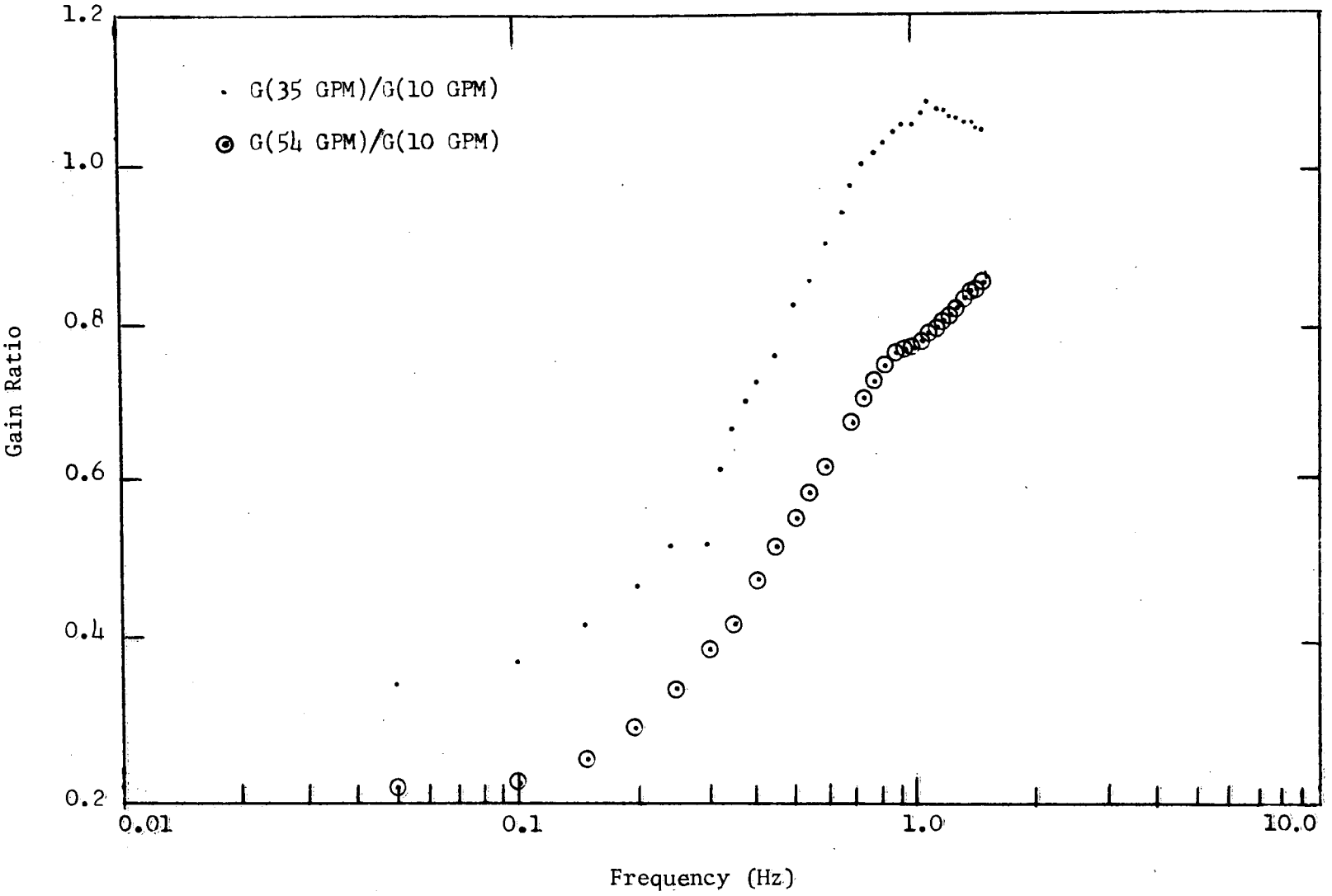

Figure B-14. Bundle 1B, gain ratios for thermocouple 0318 with rod 4 heated.

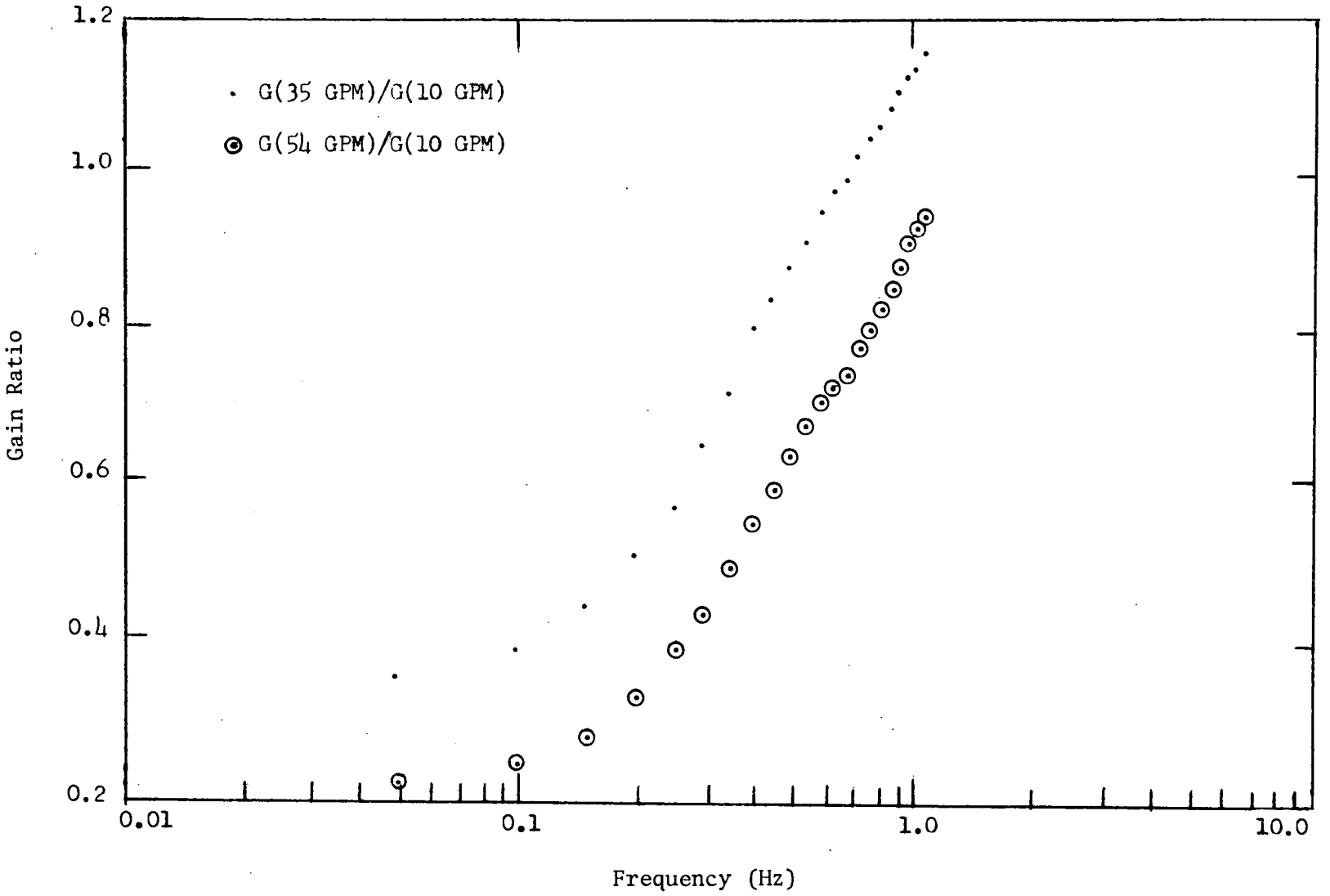

Figure B-15. Bundle 1B, gain ratios for thermocouple 0320 with rod 1 heated.

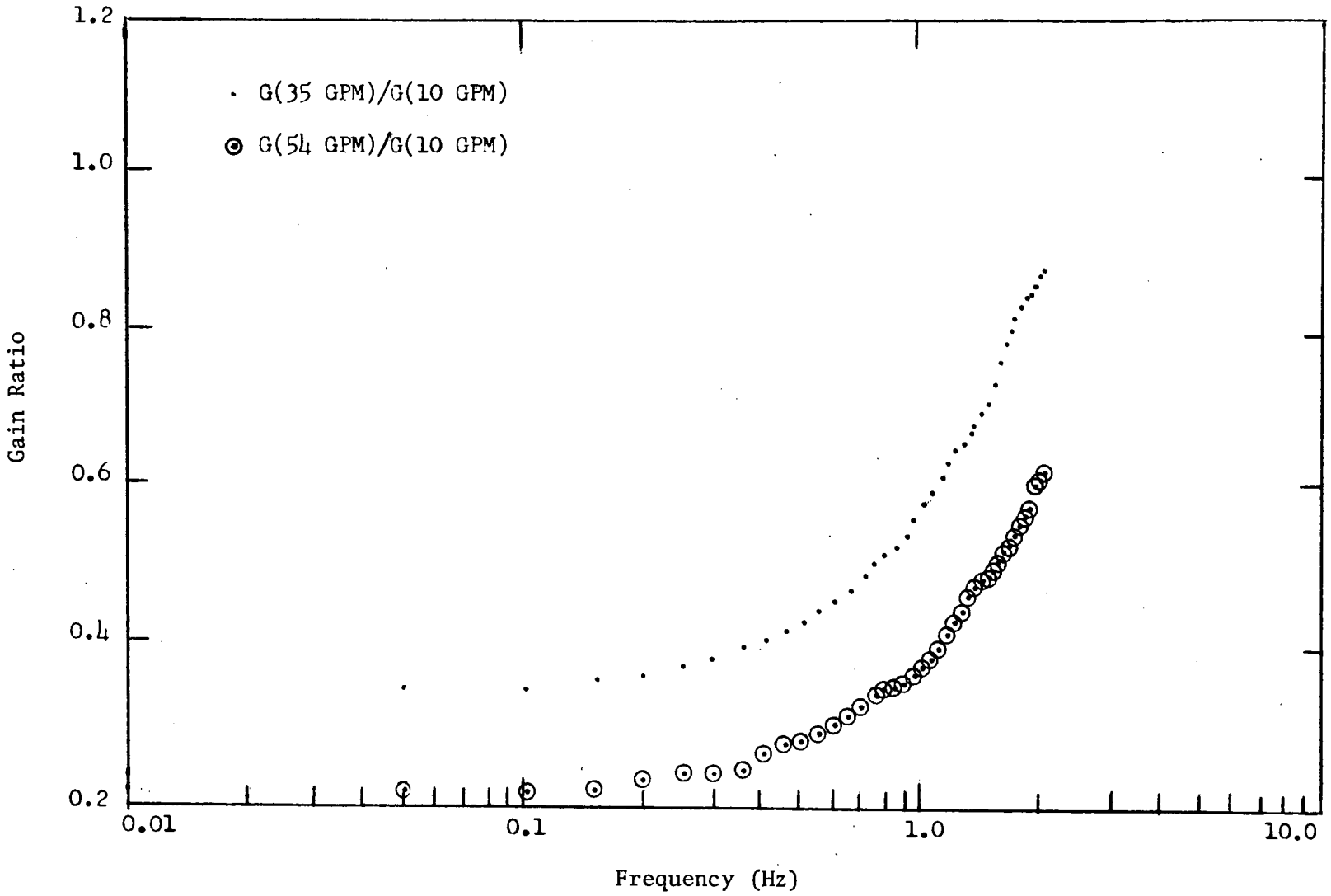

Figure B-16. Bundle 1B, gain ratios for thermocouple 0106 with rod 4 heated.

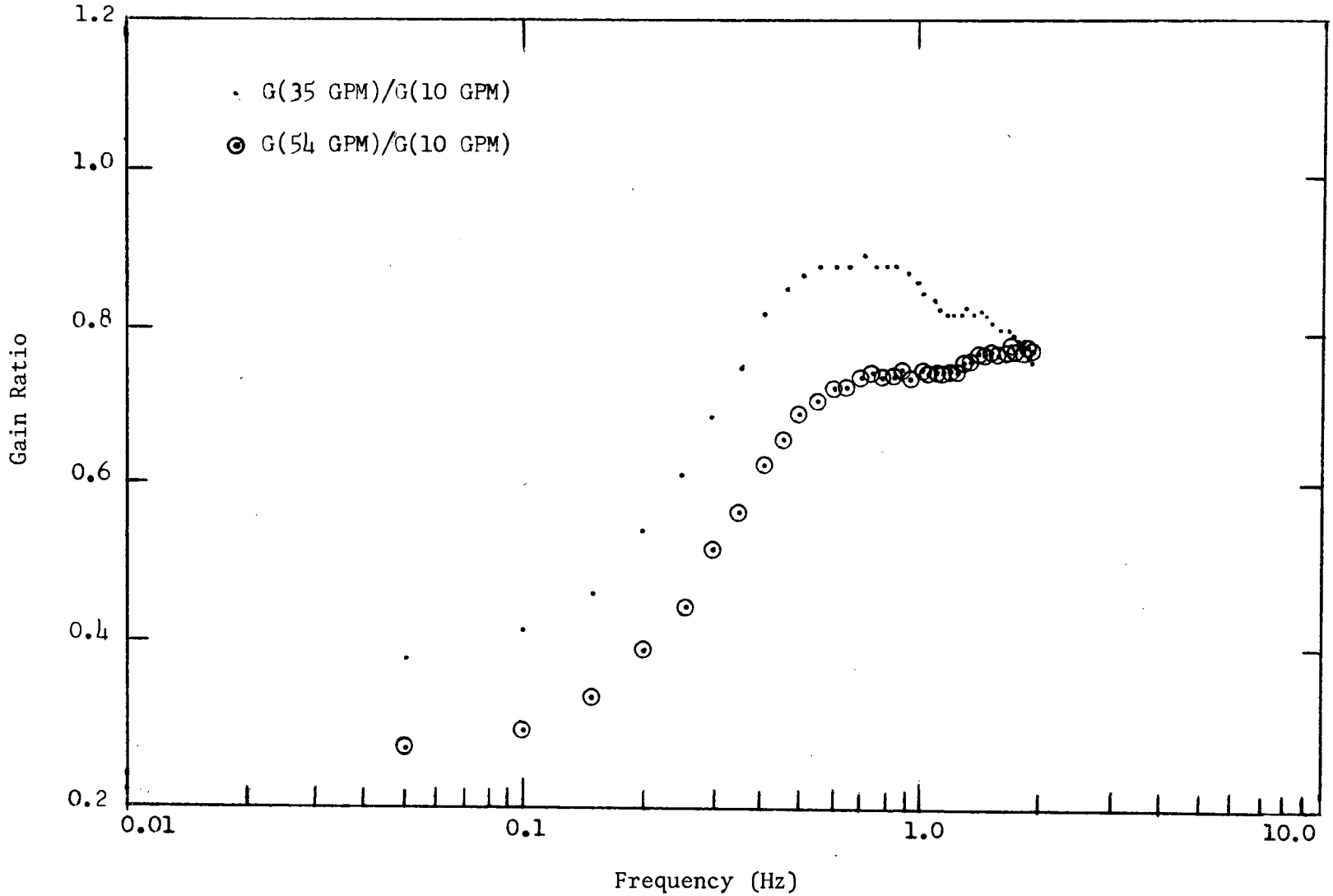

Figure B-17. Bundle 1B, gain ratios for thermocouple 0118 with rod 4 heated.

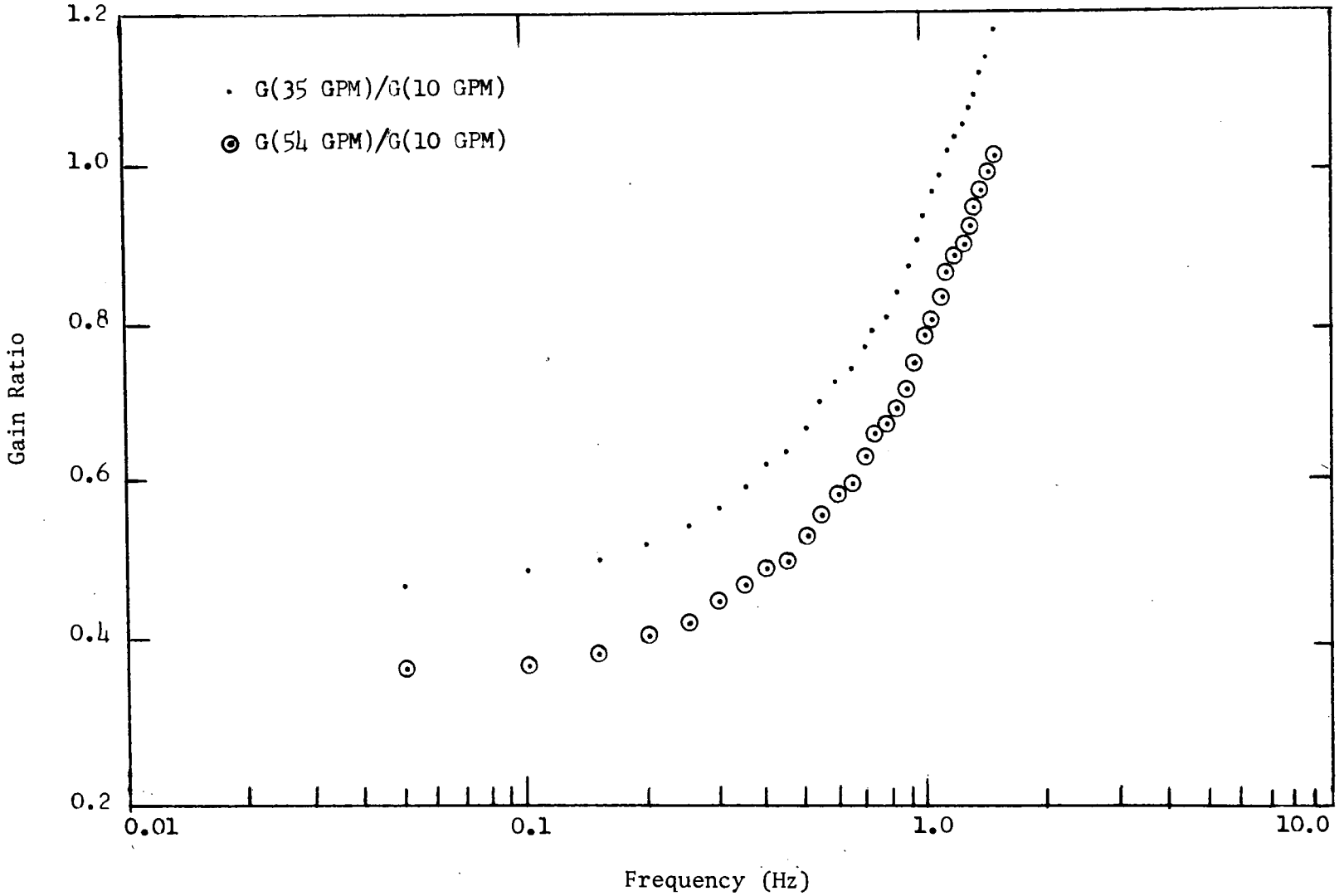

Figure B-18. Bundle 1B, gain ratios for thermocouple 0408 with rod 4 heated.

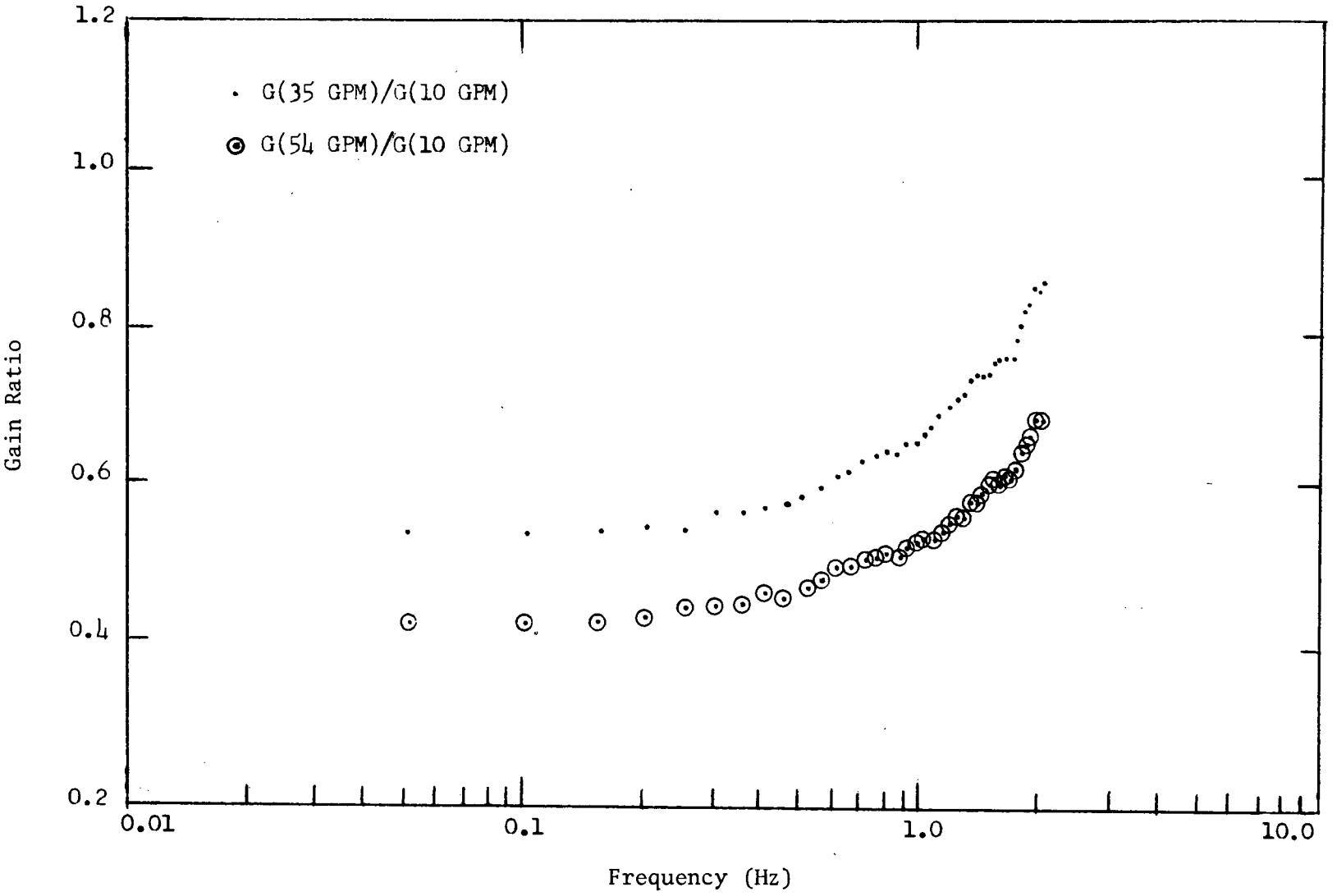

Figure B-19. Bundle 1B, gain ratios for thermocouple 0604 with rod 1 heated.

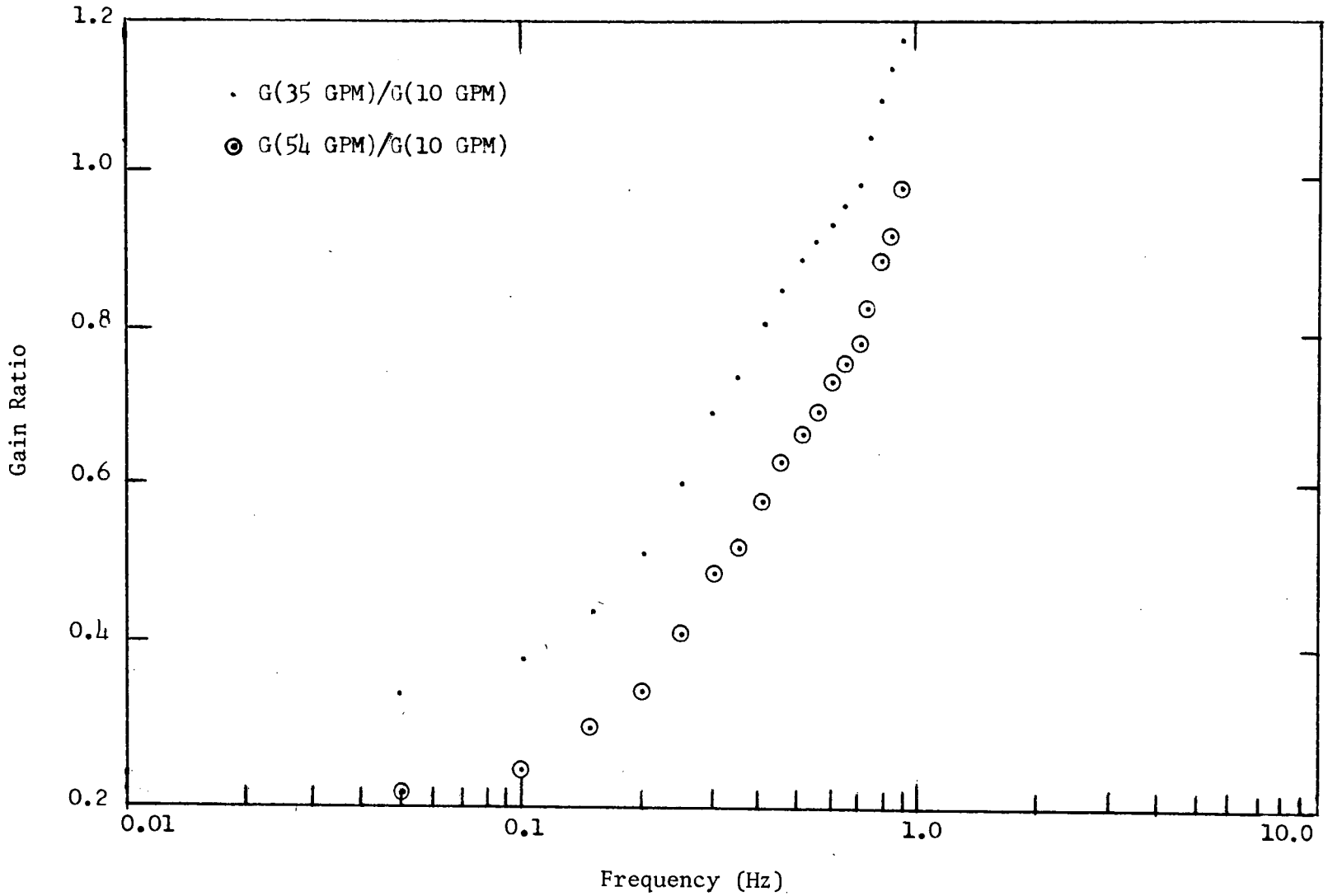

Figure B-20. Bundle 1B, gain ratios for thermocouple 1222 with rod 4 heated.

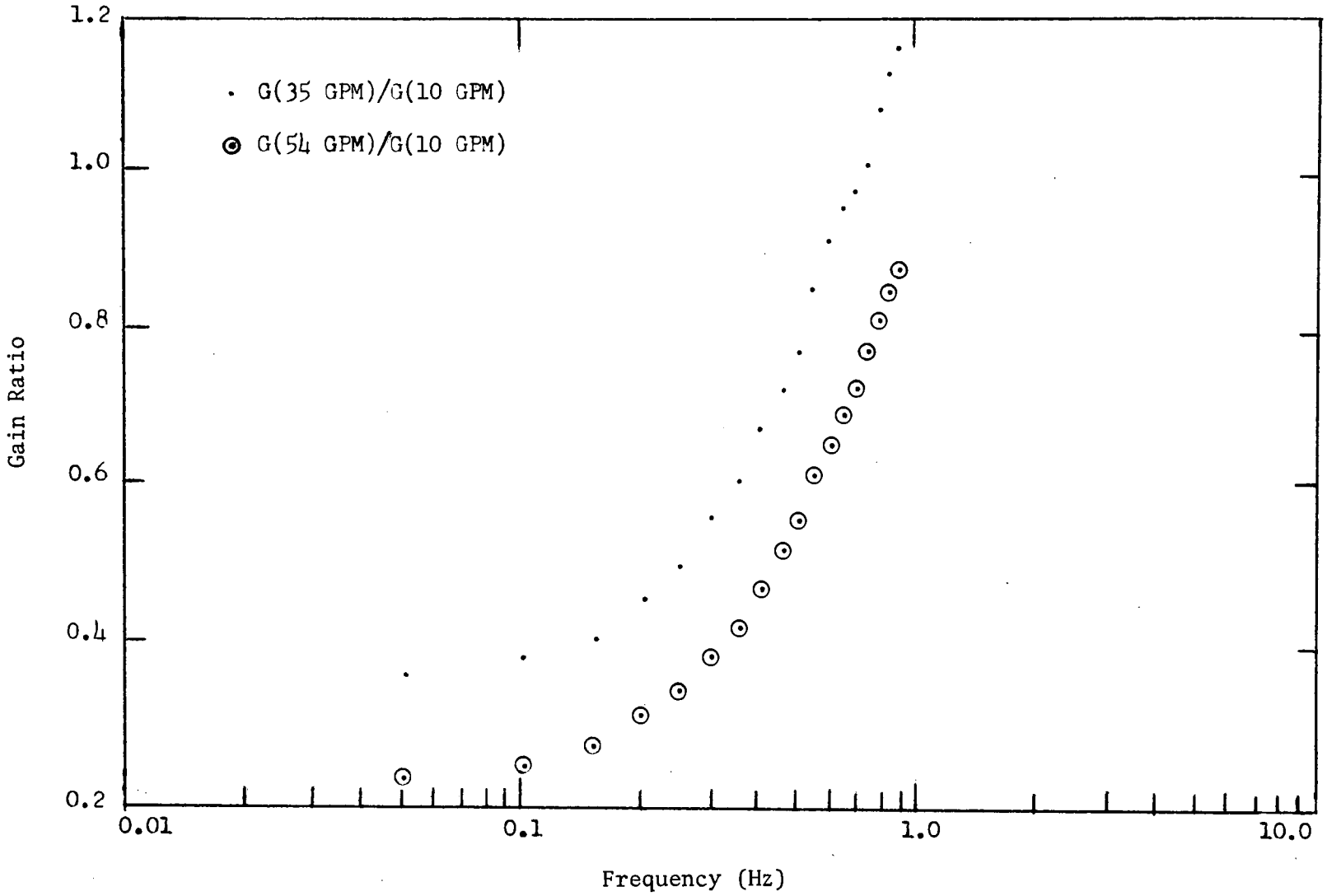

Figure B-21. Bundle 1B, gain ratios for thermocouple 0514 with rod 4 heated.

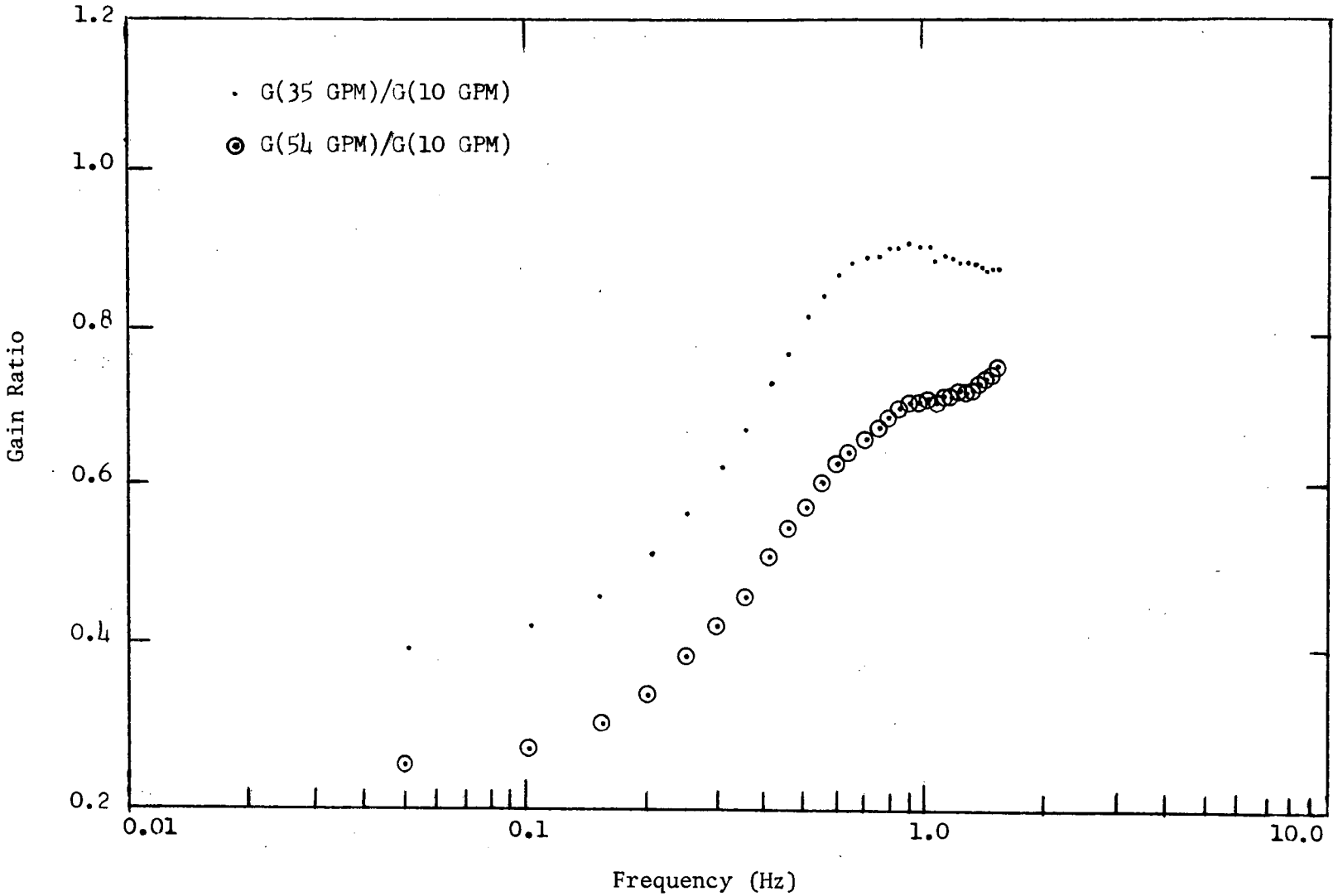

Figure B-22. Bundle 1B, gain ratios for thermocouple 1314 with rod 4 heated.

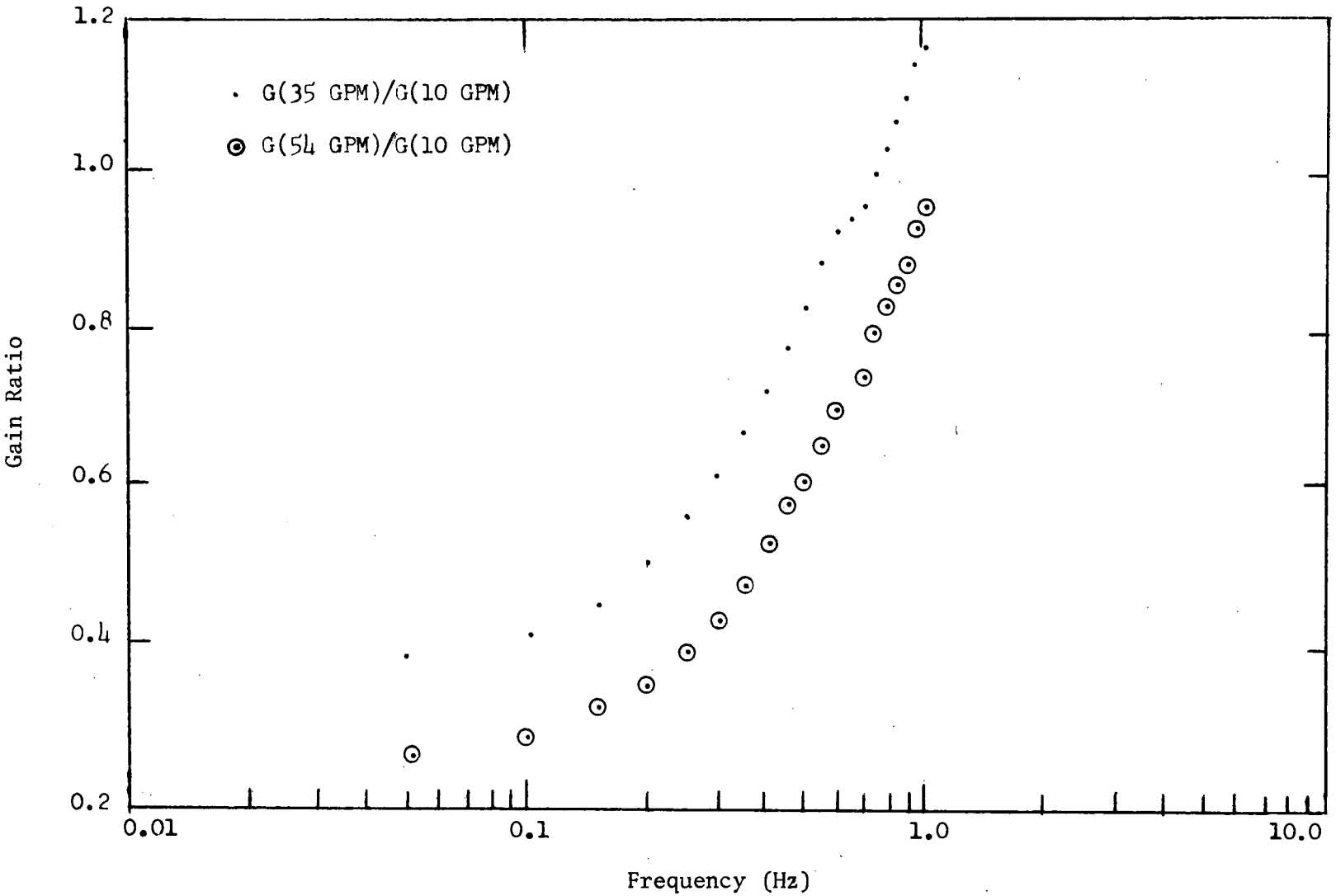

Figure B-23. Bundle 1B, gain ratios for thermocouple 1314 with rod 5 heated.

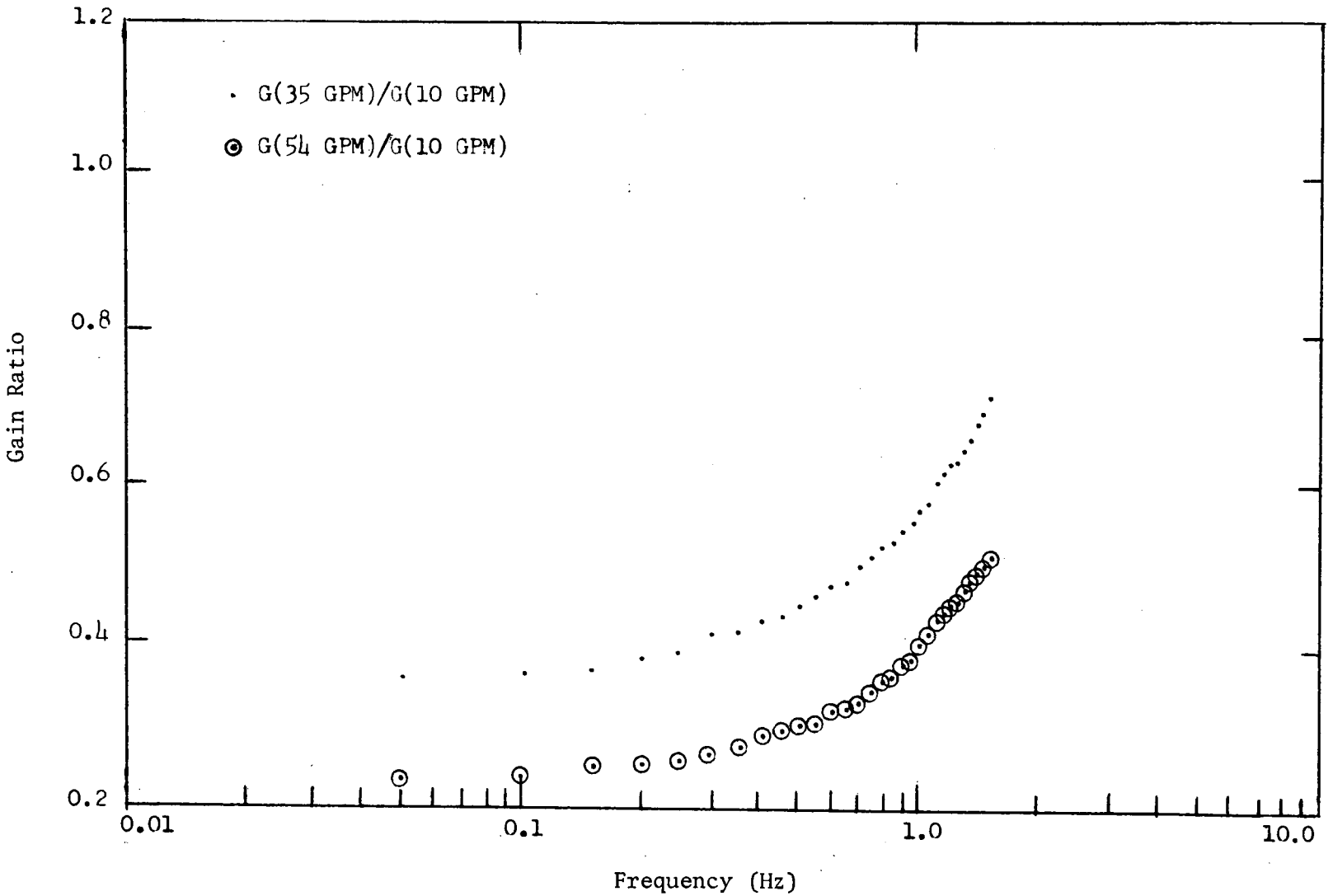

Figure B-24. Bundle 1B, gain ratios for thermocouple 0606 with rod 5 heated.

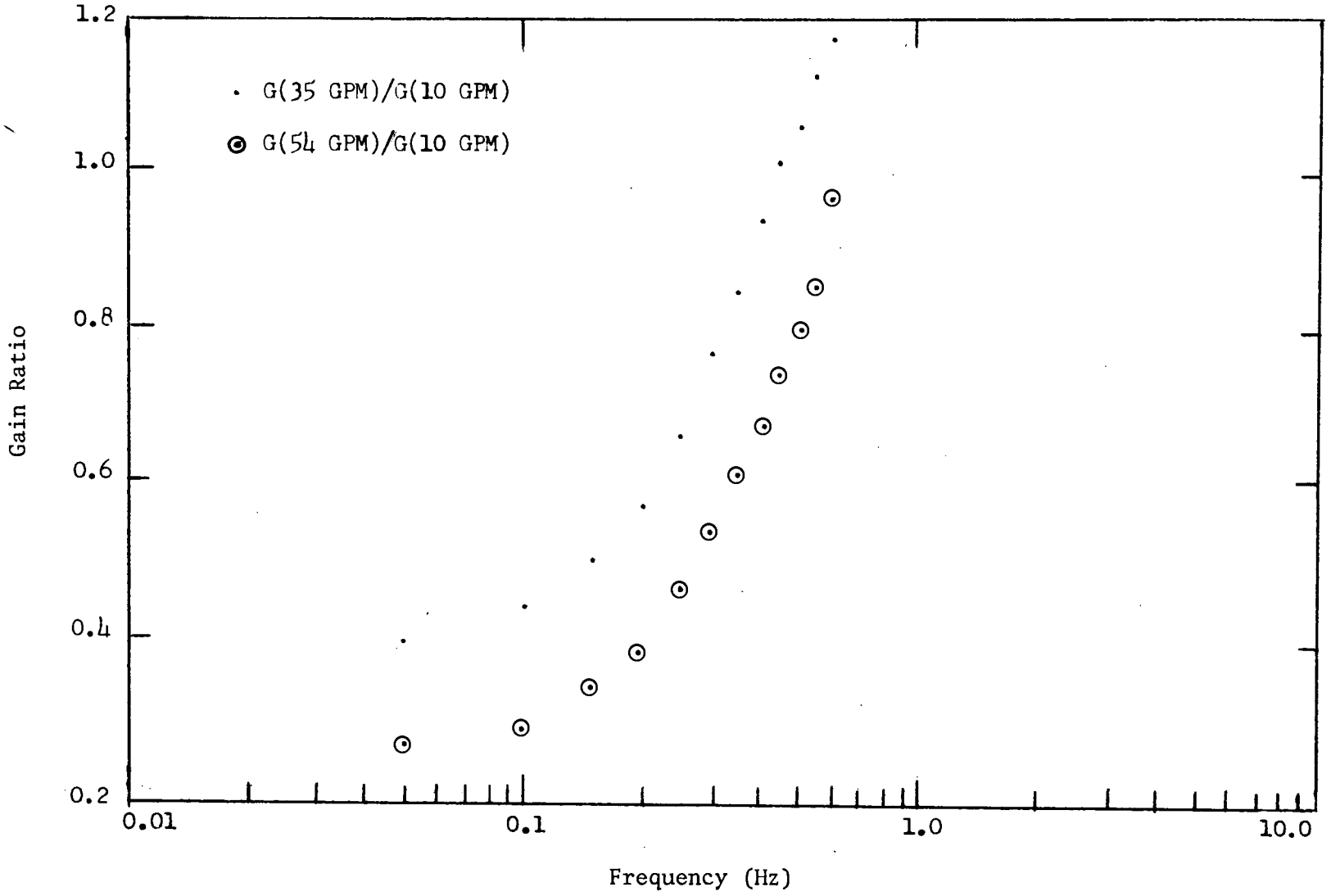

Figure B-25. Bundle 1B, gain ratios for thermocouple 0320 with rod heated.

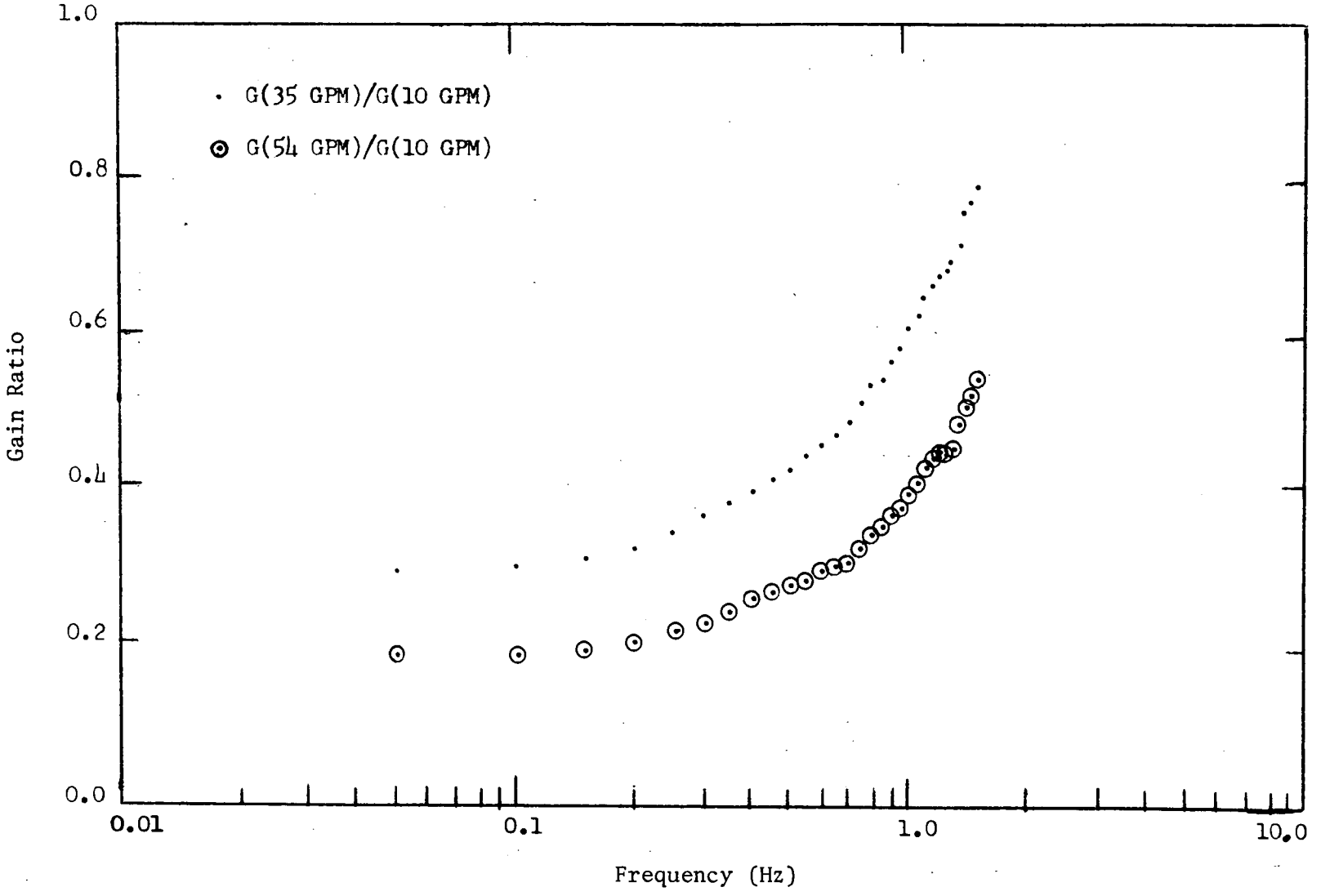

Figure B-26. Bundle 1B, gain ratios for thermocouple 0408 with rod 5 heated.

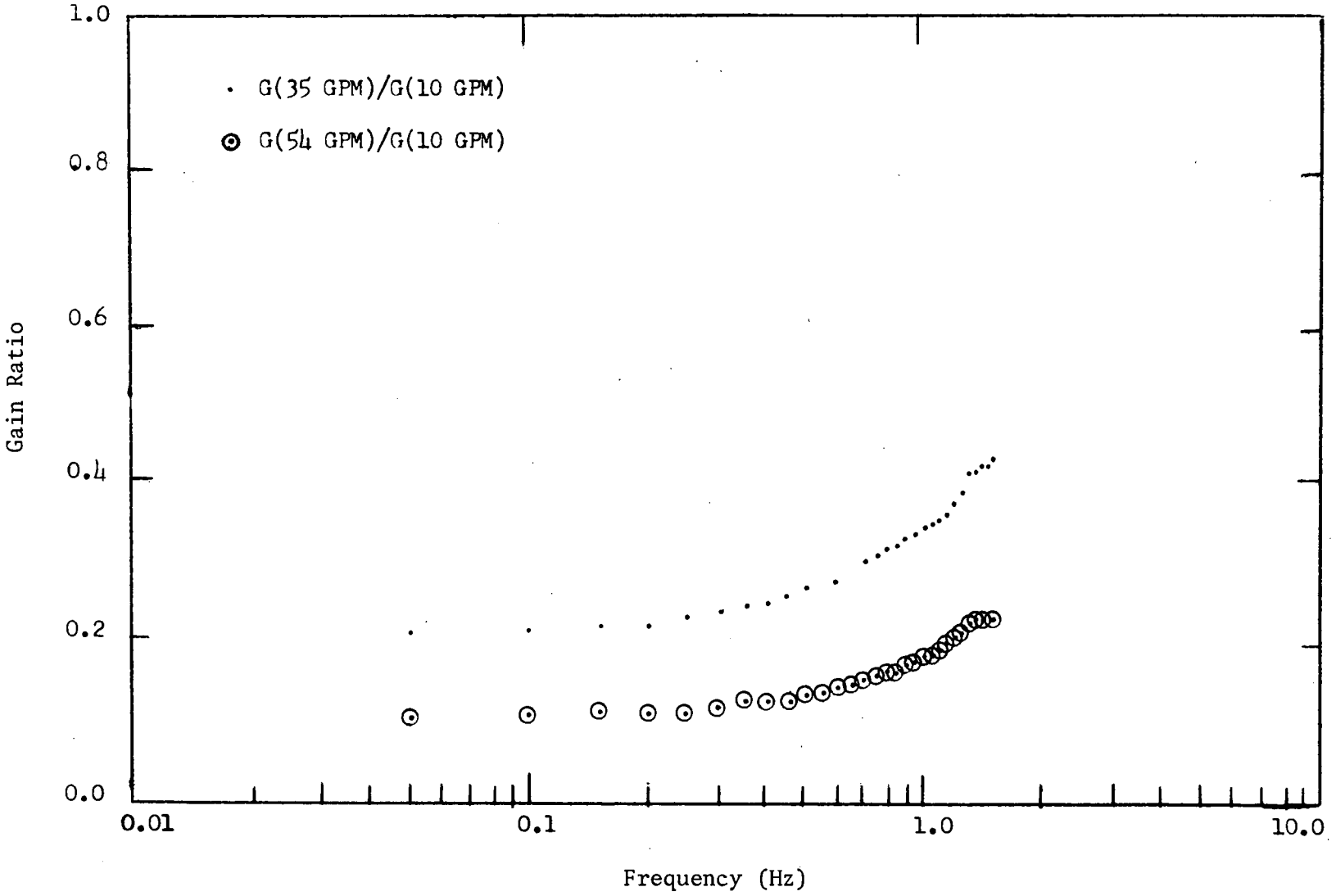

Figure B-27. Bundle 1B, gain ratios for thermocouple 0106 with rod 5 heated.

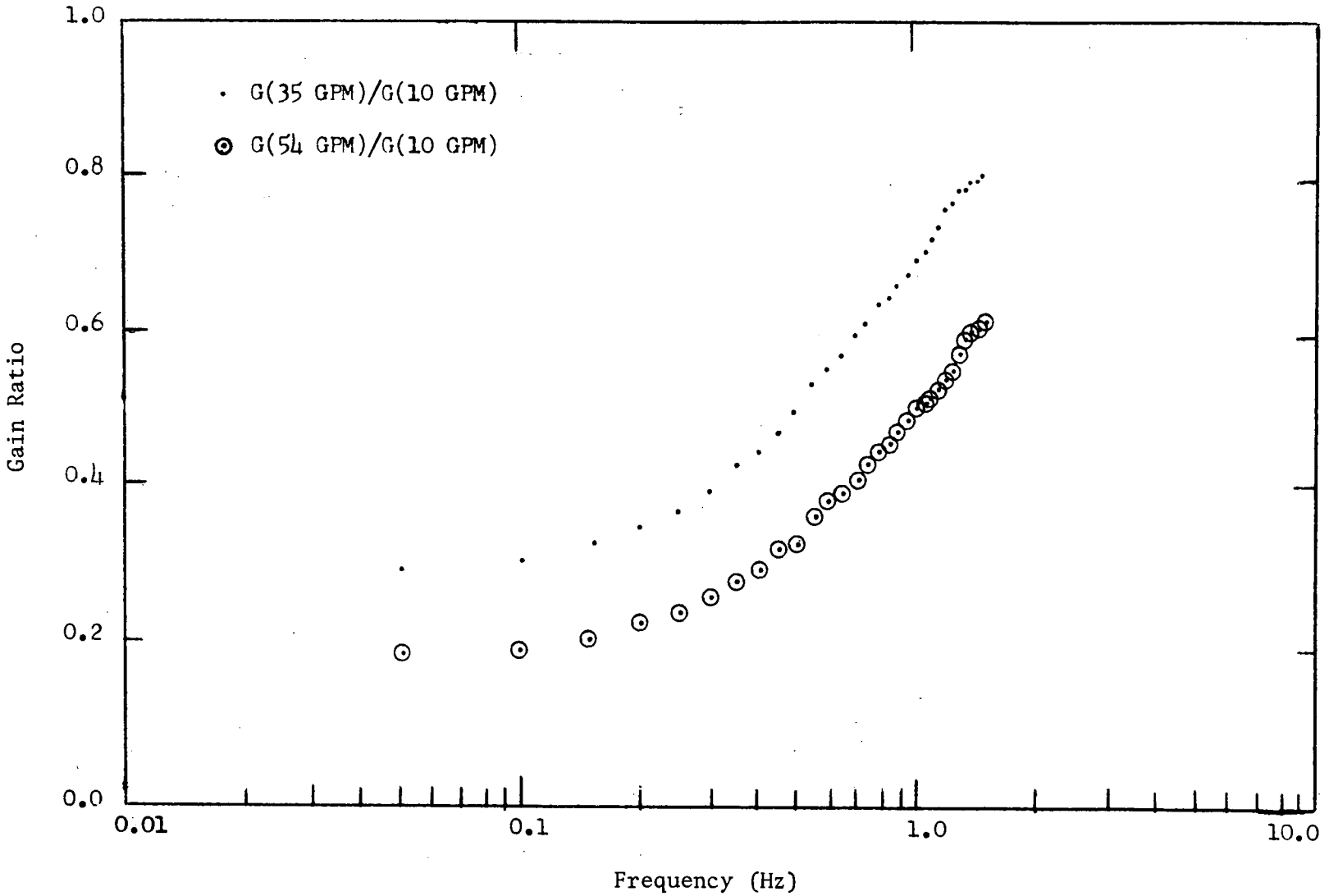

Figure B-28. Bundle 1B, gain ratios for thermocouple 1110 with rod 4 heated.

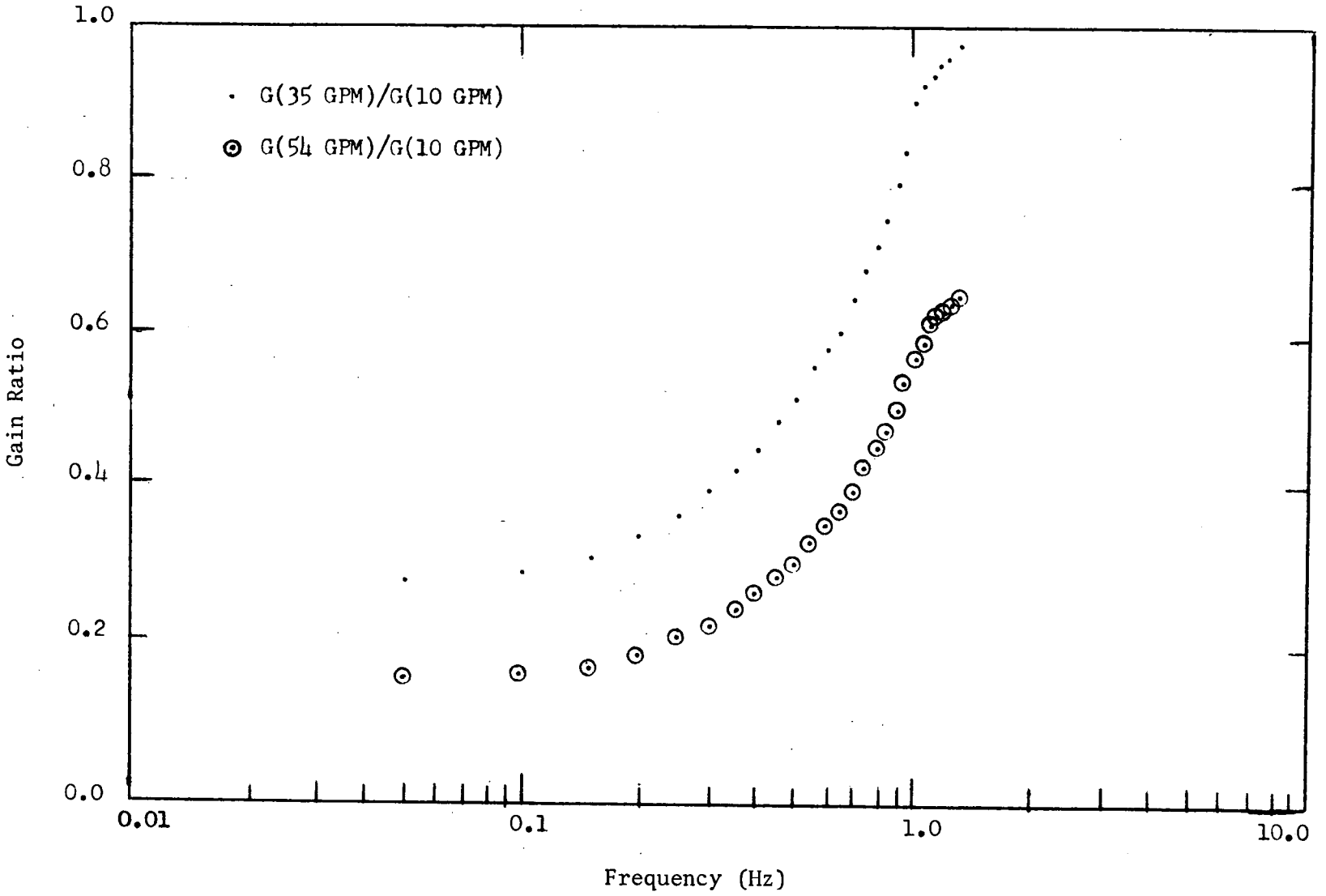

Figure B-29. Bundle 1B, gain ratios for thermocouple 1210 with rod 4 heated.

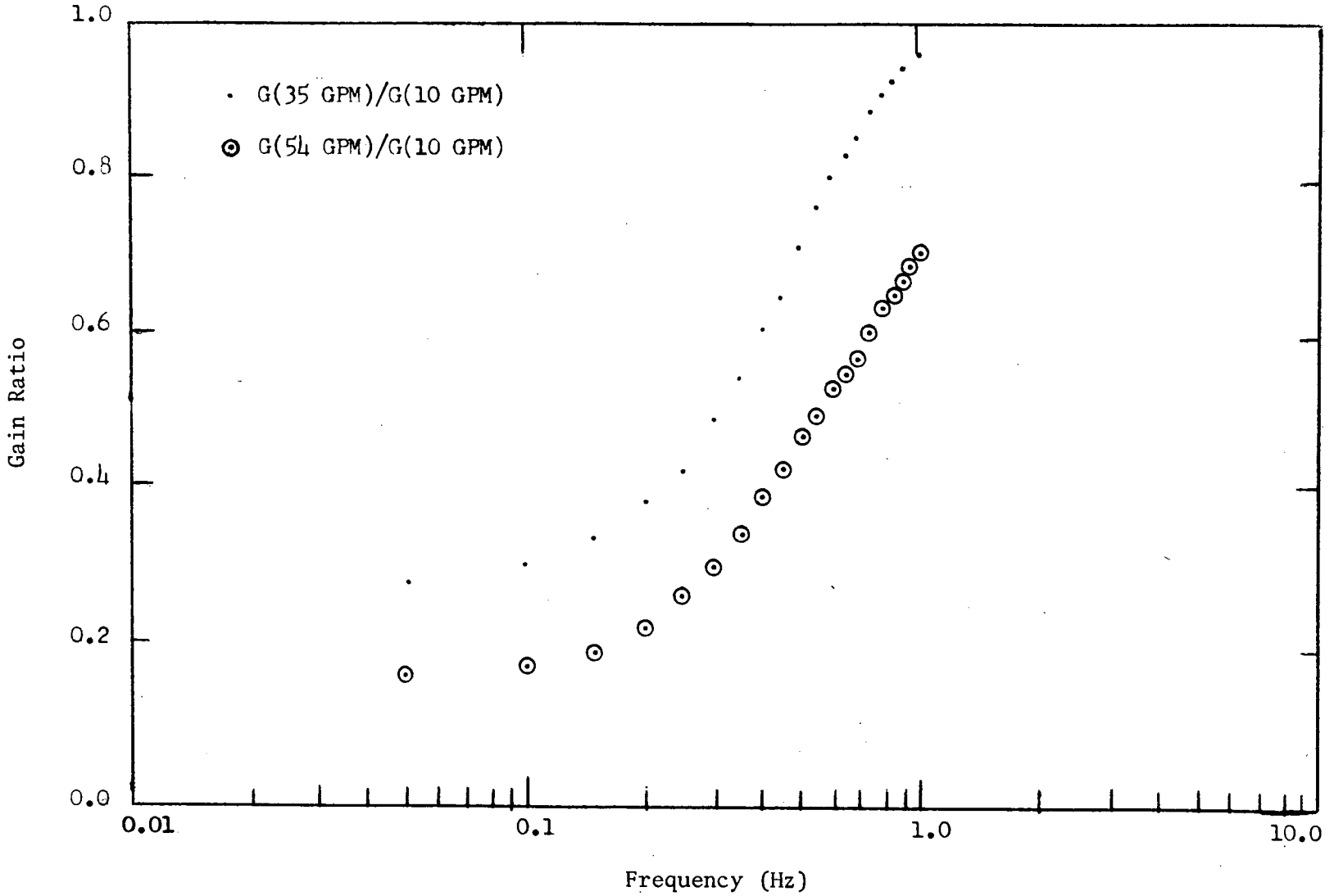

Figure B-30. Bundle 1B, gain ratios for thermocouple 0318 with rod 1 heated.

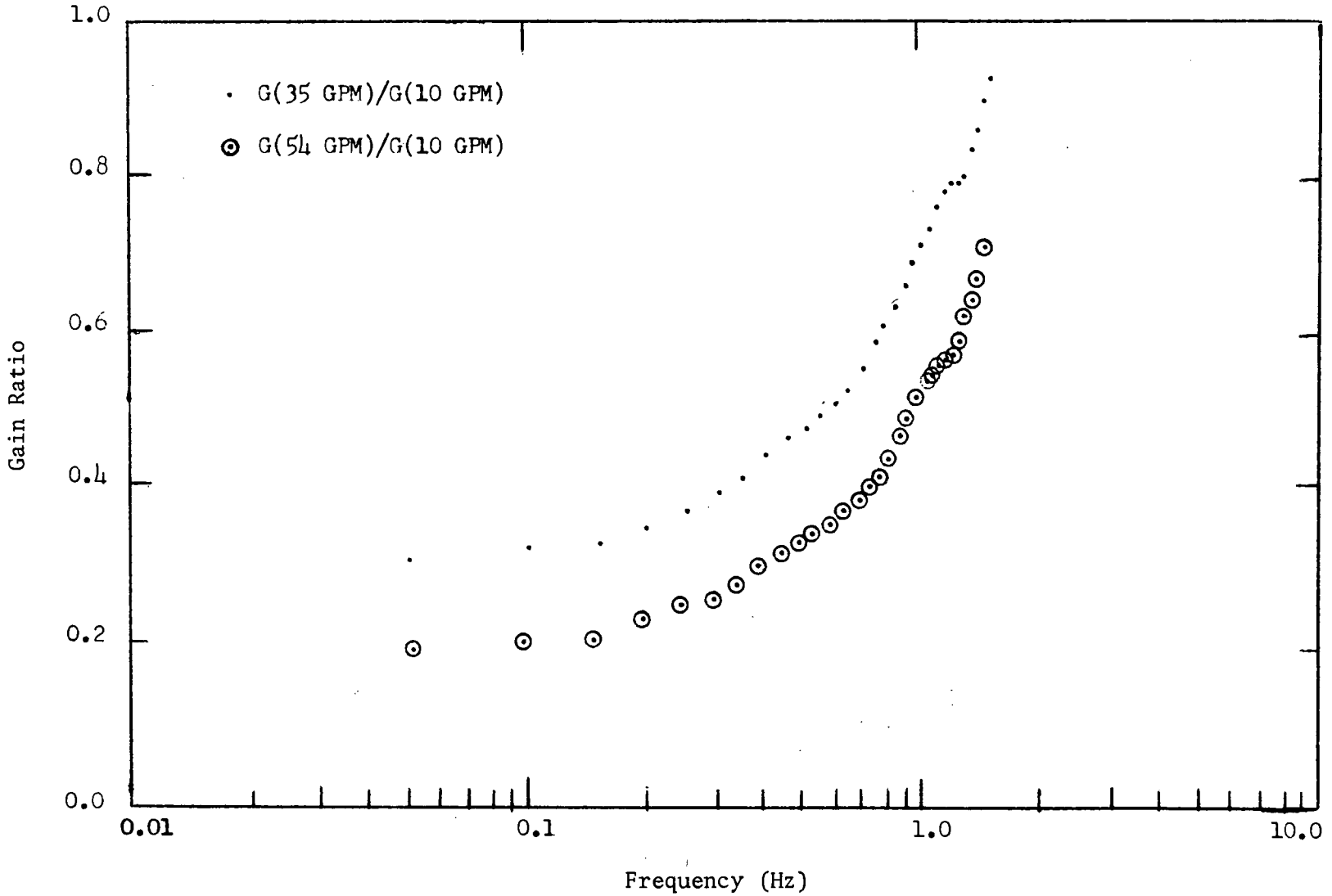

Figure B-31. Bundle 1B, gain ratios for thermocouple 0208 with rod 1 heated.

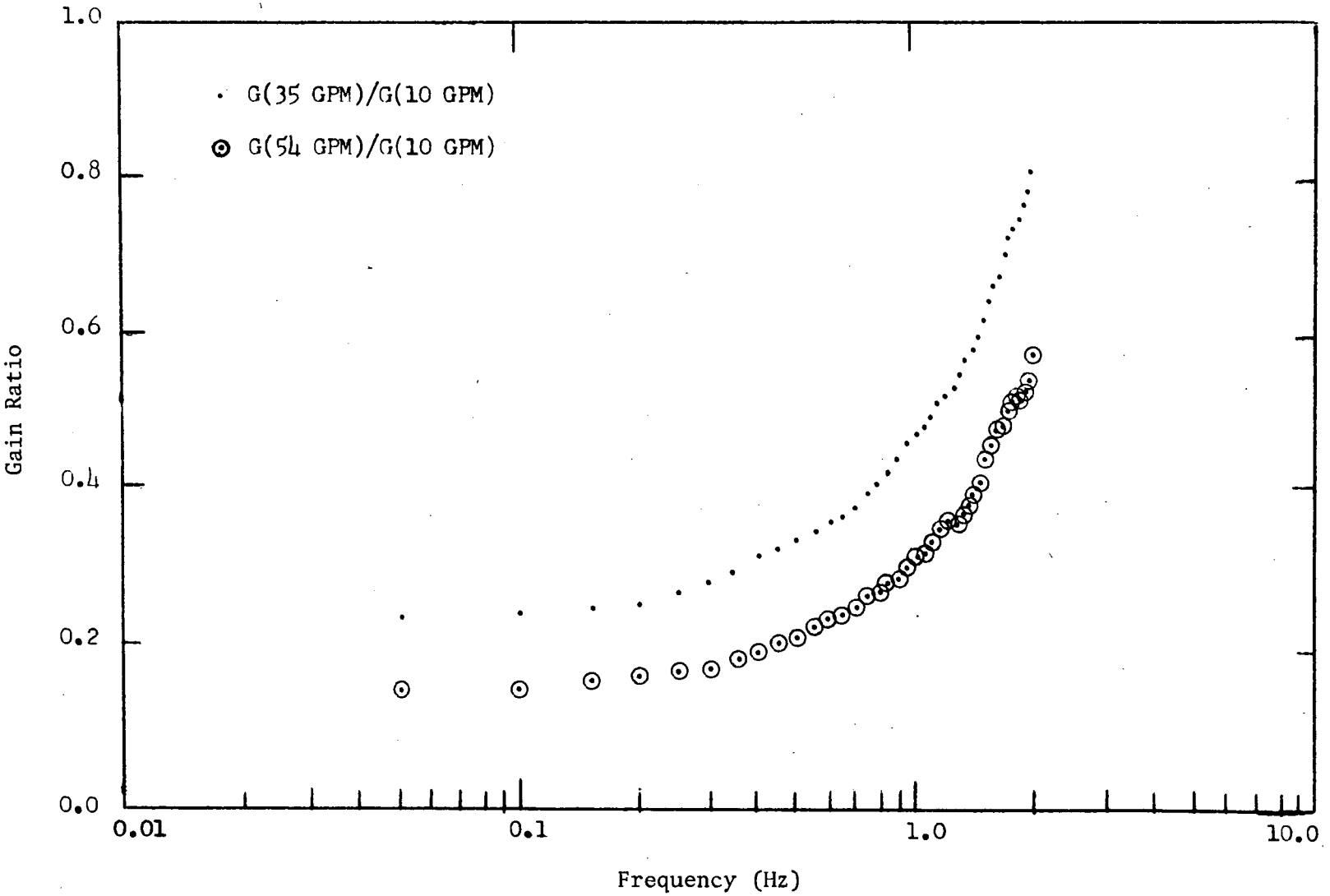

Figure B-32. Bundle 1B, gain ratios for thermocouple 1906 with rod 18 heated.

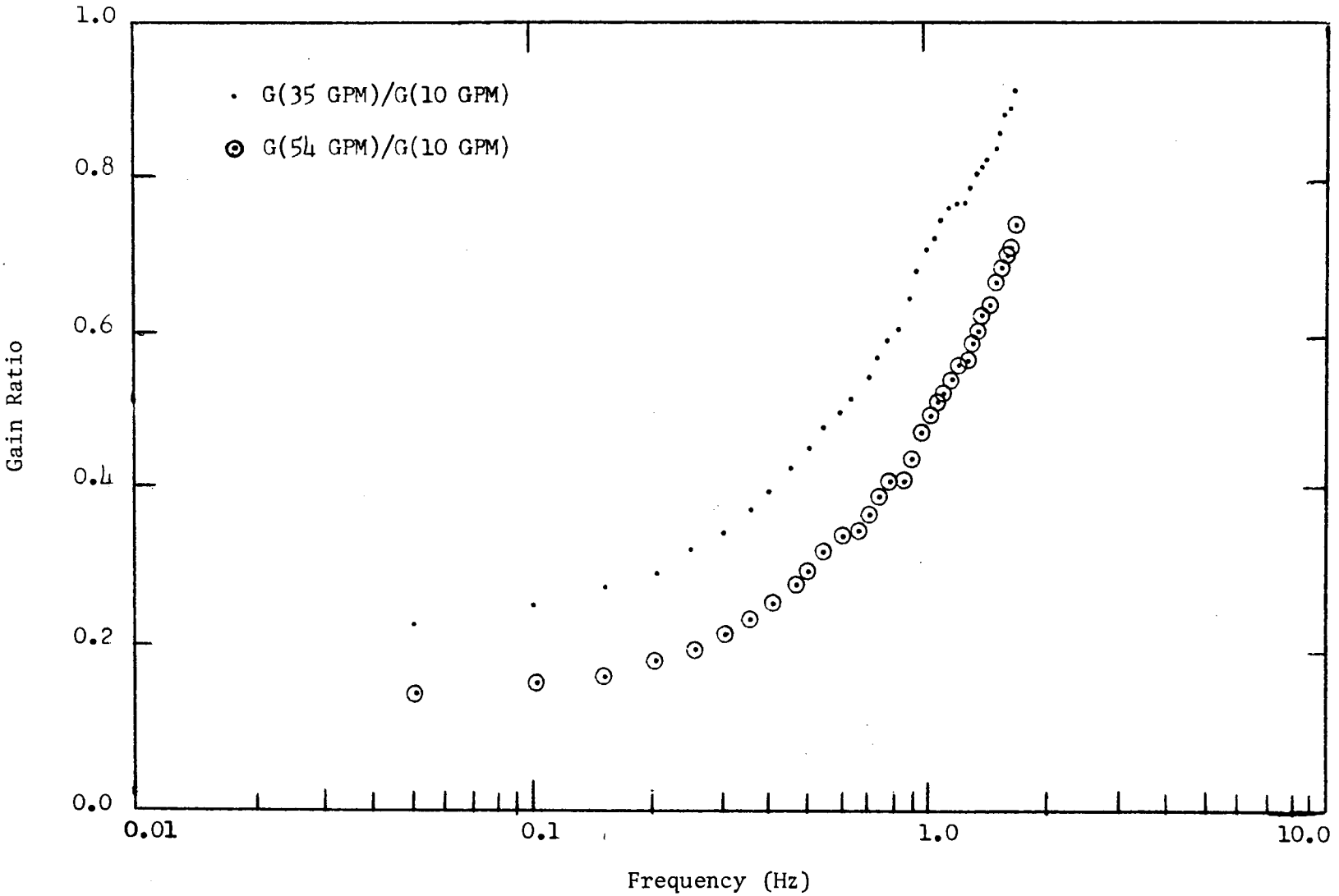

Figure B-33. Bundle 1B, gain ratios for thermocouple 0514 with rod 13 heated.

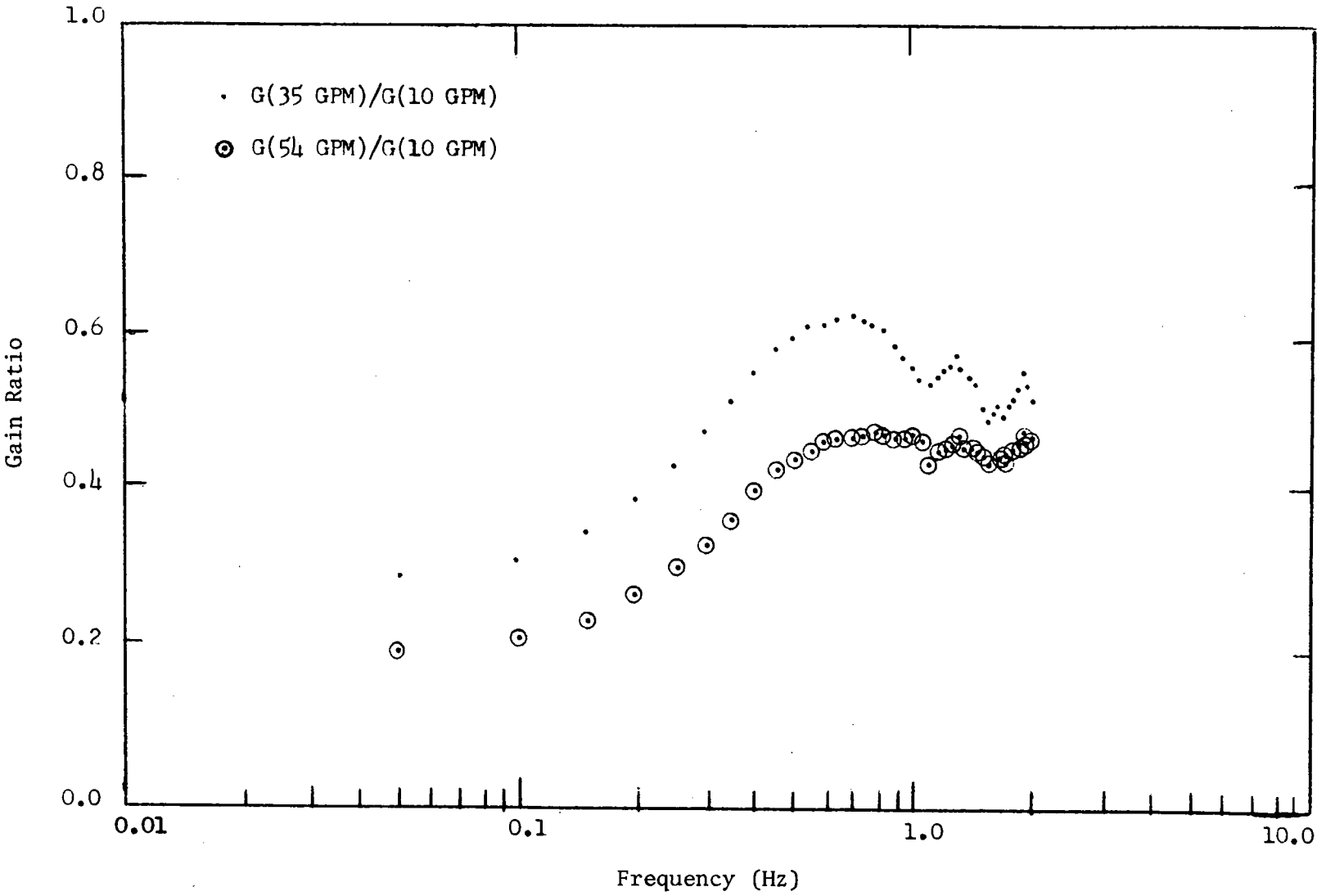

Figure B-34. Bundle 1B, gain ratios for thermocouple 1414 with rod 5 heated.

ORNL-TM-4597
UC-79, -79e and To Recipients
of -79m and -79p Who Do Not
Receive Copies Under -79e

INTERNAL DISTRIBUTION

1-3. N. J. Ackermann, Jr.
4. R. S. Booth
5. C. J. Borkowski
6-8. M. H. Fontana
9-10. D. N. Fry
11. W. O. Harms
12-14. T. W. Kerlin
15. T. S. Kress
16-17. R. C. Kryter
18. L. C. Oakes
19. L. F. Parsly
20. H. Postma
21. J. C. Robinson
22. G. S. Sadowski
23. R. L. Shepard
24-25. W. H. Sides
26. J. E. Swander
27. D. B. Trauger
28. J. L. Wantland
29-33. D. W. Wilson
34-36. Central Research Library
37. ORNL — Y-12 Technical Library
Document Reference Section
38-40. Laboratory Records Department
41. Laboratory Records, ORNL R.C.
42. ORNL Patent Office

EXTERNAL DISTRIBUTION

43. Research and Technical Support Division, AEC, ORO
44. Director, Research Division, AEC, ORO
45-46. Director, Division of Reactor Research and Development, U.S. Atomic Energy Commission, Washington, D.C. 20545
47-319. Given distribution as shown in TID-4500 under UC-79, -79e, -79m, and -79p category (25 copies — NTIS)